New insights into fluid flow and seep processes –

Case studies from the North Atlantic and offshore New Zealand

DISSERTATION

zur Erlangung des Doktorgrades

der Mathematisch-Naturwissenschaftlichen Fakultät

der Christian-Albrechts-Universität zu Kiel

vorgelegt von

Ines Dumke

Kiel, 2015

Referent: . . . . Prof. Dr. Christian Berndt

Koreferent: . . . . Prof. Dr. Sebastian Krastel

Tag der mündlichen Prüfung: . . . . 3. Juni 2015

Zum Druck genehmigt: . . . . 3. Juni 2015

. . . .

Der Dekan

Erklärung

Hiermit erkläre ich, dass ich die vorliegende Doktorarbeit selbstständig und ohne Zuhilfenahme unerlaubter Hilfsmittel angefertigt habe. Sie stellt, abgesehen von der Beratung durch meine Betreuer, nach Inhalt und Form meine eigene Arbeit dar. Weder diese noch eine ähnliche Arbeit wurde an einer anderen Abteilung oder Hochschule im Rahmen eines Prüfungsverfahrens vorgelegt, veröffentlicht oder zur Veröffentlichung vorgelegt. Ferner versichere ich, dass die Arbeit unter Einhaltung der Regeln guter wissenschaftlicher Praxis der Deutschen Forschungsgemeinschaft entstanden ist.

Kiel, den 17. März 2015

....

Ines Dumke

Abstract

In fluid flow systems, methane-rich fluids are transported from a subsurface reservoir through the overlying sediment strata to be expelled at the seafloor. Methane that passes through the water column and reaches the atmosphere will accelerate climate warming, as methane is a much stronger greenhouse gas than CO_2. As fluid flow systems such as hydrothermal vents and gas hydrate reservoirs may have released large amounts of methane into the water column and subsequently into the atmosphere, they are assumed to represent important contributors to major climate warming events, e.g. to the Paleocene-Eocene Thermal Maximum. However, the extent of this contribution is not fully understood, and hence, more detailed studies of fluid flow systems are required. In this thesis, four fluid flow systems are studied in terms of their development, venting activity, and relation to past and current climate warming periods. The studies were accomplished by using a variety of geophysical methods, including 2D and 3D seismic, sidescan sonar, and sediment echosounder methods, as well as heat flow measurements, geochemical analyses, and numerical modelling.

The first two of the studied fluid flow systems are located in the North Atlantic on the western Svalbard margin. This region is characterised by an extensive gas hydrate province inferred from bottom-simulating reflectors in seismic data. The distribution of the bottom-simulating reflector shows that gas hydrates are most abundant in a 3500 km² large area north of the Knipovich Ridge, an active spreading ridge that is part of the Mid Atlantic ridge system. This suggests that the thermal effects of the Knipovich Ridge promote thermogenic methane production in the vicinity, which is supported by heat flow increasing from the continental slope towards the ridge axis. Petroleum system modelling conducted at two sites north of the ridge shows that the conditions for thermogenic methane production have been met in the area, which may have resulted in the production of up to 0.2 Mt of bulk petroleum in two potential phases since the early Eocene. However, only the first phase in the early Eocene appears to be directly influenced by the thermal effects of the Knipovich Ridge. The second phase, which occurred in the Miocene, is mainly controlled by a rapid increase in sediment overburden.

The second study area on the Svalbard margin is located on the upper continental slope, where the base of the gas hydrate stability zone crops out at the seabed in water depths of < 400 m. The zone of intersection is characterised by numerous gas flares, which have been interpreted to indicate the release of methane from gas hydrate dissociation in response to warming bottom waters. The article of Berndt et al. (2014b), to which I contributed as a co-author, supports the hypothesis of hydrate dissociation causing the observed fluid venting, but argues that the dissociation is due to seasonal variations of bottom-water temperatures, rather than caused by global ocean warming. A 2-year time series of bottom-water temperatures shows that temperatures reach peak values (up to 4.9°C) in autumn and winter and minimum values (0.6°C) in spring. Numerical modelling of the gas hydrate stability zone shows that these temperature fluctuations result in lateral shifts of the

gas hydrate stability zone, which promote periodic dissociation and formation of hydrates near the zone of intersection. Carbonate samples from the seep sites indicate that seepage off Svalbard has been going on for several 1000 years.

Another study site is the Giant Gjallar Vent in the Norwegian Sea. The Giant Gjallar Vent is one of the largest vent systems in the North Atlantic and originated as a hydrothermal vent system at the Paleocene-Eocene transition. Previous studies based on 3D seismic data differed in their interpretations of the vent's present activity, describing the system as buried or as recently reactivated. New high-resolution 2D seismic and sediment echosounder data are used to re-interpret the Quarternary activity of the Giant Gjallar Vent. The new data show that the up to 12 m high surface elevation of the vent is caused by up-doming of the Quarternary sediments, which represent a seal to upward fluid migration. The doming therefore occurs in response to the build-up of overpressure beneath the seal. At one location, the seal has been breached and a potential leakage pathway extends from the seal up to the seafloor. Although indications for active venting were not observed, it seems that the Giant Gjallar Vent is preparing for a new phase of venting activity.

The fourth studied fluid flow system consists of 25 cold seep sites on New Zealand's Hikurangi Margin. The seeps exhibit various seabed morphologies that produce different intensity patterns in sidescan backscatter images. Classification of these patterns reveals that they fall into four distinct types that reflect variations in carbonate morphologies, including massive, up to 20-m-high structures (type 1), low-relief crusts (type 2), scattered blocks (type 3), and carbonate-free sites (type 4). The types correlate well with the occurrence of typical benthic seep fauna: communities living on sediment surfaces dominated at type 4 sites, seep fauna settling on hard substrate were found predominantly at type 2 and 3 sites, and non-seep epifauna were observed on type 1 carbonates of extinct cold seeps. Backscatter signatures in sidescan sonar images of cold seeps may therefore serve as a convenient proxy for variations in faunal habitats.

The studies show that all four fluid flow systems are unlikely to contribute significantly to the present climate warming period. Only two systems – the seeps on the upper slope off Svalbard and on the Hikurangi Margin – are actively releasing methane into the water column, but this release is not catastrophic. Rather, it is controlled by short-term variations in the fluid flow system, induced by changes in pressure and bottom-water temperature. However, gas hydrate systems and hydrothermal vent complexes must have contributed to climate warming in the past, e.g. during the Paleocene-Eocene Thermal Maximum. Quantification of the extent of these contributions should be the objective of future work.

Zusammenfassung

In Fluidflusssystemen werden methanangereicherte Fluide aus einem unterirdischen Reservoir durch die aufliegenden Sedimentschichten zum Meeresboden transportiert und dort ausgestoßen. Steigt das ausgestoßene Methan durch die Wassersäule bis an die Wasseroberfläche, tritt es in die Atmosphäre ein und kann somit zur Klimaerwärmung beitragen, denn Methan ist ein deutlich stärkeres Treibhausgas als CO_2. Fluidflusssysteme, z.B. hydrothermale Schlote und Gashydratreservoire, könnten in der Vergangenheit große Mengen Methan freigesetzt haben, welche zunächst in die Wassersäule und anschließend in die Atmosphäre gelangten. Es wird daher angenommen, dass Fluidflusssysteme einen wichtigen Beitrag zu großen Klimaerwärmungsereignissen wie dem Paläozän/Eozän-Temperaturmaximum leisteten. Das Ausmaß dieses Beitrages ist bislang jedoch nicht geklärt, weshalb detailliertere Studien zu Fluidflusssystemen erforderlich sind. In der vorliegenden Arbeit werden vier Fluidflusssysteme bezüglich ihrer Entwicklung und ihrer Gasaustrittsaktivität untersucht. Außerdem ist von Interesse, ob ein Zusammenhang mit der aktuellen Klimaerwärmungsphase sowie vergangenen Klimaereignissen besteht. Für die Untersuchungen wurden verschiedene geophysikalische Methoden wie 2D- und 3D-Seismik, Sidescan-Sonar- und Sedimentecholotmethoden eingesetzt, sowie Wärmeflussmessungen, geochemische Analyseverfahren und numerische Modellierung.

Die ersten beiden untersuchten Fluidflusssysteme befinden sich im Nordatlantik am Kontinentalrand von Spitzbergen. Diese Region zeichnet sich durch eine ausgedehnte Gashydratprovinz aus, die anhand sogenannter „bottom-simulating reflectors" (bodensimulierende Reflektoren) in seismischen Daten nachgewiesen wurde. Die Verteilung der bodensimulierenden Reflektoren zeigt, dass sich die Gashydrate vor allem auf ein 3500 km² großes Gebiet nördlich des Knipovich-Rückens konzentrieren. Da der Knipovich-Rücken Teil des Mittelatlantischen Rückensystems ist, deutet dies darauf hin, dass vom Rücken ausgehende thermale Effekte zu thermogener Methanproduktion in der Nähe des Rückens führen könnten. Unterstützt wird diese Hypothese vom Wärmefluss, welcher vom Kontinentalrand bis zum Knipovich-Rücken deutlich zunimmt. Die an zwei Stellen nördlich des Rückens durchgeführte Petroleumsystemmodellierung zeigt, dass die für thermogene Methanproduktion nötigen Bedingungen erfüllt gewesen sein könnten. Dies könnte die Produktion von bis zu 0.2 Mt Petroleum (Öl und Gas) seit dem frühen Eozän ermöglicht haben, wobei die Produktion während zwei Phasen stattfand. Nur die erste dieser beiden Phasen, welche im frühen Eozän stattfand, scheint dabei direkt durch die thermalen Effekte des Knipovich-Rückens beeinflusst worden zu sein. Die zweite Phase, die sich im Miozän ereignete, wird hauptsächlich durch eine starke Zunahme der Sedimentauflast kontrolliert.

Das zweite Untersuchungsgebiet in der Region Spitzbergen befindet sich am oberen Hang des Kontinentalrandes, wo die Untergrenze der Gashydratstabilitätszone in einer Wassertiefe von < 400 m den Meeresboden schneidet. Im Bereich des Zusammentreffens sind zahlreiche Gasfahnen zu beobachten, welche als Anzeichen für die Methanfreisetzung aus destabilisierenden Gashydraten

interpretiert werden. Es wird vermutet, dass die Gashydratauflösung durch sich erwärmendes Bodenwasser verursacht wird. Der Artikel von Berndt et al. (2014), zu dem ich als Co-Autorin beigetragen habe, unterstützt die Hypothese der Gashydratdestabilisierung als Grund für die beobachteten Fluidaustritte. Jedoch scheint die Destabilisierung eher durch saisonale Schwankungen der Bodenwassertemperatur bedingt zu sein, und nicht durch globale Ozeanerwärmung. Eine 2-Jahres-Zeitreihe der Bodenwassertemperaturen zeigt, dass die Temperaturen im Herbst bzw. Winter am höchsten sind (bis zu 4.9°C), während sie im Frühling ein Minimum erreichen (0.6°C). Die numerische Modellierung der Gashydratstabilitätszone verdeutlicht, dass die Temperaturschwankungen zu lateralen Verschiebungen der Gashydratstabilitätszone führen, welche periodische Destabilisierung und Neubildung von Gashydrat zur Folge haben. Karbonatproben aus dem Bereich der Gasaustritte deuten an, dass Methanfreisetzung vor Spitzbergen schon seit mehreren 1000 Jahren geschieht.

Ein weiteres Untersuchungsgebiet ist der Giant Gjallar Vent in der Norwegischen See. Der Giant Gjallar Vent ist eines der größten Gasaustrittssysteme im Nordatlantik und entstand ursprünglich als Hydrothermalsystem während des Übergangs vom Paläozän zum Eozän. Frühere Studien sind unterschiedlicher Auffassung, was die derzeitige Aktivität des Gasaustrittssystems betrifft. Anhand von 3D-seismischen Daten wurde der Giant Gjallar Vent entweder als inaktiv und verschüttet oder als kürzlich reaktiviert interpretiert. Neue, hochauflösende 2D-Seismik- und Sedimentecholotdaten erlauben nun eine Neuinterpretation der quartären Aktivität des Giant Gjallar Vents. Die Daten zeigen, dass die bis zu 12 m hohe Oberflächenerhebung über dem Aufstiegskanal durch Aufwölbung der quartären Sedimente verursacht wird, welche für aufsteigende Fluide weitgehend undurchlässig sind. Die Aufwölbung ist bedingt durch die Akkumulation von Fluiden unterhalb der undurchlässigen Schicht und dem damit verbundenen Aufbau von Überdruck. An einer Stelle konnten die aufliegenden Sedimente jedoch durchbrochen werden und eine potentielle Leckagezone reicht bis zum Meeresboden. Zwar wurden keine Anzeichen für aktiven Fluidaustritt beobachtet, doch es scheint, als steuere der Giant Gjallar Vent auf eine neue Fluidaustrittsphase zu.

Das vierte untersuchte Fluidflusssystem besteht aus 25 Gasaustrittsstellen (sogenannten Cold Seeps) entlang des neuseeländischen Hikurangi-Kontinentalrandes. Die Austrittsstellen sind durch eine Reihe von Meeresbodenmorphologien gekennzeichnet, welche verschiedene Rückstreuungsmuster in Sidescan-Sonar-Daten produzieren. Die Klassifizierung dieser Muster zeigt, dass sich genau vier Mustertypen feststellen lassen. Die Mustertypen beschreiben Variationen der Karbonatmorphologien und reichen von massiven, bis zu 20 m hohen Strukturen (Typ 1) über niedrige Krusten (Typ 2) und verstreute Blöcke (Typ 3) bis hin zu karbonatfreien Austrittsstellen (Typ 4). Die Mustertypen korrelieren gut mit der Verteilung typischer benthischer Meeresbodenfauna. So finden sich auf Sedimentoberflächen lebende Organismen an Typ-4-Stellen, während harte Oberflächen bevorzugende Fauna vor allem an Typ-2- und Typ-3-Stellen nachgewiesen wurde. Epifauna, welche nicht auf einen beständigen Methanfluss angewiesen ist, wurde auf Typ-1-Karbonaten inaktiver Austrittsstellen beobachtet. Rückstreuungsmuster in Sidescan-Sonar-Daten von Gasaustrittsstellen können somit wertvolle Hinweise auf Variationen in Meeresbodenhabitaten liefern.

Wie die vier Studien zeigen, ist es unwahrscheinlich, dass die untersuchten Fluidflusssysteme maßgeblich zur aktuellen Klimaerwärmung beitragen. Lediglich an zwei Systemen – die Gasaustritts-

stellen am oberen Kontinentalrand von Spitzbergen und am Hikurangi-Kontinentalrand – wird derzeit eine Freisetzung von Methan in die Wassersäule beobachtet. Diese Freisetzung ist nicht katastrophal, sondern wird stattdessen durch relativ kurzzeitige Variationen innerhalb des Fluid-flusssystems hervorgerufen. Dazu gehören beispielsweise Veränderungen im Druck und in der Bodenwassertemperatur. Trotzdem müssen Gashydratsysteme und hydrothermale Schlote in der Vergangenheit zu Klimaerwärmungsereignissen wie dem Paläozän/Eozän-Temperaturmaximum beigetragen haben. Die Quantifizierung dieser Beiträge bleibt das Ziel zukünftiger Forschung.

Contents

List of abbreviations

AOM	anaerobic oxidation of methane
BGHSZ	base of the gas hydrate stability zone
BPU	Base Pleistocene Unconformity
BSR	bottom-simulating reflector
CMP	common mid-point
CTD	conductivity, temperature, density
DSDP	Deep Sea Drilling Project
GC	gravity core
GGV	Giant Gjallar Vent
GHSZ	gas hydrate stability zone
HI	hydrogen index
IODP	Integrated Ocean Drilling Program
MASOX	Monitoring Arctic Seafloor-Ocean Exchange
mbsf	metres below seafloor
mbsl	metres below sea level
MC-ICP-MS	multi-collector inductively-coupled plasma mass spectrometry
MCS	multichannel seismic
MIC-ICP-MS	multi-ion-counting inductively-coupled plasma mass spectrometry
MOx	methane oxidation
ODP	Ocean Drilling Program
PDB	Pee Dee Belemnite
PETM	Paleocene-Eocene Thermal Maximum
Q-ICP-MS	quadrupole inductively-coupled plasma mass spectrometry
SIRMS	stable isotope ratio mass spectrometry
SMOW	standard mean ocean water
SMTZ	sulphate-methane transition zone
TF	transform fault
TOC	total organic carbon
TWT	two-way travel time
USBL	ultra-short base line
V-PDB	Vienna Pee Dee Belemnite
XRD	X-ray diffraction

Chapter 1

Introduction

The work presented in this thesis was carried out in the framework of the Kiel Cluster of Excellence "Future Ocean". The Cluster is a research network with members from the Christian-Albrechts-University in Kiel (CAU), the Helmholtz Centre for Ocean Research (GEOMAR), the Leibniz Institute for the World Economy (IfW), and the Muthesius Academy of Fine Arts and Design (MKHS). It is dedicated to the multidisciplinary study of the past and present ocean system and the application of these results to predict the future evolution of the world's oceans.

The oceans strongly influence global climate and are vitally important for human welfare. However, humans may also endanger the marine environment, and vice versa. For example, human actions such as pollution and anthropogenic CO_2 emissions increasingly affect the oceans, whereas major natural hazards originating from the oceans, e.g. submarine landslides and tsunamis, present a risk to human life. It is therefore important to improve our understanding of the basic ocean system in order to better predict its reaction to changes and establish sustainable ocean management.

Future Ocean addresses these challenges in 11 research topics. This thesis is part of research topic R09, which investigates ocean controls on climate and environment at transitions to warming periods. More specific, R09 studies past events of climate warming to identify the main ocean feedback processes on climate, which will help to understand future global warming.

One aspect is to find out what role geological carbon emissions from fluid flow systems played in driving environmental change during warming periods such as the Paleocene-Eocene Thermal Maximum (PETM). Although fluid flow systems, where methane is transported from a subsurface reservoir to the seabed, have been extensively studied world-wide (e.g. Han and Suess, 1989; Cartwright, 1994a; Pecher et al., 2004; Gay et al., 2007; Brothers et al., 2013), their contribution to the global carbon cycle is not well understood and often overlooked (Kvenvolden et al., 2001). However, fluid flow systems may have released large amounts of methane into the water column and subsequently into the atmosphere (e.g. Dickens et al., 1995; Svensen et al., 2004). Methane that reaches the atmosphere can accelerate global warming, as it is a much stronger greenhouse gas than CO_2 (Harvey and Huang, 1995). To understand how the oceans are dealing with large-scale methane input from fluid flow systems, and to constrain the geological forcing mechanisms of climate warming events such as the PETM, it is necessary to study these systems in more detail.

1.1   Fluid flow systems

Fluid flow systems are found in a variety of tectonic environments – active margins, passive margins, transform faults, and intraplate settings – and in all kinds of oceanographic settings, ranging from coastal areas to the deep ocean (e.g. Lewis and Marshall, 1996; Whiticar, 2002; Dupré et al, 2010; Gay et al., 2012; Talukder, 2012, and references therein; Leduc et al., 2013). There are many different types of fluid flow systems, such as hydrothermal vents (e.g. Jamtveit et al., 2004; Planke et al., 2005), polygonal fault systems (e.g. Cartwright, 1994b; Berndt et al., 2003), and gas chimneys (e.g. Pecher et al., 2004; Løseth et al., 2009) (Fig. 1.1). Which type of fluid flow system is formed in an area depends not only on the tectonic setting and fluid composition, but especially on the processes driving fluid production and migration. Berndt (2005) distinguishes between compaction-controlled, volcanism-controlled, petroleum, and freshwater systems.

Despite the great variety of fluid flow systems, they usually have a common structure (Judd and Hovland, 2007; Talukder, 2012). This structure consists of a fluid reservoir and a conduit for transporting fluids towards the seabed. In the case of active or past prolonged fluid venting, the systems are also often characterised by a surface expression (Judd and Hovland, 2007; Talukder, 2012).
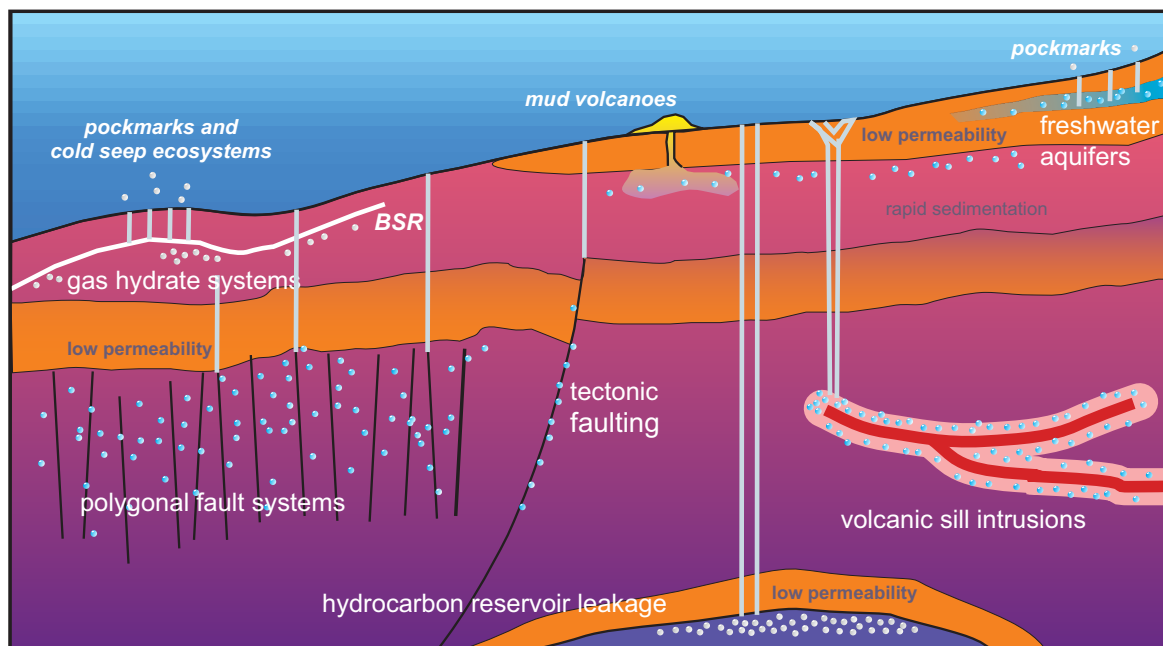
Figure 1.1: Illustration of different types of fluid flow systems that occur on passive continental margins. Most structures can also be found on active margins. Small filled circles represent gas bubbles. BSR – bottom-simulating reflector. (Berndt, 2005)

1.1.1   Fluid reservoirs

Fluids are stored in subsurface reservoirs. Reservoirs are generally zones of high porosity and permeability surrounded by sediments of lower permeability, or bounded by sealing faults (Judd

and Hovland, 2007). Fluids are thus prevented from escaping. However, reservoir seals may become unstable and once leakage occurs, fluid flow systems may develop. Examples for reservoirs include deep (<1 km) hydrocarbon reservoirs (e.g. Gay et al., 2007), gas hydrate systems (e.g. Kvenvolden, 1988), and shallow freshwater acquifers (e.g. Bokuniewicz, 1992) (Fig. 1.1).

1.1.1.1 Origin of gas

Most types of fluid flow systems are associated with methane, which is the most common gas in marine sediments (Judd and Hovland, 2007). Sedimentary methane can be of either biogenic or abiogenic origin, with the term 'biogenic' referring to microbial (or bacterial) and thermogenic methane production (Whiticar, 1999).

Microbial methane

At least 20% of natural gas accumulations world-wide are associated with methane of microbial origin (Rice and Claypool, 1981; Wiese and Kvenvolden, 1993). Microbial methane is produced by methanogenic archaea during either CO_2 reduction in sulphate-free marine sediments (Equation 1.1), or acetate fermentation in freshwater sediments (Equation 1.2) (Whiticar et al., 1986; Schoell, 1988).

$$CO_2 + 4H_2 \rightarrow CH_4 + 2H_2O \tag{1.1}$$

$$CH_3COOH \rightarrow CH_4 + CO_2 \tag{1.2}$$

Microbial methanogenesis in marine sediments requires anoxic conditions and temperatures of 4-55°C (optimum ~35°C), although one species of methanogens can also exist at temperatures of up 97°C (Rice and Claypool, 1981; Wiese and Kvenvolden, 1993). Another requirement is the presence of organic matter (>0.5% total organic carbon (TOC)) (Rice and Claypool, 1981). Large amounts of organic matter often accumulate in areas with high sediment input. However, sedimentation rates should not be too fast as burial also increases sediment temperature, which will cause methanogenesis to cease once the temperature window is exceeded. Clayton (1992) considers sedimentation rates of 200 to 1000 m Myr^{-1} as optimal. Under favourable conditions, ~10% of the TOC can be transformed into microbial methane (Clayton, 1992).

Thermogenic methane

Organic matter that is not transformed remains in the sediment and eventually becomes kerogen, i.e., insoluble organic remains (Wiese and Kvenvolden, 1993). Sedimentary rocks that contain a high amount of kerogen (>2% TOC) are referred to as source rocks, from which hydrocarbons can be produced thermogenically (Judd and Hovland, 2007). Thermogenic hydrocarbon production involves thermal cracking of kerogen. Depending on the type of kerogen, which is controlled by the H/C and O/C ratios, as well as the origin of the organic matter, different types of hydrocarbons are produced (Table 1.1) (Tissot and Welte, 1984).

Table 1.1: Overview of the different types of kerogen and associated hydrocarbons.

Kerogen				produced hydrocarbons
type	H/C ratio	O/C ratio	organic matter origin	
I	high	low	lacustrine (freshwater)	crude oil (C_{15+})
II	intermediate	intermediate	anoxic marine environments	crude oil (C_{15+}) condensate ($C_6 - C_{15}$) wet gas ($C_2 - C_5$)
III	low	high	terrestrial	dry gas (C_1, i.e., methane)

In addition to the type of kerogen, the type of hydrocarbons produced also depends on the sediment temperature and the level of maturity (Wiese and Kvenvolden, 1993). Three levels of maturity are distinguished: (1) immature, where condictions for thermogenic hydrocarbon production are not yet fulfilled; (2) mature, i.e., production can take place; and (3) post-mature or overmature, where production is no longer possible. The temperature window for thermogenic hydrocarbon production is 60-260°C. Depending on the geothermal gradient, production may occur down to depths >10 km (Judd and Hovland, 2007).

Abiogenic methane

Abiogenic methane, i.e., methane derived from inorganic processes, has been produced under laboratory conditions (Foustoukos and Seyfried, 2004), but conclusive evidence for its occurrence in natural settings is rare (e.g. Fiebig et al., 2009). Abiogenic methane production is proposed to occur at hydrothermal systems located either in sediment-free mid ocean ridge settings (Welhan, 1988) or onshore (Fiebig et al., 2009). In addition, abiogenic methane may form during serpentinization of the oceanic basement, e.g. at slow-spreading ridges (Minshull et al., 1998).

Distinguishing between origins of methane

Stable isotope analysis is the most reliable tool to distinguish between different origins of methane (e.g. Rice and Claypool, 1981; Cicerone and Oremland, 1988). The method uses the ratio of the two stable carbon isotopes, ^{13}C and ^{12}C, which differ strongly for the carbon of methane molecules of different origins. The isotope ratios are expressed in the $\delta^{13}C$ notation (Equation 1.3) for which the Pee Dee Belemnite (PDB) standard is most commonly used.

$$\delta^{13}C = \frac{^{13}C/^{12}C_{sample} - ^{13}C/^{12}C_{standard}}{^{13}C/^{12}C_{standard}} \times 100 \qquad (1.3)$$

The $\delta^{13}C$ of methane is typically combined with the stable hydrogen isotope ratio δD as shown in Fig. 1.2. δD is based on the D/H ratio, or $^2H/^1H$, relative to the SMOW (standard mean ocean water) standard (Whiticar, 1999). Microbial methane is characterised by $\delta^{13}C$ values ranging between -110‰ to -50‰ and δD of -400‰ to -150‰ (Fig. 1.2). Thermogenic methane is more enriched in ^{13}C, resulting in $\delta^{13}C$ values of about -50‰ to -20‰ (Whiticar, 1999). Even heavier $\delta^{13}C$ values (>-20‰) are associated with abiogenic methane (Fig. 1.2).
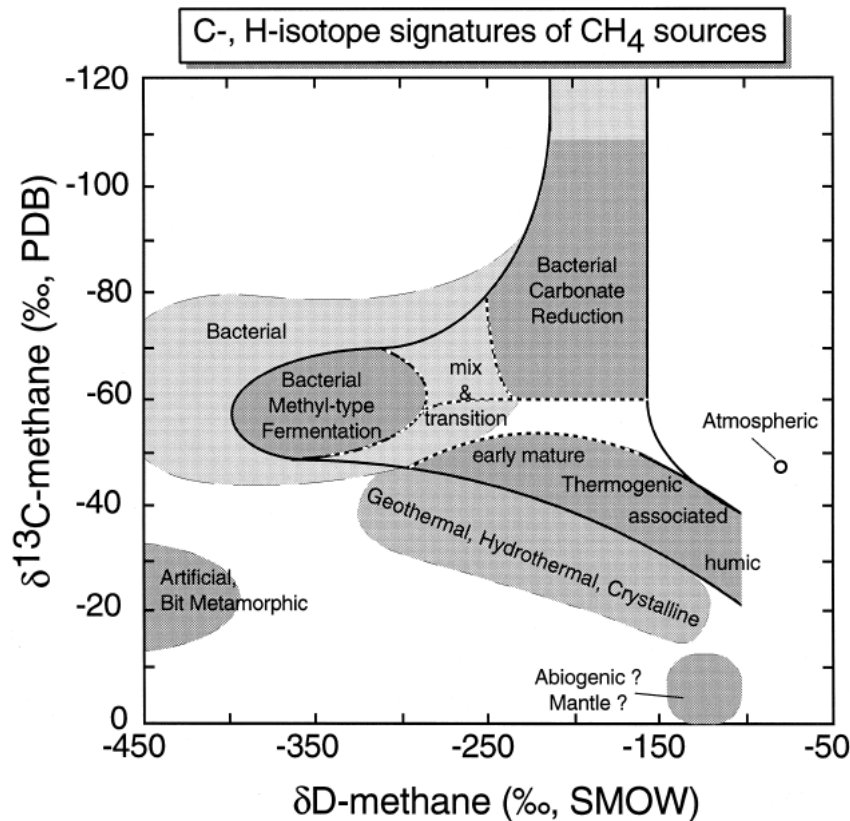
Figure 1.2: Diagram of $\delta^{13}C$ and δD, showing the classification of the different methane origins (bacterial, thermogenic, abiogenic). PDB – Pee Dee Belemnite, SMOW – standard mean ocean water. (Whiticar, 1999)

1.1.1.2 Gas hydrates

Gas hydrates are a subgroup of clathrates, i.e., solid compounds consisting of a guest molecule surrounded by a cage-like framework of molecules of a different kind (e.g. Pellenberg and Max, 2000). The guest molecule in hydrates is a gas molecule, typically methane, and the cage structure is made up of water molecules (Fig. 1.3) (Kvenvolden, 1993). Three types of hydrate structures (structures I, II, and H) are found in natural environments (Sloan, 1998). The structure determines how much methane gas can be contained in a certain amount of methane hydrate. For a fully saturated structure I hydrate - the most common structure in nature (Kvenvolden, 1995) - 1 m^3 of methane hydrate may contain up to 164 m^3 of methane gas and 0.8 m^3 of water (Kvenvolden, 1993).

The stability of gas hydrates is strongly controlled by temperature and pressure conditions (Fig. 1.4). Gas hydrates are stable only at high pressures and low temperatures, which restricts their occurrence to areas characterised by water depths >300 m and bottom-water temperatures of less than 2°C (Kvenvolden, 1995). Gas hydrates are thus only found in onshore polar regions and deep marine environments such as continental slopes (Kvenvolden, 1993, 1995, 2000). In addition, gas hydrates can only form in areas with large supplies of water and gas molecules (Hovland and Judd, 1988).

In oceanic settings, gas hydrates are usually found at water depths exceeding 300-500 m (e.g. Hyndman et al., 1992; Bouriak et al., 2000; Dillon and Max, 2000; Vanneste et al., 2005b; Haacke et al., 2007; Sarkar et al., 2012). Depending on the depth range of the gas hydrate stability zone (GHSZ), gas hydrates may be stable within the sediment as well as at and above the seabed. In general, the thickness of the GHSZ ranges between ~100 m and ~1 km (e.g. Chand et al., 2008) and is controlled by the geothermal gradient, the water temperature, the water depth (and hence pressure), the presence of inhibitors such as NaCl, and the gas composition (Sloan, 1998). The highest concentrations of hydrate are typically observed near the base of the gas hydrate stability zone (BGHSZ) (Dillon and Max, 2000).
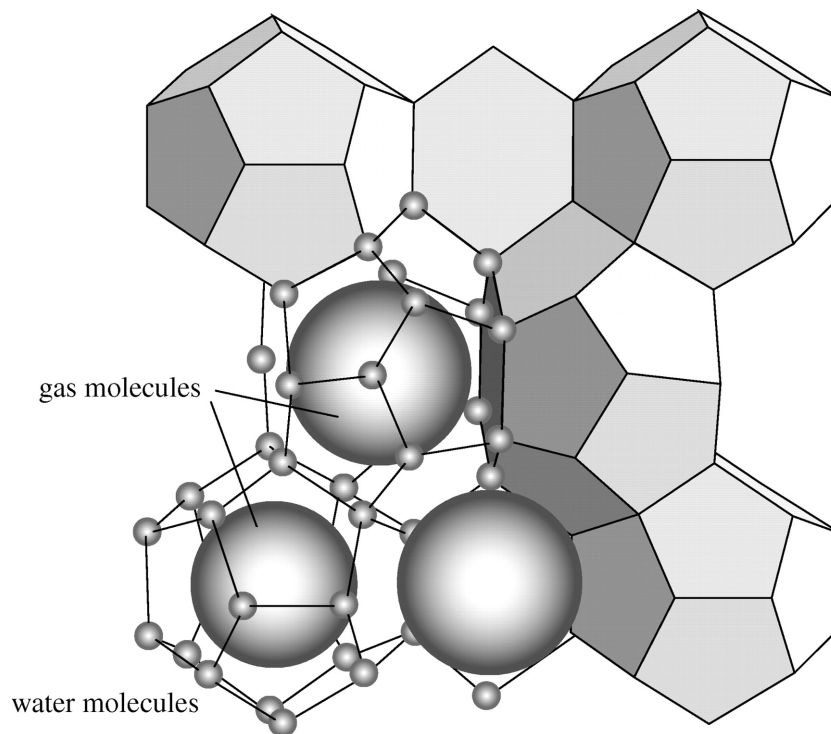
Figure 1.3: Schematic of structure I gas hydrate. Water molecules form a cage structure that traps one gas molecule within it, e.g. methane. (Maslin et al., 2010)

More than 99% of the hydrate-bound gas molecules are typically methane (C_1) with a $\delta^{13}C$ between -57 to -73‰, indicating microbial origin (Kvenvolden, 1995, 2000). However, hydrates may also contain higher hydrocarbons such as ethane (C_2) and propane (C_3). If more than 1% of higher hydrocarbons are present, this is a strong indication for the involvement of thermogenic gas. In fact, methane hydrates may hold a significant proportion of thermogenic methane, e.g. in the Gulf of Mexico (Brooks et al., 1986) and the Caspian Sea (Ginsburg et al., 1992).

Below the BGHSZ, free gas may exist, e.g. as a result of a temperature-induced vertical shift of the BGHSZ that caused hydrates at the bottom to be no longer stable (e.g. Dillon and Max, 2000). Although hydrate-cemented sediments represent a barrier to upward gas migration, fluid pressures can become high enough to enable bypass of the GHSZ and subsequent migration towards the seabed (e.g. Gorman et al., 2002; Holbrook et al., 2002; Flemings et al., 2003; Tréhu et al., 2004).

Gas hydrates are thus important components in fluid flow systems as they represent reservoirs from which fluids may be transported upwards to be expelled at the seafloor.
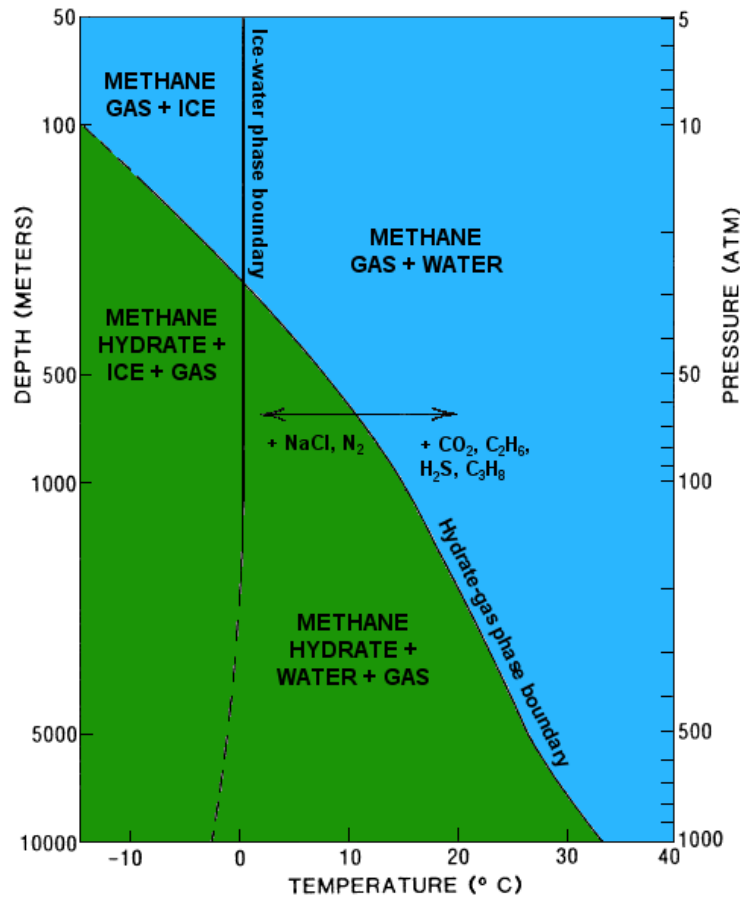
Figure 1.4: Hydrate phase diagram illustrating the boundary between methane hydrate (green) and free gas (blue). The addition of different molecules shifts the stability curve as indicated by the arrows. For the depth scale, lithostatic and hydrostatic pressure gradients of 10.1 kPa m^{-1} are assumed. Adapted from Kvenvolden (1993).

1.1.2 Fluid conduits

Due to the low density of free gas, the reservoir fluids are buoyant and tend to migrate towards the seabed. Upward migration can also be promoted by overpressure, i.e., fluid pressure exceeding hydrostatic pressure (Clayton and Hay, 1994). However, capillary effects at pore throats may reduce the mobility of water-free gas mixtures (Clayton and Hay, 1994; Henry et al., 1999), and migration may be further impeded if the overlying sediment is resistant to fracturing (Clayton and Hay, 1994). Hyndman and Davis (1992) summarise three geological settings in which upward fluid migration commonly occurs: (1) accretionary wedges, where waterlogged sediments are compacted due to tectonic movements, (2) subduction zones, where accretionary wedges are absent but underthrusting of sediments occurs, and (3) passive-margin areas of rapid sediment loading.

Fluid migration is differentiated into primary migration, i.e., from the source rock to the reservoir, and subsequent secondary migration (Judd and Hovland, 2007). Fluid transport towards the

seabed requires conduits linking the reservoir with the sediment surface. Such conduits are usually weakness zones that are either structurally or stratigraphically controlled (Krabbenhoeft et al., 2013).

Fluid flow patterns are often related to the presence of faults, as upward migration of fluids is facilitated by pre-existing fault networks, at least in the upper few 100 m (Clayton and Hay, 1994). Where faults serve as migration conduits, fluid expulsion at the seafloor is often restricted to localised zones (e.g. Barry et al., 1996; Stakes et al., 1999). Fluid flow to the seabed may continue as long as the fault network is kept open, e.g. by high pore fluid pressures. However, the closing of fault pathways will prevent further fluid migration and trap the fluids in the reservoir.

If a reservoir is effectively sealed and fluid accumulation continues, overpressure will build up due to the buoyancy of hydrocarbons (Osborne and Swarbrick, 1997). Once a critical threshold is reached, the reservoir seal will be fractured, allowing fluids to migrate into overlying sediments. Fracturing of the seal occurs by either capillary failure when the capillary resistance to migration is exceeded, or fracture failure, where the overpressure is sufficient to induce fracturing (Clayton and Hay, 1994). New pathways are then opened, but previously closed fractures can also be re-used. As the overpressure bleeds off, fractures will close again, which may result in periodic opening and closing of the seal in response to changing pore fluid pressures (Sibson et al., 1988; Cartwright, 1994a; Roberts and Nunn, 1995).

While vertical to near-vertical faults are the most common fluid migration pathways, lateral fluid advection is also observed (e.g. Stakes et al., 1999). In addition, fluid migration may be facilitated by permeable stratigraphic horizons and lenses, e.g. of sandy material. In this case, fluid pressures have to be sufficiently high to force a migration pathway (Clayton and Hay, 1994; Liu and Flemings, 2007).

1.1.3   Surface activity

Once migrating fluids reach the sediment surface, they are expelled into the water column. Depending on the type of fluids, different terminology is used to describe the site of expulsion: "vents" are associated with hydrothermal fluids, i.e., hot fluids, "seeps" refer to the venting of cold fluids, e.g. oil and gas, and "springs" occur where groundwater is expelled at the seafloor (Judd and Hovland, 2007). Prolonged fluid expulsion may affect the surrounding seabed, leading to a variety of seafloor features such as pockmarks, carbonate mounds, and mud volcanoes (e.g. Hovland and Judd, 1988).

1.1.3.1   Fluid venting

Activity of fluid venting may vary greatly, ranging from no activity at all to explosive fluid release. Also, fluid venting is often not continuous but is rather characterised by periods of activity interrupted by times of quiescence. For example, durations of active emissions may vary between minutes to hours (e.g. Greinert et al., 2006; Krabbenhoeft et al., 2010). Leifer et al. (2004) compare

such episodic fluid release to an electrical circuit consisting of capacitors which need to recharge first before a new period of activity can begin.

Short-term variations of fluid venting activity have been associated with tidal influence (Greinert et al., 2006; Krabbenhoeft et al., 2010). During low tides, the pressure from the water column (the hydraulic head) is reduced, which facilitates upward fluid migration and thus leads to increased venting activity. Alternatively, pressure changes associated with ocean swells, storm surges, and biologic pumping could induce short-term fluid flow variations (Teichert et al., 2003).

On a larger time scale, periods of increased fluid release appear to be correlated with periods of sealevel low-stand during glacial cycles (e.g. Teichert et al., 2003; Kiel, 2009). The lower sealevel during glacial times causes the BGHSZ to shift to shallower levels, leading to increased gas hydrate decomposition and hence an increase in the amount of mobile fluids. Elevated fluid flux during glacial stages may also be due to increased sediment loading of continental slopes, which increases lithostatic pressure on source rocks and reservoirs, and hence subsurface overpressure (Kiel, 2009). In addition, longterm variations of fluid venting activity can be related to tectonic processes such as earthquakes (Teichert et al., 2003). Over time, fluid venting may cease if fluid conduits are closed or the fluid reservoir becomes exhausted (Aharon et al., 1997).

The fate of methane bubbles released from seabed sources has been widely debated (e.g. Kvenvolden et al., 2001; Leifer and Patro, 2002; MacDonald et al., 2002; Leifer et al., 2006; McGinnis et al., 2006). Methane bubbles emitted from seep sites ascend through the water column with rising speeds of around 10-30 cm s^{-1} (MacDonald et al., 2002; Leifer and Judd, 2002; Greinert et al., 2006). The rising bubbles typically form a plume, which can be detected by hydracoustic systems (see 1.1.4). Such plumes may reach heights of up to 1300 m (Greinert et al., 2006) and, depending on the water depth, can thus effectively transport methane to the sea surface from where it will escape into the atmosphere.

The majority of methane, however, will be dissolved within the water column before it reaches the surface (e.g. McGinnis et al., 2006; Judd and Hovland, 2007; Schmale et al., 2010). Whether the methane bubbles survive the ascent through the water column depends on several factors, including water depth, bubble size, concentrations of dissolved gases, and temperature (Leifer and Patro, 2002). In addition, methane bubbles released from beneath the GHSZ are often protected by a hydrate coating that prevents early dissolution, thus increasing the likelihood of methane reaching the surface (Kvenvolden et al., 2001; Greinert et al., 2006; McGinnis et al., 2006). However, methane from seep sites is assumed to reach the surface only in shallow water areas (< 100 m water depth) (McGinnis et al., 2006; Schmale et al., 2010), unless rapid upwelling flows are involved, which increase the rising speed of bubbles and could enable methane release from deeper (> 250 m) waters (Leifer et al., 2006).

1.1.3.2 Cold seep systems

Cold seeps are associated with the expulsion of relatively cold fluids at the seabed. They occur in both active and passive margin settings and have been studied intensely under various geological, biological, physical, and chemical aspects (e.g. Talukder, 2012, and references therein). Their

occurrence indicates complex geological processes causing production, upward migration and subsequent seafloor venting of methane-rich fluids (Moore and Vrolijk, 1992; Judd and Hovland, 2007; Talukder, 2012).

Cold seeps represent unique seafloor ecosystems that mainly originate from microbial activity. Microbes settle in the shallow subsurface near the fluid pathways and, using sulphate as the oxidant, oxidise the supplied methane at the sulphate-methane transition zone (SMTZ), a process known as anaerobic oxidation of methane (AOM; Barnes and Goldberg, 1976) (Equation 1.4):

$$CH_4 + SO_4^{-2} \rightarrow HCO_3^- + HS^- + H_2O \qquad\qquad (1.4)$$

AOM-performing microbial communities were first discovered by Boetius et al. (2000) at Hydrate Ridge on the Cascadia Margin. During AOM, hydrogen carbonate (HCO_3^-) is produced, which decreases the pH and allows the precipitation of calcium carbonate ($CaCO_3$) from seawater.

Prolonged carbonate precipitation may lead to the formation of so-called chemoherms (Aharon 1994), i.e., seafloor carbonate structures of various morphologies. Authigenic carbonates also vary in dimensions, ranging from cm-scale carbonate cementations within the sediment (e.g. Ritger et al., 1987) over tubular structures (e.g. Stakes et al., 1999; Díaz-del-Río et al., 2003), massive blocks (e.g. Van Dover et al., 2003) and mounds (e.g. Klaucke et al., 2012) on the seafloor to steep pinnacles that have grown several tens of metres into the water column (Teichert et al., 2003). Carbonate precipitates further differ in their chemical compositions, which reflect variations in the nature of the expelled fluids, the intensity of fluid flow, and local environment conditions during formation (e.g. Stakes et al., 1999; Liebetrau et al., 2010). Authigenic carbonates thus represent valuable archives in terms of past seep activity and the development of fluid systems.

Cold seep sites are important seafloor habitats as they are commonly inhabited by abundant benthic fauna that live on carbon-based chemosymbiosis (e.g. Barry et al., 1996; Sahling et al., 2002). These include bacterial mats, vesicomyid clams, and ampharetic polychaetes at carbonate-free seepage locations, as well as mussels, siboglinid tubeworms, and sponges, which settle on the carbonate substrate of active seep sites (e.g. Barry et al., 1996; Lewis and Marshall, 1996; Sahling et al., 2002; Bowden et al., 2013). In addition, non-seep epifauna, e.g. cold-water corals, may grow on carbonate blocks after seepage ceased (Liebetrau et al., 2010; Bowden et al., 2013), e.g. through clogging of fluid pathways (Hovland, 2002). Consequently, the nature and abundance of biological communities at cold seep locations may give information on the activity of the fluid system.

1.1.4 Acoustic imaging of fluid flow systems

In acoustic records, fluid flow systems are generally identified from anomalies caused by the presence of free gas, either within the sediment or in the water column (e.g. Anderson and Bryant, 1990). Gas bubbles change the physical properties of sediments and water. In particular, they affect the impedance, i.e., the product of the acoustic velocity and the density of the medium (Sheriff and Geldart, 1995). The presence of gas bubbles thus results in a strong impedance contrast between gas-bearing and gas-free zones, which causes anomalies such as bright spots and hydroacoustic flares that are described below.

Acoustic energy that encounters a gas-bearing layer is scattered at the gas bubbles, and a higher proportion of the energy is reflected, inhibiting further penetration into the gas zone. Reflection is accompanied by phase reversal of the acoustic signal due to the negative reflection coefficient of gas (reverse polarity) (Sheriff and Geldart, 1995). Energy that is not reflected is attenuated, resulting in reduced penetration of the acoustic signal. The lower density associated with gas also causes a reduction in the P-wave velocity, whereas the S-wave velocity becomes zero as S-waves cannot travel through gas and liquids (Sheriff and Geldart, 1995).

The effect of gas on the acoustic signal strongly depends on the acoustic frequency and the size of the gas bubbles, which determines their resonance frequency. The strongest reaction is observed when the acoustic frequency is similar to the resonance frequency of the gas bubbles (Anderson and Bryant, 1990). High-frequency systems are generally more sensitive to gas. Consequently, acoustic anomalies caused by the same gas-bearing zone may vary significantly if acoustic systems of different frequencies are used.

The following list describes typical anomalies indicating the presence of gas bubbles:

- **Hydroacoustic flares** (Fig. 1.5A) are flare-shaped anomalies in the water column imaged by echosounder systems (e.g. Anderson and Bryant, 1990). They are caused by gas bubbles emanating from the seafloor at seep sites and indicate the scattering of acoustic energy in response to the impedance contrast between seawater and gas. Hydroacoustic flares can reach heights of several 100 m, with the highest (up to 1300 m) observed in the Black Sea (Greinert et al., 2006).

- **Acoustic turbidity** is the most common gas-related subsurface anomaly in acoustic records. The term refers to chaotic low-amplitude reflections that occur in sediment echosounder data and high-resolution seismic data (Judd and Hovland, 1992; Yuan et al., 1992; Whiticar, 2002). Acoustic turbidity is caused by scattering and absorption of acoustic energy by gas bubbles and commonly obscures stratigraphic reflections. The effect is often observed underneath bright spots or enhanced reflections.

- **Bright spots and enhanced reflections** are high-amplitude reflections caused by the strong impedance contrast between a gas-free zone and a relatively thin gas-bearing zone within the sediment (e.g. Løseth et al., 2009). While enhanced reflections occur in shallow (< 100 m) sediments and are therefore imaged by sediment echosounder systems, bright spots are observed below 100 m in seismic data (Hovland and Judd, 1988). Bright spots are often characterised by reverse polarity (Judd and Hovland, 1992).

- **Chimneys and pipes** are vertical anomalies that indicate upward migration of free gas or gas-bearing fluids. Their generally low amplitude in both seismic and sediment echsounder data is caused by strong attenuation of the acoustic signal, but can also be due to the destruction of the original sediment layering during migration processes (Hovland and Judd, 1988; Schroot et al., 2005). Chimneys can have diameters of several 100 m (Fig. 1.5B) and are associated with relatively slow, upward gas migration via hydro-fracturing (Løseth et al., 2009).

Pipes often have smaller diameters (<300 m) and may also be characterised by stacked high-amplitude reflections (Fig. 1.5C) (Andresen et al., 2012). Unlike chimneys, pipes can form explosively, e.g. in response to a blow-out (Løseth et al., 2001, 2009). In the literature, the terms "chimney" and "pipe" are often used interchangeably to describe the same structures, as so far there is no clear distinction between the two types (Andresen et al., 2012).

- **Down-bending reflections** (pull-down) are observed in seismic and sediment echosounder data at the lateral transition between relatively gas-free and gas-bearing zones within the sediment (Hovland and Judd, 1988). The down-bending effect towards the gas-bearing zone is caused by the lower velocity in gas-charged sediments, which results in an increased travel time of the returned signal (Judd and Hovland, 1992). This effect may also cause an apparent sagging of reflectors beneath a gas-bearing zone (e.g. Løseth et al., 2009).

- **Up-bending reflections** (pull-up) have been observed at the margins of chimney structures in seismic data (e.g. Hustoft et al., 2007, 2010; Westbrook et al., 2008b; Plaza-Faverola et al., 2011). They likely represent acoustic artefacts caused by higher-velocity material within the chimney. Gas hydrates within a chimney may cause P-wave velocities that are up to 300 m s^{-1} higher than in the surrounding sediments (Plaza-Faverola et al., 2010). Alternatively, higher velocities and associated up-bending reflections can be caused by carbonate cementing the chimney walls (e.g. Hustoft et al., 2007; Westbrook et al., 2008b).

Another type of acoustic anomaly is the bottom-simulating reflector (BSR) in seismic data. The BSR is characterised by a high-amplitude reflection that generally mimics the seafloor and is of reverse polarity (Fig. 1.5D) (Shipley et al., 1979). The BSR is caused by the strong impedance contrast between stable gas hydrates above and free gas below (Shipley et al., 1979). Thus, the BSR does not only indicate the presence of gas hydrate but also marks the lower limit of the GHSZ. However, gas hydrates may also be present without a BSR being observed in seismic data (Holbrook et al., 1996; Haacke et al., 2007).

In addition to gas, seafloor carbonates also influence the returned acoustic energy. High-backscatter anomalies in sidescan sonar and multibeam backscatter data can indicate the presence of seep carbonates on the seabed (Fig. 1.5E) (Johnson et al, 2003; Holland et al., 2006). The high backscatter results from (1) the difference in impedance contrast between carbonates and the surrounding seabed, (2) small-scale roughness of the carbonate surface, and (3) the morphology of the precipitates (Johnson et al., 2003; Holland et al., 2006). However, if the seafloor around the carbonate structures is also highly reflective, e.g. due to rock outcrops or pronounced relief, the acoustic response of seep carbonates may be difficult to distinguish from the background backscatter.
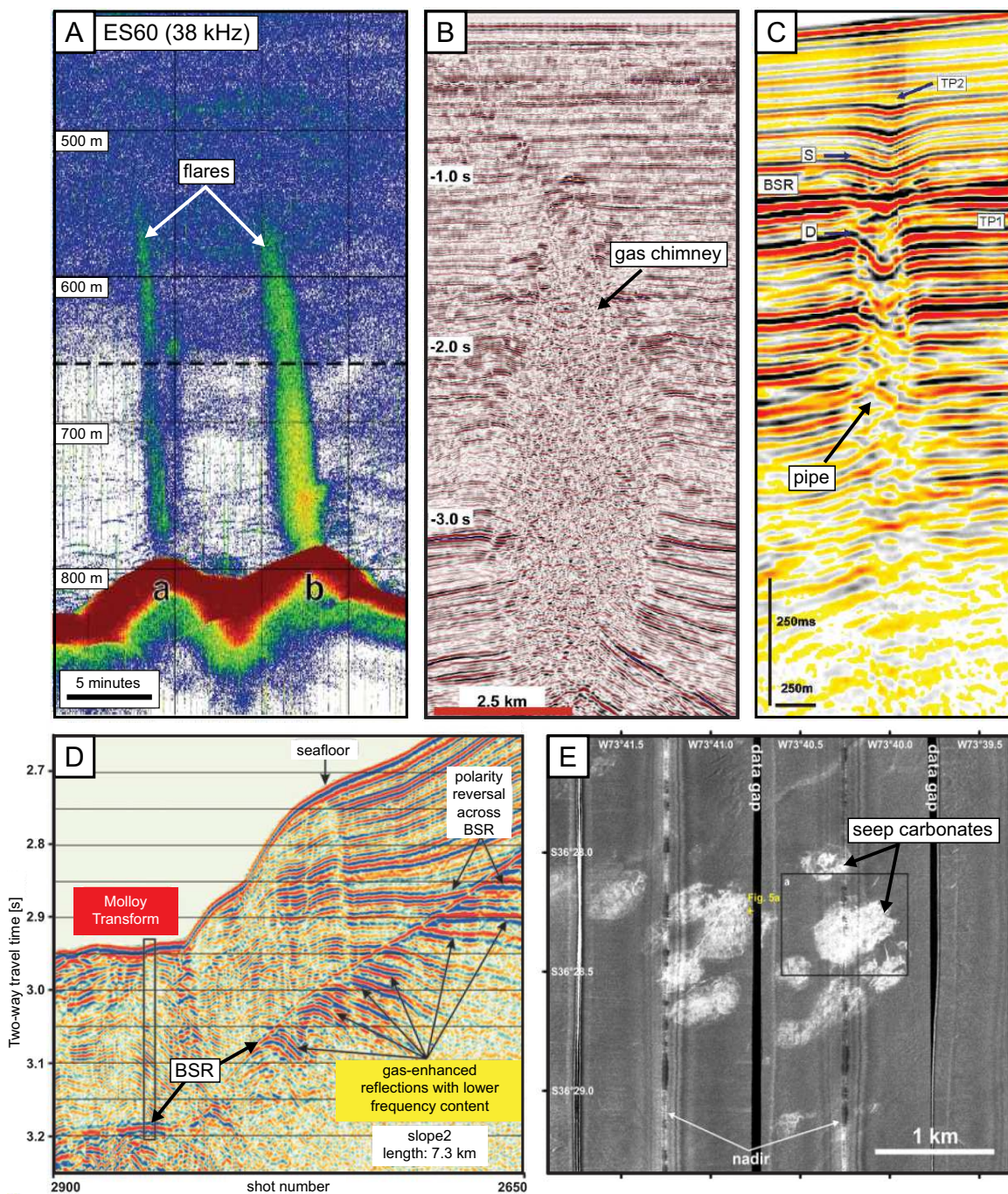
Figure 1.5: Overview of different acoustic anomalies related to fluid flow. **(A)** Hydroacoustic flares in single-beam echosounder records from offshore New Zealand. Adapted from Greinert et al. (2010). **(B)** Seismic profile across the Tommeliten Alpha gas chimney in the North Sea. Adapted from Løseth et al. (2009). **(C)** Pipe structure offshore Namibia, imaged in seismic data. Adapted from Moss and Cartwright (2010). **(D)** Bottom-simulating reflector (BSR) imaged in seismic data from the western Svalbard margin. Adapted from Vanneste et al. (2005b). **(E)** High backscatter anomalies in sidescan sonar data indicating cold seep carbonates on the Chilean margin. Adapted from Klaucke et al. (2012).

1.2 Motivation

Climate warming events have occurred several times throughout Earth's history. Major events took place at the late Permian–Triassic boundary ($\sim$253 Ma) (Wignall, 2001; Retallack and Jahren, 2008), in the early Jurassic (Toarcian; $\sim$183 Ma) (Hesselbo et al., 2000; Svensen et al., 2007), and at the Paleocene-Eocene transition (PETM; $\sim$55 Ma) (Dickens et al., 1995; Dickens, 1999). All three events were characterised by an abrupt increase in atmospheric methane concentration and a disturbance of the global carbon cycle, which has been attributed to the sudden release of large amounts of methane gas into the atmosphere (e.g. Dickens et al., 1995; Hesselbo et al., 2000; Svensen et al., 2004).

The best studied climate warming event is the PETM, which was characterised by an increase in bottom-water temperatures of at least 4°C (Dickens et al., 1995; Dickens, 1999). At the same time, carbon isotope data show an anomaly of -2 to -3‰ in the δ^{13}C of the ocean-atmosphere system (Dickens et al., 1995). This anomaly indicates a rapid injection of isotopically light carbon (^{12}C) into the oceans and atmosphere (Dickens, 1999; Röhl et al., 2007). Although the PETM lasted about 170 ka (Röhl et al., 2007), two thirds of the carbon were probably injected over a time span of only a few thousand years, indicating catastrophic carbon release (Norris and Röhl, 1999). Such rapid carbon injection requires an extensive reservoir capable of releasing large amounts of carbon over a short time span (Dickens, 1999). Several studies (e.g. Dickens et al., 1995; Norris and Röhl, 1999; Maclennan and Jones, 2006) agree that gas hydrate systems could constitute such a reservoir.

Methane release from gas hydrates, i.e., hydrate dissociation, occurs in response to changes in temperature and/or pressure that result in hydrates being no longer stable (Fig. 1.6) (e.g. Kvenvolden, 1988; Dillon and Max, 2000). Hydrate dissociation is observed today in several areas, e.g. on the Cascadia margin (Suess et al., 1999), the Norwegian margin (Mienert and Posewang, 1999; Jung and Vogt, 2004), the Svalbard margin (Westbrook et al., 2009; Berndt et al., 2014b), the U.S. Atlantic (Phrampus and Hornbach, 2012; Phrampus et al., 2014) and Pacific margins (Hill et al., 2004), and even in lacustrine settings such as Lake Baikal (van Rensbergen et al., 2003). The consequences of large-scale hydrate dissociation include ocean acidification, enhanced dewatering of marine sediments, sediment mobilisation, turnover of benthic material, and methane plumes extending into the water column and potentially reaching the atmosphere (Suess et al., 1999; Vogt and Jung, 2002; van Rensbergen et al., 2003; Biastoch et al., 2011; Reagan et al., 2011). Methane that reaches the atmosphere may contribute to a positive climate feedback as it can accelerate the warming process (e.g. Harvey and Huang, 1995).

An increase in bottom-water temperature would mostly affect shallow gas hydrate deposits, whereas deep-ocean hydrates would remain stable (Reagan and Moridis, 2007, 2008). Reagan and Moridis (2008) estimate that a 1°C temperature increase could already result in the release of substantial amounts of methane gas from shallow gas hydrates. A 3°C increase may even cause destabilisation of $\sim$85% of the global methane hydrate deposits (Buffett and Archer, 2004). For the PETM,

the 4°C increase in bottom-water temperature and subsequent hydrate dissociation are thought to have resulted in the release of about 1000-2000 Gt of carbon enriched in ^{12}C (Dickens et al., 1995; Dickens 1999). According to Dickens et al. (1995) and Dickens (1999), such quantities would be sufficient to explain the δ^{13}C anomaly.
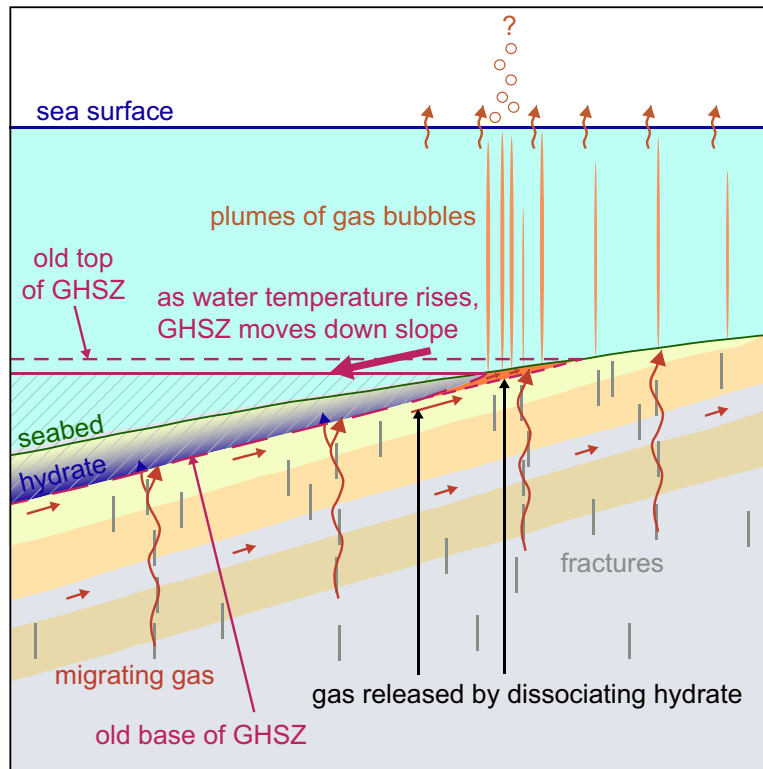
Figure 1.6: Hydrate dissociation caused by changing bottom-water temperatures. An increase in bottom-water temperature causes the GHSZ to move downslope, resulting in the dissociation of hydrates to methane gas and water. The released gas is free to move to the seabed where it escapes into the water column and possibly the atmosphere. Redrawn after Westbrook et al. (2009).

In addition, hydrate dissociation may also be caused by tectonic uplift as this results in depressurisation. Depressurisation can cause hydrates to become unstable even if bottom-water temperatures remain constant (Sloan, 1998). Maclennan and Jones (2006) propose that regional uplift occurred at the onset of the PETM and may thus have contributed to carbon release from destabilising methane hydrates.

In order to assess which areas are most vulnerable to large-scale hydrate dissociation and methane release under warming conditions, knowledge of the amount and distribution of hydrates in marine sediments is required. One approach is numerical modelling, which takes into account the deposition and degradation of organic matter, burial history, and bottom-water temperatures. The resulting estimates of the global amount of carbon stored in methane hydrates vary between 3-455 Gt (Piñero et al., 2013), ⩾455 Gt (Wallmann et al., 2012), 4-995 Gt (Burwicz et al., 2011), 500-2500 Gt (Milkov, 2004), 1146 Gt (Kretschmer et al., submitted), and 1600-2000 Gt (Archer et al., 2009). Buffett and Archer (2004) estimated a total of 5000 Gt of which 3000 Gt are stored in hydrates and 2000 Gt in free methane bubbles.

Numerical modelling provides a good overview of the areas where hydrates would be stable, which are generally restricted to continental slope and shelf regions (Maslin et al., 2010, and references therein). An alternative method to assess hydrate distribution is the mapping of the BSR, which requires seismic data and can therefore only be applied in regional studies. This approach is more precise than numerical modelling but may result in a minimum hydrate distribution, as gas hydrates do not always cause a BSR in seismic data (Holbrook et al., 1996; Haacke et al., 2007).
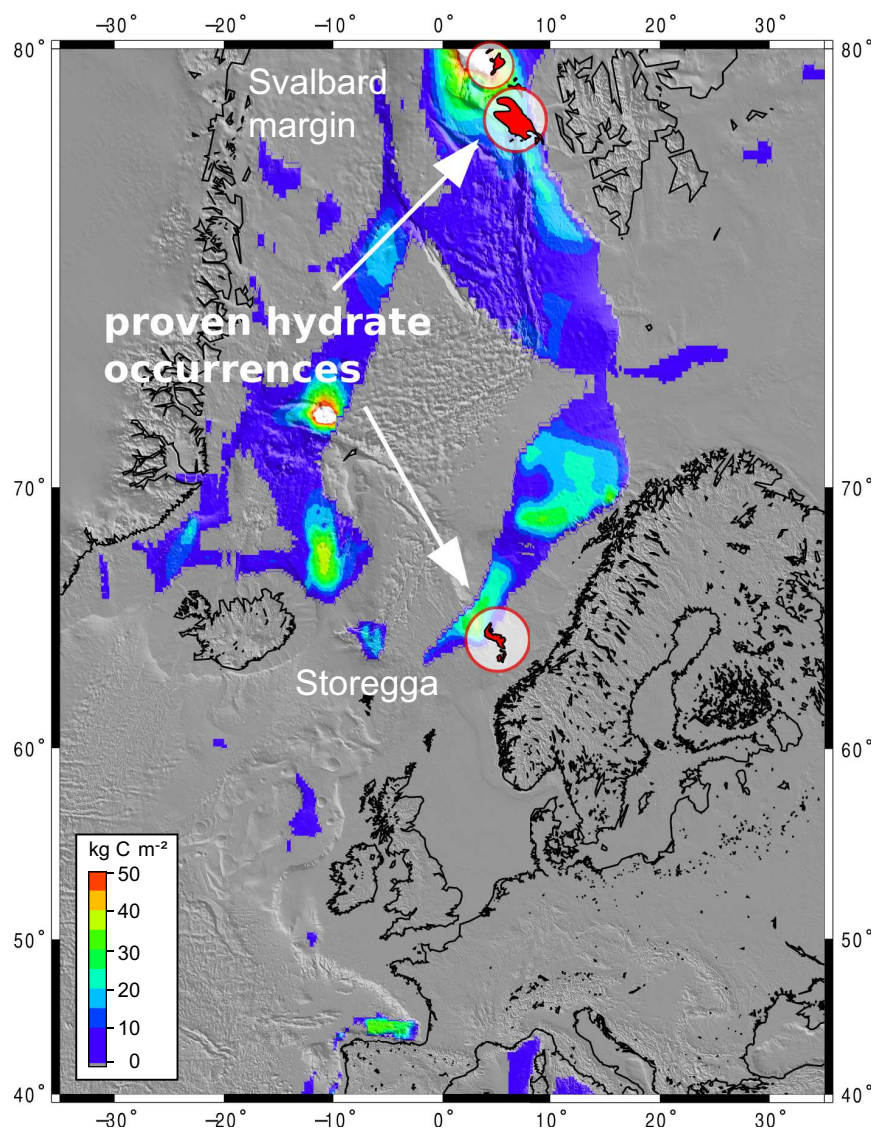
Figure 1.7: Predicted distribution of gas hydrates based on global models (Kretschmer et al., submitted). Colours denote the amount of carbon stored in hydrates in mass per area. The predicted hydrate distribution is overlain with the distribution of actually observed hydrates based on the seismic BSR and drill cores (red areas).

Comparison of the two approaches shows that their results may differ significantly, e.g. in the North Atlantic (Fig. 1.7). While numerical modelling suggests that most of the eastern North Atlantic margin is within the zone of gas hydrate stability (Kretschmer et al., submitted), seismic BSRs indicate the presence of hydrates in only two comparatively small areas: on the western Svalbard margin (e.g. Vanneste et al., 2005a, 2005b; Bünz et al., 2008, 2012) and at the headwall

of the Storegga Slide (e.g. Mienert et al., 1998; Bünz et al., 2003, 2004, 2005). Even if taken into account that the absence of a BSR does not necessarily rule out the presence of hydrates (Holbrook et al., 1996; Haacke et al., 2007), the mismatch between areas of predicted and BSR-derived hydrate occurrence is obvious. This suggests that model-based estimations of the amount of carbon stored in hydrates may be overestimations that do not reflect actual observations.

If the real amount of hydrate-bound carbon is considerably smaller than that estimated from models, the amount of carbon released during warming-induced hydrate dissociation would also be smaller than estimated, and may thus not be sufficient to explain the carbon anomaly associated with the PETM. This is supported by Higgins and Schrag (2006), who believe that hydrate dissociation alone is insufficient to explain the substantial carbon addition to the atmosphere. Consequently, to assess the causes of methane release during climate warming events, it is also necessary to take into account other possible contributors.

Several other potential contributors to catastrophic methane release have been discussed, including thawing of permafrost soils (e.g. Schuur et al., 2009), burning peatlands (Higgins and Schrag, 2006) and a bolide impact (Cramer and Kent, 2005). The most likely contributor, however, are hydrothermal vent systems that result from magmatic intrusions into organic-rich sediments (Svensen et al., 2004). Contact metamorphism around the intrusions produces large amounts of thermogenic methane, promoting the development of fluid pipes and explosive fluid venting (Fig. 1.8) (Jamtveit et al., 2004; Svensen et al., 2004; Planke et al., 2005; Aarnes et al., 2010). Although the venting activity following the intrusion emplacement is relatively short-lived (10-1000 years; Svensen et al., 2004; Aarnes et al., 2010), the pipe structures may be re-used at later times (Svensen et al., 2003; Planke et al., 2005).

Both types of fluid flow systems that represent potential main contributors to climate warming events – gas hydrate systems and hydrothermal vent complexes – can be studied in the North Atlantic, which is also most sensitive to climate warming effects (Spielhagen et al., 2011). On the Svalbard margin, a large gas hydrate system extends from the continental slope to the Mid Atlantic Ridge system (Vanneste et al., 2005a, 2005b; Bünz et al., 2008, 2012; Hustoft et al., 2009). The presence of extensive gas hydrates could be related to methane production influenced by the proximity of active spreading ridges such as the Knipovich Ridge, as the associated high heat flow could promote thermogenic methane production (Vanneste et al., 2005a; Smith et al., 2014). On the upper slope, the BGHSZ crops out at the seafloor in water depths of less than 400 m (Westbrook et al., 2009). This zone is therefore most vulnerable with respect to an increase in bottom-water temperature. Over the past 30 years, bottom-water temperatures off Svalbard have increased by 0.3-2.0°C (Schauer et al., 2008; Ferré et al., 2012), and the observation of more than 250 gas flares at the intersection of the BGHSZ and the seafloor has been attributed to hydrate dissociation caused by a downslope retreat of the BGHSZ in response to higher bottom-water temperatures (Westbrook et al., 2009).

Further south, on the Norwegian margin, an 80,000 km² large sill complex was emplaced at the Paleocene-Eocene transition during the opening of the North Atlantic. The sill intrusion was associated with explosive methane venting and the formation of at least 2000-3000 hydrothermal vent complexes in the Vøring and Møre basins (Svensen et al., 2004; Planke et al., 2005). A total

of 734 vent complexes have so far been identified on seismic data (Svensen et al., 2004; Planke et al., 2005). One of these is the Giant Gjallar Vent (Gay et al., 2012), which is one of the largest fluid escape structures found in the North Atlantic. Although two large pipe structures indicate fluid migration activity long after the initial hydrothermal system formed, opinions on the present activity status differ, suggesting either reactivation (Gay et al., 2012) or extinction (Hansen et al., 2005).
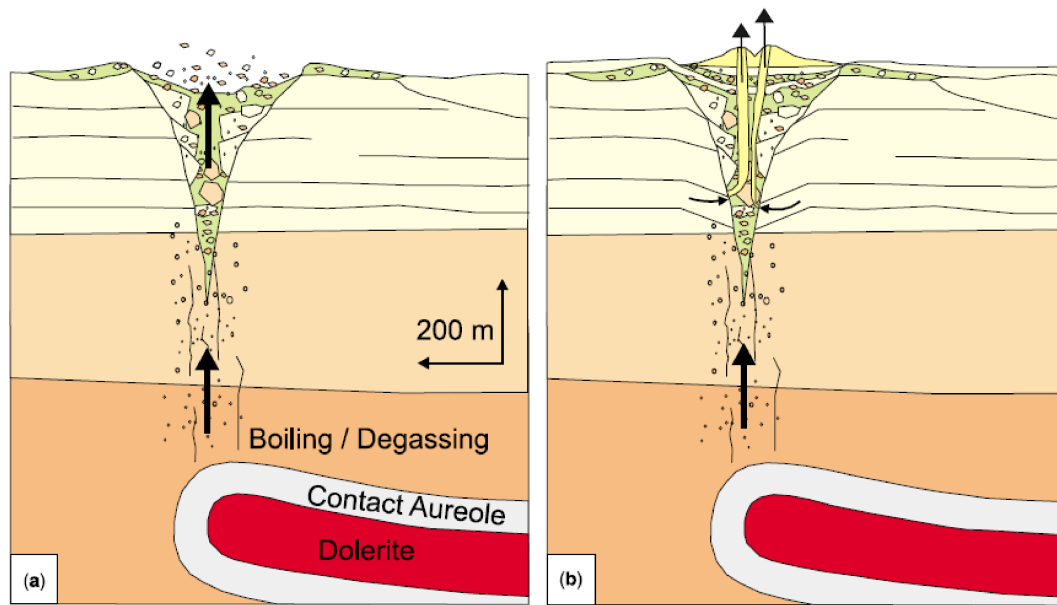
Figure 1.8: Schematic illustrating the formation of a hydrothermal vent complex. **(A)** During sill intrusion, boiling pore fluids and gas formed due to metamorphic reactions cause a build-up of fluid pressure and explosive formation of a cone-shaped hydrothermal complex. The initial fluid expulsion is short-lived (10-1000 years) and associated with the generation of hydrothermal breccias. **(B)** Later, smaller pipes may develop within the cone structure, cross-cutting the breccias and enabling renewed fluid venting. (Jamtveit et al., 2004; Planke et al., 2005)

1.3 Study objectives

The overall aim of this thesis is to better understand fluid flow systems in terms of past and ongoing activity, and their impact on oceans and the atmosphere. In particular, it is of interest if such systems may have contributed significantly to climate warming events such as the PETM.

In this thesis, four fluid flow systems are studied through a variety of geophysical methods, ranging from reflection seismic and hydroacoustic (Parasound, sidescan sonar, multibeam echosounder) methods to numerical modelling. The fluid flow systems are in different stages of development with respect to the classic fluid flow system structure described in 1.1. They also differ in their tectonic settings, which include both active and passive margins. Study areas are the western Svalbard margin, where two locations are studied – the area north of the Knipovich Ridge and the upper continental slope –, as well as the Giant Gjallar Vent in the Norwegian Sea and the Hikurangi Margin offshore New Zealand.

The main questions posed for each study area are:

Svalbard margin – Knipovich Ridge

- Did the Knipovich Ridge influence petroleum generation on the Svalbard margin?

- What is/are the source(s) of fluids in this area?

Svalbard margin – seeps on upper slope

- What is the role of short-term variability of bottom-water temperatures for seepage at the BGHSZ seafloor intersection off Svalbard?

- What is the minimum age for the onset of marine methane release from the seafloor?

Giant Gjallar Vent (GGV)

- Is the GGV still active or does the observed surface relief reflect past activity of a now inactive system?

- Can the GGV be used as a study site for constraining the geological processes that are or were active in the deep part of the Vøring Basin?

Hikurangi Margin

- How do surface expressions of cold seeps differ in terms of backscatter intensity in sidescan sonar images?

- Can sidescan sonar data be used as a proxy for faunal habitats?

1.4 Thesis outline

This thesis consists of an introductory chapter (Chapter 1), followed by four case studies that describe fluid flow systems in different stages of development (Chapters 2-5), and a concluding chapter (Chapter 6). The case studies represent stand-alone manuscripts with their own abstract, introduction, methods, results, discussion, and conclusion sections. They have either been published by or will be submitted to international peer-reviewed journals.

Chapter 2 presents a fluid flow system early in its development, located north of the Knipovich Ridge on the western Svalbard margin. Gas hydrates in this region are more widespread than anywhere else in the eastern North Atlantic, indicating a substantial gas reservoir. The origin

of the gas is discussed, as are the source rock potential on the Svalbard margin and the role of the Knipovich Ridge with respect to thermogenic gas production. This chapter will be submitted under the title *Gas hydrate distribution and hydrocarbon maturation north of the Knipovich Ridge, western Svalbard margin* by I. Dumke, E. Burwicz, C. Berndt, D. Klaeschen, T. Feseker, W. Geissler, and S. Sarkar to the *Journal of Geophysical Research: Solid Earth*. Supporting information can be found in Appendix A.1.

Contributions to Chapter 2: C. Berndt led the survey. E. Burwicz performed the petroleum system modelling and wrote part of the model description. D. Klaeschen processed the seismic data and wrote the description of the data processing. T. Feseker conducted the heat flow measurements. I contributed to the seismic data acquisition, analysed the data, provided the geological input model for the petroleum system modelling, and wrote the manuscript. All co-authors helped improving and revising the manuscript.

Chapter 3 focuses on a more developed fluid flow system, the Giant Gjallar Vent in the Norwegian Sea. This vent system is one of the largest in the North Atlantic and is characterised by two prominent conduits that terminate beneath the seabed. Based on new seismic data, the activity history of the vent is re-interpreted and implications on the future development of this structure are discussed. This chapter is published by the journal *Marine Geology* as *Dumke, I., Berndt, C., Crutchley, G. J., Krause, S., Liebetrau, V., Gay, A., and Couillard, M. (2014). Seal bypass at the Giant Gjallar Vent (Norwegian Sea): Indications for a new phase of fluid venting at a 56-Ma-old fluid migration system. Marine Geology 351, 38-52.*

Contributions to Chapter 3: C. Berndt led the survey. G. J. Crutchley, M. Couillard, and I contributed to the acquisition of the seismic and Parasound data. S. Krause collected and analysed the gravity core samples. G. J. Crutchley processed the seismic and sediment echosounder data. I analysed the data and wrote the manuscript. All co-authors, the editor, and two external reviewers helped improving and revising the manuscript.

Chapter 4 deals with a deviation from the classic fluid flow system: on the upper continental margin offshore Svalbard, fluid venting occurs without fluid conduits being present, as the reservoir crops out at the seabed. Seepage is linked to dissociation of gas hydrates, which is caused by seasonal fluctuations of bottom-water temperatures. The onset of periodic gas hydrate formation and dissociation is constrained from carbonate samples and discussed with respect to ongoing decadal-scale global warming. This chapter is published by the journal *Science* as *Berndt, C., Feseker, T., Treude, T., Krastel, S., Liebetrau, V., Niemann, H., Bertics, V. J., Dumke, I., Dünnbier, K., Ferré, B., Graves, C., Gross, F., Hissmann, K., Hühnerbach, V., Krause, S., Lieser, K., Schauer, J., and Steinle, L. (2014). Temporal constraints on hydrate-controlled methane seepage off Svalbard. Science 343, 284-287.* Supporting information can be found in Appendix A.2.

Contributions to Chapter 4: C. Berndt led the field survey and wrote the paper. T. Feseker conducted the heat flow measurements and modelled the GHSZ. T. Treude, S. Krastel, H. Niemann, V. J. Bertics, C. Graves, K. Hissmann, V. Hühnerbach, S. Krause, J. Schauer, L. Steinle, and I conducted the submersible dives. V. Liebetrau, S. Krause, and I analysed the carbonate samples. T. Treude, S. Krause, and V. J. Bertics analysed the geochemistry of the surface sediments, and H.

Niemann, L. Steinle, and C. Graves analysed biogeochemical parameters of the water column. S. Krastel, K. Dünnbier, K. Lieser, and F. Gross processed and interpreted the Parasound data. B. Ferré and V. Hühnerbach carried out the bottom-water temperature measurements. All authors contributed to writing and revising the manuscript. Two external reviewers helped improving and revising the manuscript.

Chapter 5 looks at cold seeps on the Hikurangi Margin offshore New Zealand, which represent a fully developed fluid flow system. Seafloor expressions imaged with sidescan sonar fall into four distinct types of backscatter pattern. These patterns are integrated with observations of seabed fauna and discussed with respect to cold seep development. This chapter is published in a special issue of the journal *Geo-Marine Letters* as *Dumke, I., Klaucke, I., Berndt, C., and Bialas, J. (2014). Sidescan backscatter variations of cold seeps on the Hikurangi Margin (New Zealand): indications for different stages in seep development. Geo-Marine Letters 34, 169-184.*

Contributions to Chapter 5: J. Bialas led the survey and I. Klaucke proposed the study locations. I processed and analysed the data and wrote the manuscript. All co-authors and one external reviewer helped improving and revising the manuscript.

Chapter 6 summarizes the findings of the four case studies, discusses them in the light of the overall motivation of this thesis, and provides an outlook on future work.

Chapter 2

Case study 1 - Knipovich Ridge

Gas hydrate distribution and hydrocarbon maturation north of the Knipovich Ridge, western Svalbard margin[1]

Ines Dumke, Ewa Burwicz, Christian Berndt, Dirk Klaeschen, Tomas Feseker, Wolfram Geissler, Sudipta Sarkar

2.1 Abstract

A bottom-simulating reflector (BSR) occurs west of Svalbard in water depths greater than 600 m, indicating that gas hydrate occurrence in marine sediments is more extensive in this region than anywhere else on the continental margins of Europe. Regional mapping of the BSR shows that hydrate is most abundant at the northern edge of the Knipovich Ridge, a slow-spreading ridge segment of the Mid Atlantic Ridge system. Here, heat flow is high (up to 330 mW m^{-2}) and increases towards the ridge axis. The coinciding maxima in across-margin BSR width and heat flow suggest that the Knipovich Ridge influenced methane generation in this area. This is supported by recent finds of thermogenic methane at cold seeps just north of the ridge termination. To evaluate the source rock potential on the western Svalbard margin, we have applied 1D petroleum system modelling at three sites. The modelling shows that temperature and burial conditions in the vicinity of the ridge were likely sufficient to cause thermogenic methane production, which would explain the more widespread presence of gas hydrates north of the Knipovich Ridge. Most likely, source rocks are Miocene organic-rich sediments and a potential Eocene source rock that may exist in the area if early rifting created sufficiently deep depocenters.

---

[1]This chapter will be submitted to the Journal of Geophysical Research: Solid Earth.

2.2 Introduction

Naturally-occurring gas hydrates store large amounts of methane as well as other gaseous hydro-carbons and non-hydrocarbons. While microbial methane is typically considered as the dominant component of marine gas hydrates (Kvenvolden, 1995, and references therein), other sources of hydrocarbon such as thermogenic methane are often ignored. However, thermogenic methane may constitute a substantial component of hydrate-bound methane (e.g. Brooks et al., 1986; Ginsburg et al., 1992; Kvenvolden, 1995).

An appraisal of thermogenic methane stored in marine gas hydrates and later expelled at the seabed is crucial in several contexts. These include basin prospecting, evaluating source rock maturation, quantifying produced hydrocarbons, assessing hydrocarbon migration into and out of shallow hydrate reservoirs, and leakage into oceans and the atmosphere. Methane release from hydrates into the atmosphere has the potential to increase climate warming (e.g. Harvey and Huang, 1995). This especially affects polar regions such as the northern North Atlantic, which are most sensitive to climate warming (Spielhagen et al., 2011) and host substantial gas hydrate reservoirs.

Most of the eastern North Atlantic margin lies within the zone of gas hydrate stability (Kretschmer et al., submitted). However, gas hydrates have been found in only two areas – on the Svalbard margin (Vanneste et al., 2005a, 2005b; Bünz et al., 2008, 2012; Westbrook et al., 2009; Sarkar et al., 2012; Berndt et al., 2014b) and at the Storegga Slide headwall (Mienert et al., 1998; Bouriak et al., 2000; Bünz et al., 2003, 2004, 2005; Ivanov, 2007) – even though free gas is also present in other parts of the margin, e.g. in the Vøring Basin (Kvenvolden et al., 1989; Svensen et al., 2004). It is therefore important to study these areas in order to constrain the factors controlling the presence of gas hydrates.

On the western Svalbard margin, gas hydrates have been inferred at the continental slope where the base of the gas hydrate stability zone (BGHSZ) crops out at the seafloor in ~400 m water depth, causing active seepage (Westbrook et al., 2009; Berndt et al., 2014b). Seepage is associated with hydrate dissociation that varies in extent and intensity depending on seasonal changes in bottom water temperatures (Berndt et al., 2014b).

Further west, gas hydrates are indicated by the presence of a bottom-simulating reflector (BSR) in seismic data (e.g. Vanneste et al., 2005b; Sarkar et al., 2012). The BSR marks the interface between stable gas hydrates above and free gas below (Shipley et al., 1979). A large BSR area occurs north of the Knipovich Ridge (Vanneste et al., 2005b), extending as far north as Vestnesa Ridge (Bünz et al., 2008, 2012; Hustoft et al., 2009). Vanneste et al. (2005a) proposed that elevated heat flow at the Knipovich Ridge could promote the presence of gas and hydrates.

Heat flow can be estimated from the depth of the BSR (Yamano et al., 1982), which has been applied in a number of studies (e.g. Townend, 1997; Ganguly et al., 2000; Kinoshita et al., 2011) in order to assess the thermal situation of an area. This approach requires knowledge of the hydrate composition, bottom-water temperature, and thermal conductivity (Yamano et al., 1982). Similarly, if the temperature field is known it can be used to estimate the theoretical depth of the BSR (Hornbach et al., 2012).

Using measured heat flow values, Vanneste et al. (2005b) found that the observed depth of the BSR agrees well with the theoretical BSR depth calculated for a pure-methane and seawater hydrate composition, from which they inferred a microbial origin of the gas. This is supported by the geochemical signatures of vent gas samples from the continental slope and outer shelf, which revealed gas compositions of $>99.7\%$ methane and average $\delta^{13}C$ values of -55.7‰ (Sahling et al., 2014). In contrast, geochemical signatures of methane from hydrate samples collected at Vestnesa Ridge indicate a thermogenic origin (Fisher et al., 2011; Smith et al., 2014). Smith et al. (2014) attribute thermogenic methane production to the proximity of the Knipovich Ridge, which could promote maturation of organic matter.

Thermogenic methane production requires the presence of a source rock. An Eocene source rock exists in the Arctic Basin (Stein et al., 2006; Mann et al., 2009) and a Miocene source rock was drilled at ODP Site 909 north of the Hovgård Ridge (Shipboard Scientific Party, 1995b; Knies and Mann, 2002). For the Arctic Basin, petroleum system modelling was used to determine maturity and petroleum generation potential of the Eocene source rock (Mann et al., 2009). For the Svalbard margin, the Miocene sequence is proposed to have a good to excellent source rock potential (Knies and Mann, 2002), but petroleum system modelling has not been applied.

Here, we test the hypothesis that substantial amounts of methane stored in gas hydrate reservoirs on the western Svalbard margin result from thermogenic reactions within potential source rocks that are driven by higher heat flow in the vicinity of the slow-spreading Knipovich Ridge. For this purpose, we (1) map the extent of gas hydrates on the Svalbard margin based on the BSR observed in seismic data, (2) assess the thermal situation north of the Knipovich Ridge using BSR-derived heat flow and probe measurements, and (3) evaluate the source rock potential via petroleum system modelling and determine if thermogenic methane can contribute to the gas hydrate reservoir.

2.3 Geological setting

2.3.1 Tectonic framework

The western Svalbard margin is tectonically a passive margin, but most of it lies within 100 km of the Mid Atlantic Ridge system (Crane et al., 1991). Between 73°N and 82°N, the Mid Atlantic Ridge system consists of four spreading segments – the Mohns Ridge, Knipovich Ridge, Molloy Ridge, and Lena Trough – that are offset by two transform faults (TF): the Molloy TF between the Knipovich and Molloy segments, and the Spitsbergen TF between the Molloy and Lena segments (Fig. 2.1).

Before the opening of the North Atlantic, the Svalbard margin was characterised by the Spitsbergen Shear Zone, which comprised several elongate basins offset in an en-echelon manner (Crane et al., 2001). These basins were interpreted as pull-apart basins (Crane et al., 1982, 1991; Thiede et al., 1990). Pull-apart rifting is often observed in major shear zones (e.g. Ebinger, 1989).

The opening of the North Atlantic started in the early Eocene ($\sim$56 Ma) and proceeded from south to north (Talwani and Eldholm, 1977). Seafloor spreading first occurred along the Mohns Ridge

(Talwani and Eldholm, 1977), until the ridge encountered the ancient Spitsbergen Shear Zone. The spreading direction then changed abruptly as the Knipovich Ridge propagated into the N-S oriented shear zone (Crane et al., 1988).
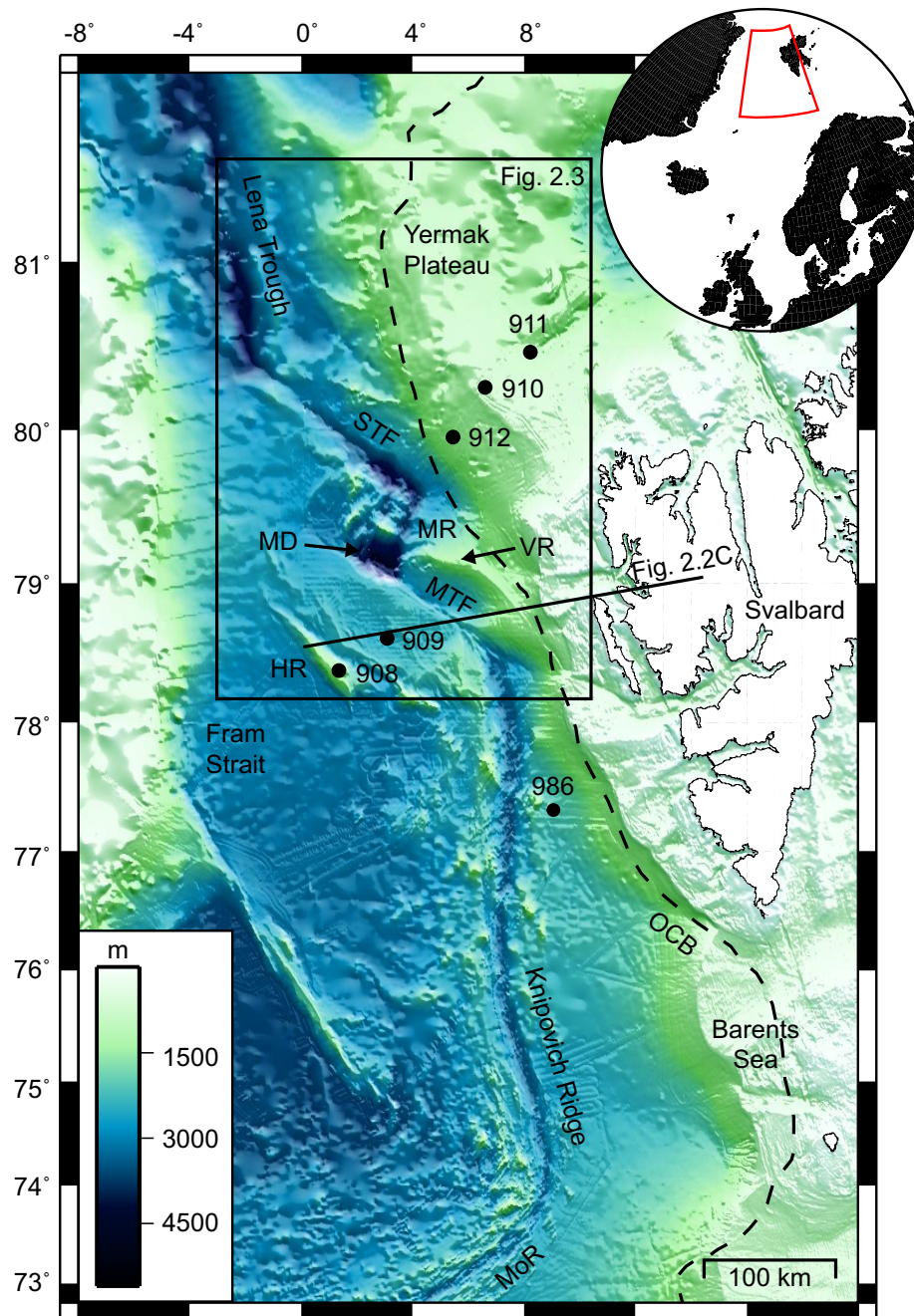

Figure 2.1: Bathymetric map of the western Svalbard margin, located in the northern North Atlantic (inset). Black dots mark locations of ODP boreholes. HR – Hovgård Ridge, MD – Molloy Deep, MTF – Molloy Transform Fault, MoR – Mohns Ridge, MR – Molloy Ridge, OCB – ocean-continent boundary after Engen et al. (2008), STF – Spitsbergen Transform Fault, VR – Vestnesa Ridge.

The timing for break-up along the Knipovich Ridge is unclear. While Eldholm et al. (1984) propose that seafloor spreading along the entire ridge was not established until middle Miocene, Crane et al. (1988, 1991) suggest that spreading accompanied by oceanic crust formation had reached the northern end of the ridge (around 78°N) by 40-50 Ma, only 5-10 Myr after the Mohns Ridge. However, Engen et al. (2008) inferred from magnetic anomalies that the present-day, regular mode of seafloor spreading did not establish until late Miocene (chron 5, 9.8 Ma).

Due to the abrupt change in direction, spreading along the Knipovich Ridge is asymmetric, with spreading rates being 1.5 times faster west of the ridge axis than east of it (Crane et al., 1988). Also, spreading rates decrease towards the north, from 4.3-4.9 mm yr^{-1} at 75°N to generally <3 mm yr^{-1} at 78°N (Crane et al., 1988).

As spreading is slow compared to most other mid ocean ridge segments, the Knipovich Ridge is classified as a slow- to ultraslow-spreading ridge (Dick et al., 2003). Slow-spreading ridges commonly exhibit a central rift valley. At the Knipovich Ridge, the rift valley is 8-10 km wide and 3300-3700 m deep, and characterised by steep rift flanks (Crane et al., 2001; Kvarven et al., 2014).

2.3.2 Regional stratigraphy and petroleum source rock potential

Sediment thicknesses are 1-3 km along the western Svalbard margin, with the exception of Vestnesa Ridge, where thicknesses reach up to 5 km (Eiken and Hinz, 1993; Ritzmann et al., 2004). On the Knipovich Ridge, sediment thicknesses are ∼1500 m on the eastern flank and 800-1000 m on the western flank (Kvarven et al., 2014). The difference is due to sediments from the Svalbard margin being mainly deposited against the eastern ridge flank (Crane et al., 1988), whereas the western flank was cut off from sediment transport routes early in its development (Kvarven et al., 2014).

Sedimentation rates on the margin are very high. Until middle Miocene, the sedimentation rate was ∼100 mm yr^{-1}; since then, it has increased to >300 mm yr^{-1} (Myhre and Eldholm, 1988). Due to several ice sheet advances across the shelf since 1 Ma (Faleide et al., 1996), the areas near the shelf are characterised by glacial sediments (Eiken and Hinz, 1993). In contrast, contourites dominate towards the ridges. The oldest contourites are probably late Miocene to Pliocene in age (Eiken and Hinz, 1993), which is consistent with the establishment of an oceanic gateway between the Fram Strait and the Arctic Basin (e.g. Engen et al., 2008).

Several ODP drill holes provide information on the lithology of the marine sediments (Fig. 2.1). However, at most sites drilling did not penetrate deeper than Pliocene sediments. The only exception is Site 909 north of the Hovgård Ridge, which was drilled down to Oligocene sediments (Myhre et al., 1995; Shipboard Scientific Party, 1995b). The sediment recovered at Site 909 was mostly clay and silt. Four units (I, II, IIIA, IIIB) can be distinguished based on varying amounts of organic material, dropstones, nannofossils and carbonate (Table 2.1) (Shipboard Scientific Party, 1995b). Unit IIIB (lower Miocene) is further divided into three subunits based on organic matter characteristics, i.e., total organic carbon (TOC), hydrogen index (HI), and vitrinite reflectance (Table 2.1) (Knies and Mann, 2002).

Unit IIIB has been interpreted as a potential source rock for hydrocarbon generation (Knies and Mann, 2002). During the drilling process, the presence of methane as well as heavier hydrocarbons,

which increased abruptly in concentration, required the termination of drilling at 1061.8 metres below seafloor (mbsf) (Shipboard Scientific Party, 1995b). Although Knies and Mann (2002) interpreted subunits 2 and 3 as presently immature based on T_{max} values (<435°C) and vitrinite reflectance (0.4-0.5%), they suggested a fair to good source rock potential for unit IIIB. Source rock quality is proposed to increase (good to very good) towards the Hovgård Ridge and Svalbard margin, where the sequences are buried more deeply (Knies and Mann, 2002).

Another potential source rock is located further north in the Arctic Basin (Stein et al., 2006; Mann et al., 2009). This source rock is of early to middle Eocene age and associated with the deposition of the freshwater fern *Azolla* (Mann et al., 2009). On the Lomonosov Ridge, IODP boreholes (Expedition 302 Scientists, 2006) revealed a 93-m-thick Eocene sequence of good to very good source rock potential (Stein, 2007). Because of shallow (<200 m) burial of this sequence, in-situ hydrocarbon generation was excluded for the Lomonosov Ridge, however, it may have occurred in the adjacent Amundsen Basin where the overburden is higher (>1000 m) (Mann et al., 2009).

2.3.3 Gas hydrates on the western Svalbard margin

Gas hydrates on the Svalbard margin have been examined in detail over the last decade. Studies focused on the area north of the interception of the Knipovich Ridge and the Molloy TF (Posewang and Mienert, 1999; Carcione et al., 2005; Vanneste et al., 2005a, 2005b; Westbrook et al., 2008a), as well as on Vestnesa Ridge (e.g. Vogt et al., 1999; Bünz et al., 2008, 2012; Hustoft et al., 2009; Plaza-Faverola et al., 2015) and offshore Prins Karls Forland where the predicted BGHSZ crops out at the seafloor (e.g. Westbrook et al., 2009; Berndt et al., 2014b).

The thickness of the gas hydrate stability zone (GHSZ) varies on the Svalbard margin. While the GHSZ tapers out at ∼400 m water depth, resulting in zero thickness (Westbrook et al., 2009), it reaches thicknesses of up to 300 m towards the Lena Trough (Geissler et al., 2014b). Thickness of the GHSZ, and hence the BSR depth, mainly depends on the geothermal gradient and the bottom water temperature, which decreases from >1.5°C on the upper slope to -0.9°C near the Molloy TF (Vanneste et al., 2005b).

Hydrate concentrations have been estimated in several studies, using seismic velocity data and theoretical models. The results generally range between 6% and 12% of the pore space (Vanneste et al., 2005a; Westbrook et al., 2008a). Carcione et al. (2005) calculated hydrate concentrations of up to 25%, but with an average of 7.2%. Hydrate concentrations also vary with depth, with the highest concentrations occurring near the BSR (Carcione et al., 2005).

Geochemical analyses were performed on hydrate samples recovered in two sediment cores on Vestnesa Ridge (Fisher et al., 2011; Smith et al., 2014), and another core from a seep site between Vestnesa Ridge and the continental slope (Fisher et al., 2011). Also, gas bubbles emitted at the upper continental slope were sampled and analysed (Sahling et al., 2014). The results differ between the deep-water Vestnesa samples (∼1200 m water depth) and the other, shallower (240-890 m water depth) samples. On Vestnesa Ridge, Smith et al. (2014) measured average hydrate compositions of 96.31% methane (C_1), 3.36% ethane (C_2), 0.21% propane (C_3), 0.11% isobutane

(i − C_4), and 0.01% n-butane (n − C_4), as well as $\delta^{13}C$ values of -47.7‰ for C_1, which agree with the -45.7±2.7‰ of Fisher et al. (2011). In contrast, the shallower samples from the slope reveal a composition of >99.7% methane and a $\delta^{13}C$ of -55.7‰ (Sahling et al., 2014). A similar $\delta^{13}C$ value of -54.6±1.7‰ was measured at the plume field site (Fisher et al., 2011). On the shelf, isotopic signatures indicated a mainly microbial origin, however, Knies et al. (2004) also found evidence for migrated thermogenic gas, e.g. in the Van Mijenfjorden and Storfjorden.

The isotopic signatures suggest that the origin of the observed gas is spatially variant. While the results of Knies et al. (2004), Fisher et al. (2011), and Sahling et al. (2014) support a microbial origin for the shelf and water depth down to about 800 m, Smith at al. (2014) suggest at least partially thermogenic methane production, which is inferred from the heavier $\delta^{13}C$ values and the presence of higher hydrocarbons (C_{3+}). Thermogenic gas production also occurs close to the coast of the Kongsfjord (Knies et al., 2004). Alternatively, it has been discussed that some of the gas could be sourced from serpentinization of the oceanic basement (Rajan et al., 2012b). However, Smith et al. (2014) argue that the involvement of serpentinization would require heavier $\delta^{13}C$ values of around -25‰, which are not observed.

2.4 Materials and methods

2.4.1 Reflection seismic data

During RV Maria S. Merian cruise MSM21/4 in 2012, we acquired multichannel 2D seismic (MCS) data at the northern end of the Knipovich Ridge (Berndt et al., 2014a). The data were recorded using a 120-channel streamer and an 88-channel streamer. The data were sampled at 2 kHz and the recording length was 5-6.5 s. A GI-Gun (2×1.7 l) was used as a source and operated at a shot interval of 6-8 s.

Positions for each channel were calculated by backtracking along the profiles from the GI-Gun GPS positions. The shot gathers were analysed for abnormal amplitudes below the seafloor reflection by comparing neighbouring traces in different frequency bands within sliding time windows. To suppress surface-generated water noise, a τ-p filter was applied in the shot gather domain. Common mid-point (CMP) profiles were then generated through crooked-line binning with a CMP spacing of 1.5625 m. A zero-phase band-pass filter was applied to the data, using corner frequencies of 60 Hz and 360 Hz. Based on regional velocity information from MCS data (Sarkar, 2012), an interpolated and extrapolated 3D interval velocity model was created below the digitised seafloor reflection of the high-resolution streamer data. This velocity model was used to apply a CMP stack and an amplitude-preserving Kirchhoff post-stack time migration.

In addition, we used 2D seismic data acquired along the Svalbard margin and in the Fram Strait during cruises JR211 in 2008 (see Sarkar et al. (2012) for more details) and MSM31 in 2013 (Geissler et al., 2014a), as well as seismic data provided by AWI Bremerhaven (Geissler et al., 2011, 2014b). All data underwent standard processing including time migration.

2.4.2 Heat flow measurements

In-situ measurements of sediment temperature and thermal conductivity were performed during cruise MSM21/4, using a standard violin-bow type heat flow probe by FIELAX GmbH, Bremerhaven. The probe consists of 22 temperature sensors distributed evenly over an active length of 5.46 m. The sensors were calibrated to a precision of 0.002°C at a water depth of 1400 m.

We conducted measurements at four stations north of the Knipovich Ridge. Each time, the sediment temperature profile was measured for 7 min after penetration into the sediment. Equilibrium temperatures were obtained by extrapolation from the recorded time series, using the method of Villinger and Davis (1987). After the temperature measurement, thermal conductivity was determined by measuring the decay of a heat pulse emitted from a heater wire along the entire length of the probe.

2.4.3 BSR-based heat flow calculation

2.4.3.1 Calculation method

Geothermal gradients and heat flow were calculated from the BSR observed in the seismic data of cruises MSM21/4 and JR211, using the method after Yamano et al. (1982). This method requires knowledge of the depth of the BSR and seafloor, the phase relation of the hydrate system, and the thermal conductivity of the sediments.

The BSR and seafloor were picked in the seismic data using the Kingdom Suite software (IHS). The picks were then exported to Matlab® (Mathworks Inc.) and converted to depth. We applied a basic velocity model based on MSM21/4 CTD data and depth-migrated seismic data from cruise JR211, with velocities of 1460 m s^{-1} for the water layer and 1695 m s^{-1} between seafloor and BSR.

To determine the pressure at BSR level, we assumed hydrostatic pressure (Townend, 1997; Kinoshita et al., 2011; Li et al., 2012; Martin et al., 2004). We used a seawater density of 1027 kg m^{-3} (Ehlers and Jokat, 2013).

To calculate temperatures at the BSR, several studies (e.g. Li et al., 2012, Martin et al., 2004, Ganguly et al., 2000) used the methane hydrate stability curve of Dickens and Quinby-Hunt (1994). However, this curve is valid only for pressures of up to 10 MPa, whereas our data reached pressures of up to 35 MPa. We therefore applied the CSMHYD program by Sloan (1998) to generate a new curve of methane hydrate stability (Fig. A.1, supporting information in Appendix A.1), using as components seawater (pure water + 3.5 wt% NaCl) and the hydrate composition of Smith et al. (2014) from Vestnesa Ridge. This approach resulted in the following equation

$$T_{BSR} = 7.5877\ln(\text{p}_{\text{BSR}}) + 216.76 \tag{2.1}$$

where p_{BSR} (in kPa) is the pressure at BSR level. The resulting T_{BSR} is given in K.

The geothermal gradient was calculated via

$$\text{gradT} = \frac{dT}{dz} = \frac{T_{BSR} - T_{sea}}{z_{BSR}} \tag{2.2}$$

where gradT is in K km^{-1}, T_{BSR} and T_{sea} (in K) are the temperatures at the BSR and the seafloor, respectively, and z_{BSR} is the depth of the BSR in mbsf. We assumed that seafloor temperatures equal bottom-water temperatures, which vary in the study area due to the large water depth range from <1000 m to >3000 m. We therefore used a seafloor temperature-depth function based on CTD data of MSM21/4 and Sarkar (2012).

Heat flow was then calculated by

$$H = k \times \text{gradT} \tag{2.3}$$

where H is in mW m^{-2}, k (in W m^{-1} K^{-1}) is the thermal conductivity of the sediments and gradT (in K km^{-1}) is the geothermal gradient. For the thermal conductivity, a constant value of 1.3 W m^{-1} K^{-1} was chosen, which is the average of thermal conductivities measured at ODP sites 908 and 909 (Shipboard Scientific Party, 1995a, 1995b). This calculation method was associated with final absolute uncertainties of 11-24% for the geothermal gradient and 19-34% for the heat flow (see supporting information in Appendix A.1).

2.4.4   1D petroleum system modelling

We used the PetroMod software by Schlumberger for the numerical modelling of potential petroleum generation on the Svalbard margin. The modelling was conducted at two sites chosen based on their different heat flow characteristics and locations with respect to the Knipovich Ridge axis: site A was located north of the present ridge axis in 1670 m water depth, while site B (1465 m water depth) was east of the ridge and landward of the ocean-continent boundary of Engen et al. (2008) (Fig. 2.2A). Site 909 (2518 m water depth) was used as a reference site.

The modelling method involved a full 1D reconstruction of the basin stratigraphy at the modelling sites throughout their geological history. First, present-day geological layers were back-stripped to give a proxy for initial layer thicknesses, ages, and densities at the time of deposition. The decompacted sedimentary layers were then used to restore stratigraphic units separately for each site. Standard values for physical properties of dominant lithologies (mostly clays and silts; Table 2.1), including initial seafloor porosity, compaction length scale, density, and permeability as well as thermal properties (thermal conductivity, heat capacity, radiogenic heat), were taken from the inbuilt PetroMod library. Finally, a multi-layer package including assigned stratigraphy, lithology, ages of layers, and their potential petroleum productivity was derived and used as a base for four modelling runs.

2.4.4.1   Modelling input

Due to a lack of precise paleo-bathymetry and paleo-temperature data, boundary conditions assuming constant water depths and a constant seafloor/bottom-water temperature of 2°C were assigned over the entire history of the modelled sites.

Table 2.1: Geological model for the 1D petroleum system modelling. Depth ranges and layer thicknesses differ for the model runs: 1) ODP site 909 as reference: normal stratigraphy (only Miocene source rock) and with Eocene added underneath; 2A) Miocene + Eocene source rock for site A (scaled to 5 km sediment thickness); 2B) Miocene + Eocene source rock for site B (scaled to 4.5 km); 3A) Miocene source rock for site A (scaled to 5 km); 3B) Miocene source rock for site B (scaled to 4.5 km).

layer	unit	lithology	z range [mbsf]	thickness [m]	epoch	age [Ma]	TOC [%]	HI [mg HC/g TOC]	vitrinite reflectance [%]
9		Water		1) 2518[a] 2A) 1670 2B) 1465 3A) 1670 3B) 1465					
8	I[a]	Clay, silty clay[a]	1) 0-249[a] 2A) 0-983 2B) 0-885 3A) 0-1172 3B) 0-1055	1) 249[a] 2A) 983 2B) 885 3A) 1172 3B) 1055	Quarternary-Pliocene[a]	0-3.6			
7	II[a]	Silty clay, clayey silt[a]	1) 249-518[a] 2A) 983-2046 2B) 885-1841 3A) 1172-2439 3B) 1055-2195	1) 269[a] 2A) 1063 2B) 956 3A) 1267 3B) 1140	Pliocene-Miocene[a]	3.6-10.0			
6	IIIa[a]	Silty clay, clayey silt[a]	1) 518-923[a] 2A) 2046-3645 2B) 1841-3281 3A) 2439-4345 3B) 2195-3911	1) 405[a] 2A) 1599 2B) 1440 3A) 1906 3B) 1716	Miocene[a]	10.0-13.5			

5	IIIb-1[b]	Silty clay, clayey silt[a]	1) 923-975[a,b] 2A) 3645-3851 2B) 3281-3466 3A) 4345-4590 3B) 3911-4131	1) 52[a,b] 2A) 206 2B) 185 3A) 245 3B) 220	Miocene[a]	13.5-14.8[b]	0.8-1.2[a,b] (1.0)	30-130[a,d] (80)	>1.0[b]
4	IIIb-2[b]	Silty clay, clayey silt[a]	1) 975-1023[a,b] 2A) 3851-4040 2B) 3466-3636 3A) 4590-4816 3B) 4131-4335	1) 48[a,b] 2A) 189 2B) 170 3A) 226 3B) 204	Miocene[a]	14.8[b]-16.2[b]	0.8-1.2[a,b] (1.0)	30-130[a,d] (80)	>1.0[b]
3	IIIb-3[b] / 1/6[c]	Silty clay, clayey silt[a,c]	1) 1023-1062[a,b,c] 2A) 4040-4194 2B) 3636-3775 3A) 4816-5000 3B) 4335-4500	1) 39[a,b,c] 2A) 154 2B) 139 3A) 184 3B) 165	Mid-Miocene[a,b] - mid-Eocene[c]	16.2[b]-44.0	2.0-3.0[a,b] (2.5)	140-250[a,d] (170)	0.4-0.5[b]
2	2[c]	Biosiliceous ooze[c]	1) 1062-1155[c] 2A) 4194-4562 2B) 3775-4105 3A) – 3B) –	1) 93[c] 2A) 368 2B) 330 3A) – 3B) –	Mid-Eocene[c]	44.0[e] - 50.0	2.0-3.0[c] (2.5)	150-350[c,e] (200)	0.25[e]
1	3[c]	Clay, silty clay[c]	1) 1155-1266[c] 2A) 4562-5000 2B) 4105-4500 3A) – 3B) –	1) 111[c] 2A) 438 2B) 395 3A) – 3B) –	Late Paleocene-mid-Eocene[c]	50.0-56.0[e]	1.0-2.5[c] (1.8)	50-300[c,e] (150)	<0.5[e]

[a] Shipboard Scientific Party (1995b), [b] Knies and Mann (2002), [c] Expedition 302 Scientists (2006), [d] Stein et al. (1996), [e] Stein et al. (2006)

Heat flow

An important input for the petroleum system modelling was the thermal history at the modelling sites. As the precise onset of seafloor spreading at the Knipovich Ridge and the timing of break-up differ (e.g. Eldholm et al., 1984; Crane et al., 1991; Engen et al., 2008), we assumed that heat flow changed at sites A and B as spreading along the ridge progressed. Over time, the spreading axis moved westward, away from site B and towards site A (Fig. 2.2A). Site A thus experienced heating, while site B was characterised by cooling.
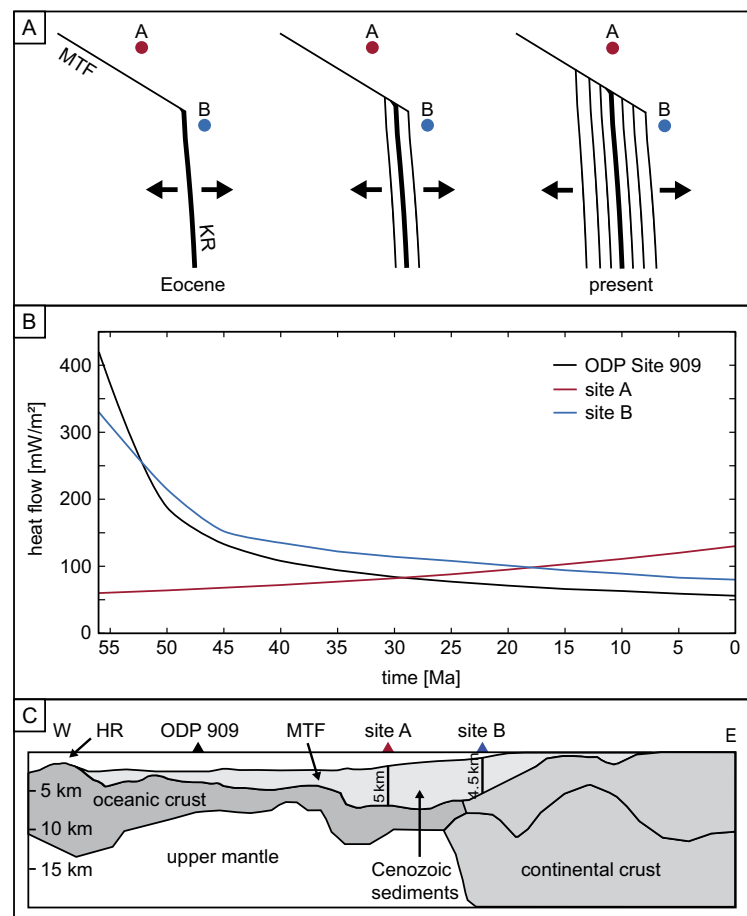
Figure 2.2: Heat flow evolution at the two modelling sites, following Eocene break-up along the Knipovich Ridge (KR). **(A)** As rifting progressed, the spreading axis moved away from site B and towards site A, causing heat flow to increase at site A and decrease at site B. MTF – Molloy Transform Fault. **(B)** Heat flow curves for site A, site B. and ODP Site 909. **(C)** Schematic of a crustal transect from Hovgård Ridge (HR) to Kongsfjorden, illustrating total sediment thicknesses at sites A and B. Note that sites A, B and ODP 909 are not located on this transect but have been projected onto it. Transect location is shown in Fig. 2.1. MTF – Molloy Transform Fault. After Ritzmann et al. (2004).

As we only knew the present-day heat flow inferred from the BSR, we made assumptions regarding the heat flow evolution since the initiation of rifting. For site A, we assumed a linear increase in heat flow from 60 mW m^{-2}, which agrees with the regional background heat flow of 50-75 mW m^{-2} (Vogt and Sundvor, 1996), to the 130 mW m^{-2} derived from the BSR (Fig. 2.2B). The cooling curve of site B is exponential, with a decrease from 330 mW m^{-2}, corresponding to the maximum

heat flow observed today in the center of the rift, to the present heat flow of 80 mW m^{-2} (Fig. 2.2B). For Site 909, we derived a heat flow curve from the plate cooling curve of Sundvor et al. (2000) (Fig. 2.2B).

Geological model

There are no deep drill sites in the area north of the Knipovich Ridge and hence stratigraphic information is not available, which complicated the design of a geological input model. The closest ODP site is Site 909 (Fig. 2.1), and we therefore assumed the same lithology at our modelling sites (Table 2.1), including the Miocene sequence that was interpreted as a potential but immature source rock (unit IIIB in Knies and Mann (2002)). The petroleum generation potential of the source rock depends on its initial TOC content and HI, which we obtained from the literature as detailed in Table 2.1.

In addition to a Miocene source rock, we also tested the petroleum generation potential for a potential Eocene source rock with the same characteristics as the Eocene sediments in the Arctic Basin (Mann et al., 2009). The Eocene layers, corresponding to layers 1-3 of IODP sites M0002-M0004 in the Arctic Basin (Expedition 302 Scientists, 2006), were therefore added underneath the stratigraphic record from Site 909. As the lithology and Eocene-Miocene age of unit IIIB of Site 909 agreed well with unit 1/6 of Sites M0002-M0004, they were treated as one layer in the geological model. The geological model for sites A and B thus consisted of nine layers including the water layer (layer 9), Miocene source rock (layers 3-5), and Eocene source rock (layers 1-2) (Table 2.1).

Cenozoic sediment thicknesses down to the basement were inferred from a wide-angle seismic transect of Ritzmann et al. (2004) from Kongsfjorden to the Hovgård Ridge. Total sediment thicknesses amount to 5 km at site A and 4.5 km at site B (Fig. 2.2C), which is supported by Geissler et al. (2011). The layer thicknesses inferred from the ODP and IODP sites were scaled to these thicknesses as detailed in 2.4.4.2.

Kinetics

Kinetics of hydrocarbon generation are not known for the Svalbard margin or for the North Atlantic-Artic region in general. We therefore used standard global kinetics from Pepper and Corvi (1995) – type B, siliclastic lithofacies in marine environments – for both source rocks. These general kinetics were previously tested in modelling of hydrocarbon generation from specific kerogen organofacies with separate oil and gas fractions. The type B kinetics imply an oil to gas ratio of 83% to 17% (Pepper and Corvi, 1995).

2.4.4.2 Modelling approach

We tested several 1D modelling approaches of the hydrocarbon generation process without considering migration of oil and/or gas fractions. Determination of the regional impact of gas migration

towards the GHSZ and subsequent potential hydrate formation or fluid venting is therefore beyond the scope of this study.

Petroleum generation was modelled with a constant time step of 1 Ma and a vertical resolution of 10 m during four separate runs, which mainly differed in the layer thicknesses applied (Table 2.1). Run 1 (Site 909) was used as a reference and involved modelling for a Miocene source rock with and without an Eocene source rock. Run 2 included a Miocene and an Eocene source rock at sites A and B, with the stratigraphy scaled to total sediment thicknesses of 5 km and 4.5 km, respectively. Run 3 involved only the Miocene source rock (layers 3-9 in Table 2.1), again with total sediment thicknesses of 5 km and 4.5 km for sites A and B, respectively. Runs 2 and 3 were conducted three times for mean, minimum and maximum TOC and HI values as shown in Table 2.1.

Run 4 served to model the effects of an increasing overburden on petroleum generation from the Miocene source rock. Starting with the original layer thicknesses of ODP site 909 (100%), layer thicknesses were increased at 50% intervals to 350% of the original thicknesses (Table A.1, supporting information in Appendix A.1), and petroleum generation was modelled for each case. Run 4 involved mean TOC and HI values at both site A and site B, which differed in their water depths and thus in the thickness of layer 9.

2.5   Results

2.5.1   BSR distribution

Based on the available seismic lines, we identified three main centers of BSR occurrence on the Svalbard margin (Fig. 2.3). All three are located in the vicinity of spreading segments, i.e., the Knipovich Ridge, the Molloy Ridge, and the Lena Trough.

The southernmost and largest area of BSR occurrence lies close to the northern end of the Knipovich Ridge. It covers an area of $\sim$3500 km^2 and extends in a northwestern direction along the Molloy TF, with a width of up to 40 km. The BSR is mostly found in the area northeast of the Molloy TF, but also occurs in a few locations on the western flank of the Knipovich Ridge. As the southern BSR area also has the best data coverage, we will focus on this area for the rest of the paper and refer to it as our study area.

The other two BSR areas are located east of the Lena Trough (2400 km^2) (Geissler et al., 2014b) and north of the Molloy Ridge. The Molloy Ridge BSR area covers $\sim$1400 km^2 and extends to the northwest, parallel to the Spitsbergen TF. There is another, smaller ($\sim$300 km^2) BSR area inferred from JR211 profiles located northeast of Vestnesa Ridge at the eastern end of the Spitsbergen TF.

In between the centers of BSR occurrence, we observed two types of BSR gaps: (1) apparent gaps, where seismic data are not available and hence it is not known whether a BSR does exist, and (2) true gaps for which seismic data exist but lack a BSR. True gaps were, for example, found west of Vestnesa Ridge and the Molloy TF (Vanneste et al., 2005b). For most parts of the Lena Trough and southern BSR areas, a BSR was also absent east of the ocean-continent boundary of Engen

et al. (2008). In addition, a BSR was not observed along some of the seismic lines of Geissler et al. (2014b), e.g. on the southernmost lines and south of the Lena Trough BSR area, where a BSR was absent except for a ~13 km long profile section. However, these data are of lower resolution, which made BSR identification difficult, and hence the presence of hydrate cannot be excluded completely along these profiles.
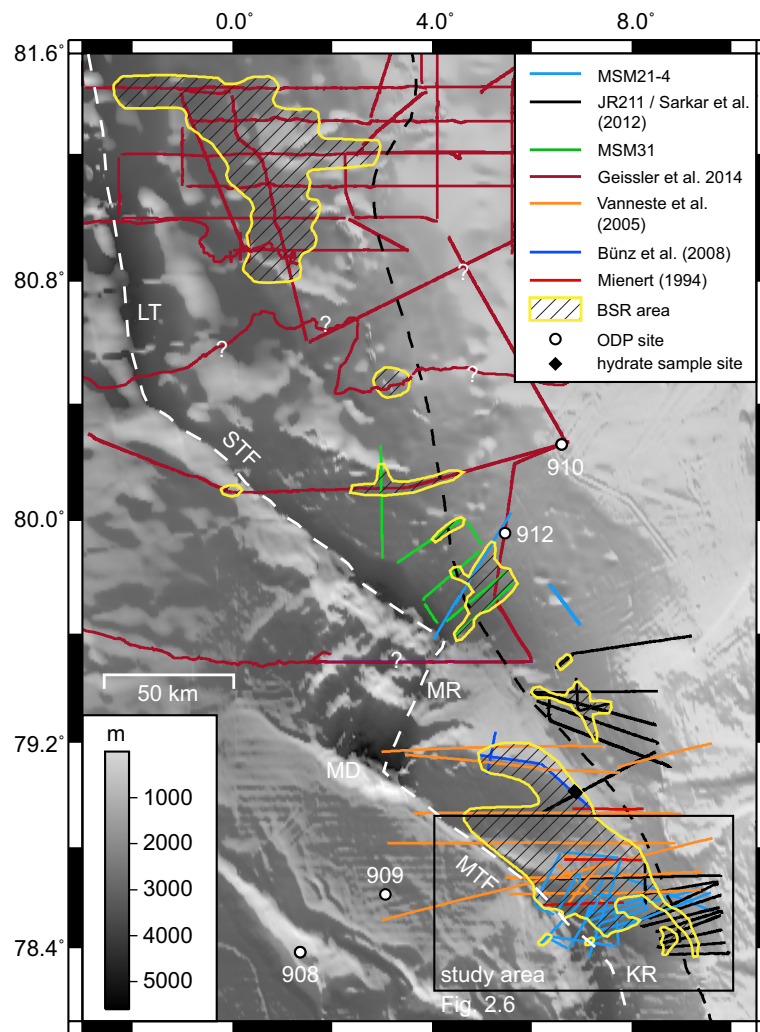

Figure 2.3: Map of the BSR distribution along the Svalbard margin, based on 2D seismic data collected on different surveys. The BSR indicates the presence of gas hydrates. Stippled lines mark the ocean-continent boundary after Engen et al. (2008) (black) and the present-day plate boundary (white). Black dots mark ODP site locations. Question marks indicate profile sections where the seismic data are not conclusive about the existence of a BSR. Figure location is shown in Fig. 2.1. LT – Lena Trough, MD – Molloy Deep, MTF – Molloy Transform Fault, MR – Molloy Ridge, STF – Spitsbergen Transform Fault.

In general, gas hydrate can also be present without a BSR (Haacke et al., 2007), because a BSR depends on the lithology besides the existence of free gas. Alternatively, a BSR could be hidden in case of parallel sediment layering, which may apply to some of the profiles of Geissler et al. (2014b). Consequently, the gas hydrate extent inferred from the presence of a BSR in seismic data is considered a minimum extent.

2.5.2 BSR character

The BSR is well imaged in the MSM21/4 and JR211 seismic datasets (see also Sarkar et al. (2012) for a description of the JR211 data). It is characterised by a reflection of negative polarity that generally follows the seafloor (Fig. 2.4A and 2.5A) at a depth of 90-290 mbsf (on average 200 mbsf). Enhanced amplitudes are observed immediately beneath the BSR (Fig. 2.5A). On most profiles, the BSR is either continuous over distances of 8-18 km (Fig. 2.4A), or shorter and often interrupted (Fig. 2.5A).

Some profiles show a distinct change from a normal seismic reflection character above the BSR to higher amplitudes and larger seismic wavelengths below the BSR (Fig. 2.4A). This boundary is also very obvious in the instantaneous frequency attribute of the seismic data (Fig. 2.4B), which indicate a drop from >110 Hz above the BSR to <90 Hz below, and thus a strong attenuation of higher seismic frequencies at the BSR. This anomaly occurs in a >360 km^2 large area about 20 km north of the Knipovich Ridge (Fig. 2.6A) and is observed in both the MSM21/4 and JR211 data.
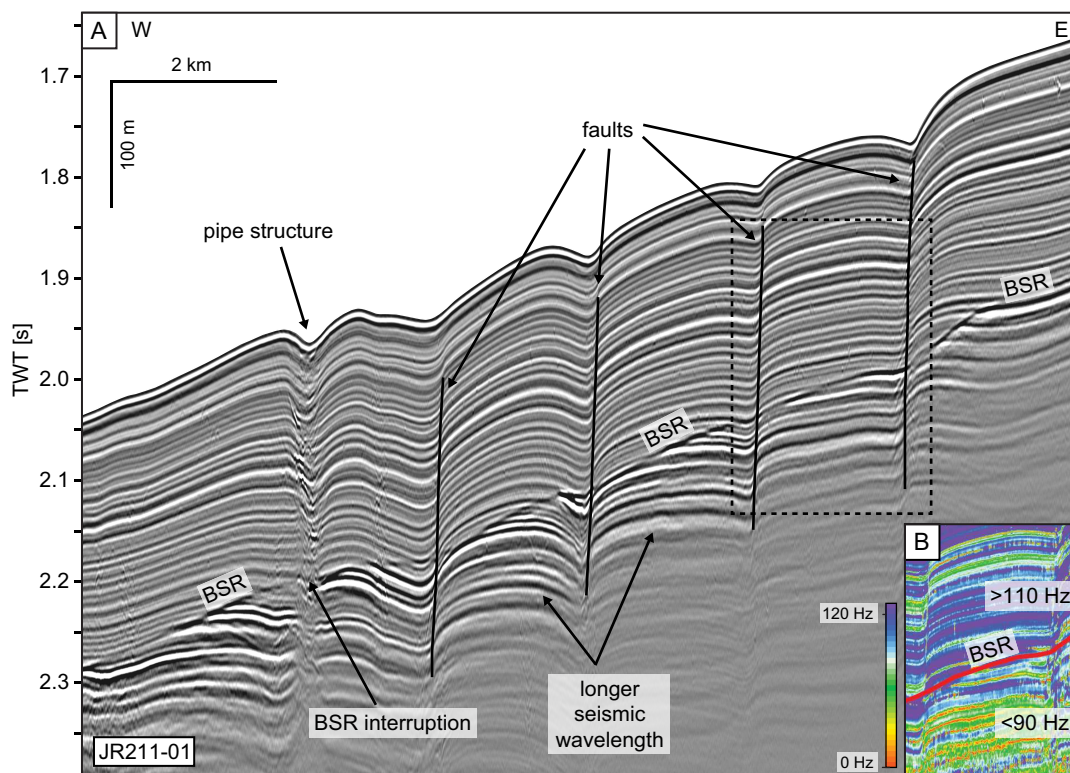
Figure 2.4: **(A)** Example of a well-imaged long BSR (>18 km, continuing outside the section shown here) along profile JR211-01. At the near-vertical faults, the BSR is undisturbed, but it is interrupted and slightly up-bending at the pipe structure, indicating a change in the thermal field. The pipe structure is characterised by downbending, slightly chaotic reflections. Stippled rectangle marks the inset shown in (B). **(B)** Instantaneous frequency attribute of the same section. The frequency of the reflected seismic signal differs strongly between the sediments above the BSR (>110 Hz) and below (<90 Hz), indicating strong attenuation of higher frequencies. Location is shown in Fig. 2.6A.

2.5.3 Vertical seismic anomalies

Two types of vertical seismic anomalies exist in the study area: faults and pipe structures (see also Sarkar et al. (2012)). The faults are mostly near-vertical normal faults, many of which do not reach the seafloor. Where a BSR is present at a fault, the BSR remains undisturbed (Fig. 2.4A and 2.5A).
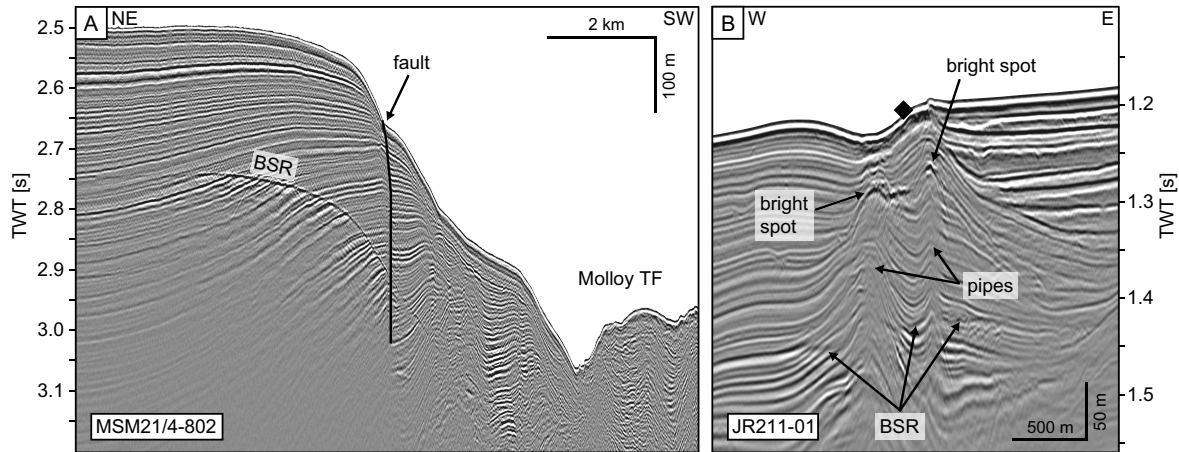

Figure 2.5: **(A)** Shorter, well-imaged BSR on the northeast of the Molloy Transform Fault. The BSR is not interrupted by the near-vertical normal fault. **(B)** Two pipes characterised by up-bending reflectors, bright spots and an interrupted BSR. Black diamond shape marks the shallower sample site of Fisher et al. (2011). Locations are shown in Fig. 2.6A.

Five pipes were identified in the study area: three are characterised by up-bending and two by down-bending reflections. Up-bending pipes are narrow (100-150 m) and do not reach the seafloor, with two of them terminating at bright spots. The two down-bending pipes are ~230 m and ~340 m wide and show a chaotic internal reflection pattern (Fig. 2.4A). They reach the seafloor where they terminate in ~5-10 m deep depressions. All pipe structures occur where a BSR is present and at each pipe the BSR is interrupted and sometimes vertically offset on the other side of the pipe (Fig. 2.4A).

In addition, there are two vertical anomalies characterised by reduced seismic amplitudes. One of these, a ~400-m-wide structure located outside the BSR area, has been described as a chimney structure (Sarkar et al., 2012). The other anomaly is >1.5 km wide and comprises two vertical zones of slightly lower amplitudes that terminate at bright spots about 50 m beneath a ~15-m-deep seafloor depression (Fig. 2.5B). It is further characterised by strong up-bending of reflections. Its location corresponds to the "plume field" sample site of Fisher et al. (2011).

2.5.4 Heat flow

2.5.4.1 BSR-derived heat flow

The BSR-derived heat flow ranges between ~80 mW m^{-2} and 330 mW m^{-2}, with an average of 116 mW m^{-2} (Fig. 2.6A). The geothermal gradient varies between ~60 °C km^{-1} and 260 °C

km^{-1} (average 90 °C km^{-1}). In general, heat flow increases from the continental slope towards the Knipovich Ridge and the Molloy TF (Fig. 2.6A). This trend is also supported by the average heat flow values, which are higher for the MSM21/4 data (120 mW m^{-2}) than for the JR211 data (109 mW m^{-2}), which were collected closer to the continental slope. The highest heat flow occurs at the centre of the rift zone, at the transition of the Knipovich Ridge and the Molloy TF (Fig. 2.6A).
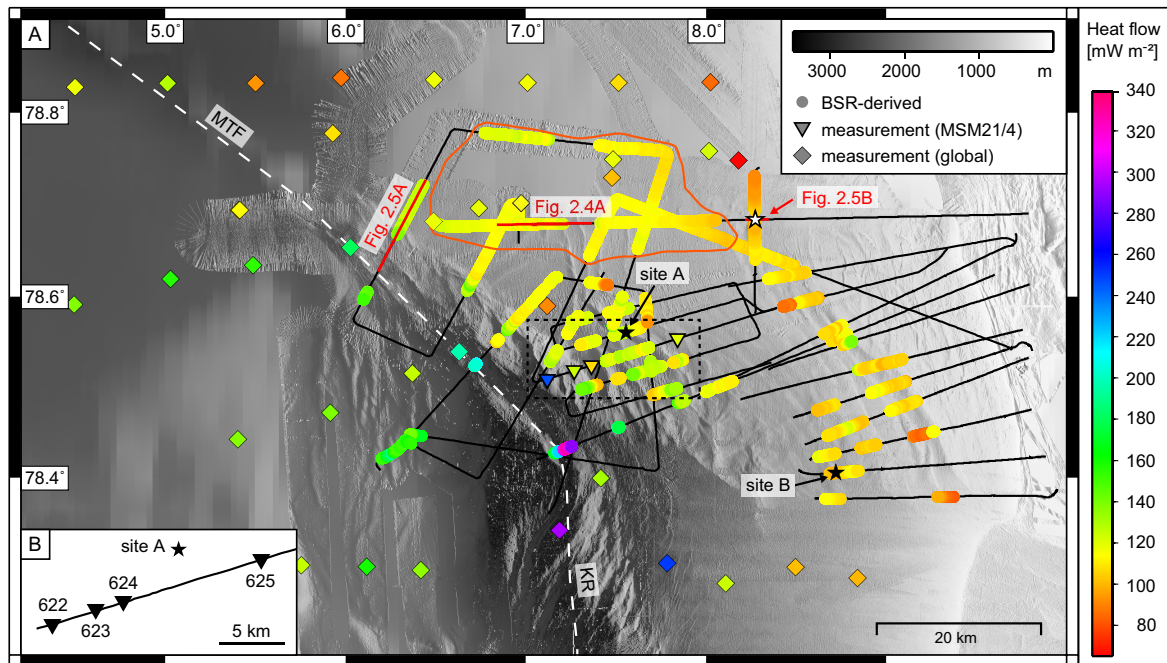

Figure 2.6: **(A)** Heat flow map showing the BSR-derived values along with heat flow measurements at the northern end of the Knipovich Ridge. Black stars mark sites A and B for which the petroleum system modelling was carried out in order to test the petroleum generation potential of the area. The white star marks the shallower sample site of Fisher et al. (2011). The red polygon indicates the area in which strong attenuation of seismic frequencies below the BSR was observed (shown in Fig. 2.4A) White stippled line marks the present-day rifting boundary. Stippled rectangle shows location of the inset shown in (B). Location is shown in Fig. 2.3. KR – Knipovich Ridge, MTF – Molloy Transform Fault. **(B)** Inset showing heat flow stations of cruise MSM21/4.

2.5.4.2   Heat flow probe measurements

Heat flow inferred from the four probe measurements ranges between ∼110 mW m^{-2} and ∼250 mW m^{-2} (Table 2.2). However, the heat flow values of the two western stations (622 and 623; Fig. 2.6B) are not entirely reliable as only about half of the thermal conductivity sensors recorded values, probably because the probe did not fully penetrate into the sediment. Consequently, thermal conductivity values and hence heat flow values may be too high at these stations.

A direct comparison of measured and BSR-derived heat flow values was not possible as a BSR was not observed at any of the heat flow stations. Still, the ∼108 mW m^{-2} and ∼110 mW m^{-2} at the two eastern stations (624 and 625; Fig. 2.6B) agree well with the calculated heat flow of nearby BSR sections (Fig. 2.6A).

Table 2.2: Heat flow probe measurements of the geothermal gradient and thermal conductivity k on cruise MSM21/4, and the resulting heat flow. Location of stations is shown in Fig. 2.6B.

station	latitude [°N]	longitude [°E]	no. of T sensors (of 22 total)	grad T [°C km^{-1}]	no. of k sensors (of 22 total)	k mean [W m^{-1} K^{-1}]	resulting heat flow [mW m^{-2}]
622	78.5100	7.1180	22	142.8	12	1.74	246.9
623	78.5192	7.2705	22	73.5	10	1.71	124.9
624	78.5250	7.3650	22	72.7	21	1.45	107.9
625	78.5545	7.8425	22	88.7	21	1.33	110.6

2.5.5 Modelling results

In general, the modelling results show that bulk petroleum production (i.e., oil and gas) occurs at all three sites (site A, site B, and Site 909) for each source rock scenario. However, the generated mass of petroleum at Site 909 is two magnitudes lower than at sites A and B.

For the true stratigraphy of Site 909, which included the Miocene source rock, production did not occur until middle Miocene (10 Ma). Until present, it reached a generated mass of ~0.3 kt, assuming mean TOC and HI values (Run 1; Fig. 2.7A). When the Eocene source rock was added underneath, production started earlier (~40 Ma) but remained almost zero until ~14 Ma, when it began to increase to ~1.2 kt (again for mean TOC and HI) until present (Fig. 2.7A).

For Run 2 (Miocene and Eocene source rock), no significant production occurred at site A until middle Miocene (Fig. 2.7C). A strong increase in production took place between 15 Ma and 10 Ma, reaching a generated mass of 0.07 Mt (for mean TOC and HI; 0.19 Mt for max.) until present. The associated burial curve (Fig. 2.7B) shows a rapid increase of overburden (~2000 m) in the interval of 15-10 Ma, corresponding to the timing of the production increase. Unlike site A, site B was characterised by two production phases in Run 2: the first phase occured in the Eocene prior to ~40 Ma, while the second phase began in middle Miocene at ~14 Ma (Fig. 2.7D). The second phase was characterised by a strong increase in production until 10 Ma, followed by reduced production until present (~0.07 Mt for mean TOC and HI, ~0.19 Mt for max.).

In contrast to Run 2, the results of Run 3 (Miocene source rock only) were relatively similar for sites A and B (Fig. 2.8A and 2.8B). At both sites, petroleum production started at 13.5 Ma and increased rapidly until 10 Ma, although the increase was stronger at site A than at site B. At site A, the bulk production until present was ~0.11 Mt for mean TOC and HI (~0.19 Mt for max.); at site B, it was slightly lower (~0.10 Mt for mean, ~0.18 Mt for max. TOC and HI).

When layer thicknesses were gradually increased from the thicknesses determined at Site 909 to those used for Run 3, the generated mass of petroleum also increased (Run 4; Fig. 2.8C and 2.8D). At site A, the bulk petroleum production for mean TOC and HI increased from <0.01 Mt for 100% layer thicknesses of Site 909 to >0.10 Mt for the layer thicknesses of Run 3 (Fig. 2.8C). At site B, production also increased to >0.10 Ma for the thicknesses of Run 3, however, petroleum generation did not occur for 100% layer thicknesses of Site 909 (Fig. 2.8D).
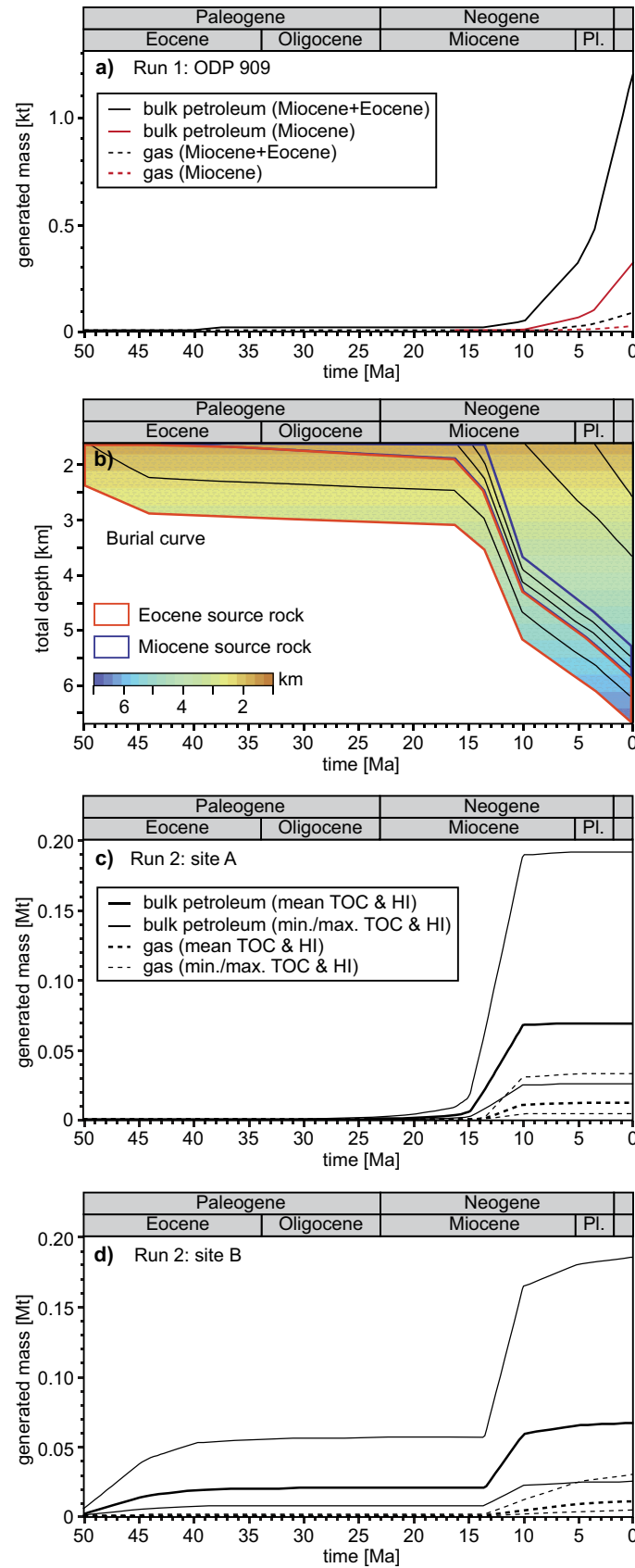
Figure 2.7: Results of the 1D petroleum system modelling. Note that the generated mass of petroleum is given in kt in (A) and in Mt for (C) and (D). **(A)** Run 1 for Miocene (red) and Miocene and Eocene (black) source rocks at ODP Site 909. **(B)** Burial curve for site A (Run 2A). **(C)** Petroleum generation for Miocene and Eocene source rocks at site A (Run 2A). **(D)** Petroleum generation for Miocene and Eocene source rocks at site B (Run 2B). Note that there are two generation phases, one in the Eocene and one in the middle Miocene. Legend is shown in (C). Pl. – Pleistocene, TOC – total organic carbon, HI – hydrogen index.
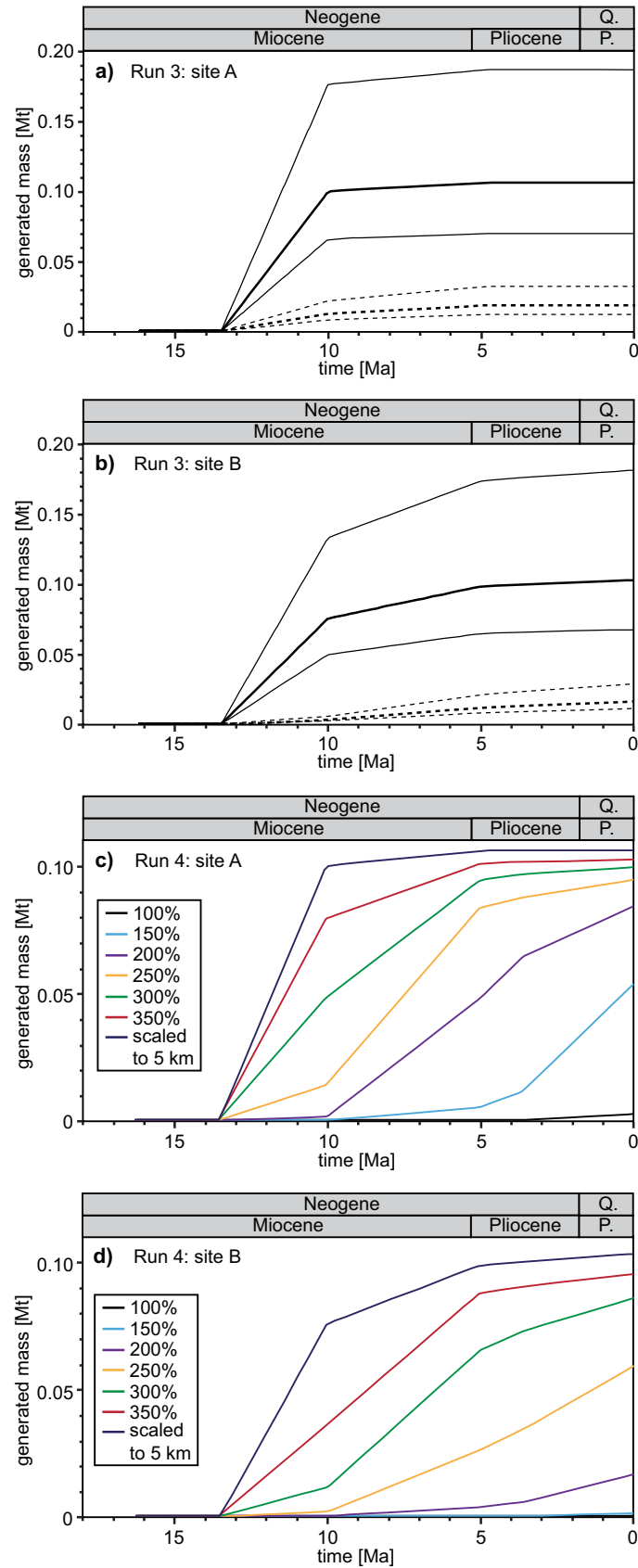
Figure 2.8: Results of the 1D petroleum system modelling. Legend is shown in Fig. 2.7C. (A) Petroleum generation for a Miocene source rock at site A (Run 3A). (B) Petroleum generation for a Miocene source rock at site B (Run 3B). (C) Petroleum generation for varying total sediment thicknesses in percentages of sediment thicknesses at Site 909 (site A). (D) Petroleum generation for varying total sediment thicknesses in percentages of sediment thicknesses at Site 909 (site B). Pl. – Pleistocene, TOC – total organic carbon, HI – hydrogen index.

With increasing overburden, petroleum production started earlier. At site A, the onset of production changed from ~3.5 Ma for the 100% case to ~13.5 Ma for the layer thicknesses of Run 3 (Fig. 2.8C). Similarly, at site B the onset changed from ~3.0 Ma (150%) to ~13.5 Ma for Run 3 thicknesses (Fig. 2.8D).

The slope of the production curves, and hence the production rate, also changed with increasing overburden. For a thicker overburden (>300%), production started with relatively high rates and slowed down around 11-10 Ma and at the beginning of the Pliocene (Fig. 2.8C and 2.8D). For a thinner overburden (<300%), production rates were initially low but increased at ~10 Ma. In the Pliocene, production rates then either decreased (e.g. for 200% and 250% at site A) or increased (e.g. for 150% at site A).

At site A, the production curves leveled off in the Pliocene for the 350% and Run 3 curves, i.e., production ceased in Pliocene times (Fig. 2.8C). Saturation was neither observed in the other curves nor at site B. Instead, production is presently ongoing at different rates. The highest present-day rates occur for the 150% case at site A and 250% at site B.

2.6 Discussion

2.6.1 Fluid migration

Compared to Vestnesa Ridge (e.g. Bünz et al., 2008, 2012), there are not many indications for vertical fluid migration in the seismic data of our study area. In the study area, potential pathways for vertical fluid migration are faults and pipe structures (Hustoft et al., 2009; Sarkar et al., 2012).

We interpret the undisturbed BSR at the faults to indicate that the faults are probably not actively transporting fluids. This is in agreement with the absence of seismic amplitude anomalies in seismic data adjacent to the faults, and with Sarkar et al. (2012), who could not find evidence for fault-controlled gas migration in the shallow parts of the Svalbard margin. We note, however, that fluid dissipation could take place along the faults but that it is not fast enough to affect the thermal field and the BSR.

In contrast, the interruption of the BSR at the pipe structures indicates a disruption of the thermal field. The chaotic reflection character within the down-bending pipes, as well as bright spots at other pipes, suggests the presence of free gas and therefore the possibility of vertical fluid migration. At the two pipes that reach the seafloor, active fluid venting could possibly be going on, but sediment cores taken in the vicinity did not show signs of active seepage. The pipe structures that do not reach the seafloor may either be still-developing structures or extinct and buried.

Although it seems more likely that fluid migration occurs at pipe structures than at faults, the small number of potential fluid flow features suggests that vertical fluid migration is presently very limited in the study area. Vanneste et al. (2005b) propose that the outer Svalbard margin is undergoing extension and that the long and continuous BSR and its bottom-simulating behaviour indicate that this extension has not yet affected the fluid flow system. However, the role of fluid migration

could increase in the future, which would cause a more irregular and less seabed-following BSR (Vanneste et al., 2005b). Both the absence of fluid migration markers and the undisturbed BSR indicate that the strata above the BSR are not strongly affected by gas production at depth, and that gas ascending to the base of the gas hydrate stability zone turns into hydrate instead of penetrating the hydrate stability zone.

2.6.2 Source rock potential in the study area

Due to the lack of information on some of the modelling input parameters, several assumptions had to be made that affected the final outcome of the petroleum system modelling. While the geological model is relatively well constrained, uncertainties are high for the heat flow evolution at the modelling sites and for the kinetics of hydrocarbon generation. We therefore refrain from discussing the exact amounts of petroleum that are potentially generated, but only consider the general trends.

Given the assumptions discussed in 2.4.4.2, hydrocarbons, including oil and gas, form from the Miocene source rock north of the Knipovich Ridge. Even if sediment thicknesses at the modelling sites are not as assumed for Run 3 (Fig. 2.8A and 2.8B), the results of Run 4 (Fig. 2.8C and 2.8D) show that reduced sediment thicknesses still allow petroleum production at both site A and B. Petroleum production also occurs at Site 909 (Run 1; Fig. 2.7A), although the generated mass is small in comparison. However, if production occurs at Site 909 where the Cenozoic sediments are thinnest, then it is reasonable to assume that production is also possible further landward where sediment thicknesses are greater (Ritzmann et al., 2004).

Our results support the idea of Smith et al. (2014), who suggested that thermogenic gas on Vestnesa Ridge could be related to petroleum production from Miocene source rocks. However, due to the large input-associated uncertainties of the generated mass of petroleum, we cannot tell if the generated amount is sufficient to explain the wide distribution of gas inferred from the BSR extent.

In the case that both a Miocene and an Eocene source rock are present in the study area, it is not possible to derive from the production curves whether both source rocks contributed to the generated amount of petroleum observed. However, the results of site A (Fig. 2.7C) show that if petroleum is produced from Eocene sediments, the Eocene source rock is not mature enough until Miocene times. This is different for site B (Fig. 2.7B), where an Eocene as well as a Miocene production phase are observed – with the Eocene phase obviously being related to the Eocene source rock. Thus, during the Eocene the source rock was sufficiently mature for petroleum production at site B but not at site A, even though the two sites are only ~30 km apart.

Similar observations were made in the Arctic Basin where the same Eocene source rock is mature in the Amundsen Basin but not at the adjacent Lomonosov Ridge (Mann et al., 2009). Mann et al. (2009) attributed the difference to the higher overburden and deeper burial in the Amundsen Basin. In our study area, however, a higher overburden cannot explain the observed differences during the Eocene as there was no overburden above the Eocene source rock. We therefore need to consider other parameters.

Apart from the sedimentary overburden, parameters that influence modelled source rock maturity and petroleum generation are organic matter characteristics, kinetics of hydrocarbon generation, and heat flow. Organic matter characteristics were assumed to be the same at site A and B, as were the kinetics of hydrocarbon generation. Heat flow, however, differed: during the Eocene, heat flow was high (200-300 mW m^{-2}) at site B and low (60-70 mW m^{-2}) at site A, due to the close proximity of site B to the Eocene spreading centre. We believe that the Eocene heat flow was high enough to cause petroleum generation at site B but not at site A.

The difference in heat flow also explains why there were two phases of petroleum generation at site B and only one at site A. The Eocene phase was mainly controlled by temperature, i.e., heat flow, which was too low at site A to induce production. In the Miocene phase, heat flow was similar at both sites (Fig. 2.2B). This phase appears instead to be controlled by sediment deposition as indicated by the burial curve (Fig. 2.7B), which shows rapid burial during 15-10 Ma, coeval with the second phase of petroleum generation.

As the heat flow in the study area is strongly controlled by the Knipovich Ridge, which is inferred from heat flow increasing towards the ridge axis (Fig. 2.6A), the Eocene phase of petroleum generation appears to be influenced by the Knipovich Ridge. In contrast, the Miocene phase seems largely independent from the ridge and is controlled primarily by sedimentation processes.

2.6.3   Conditions for the existence of Eocene rocks north of the Knipovich Ridge

It is not known if the same source rock as in the Arctic Basin also exists in our study area. The only stratigraphic information for the Svalbard margin comes from ODP sites, which have not been drilled down to the depths of potential Eocene sequences (Myhre et al., 1995). It is therefore important to consider the conditions under which an Eocene source rock similar to that of the Arctic Basin could have been deposited on the Svalbard margin.

The Eocene source rock found in the Arctic Basin is associated with the deposition of the fern *Azolla* during early to middle Eocene (Brinkhuis et al., 2006; Mann et al., 2009). Conditions for the deposition of *Azolla*, which is a freshwater plant, include well-stratified waters and "Black-Sea-type" anoxia (Brinkhuis et al., 2006) that are generally restricted to relatively closed basins. The Arctic Ocean remained a closed basin until the Miocene (Jakobsson et al., 2007), thus allowing no exchange of organic matter. However, the deposition of *Azolla* was not limited to the Arctic Basin. Brinkhuis et al. (2006) show that *Azolla* deposits were found as far south as the North Sea, including in Svalbard, although they do not give an exact location.

If *Azolla*-derived organic matter was deposited on the Svalbard margin, it must have occurred in a closed basin setting. Multiple basins may have existed during the Eocene, in the form of pull-apart basins that were part of the ancient Spitsbergen Shear Zone (Crane et al., 1982, 2001). These pull-apart basins later developed into mid-ocean ridge segments offset by transform faults, such as the Molloy Ridge and Transform Fault (Crane et al., 1982; Thiede et al., 1990). It is therefore possible that there was also a pull-apart basin, e.g. similar to today's Molloy Deep, north of the Knipovich Ridge.

In such pull-apart basins, favourable conditions for the deposition of *Azolla* could have been met and maintained into the early stages of rifting, thus enabling the development of a source rock comparable to that found in the Arctic Basin. Brinkhuis et al. (2006) note that during the middle Eocene, surface waters of the Atlantic Ocean were sufficiently fresh for *Azolla* to grow and spread. Nevertheless, it remains speculative that *Azolla*-derived organic matter was deposited in our study area during the Eocene and resulted in the formation of a sufficiently thick source rock sequence. Without deeper drilling, one cannot prove the existence of an Eocene source rock on the western Svalbard margin.

2.6.4 Discussion of the results in the light of thermogenic gas finds on Vestnesa Ridge

Our results are consistent with the observation of thermogenic gas at Vestnesa Ridge. First, we observe a widespread BSR in an area of increased heat flow, i.e., at the intersection of the Knipovich Ridge and the Molloy TF. Second, the petroleum system modelling shows that in-situ thermogenic petroleum production, including gas, is possible from both existing Miocene sediments and a potential Eocene source rock. Consequently, some petroleum generation must have occurred on the Svalbard margin, which is in agreement with the thermogenic gas finds of Fisher et al. (2011) and Smith et al. (2014).

Alternatively, serpentinization could be a source for extensive gas hydrate occurrence. Serpentinization requires seawater to enter the upper mantle, which typically occurs at slow-spreading ridges (Minshull et al., 1998). Serpentinization processes and associated methane generation have been proposed for the central (Kandilarov et al., 2008; Rajan et al., 2012b) and southern Knipovich Ridge (Connelly et al., 2007). However, methane samples with isotopic signatures that could confirm an abiogenic origin do not exist for any of these areas.

For Vestnesa Ridge, Smith et al. (2014) exclude the possibility of serpentinization-derived methane based on the geochemical signatures of the recovered gas hydrate samples. If serpentinization played a role in this area, $\delta^{13}C$ values of methane should be heavier than the measured -47.7‰, i.e., around -25‰, but such values were not observed (Smith et al., 2014).

Serpentinization at the northern Knipovich Ridge may have been possible in the early rifting stages when the overburden was thin and the mantle could have been exposed to seawater in places. Since then, however, the oceanic crust has been covered by more than 1 km of sediment, and the seismic data (also Sarkar et al., 2012) do not show any evidence for deep-reaching faults that could act as pathways for seawater to the upper mantle. Even if serpentinization did occur in early Eocene, it probably cannot have affected an area large enough to account for the amount of gas observed today.

We cannot completely exclude the possibility of serpentinization-derived methane north of the Knipovich Ridge, but we think it unlikely, as this implies that, in addition to bacterial production at the slope (Sahling et al., 2014), there are two more methane sources on the Svalbard margin: thermogenic production and serpentinization. Neither the geophysical nor the geochemical data

are conclusive about the existence of three separate sources. We therefore share the interpretation of Smith et al. (2014) that the gas north of the Knipovich Ridge is mostly of thermogenic origin.

2.7   Conclusions

The western Svalbard margin is characterised by extensive occurrence of gas hydrates with a maximum abundance in the vicinity of the Knipovich Ridge, the Molloy Ridge, and the Lena Trough. The largest area of gas hydrate accumulation inferred from the BSR is north of the Knipovich Ridge. Within this area, heat flow increases from 80 mW m^{-2} near the continental slope to >300 mW m^{-2} at the rifting axis.

While bacterial methane is produced at the continental slope and methane associated with serpentinization processes may exist along the central and southern Knipovich Ridge, our results support the interpretation of a thermogenic origin for the gas observed north of the ridge. Petroleum system modelling has shown that the bulk petroleum mass produced since the Eocene is at least 5 kt and could be as high as $\sim$0.2 Mt. Thermogenic methane is thus an important contributor to the gas hydrate reservoir on the Svalbard margin.

Although the Knipovich Ridge strongly controls the heat flow distribution on this part of the Svalbard margin, its influence on the amount and timing of thermogenic petroleum production appears minor. The petroleum system modelling shows that thermogenic methane generation happened mainly in the Miocene and is attributed to rapid burial of early Miocene source rocks. However, if Eocene source rocks are present in the study area, petroleum production may also have taken place during the Eocene due to high heat flow in the early stages of rifting. In this case, production would have been strongly influenced by the thermal effects of the Knipovich Ridge.

2.8   Acknowledgements

Chapter 3

Case study 2 - Giant Gjallar Vent

Seal bypass at the Giant Gjallar Vent (Norwegian Sea): indications for a new phase of fluid venting at a 56-Ma-old fluid migration system[1]

Ines Dumke, Christian Berndt, Gareth J. Crutchley, Stefan Krause, Volker Liebetrau, Aurélien Gay, Mélanie Couillard

3.1 Abstract

The Giant Gjallar Vent (GGV), located in the Vøring Basin off mid-Norway, is one of the largest (~5×3 km) vent systems in the North Atlantic. The vent represents a reactivated former hydrothermal system that formed at about 56 Ma. It is fed by two pipes of 440 m and 480 m diameter that extend from the Lower Eocene section up to the Base Pleistocene Unconformity (BPU). Previous studies based on 3D seismic data differ in their interpretations of the present activity of the GGV, describing the system as buried and as reactivated in the Upper Pliocene. We present a new interpretation of the GGV's reactivation, using high-resolution 2D seismic and Parasound data. Despite the absence of geochemical and hydroacoustic indications for fluid escape into the water column, the GGV appears to be active because of various seismic anomalies which we interpret to indicate the presence of free gas in the subsurface. The anomalies are confined to the Kai Formation beneath the BPU and the overlying Naust Formation, which are interpreted to act as a seal to upward fluid migration. The seal is breached by focused fluid migration at one location where an up to 100 m wide chimney-like anomaly extends from the BPU up to the seafloor. We propose that further overpressure build-up in response to sediment loading and continued gas ascent beneath the BPU will eventually lead to large-scale seal bypass, starting a new phase of venting at the GGV.

3.2   Introduction

Seal bypass systems are large-scale geological features that promote fluid migration across relatively impermeable sealing sequences (Cartwright et al., 2007). Before seal bypass occurs, upward fluid migration is inhibited by the seal and fluids accumulate beneath it. Overpressure build-up in the sealed sequence is favoured by rapid burial, which leads to disequilibrium compaction, e.g. in clays and mud rocks (Osborne and Swarbrick, 1997). In addition, overpressure may be generated due to the buoyancy of hydrocarbons (Osborne and Swarbrick, 1997). Once fluid pressure beneath the seal exceeds the fracture gradient, the seal begins to fracture, allowing fluids to migrate into overlying sediments, until fractures close again as overpressure bleeds off (Sibson et al., 1988; Roberts and Nunn, 1995).

Seal bypass systems are commonly found in petroliferous basins and comprise faults, intrusions, and pipes (Cartwright et al., 2007). Faults are divided into trap-defining and supratrap faults (Cartwright et al., 2007), and intrusions include intrusions of sand (Jolly and Lonergan, 2002; Andresen et al., 2009), mud (Brown and Westbrook, 1988; Hjelstuen et al., 1997; Hovland et al., 1998;), salt (Poliakov et al., 1996), and igneous material (Planke et al., 2005; Svensen et al., 2012). Pipes include hydrothermal pipes (Izawa and Cunningham, 1989; Jamtveit et al., 2004), blowout pipes (Løseth et al., 2001, 2011), and dissolution pipes (Walsh and Morawiecka-Zacharz, 2001). All three classes of seal bypass systems – faults, intrusions, and pipes – may be found within the same basin (Cartwright et al., 2007).

Hydrothermal pipes, for example, are closely linked to igneous intrusions. When sills intrude into organic-rich sediments, large volumes of methane are produced by contact metamorphism around the intrusions, promoting explosive and relatively short-lived (10-1000 years) fluid venting (Svensen et al., 2004; Planke et al., 2005; Aarnes et al., 2010). In the Vøring and Møre basins off mid-Norway, an 80,000 km² large sill complex and subsequent explosive methane venting created 734 known hydrothermal vent complexes, although it is estimated that there are at least 2000-3000 complexes in the Vøring and Møre basins (Svensen et al., 2004; Planke et al., 2005). Some have been reactivated and channelled upward-migrating fluids at later times (Svensen et al., 2003; Planke et al., 2005).

One of these hydrothermal vent complexes is the GGV, located at the northern Gjallar Ridge in the Vøring Basin (Fig. 3.1; Gay et al., 2012). With a seafloor area of ~5×3 km and relief of up to 12 m, the GGV is one of the largest single vent sites in the North Atlantic. The vent system extends from the Lower Eocene successions up to the BPU. This distinguishes the GGV from most break-up-related hydrothermal systems of the Norwegian margin, which were active only until the Early Eocene (Svensen et al., 2004).

The GGV thus has the potential to serve as a study site for constraining the geological processes that were active in the deep part of the Vøring Basin, such as diagenesis, clay structure transitions, hydrocarbon maturation, and hydrothermal activity due to break-up magmatism. Moreover, porewater samples from Naust Formation sediments may provide information on long-term carbon venting from the deeper Vøring Basin, which may be due to both hydrothermal maturation of organic carbon associated with break-up magmatism (Svensen et al., 2003, 2004), and later processes.

Despite previous studies, the present fluid-flow activity of the GGV remains unclear. Hansen et al. (2005) interpreted the GGV as a now buried, single-event mud volcano initiated in the Upper Pliocene through reactivation of an underlying mud diapir, whereas Gay et al. (2012) proposed that fluid migration resumed in the Upper Pliocene after a period of quiescence, suggesting that the GGV is still at an early stage of development. Both studies were based on 3D seismic data acquired by Saga Petroleum, which were the only available seismic data at that time across the GGV.

In this paper, we present a re-interpretation of the Quarternary functioning of the GGV based on new high-resolution 2D seismic and sediment echosounder data, as well as the first high-resolution bathymetry data. Our aims are to test whether the GGV is presently active, and to discuss whether the observed surface relief reflects past activity of a now inactive system, or relatively recent reactivation. In addition, we constrain the evolution of the GGV over the last 2.6 Myr. Based on our findings, we then re-evaluate the suggestion of Gay et al. (2012) that the GGV can be used as a study site for constraining the geological processes that are or were active in the deep part of the Vøring Basin.

3.3 Regional setting and previous results

3.3.1 Geological background

From east to west, the Norwegian Sea may be divided into three geological provinces: the Trøndelag Platform, the Vøring Basin, and the Vøring Marginal High which is bounded in the east by the Vøring Escarpment (Fig. 3.1A; Blystadt et al., 1995). The Vøring Basin comprises several sub-basins (Fenris Graben, Vigrid and Någrind synclines, Rås and Træna basins) separated by the NE-SW trending basement highs Gjallar Ridge, Nyk High, and Utgard High (Blystad et al., 1995).

Evolution of the Vøring Basin started during the Upper Jurassic – Lower Cretaceous rift episode characterised by E-W extension during the Upper Jurassic and northward propagating NW-SE rifting in the Lower Cretaceous (Doré et al., 1999). Rifting and subsequent subsidence created several deep basins off Norway and in the SW Barents Sea, including the Vøring Basin and the Møre Basin further to the south (Doré et al., 1999; Faleide et al., 2008).

The next rifting phase began in the Upper Cretaceous (Campanian-Maastrichtian) around 81 Ma (Ren et al., 2003) and was characterised by rotation of tilted fault blocks, crustal thinning, and uplift of structural highs (Hjelstuen et al., 1999a; Corfield et al., 2004). This phase culminated in lithospheric break-up accompanied by extensive transient volcanism near the Paleocene-Eocene transition (Skogseid et al., 1987; Eldholm et al., 1989) at about 56 Ma (Gradstein et al., 2012). A sill complex extending for at least 80,000 km² intruded into thick, organic-bearing Cretaceous sequences of the Vøring and Møre basins, producing large amounts of methane (Svensen et al., 2004; Planke et al., 2005). Subsequent explosive methane venting created at least 734 hydrothermal vent complexes (Svensen et al., 2004; Planke et al., 2005).

Post break-up margin evolution includes compressional deformation and subsidence during the mid-Cenozoic, and the onset of the Northern Hemisphere glaciation associated with highly in-
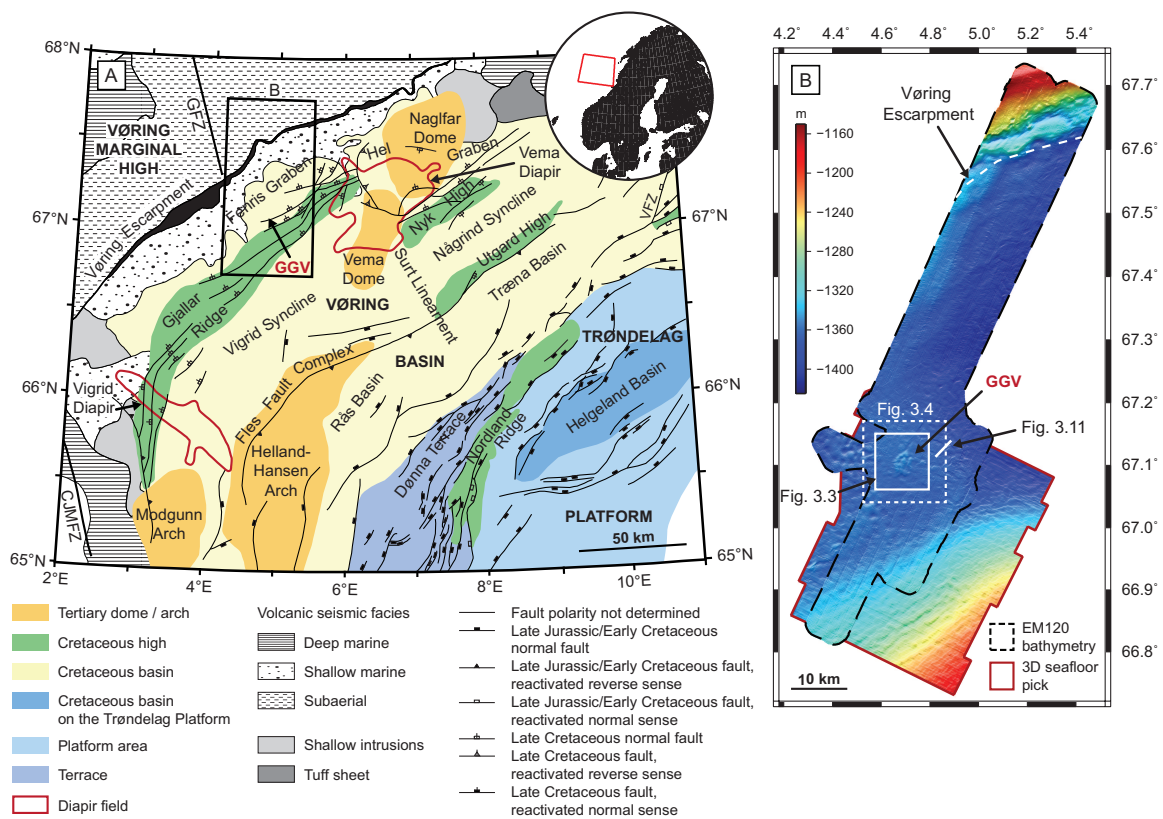
Figure 3.1: **(A)** Regional setting of the Giant Gjallar Vent (GGV). Tectonic structures are from Blystad et al. (1995) and Hjelstuen et al. (1999a), volcanic seismic facies from Berndt et al. (2001). **(B)** Bathymetry of the study area, showing locations of the 3D dataset and the M87-2 survey area.

creased erosion and sedimentation rates (e.g. Doré et al., 1999; Ottesen et al., 2009). The sedimentary sequence of the Vøring Basin since the Lower Eocene is characterised by three stratigraphic formations: the Brygge Formation, which belongs to the Hordaland Group, and the Kai and Naust formations, which represent the Nordland Group (Fig. 3.2).

The Brygge Formation (Lower Eocene to Lower Miocene) comprises mainly claystone interbedded with sandstone, silt, and limestone (Dalland et al., 1988), although biogenic ooze dominates in the deeper Vøring Basin (Eidvin et al., 2007). The uppermost Brygge Formation is characterised by polygonal faults (Berndt et al., 2003).

The Kai Formation was supposedly deposited from Lower Miocene to Upper Pliocene (Dalland et al., 1988), while Løseth and Henriksen (2005) assume it to be of late Middle to Upper Miocene age in the central Vøring Basin. Deposition of the Kai Formation focused on the depressions between synclines, with the largest sediment thickness occurring in the outer Vøring Basin close to the Vøring Escarpment (Chand et al., 2011). The composition of the Kai Formation varies laterally. Near the shelf, it consists mostly of claystone (Eidvin et al., 1998; Hjelstuen et al., 2004a), while the outer margin is dominated by siliceous biogenic ooze (Caston, 1976; Hempel et al., 1989; Hjelstuen et al., 1999a) that is rich in smectite (Forsberg and Locat, 2005). Caston (1976) determined a mean porosity of 82% and a mean bulk wet density of 1.324 g cm^{-3} from DSDP wells 339, 340 and

341, located at about 70 km NE of the GGV. A high-amplitude seismic reflection observed in both the Vøring and Møre basins marks the fossilised transition from Opal A to Opal C/T (Fig. 3.2) (Davies and Cartwright, 2002; Berndt et al., 2004).
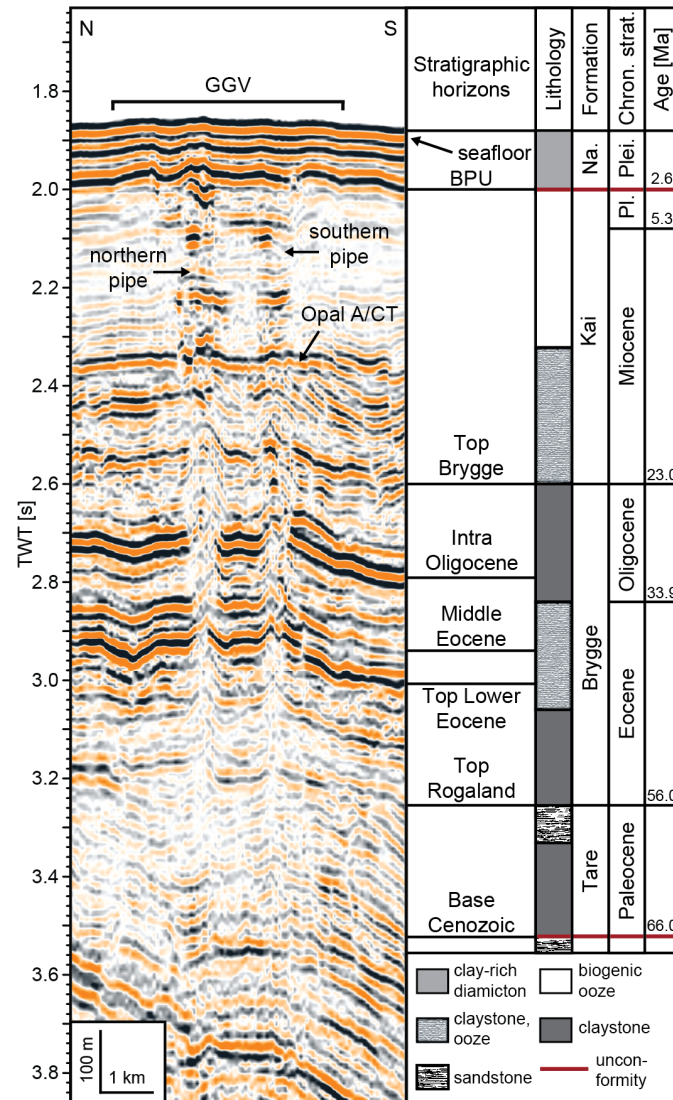
Figure 3.2: 3D seismic crossline illustrating the stratigraphic setting of the GGV, main lithological units, and unconformities. Chronostratigraphic information and ages are from Hansen et al. (2005) and Gradstein et al. (2012). BPU – Base Pleistocene Unconformity, Na. – Naust, Plei – Pleistocene, Pl. – Pliocene. Location is shown in Fig. 3.3.

The uppermost part of the Kai Formation is missing in the Vøring Basin. Jansen and Sjøholm (1991) report a depositional hiatus from 3.1 Ma to 2.5 Ma between the Naust Formation and the preserved part of the Kai Formation from ODP well 642B in the Vøring Basin. The hiatus may be due to a period of transgression at the end of a Middle to Upper Miocene compressional phase, which resulted in strongly reduced deposition rates (Eidvin et al., 2000; Løseth and Henriksen, 2005). In addition, a period of regression between 4.2 Ma and 2.8 Ma (Vail and Hardenbol, 1979) may have caused erosion of the upper Kai Formation along most of the Norwegian margin (Eidvin et al., 2000).

The Kai Formation is further characterised by intense polygonal faulting. Polygonal faults developed due to continuous volumetric contraction, probably during deposition of the Kai Formation and before burial by the overlying Naust Formation (Berndt et al., 2003; Gay and Berndt, 2007). Sediment unloading associated with the erosional event then stopped the propagation of polygonal faults (Gay and Berndt, 2007). However, some polygonal faults extend through the Naust Formation and reach the seafloor. These faults have been reactivated by dip-linkage during rapid deposition of the Naust Formation (Laurent et al., 2012).

The Naust Formation was deposited during Upper Pliocene and Pleistocene according to Caston (1976), Eidvin et al. (1998) and Hjelstuen et al. (2004a), which puts it into the Pleistocene in the Geologic Time Scale of 2012 (Gradstein et al., 2012). Naust Formation sediments built up well-stratified sequences termed Naust N, A, U, S, and T, with N being the oldest sequence (Rise et al., 2006). The sequences represent massive prograding wedges resulting from glacigenic debris flows (Henriksen and Vorren, 1996; Ottesen et al., 2009). Deposition of these units reflects the advances of several major ice sheets across the continental shelf. Ice-rafted debris pebbles found in drill cores indicate an intensified glaciation starting at about 2.57 Ma (Henrich, 1989; Jansen and Sjøholm, 1991). Average sedimentation rates in the Vøring Basin sharply increased from 0.18 m kyr^{-1} during Naust N to 0.50 m kyr^{-1} during Naust T (Dowdeswell et al., 2010), with a peak of 36 m kyr^{-1} at about 16 ka (Hjelstuen et al., 2004b). Differential loading by Naust Formation sediments led to mobilisation of the underlying Miocene ooze, forming the Vema and Vigrid diapir fields (Hjelstuen et al., 1997; Hovland et al., 1998).

In the study area, the Naust Formation consists of a clay-rich diamicton with small proportions of silt and sand (Eidvin et al., 1998; Hjelstuen et al., 2004a; Ottesen et al., 2009), based on several wells in the Vøring Basin. At DSDP wells 339, 340 and 341, ~70 km NE of the GGV, Caston (1976) determined a mean porosity of 51% and a mean bulk wet density of 1.846 g cm^{-3}.

A regional unconformity between the Kai and Naust formations marks the onset of glacially dominated deposition (Faleide et al., 1996). In the study area, the unconformity appears as a strong peak reflection in seismic records (Fig. 3.2). This reflector has been previously called Base Late Pliocene Unconformity (Hjelstuen et al., 1997, 1999a), Base Pliocene reflector (Reemst et al., 1996), Base Upper Pliocene (Eidvin et al. 1998; Corfield et al., 2004), and Top Kai (Hansen et al., 2005; Gay et al., 2012). Throughout this paper, we use the term Base Pleistocene Unconformity (BPU), which is in agreement with the Geologic Time Scale of 2012 (Gradstein et al., 2012).

The BPU reflects major changes in sediment composition, with relatively low-porosity, high-density Naust Formation sediments above and higher-porosity, lower-density Kai Formation ooze below. The lithological changes produce a velocity inversion across the BPU, which was observed at 12 wells on the Trøndelag Platform, Nordland Ridge and the eastern Vøring Basin (Reemst et al., 1996). With a seismic velocity of 3.09 km s^{-1} at the base of the Naust Formation and 2.14 km s^{-1} at the top of the Kai Formation, the velocity inversion is on average 0.55 km s^{-1}, leading to a low-velocity zone beneath the BPU (Reemst et al., 1996). This velocity inversion may be due to high fluid pressures beneath the less permeable Naust Formation sediments (Reemst et al., 1996).

3.3.2 The Giant Gjallar Vent

The GGV is one of the largest focused fluid flow systems on the Norwegian Margin and is situated at the northern Gjallar Ridge in water depths of 1348 m to 1360 m (Fig. 3.1). Located above a sill complex, the GGV formed as the result of explosive methane venting after the intrusive event at c. 56 Ma (Planke et al., 2005; Gay et al., 2012). The vent is characterised by two pipe-like structures extending upwards from the Eocene sequence, each forming a V-shaped structure that terminates at the BPU (Gay et al., 2012). Both pipes are marked by stacked high-amplitude reflections and chaotic reflectivity above the Top Brygge horizon (Hansen et al., 2005). Hummocky reflections characterise the BPU and overlying strata at the GGV (Gay et al., 2012). At the seabed, the GGV consists of three NE-SW trending ridges with heights of up to 12 m above the surrounding seafloor, extending for ~5 km in a NE-SW direction and ~3 km in a NW-SE direction (Gay et al., 2012).

The evolution of the GGV after the hydrothermal stage is under debate. According to Hansen et al. (2005), the vent complex represents one of three types of mound structures (Type A, B, and C) associated with fluid flow that exist in the Vøring Basin. Types C and A originated from mud mobilisation at the Paleocene-Eocene transition and during Middle Oligocene, respectively. Type B structures, which include the GGV, developed as mud diapirs during Middle to Upper Oligocene, although some extend up to Top Brygge level. A later phase of reactivation led to mud expulsion at the Upper Pliocene seabed. Today, type B structures are inactive and represent buried mud volcanoes (Hansen et al., 2005).

An alternative evolution of the GGV was proposed by Gay et al. (2012). Based on the lack of deformed horizons in the interval between the Intra-Oligocene horizon and the BPU, the authors suggested that fluid/mud migration activity ceased in mid-Oligocene. Deformation at BPU level is interpreted to indicate reactivation of the vent complex at the transition between Kai Formation and Naust Formation. The GGV may therefore be at an early stage of development. Gay et al. (2012) proposed a future collapse of the vent complex and subsequent pockmark formation.

3.4 Materials and methods

3.4.1 Seismic data

The 3D seismic data SG9604 were acquired by Saga Petroleum in 1996. The data cover a 40×50 km area at the northern Gjallar Ridge between 4°8'E - 5°23'E and 66°43'N - 67°18'N (Fig. 3.1B). The data have a dominant frequency of ~40-50 Hz and an inline and crossline spacing of 56 m. Vertical and horizontal resolutions are approximately 10 m and 30-50 m, respectively (Hansen et al. 2005). The data underwent standard industry processing including time migration.

During RV METEOR cruise M87-2 in 2012, we acquired high-resolution 2D seismic data along seven profiles of 11-28 km length, using a 150 m long 96-channel streamer. In addition, two profiles were acquired using an 8-channel streamer of 12.5 m length. Locations of profiles discussed in this paper are shown in Fig. 3.3.
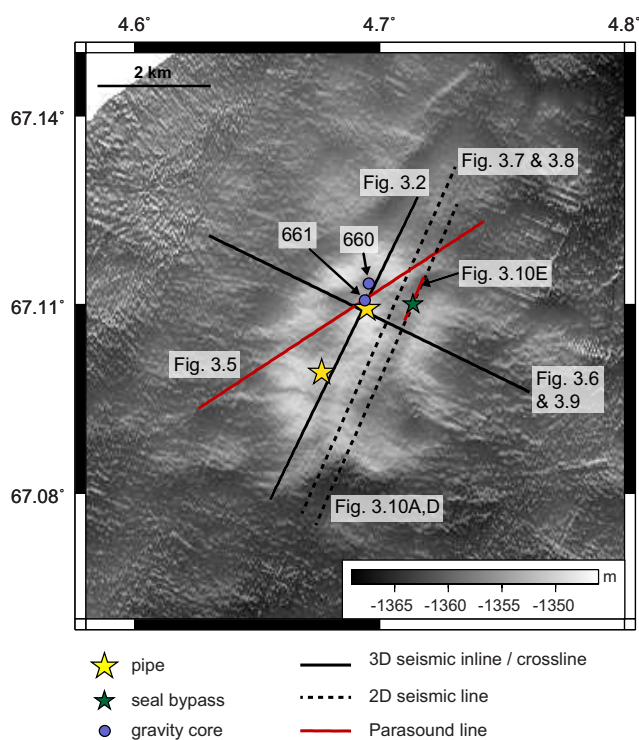
Figure 3.3: Bathymetry map showing locations of profiles, sediment cores, pipes and seal bypass feature. Map location is shown in Fig. 3.2.

All 2D seismic data were sampled at 2 kHz and recorded for 4 s. A 210 in^3 GI gun was used as a source and operated at a 5 s shot interval. The average shot spacing was 8 m for a ship speed of 3 kn. Processing was done using Seismic Unix (Stockwell, 1997) and included CMP (common midpoint) sorting and frequency filtering. A filter with low-cut corner frequencies of 25 and 55 Hz was applied to the 96-channel data to attenuate low-frequency noise. A slightly higher low-cut filter (36 and 60 Hz corner frequencies) was applied for the same purpose to the lower-fold 8-channel data. Further processing included stacking and Stolt migration with a constant velocity of 1500 m s^{-1}.

The Kingdom Suite software (SMT) was used to pick and correlate reflections in the different datasets. Picked reflections include the seafloor, BPU, Opal A/CT transition, Top Brygge, Intra-Oligocene, Top Lower Eocene, and three reflections within the Naust Formation (Naust 1, 2 and 3) that were arbitrarily named and do not necessarily represent the intra-Naust formation tops (N, A, U, S, T; Rise et al., 2006). We also used Kingdom Suite to calculate instantaneous frequencies of the 3D data in order to investigate if free gas, manifested by increased attenuation of higher frequencies, is present in the subsurface. In addition, the BPU horizon was flattened to analyse sediment thicknesses of the overlying Naust Formation.

3.4.2   Hydroacoustic data

In addition to seismic data, sediment echosounder profiles were collected with the ATLAS Parasound system operating at 4 kHz. Parasound data were acquired across the vent structure but also

up to 70 km further northeast, including during the seismic surveys. The data were analysed for faults within 5 km distance intervals from the vent, with the starting point (0 km) set at the centre of the northern pipe. In order to exclude bias from profile coverage, the number of faults found in each distance interval was normalised to profile kilometres acquired within that distance interval. Fault locations were compared to the locations of upper terminations of Miocene polygonal faults in 3D seismic data to investigate if shallow faults may be connected to deeper polygonal faults.

On all seismic and Parasound profiles, multibeam echosounder data were recorded with the Kongsberg EM122 system (12 kHz, 288 beams) (Fig. 3.1B). Using the open source software package MB System, the multibeam data were manually edited and processed to obtain bathymetry grids with cell sizes of 30 m and 50 m. In addition, the EM122's tool for water column imaging was operated during the survey.

3.5 Results

3.5.1 Seafloor and water column

Multibeam bathymetry of the GGV is of higher resolution than the seafloor pick of the 3D seismic data and confirms that the surface expression of the vent consists of three NE-SW trending ridges (Fig. 3.4A). Maximum relief is about 12 m above the surrounding seafloor, with the highest point located above the northern pipe in 1348 m water depth. Water column imaging did not reveal any anomalies during the survey.
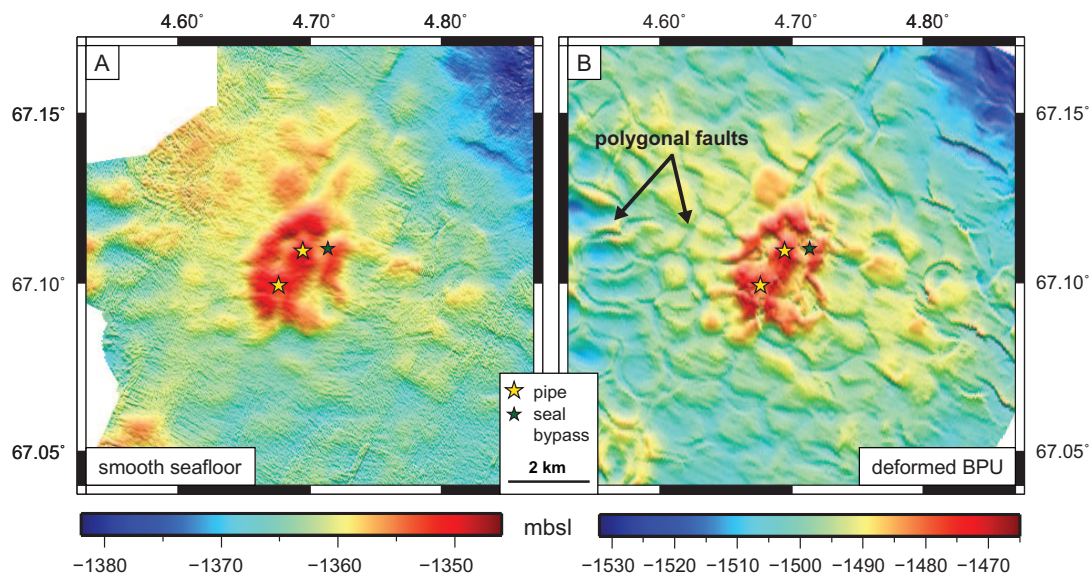

Figure 3.4: Maps of **(A)** bathymetry and **(B)** topography of the Base Pleistocene Unconformity (BPU) horizon as picked in the 3D seismic data, showing locations of pipes and seal bypass feature. mbsl – metres below sealevel. Map location is shown in Fig. 3.2.

3.5.2 Subsurface

3.5.2.1 Seismic stratigraphy outside the vent zone

Outside the vent zone, the Naust Formation is characterised by continuous, undisturbed reflections that are well imaged in Parasound data and appear as a conformable drape of the BPU (Fig. 3.5). The BPU reflection has a negative polarity and appears hummocky at the GGV (Fig. 3.6). Hummocky reflections occur over an elliptical (5.8×4.2 km) area oriented in a NW-SE direction, which is slightly larger than the area of seabed elevation (5×3 km). The relief of the BPU hummocky area is up to 0.05 s TWT (∼38 m for a seismic velocity of 1500 m s^{-1}) higher than the surrounding area and is characterized by polygonal faulting (Fig. 3.4B).
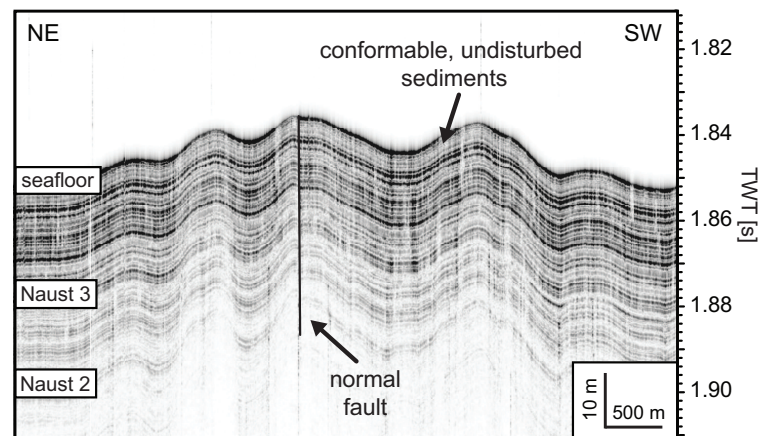

Figure 3.5: Parasound profile across the northern pipe showing conformable, undisturbed sedimentary reflections of the Naust Formation. The normal fault is located above the centre of the pipe. Location is shown in Fig. 3.3.

The thickness of the Naust Formation is reduced by up to 0.02 s TWT above the vent (Fig. 3.7), equivalent to a reduction of 15 m for a seismic velocity of 1500 m s^{-1}. The extent of the reduced thickness corresponds well to the extent of chaotic reflections beneath the BPU. Reflections within the area of reduced thickness become increasingly hummocky from the flattened BPU horizon towards the seafloor. This is particularly evident from the flank steepness, which increases towards shallower sediment depths (Fig. 3.7).

In contrast to the shallower Naust Formation, the lower half of the BPU – Naust 1 interval appears only slightly hummocky (Fig. 3.7). To get a rough age estimate for the upper boundary of this interval, reflector R, we used the travel time difference (ΔTWT) between R and the BPU (0.021 s TWT), a seismic velocity of 3.09 km s^{-1} (Reemst et al., 1996), and an average sedimentation rate of 0.18 m kyr^{-1} for the Naust N sequence (1.5-2.6 Ma) on the Vøring margin (Dowdeswell et al., 2010). These values give an approximate timing of 180,000 years after the BPU for reflector R.

Between the BPU and the Opal A/CT reflection, internal reflections of the Kai Formation are of low amplitudes. Reflections between the Opal A/CT reflection and Top Lower Eocene are characterised by higher amplitudes (Figs. 3.2 and 3.6).

3.5.2.2 Seismic amplitude and frequency anomalies

The subsurface of the GGV features several acoustic anomalies, including chaotic or discontinuous reflections, high-amplitude reflections, reverse polarity, increased frequency attenuation, reflection down-bending, and acoustic blanking.

Chaotic, discontinuous reflections occur in the uppermost Kai Formation immediately beneath the BPU (Fig. 3.8). They are apparent in the 2D seismic data but not in the lower-resolution 3D seismic data and are restricted to the area of BPU up-doming.

Discontinuous high-amplitude reflections exist within the chaotic reflections beneath the BPU in 2D and 3D seismic data (Figs. 3.6 and 3.8). High-amplitude reflections also exist in 3D data within the two pipes down to Top Brygge level (Fig. 3.6), as previously noted by Hansen et al. (2005) and Gay et al. (2012). Some of these reflections exhibit reversed polarity (Fig. 3.6).

Based on different amplitude characteristics, the two pipes of the GGV were divided into two units: a high-amplitude unit between the BPU and Top Brygge (unit 1), and an opaque unit in the underlying Brygge Formation where high-amplitude reflections are absent (unit 2) (Fig. 3.6).
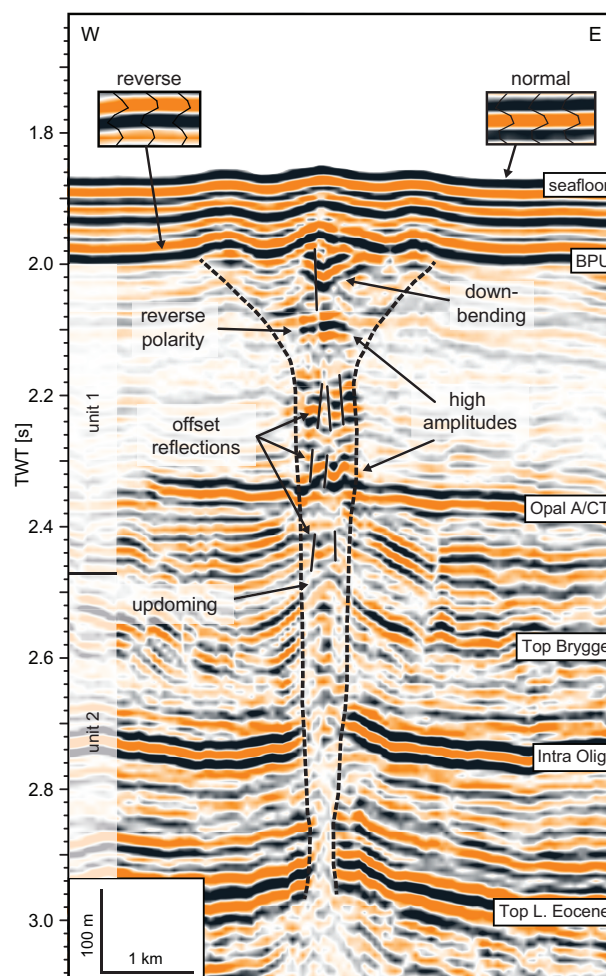
Figure 3.6: 3D seismic inline across the northern pipe (marked by stippled line). BPU – Base Pleistocene Unconformity. Location is shown in Fig. 3.3.
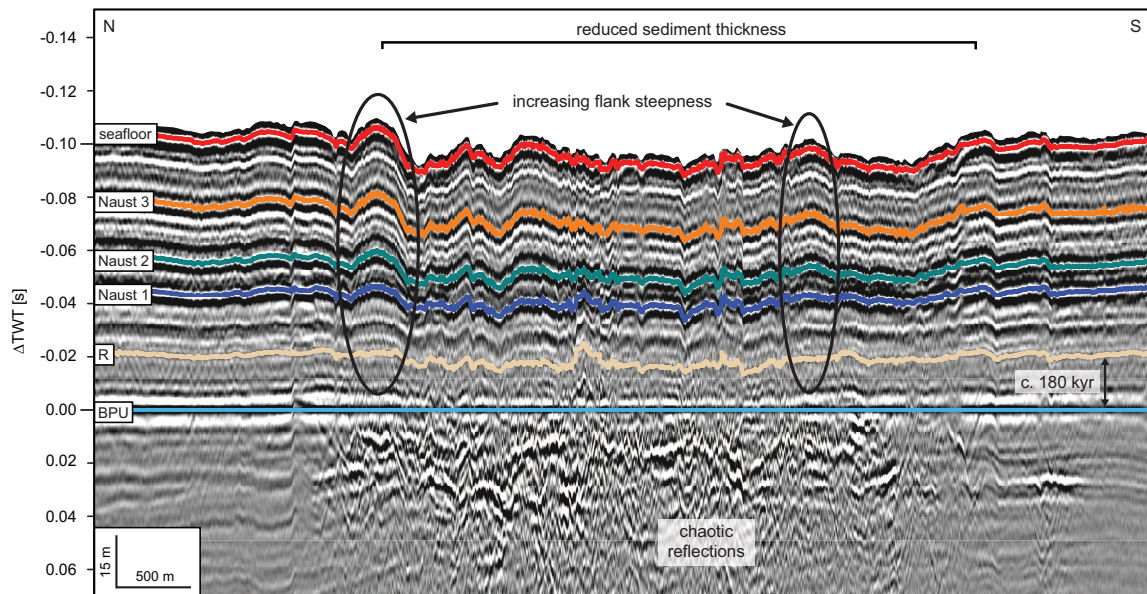
Figure 3.7: 96-channel 2D seismic profile across the eastern edge of the northern pipe. The BPU horizon was flattened to illustrate sediment thicknesses of the overlying Naust Formation. Reflector R represents the upper boundary of the relatively undeformed lowermost part of the Naust Formation. BPU – Base Pleistocene Unconformity. Location is shown in Fig. 3.3.

Figure 3.8: 96-channel 2D seismic profile across the eastern edge of the northern pipe, showing chaotic and high-amplitude reflections and faulting. BPU – Base Pleistocene Unconformity. Location is shown in Fig. 3.3.
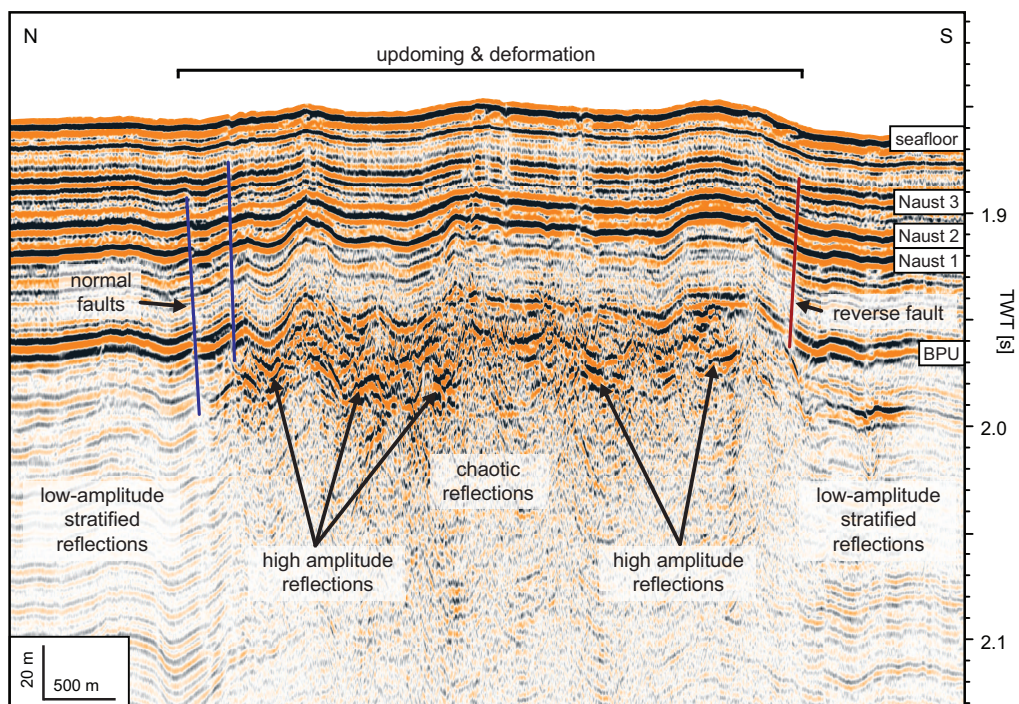
Instantaneous frequencies from 3D seismic data show strong attenuation of higher frequencies beneath the BPU at the vent and within the pipes (Fig. 3.9). Slightly increased frequency attenuation was also observed in the lower Naust Formation above both pipe centres.

At the northern pipe, a down-bending reflection was observed in 3D seismic data at the centre of the pipe, directly beneath the BPU (Fig. 3.6). At greater depths, the Top Brygge horizon bends steeply upwards towards the centre of each pipe. Such up-bending is also observed at smaller pipe-like features in the southern half of the 3D survey area.
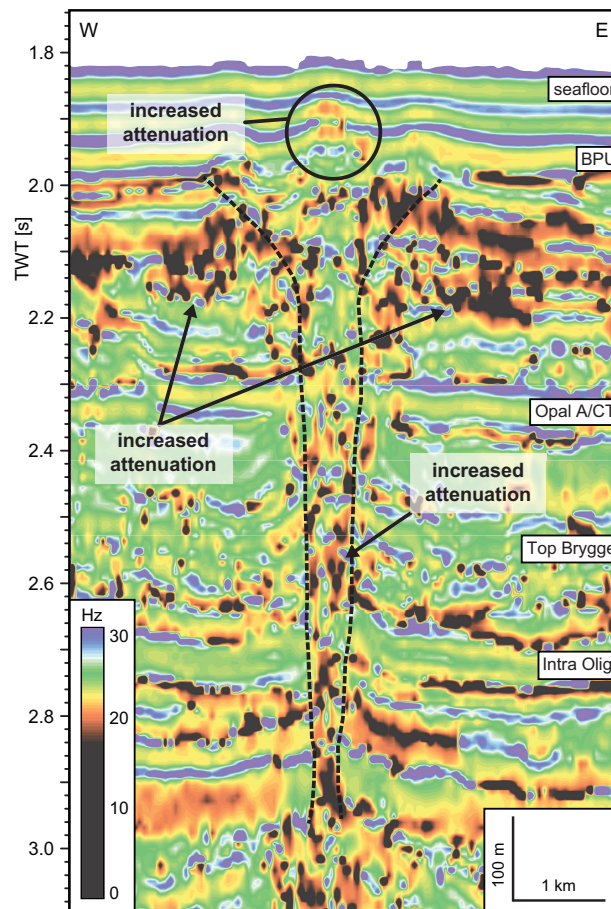
Figure 3.9: Instantaneous frequencies of the 3D seismic data from the inline shown in Fig. 3.6. Stippled line marks pipe extent as in Fig. 3.6. BPU – Base Pleistocene Unconformity.

About 900 m NE of the northern pipe, a shallow vertical anomaly was observed, which has different characteristics in 2D and 3D seismic data and Parasound records. On the 3D seismic line, the anomaly appears as a subtle feature extending from the BPU into the Naust Formation. It is marked by upbending and downbending of reflections, as well as a higher-amplitude reflection beneath the BPU (Fig. 3.10A, B). At the BPU and immediately beneath it, instantaneous frequencies show increased attenuation of higher frequencies (Fig. 3.10C).

On the higher-resolution 2D seismic profile, the anomaly is more distinct and characterised by reduced seismic amplitudes, stopping at Naust 3 level (Fig. 3.10D). However, the Parasound data clearly show that it reaches up to the seafloor, terminating in a shallow depression about 130 m

wide and 1 m deep (Fig. 3.10E). The anomaly is up to 100 m wide and marked by high amplitudes above Naust 3 level and acoustic blanking below. Above this horizon, reflections on either side of the feature bend down towards its centre, whereas reflection up-bending occurs beneath Naust 3. However, this is difficult to discern as these depths are at the limit of Parasound penetration.

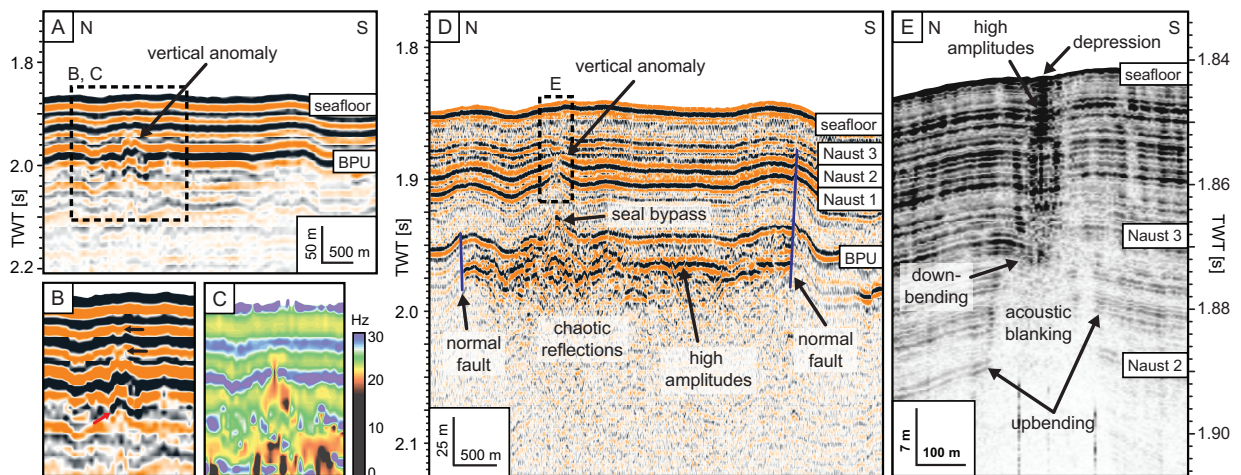**Figure 3.10:** Vertical seismic anomaly ∼900 m east of the northern pipe at different resolutions. **(A)** 3D seismic line showing a vertical anomaly marked by upward and downward bending reflections. **(B)** Zoom of vertical anomaly in the 3D seismic line (section indicated in A). Black arrows indicate reflection downbending, red arrow indicates higher amplitudes beneath BPU. **(C)** Instantaneous frequencies of same section as in (B) show increased attenuation of higher frequencies at the location of the seismic anomaly. **(D)** Higher-resolution 8-channel 2D seismic line of the same section as in (A), showing a vertical amplitude anomaly or chimney that extends into the Naust Formation, indicating bypass of the BPU seal. **(E)** A 4-kHz Parasound profile shows that the anomaly extends up to the seabed, terminating in a depression. Locations of all profiles are shown in in Fig. 3.3. BPU – Base Pleistocene Unconformity.

3.5.2.3   Faults related to shallow deformation

Faults were found across the entire survey area. However, data coverage at distances greater than 35 km from the GGV is limited to the area NNE of the GGV and consequently, all mapped faults beyond this distance are located NNE of the vent. Within 35 km from the pipes, more extensive coverage reduces directional bias.

We observed three groups of faults in the dataset: (1) shallow faults with throws of up to 3 m in the upper 50-80 m, identified in Parasound data, (2) faults with throws of up to 10 m in the lower Naust Formation, observed in 2D seismic data, and (3) polygonal faults imaged by the 3D data. The latter have been described by Laurent et al. (2012), who determined maximum fault throws of 20 ms TWT.

Of the 143 shallow faults found in Parasound data, most are normal faults; only 18 showed up-dip displacement of reflectors indicating reverse faulting. About one third (48) of the shallow faults are located directly above polygonal faults (Table 3.1, Fig. 3.11), and one third (49) are independent, i.e., not associated with deeper polygonal faults. The remaining 46 faults are located outside the area of the 3D survey, and hence a comparison was not possible.
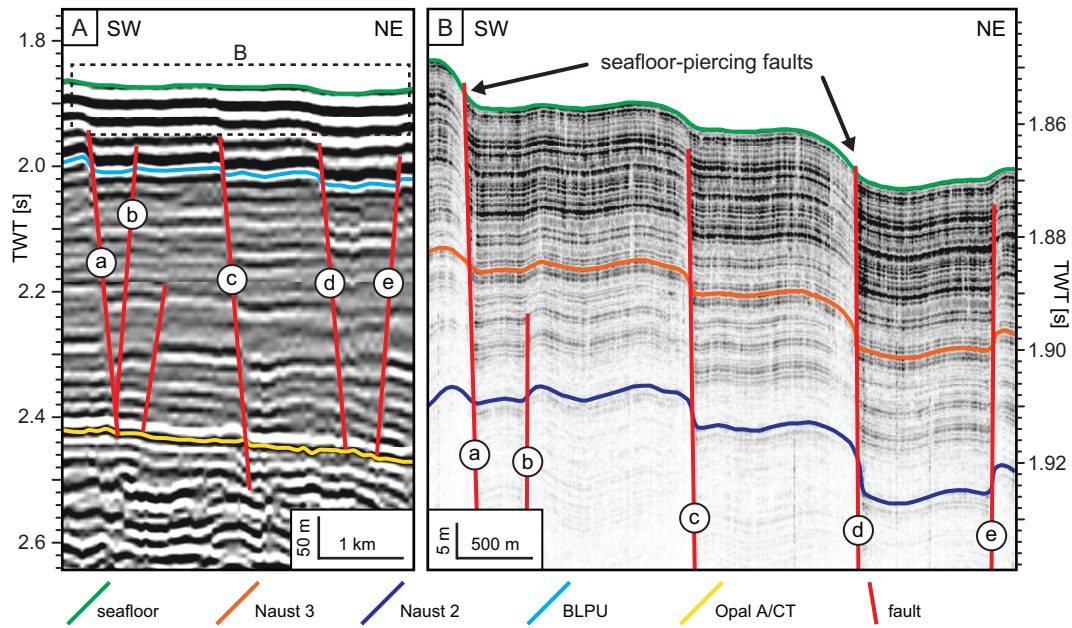
Figure 3.11: (A) Polygonal faults (a–e) on a profile from the 3D seismic data, extending from the Kai Formation into the Naust Formation. **(B)** Shallow faults in Parasound data along the same line, interpreted as continuations of polygonal faults a–e in (A). BPU – Base Pleistocene Unconformity. Location is shown in Fig. 3.3.

Table 3.1: Occurrences of shallow faults identified in Parasound data within 5 km distance intervals from the northern pipe. pf – polygonal fault, ind. – independent.

interval [km]	all faults				seafloor-piercing faults			
	no. of faults (total)	no. of pf-related faults	no. of ind. faults	no. of faults outside 3D survey	no. of faults (total)	no. of pf-related faults	no. of ind. faults	no. of faults outside 3D survey
0-5	26	11	15	-	2	1	1	-
5-10	53	30	19	4	10	9	1	-
10-15	36	7	12	17	3	1	-	2
15-20	6	-	1	5	-	-	-	-
20-25	5	-	2	3	-	-	-	-
25-30	1	-	-	1	1	-	-	1
30-35	1	-	-	1	1	-	-	1
35-40	1	-	-	1	1	-	-	1
40-45	1	-	-	1	-	-	-	-
45-50	1	-	-	1	-	-	-	-
50-55	1	-	-	1	-	-	-	-
55-60	4	-	-	4	2	-	-	2
60-65	3	-	-	3	1	-	-	1
65-70	4	-	-	4	2	-	-	2

Although shallow faults occur up to 70 km away from the GGV, most are within 25 km of the pipes (Table 3.2, Fig. 3.12A). Both independent faults and faults related to polygonal faults were observed mostly within 15 km from the central GGV, with the highest number of faults occurring within 5-10 km distance. Two faults are located directly above the northern pipe (Fig. 3.5).

Table 3.2: Occurrences of shallow faults identified in Parasound data, normalised to acquired profile kilometres within the 5 km distance intervals. pf – polygonal fault.

interval [km]	profile length [km]	all faults			seafloor-piercing faults
		pf-related faults per km	independent faults per km	faults outside 3D survey per km	faults per km
0-5	157.85	0.070	0.095	-	0.013
5-10	184.34	0.163	0.103	0.022	0.054
10-15	145.71	0.048	0.082	0.117	0.021
15-20	55.87	-	0.018	0.089	-
20-25	37.29	-	0.054	0.080	-
25-30	29.67	-	-	0.034	0.034
30-35	31.53	-	-	0.032	0.032
35-40	19.84	-	-	0.050	0.050
40-45	19.95	-	-	0.050	-
45-50	20.60	-	-	0.049	-
50-55	19.21	-	-	0.052	-
55-60	20.99	-	-	0.191	0.095
60-65	19.82	-	-	0.151	0.050
65-70	20.02	-	-	0.200	0.100

While most shallow faults appear to terminate within the Naust Formation, 22 faults reach the seafloor. Half of these faults are located above polygonal faults (Table 3.1). The seafloor-piercing faults are found at three centres: (1) within 15 km of the pipes, (2) at distances of 25-40 km, and (3) between 55 km and 70 km (Table 3.2, Fig. 3.12B).

In the 2D seismic data, normal and reverse faults were observed at the edges of the zone of chaotic, high-amplitude reflections (Figs. 3.8 and 3.10). These faults penetrate the BPU and the lower Naust Formation. Some faults extend up to the Naust 3 horizon but none reaches the seafloor.

3.6 Discussion

3.6.1 Present-day activity of the GGV

The new data provide much higher resolution of the shallow sediment succession, i.e., the Naust Formation and upper Kai Formation, than previously available for the area. Although we did not observe acoustic indications for fluid release, such as acoustic flares in echosounder data, there are several indications for present activity of the GGV both in terms of fluid migration and structural deformation.
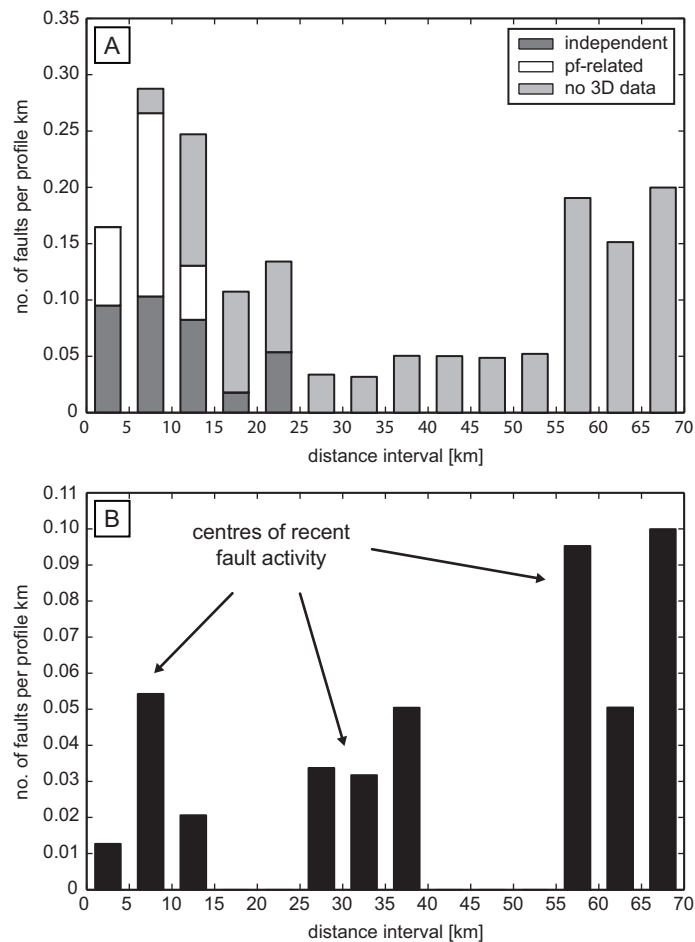
Figure 3.12: Number of faults normalised to Parasound profile km, plotted against 5 km distance intervals from the northern pipe. **(A)** All faults divided into categories (independent, related to polygonal faults, faults outside the 3D survey). pf – polygonal fault. **(B)** Faults piercing the seafloor, indicating most recent activity which is concentrated in three centres.

3.6.1.1   Fluid migration

The presence of free gas beneath the BPU is indicated by chaotic and high-amplitude reflections, and by increased attenuation of higher frequencies. From the slightly increased frequency attenuation within the pipes, as well as high-amplitude reflections and localised segments of reversed polarity (Fig. 3.6), we infer that gas or gas-rich fluids are present within the pipes. Fluids migrate upwards from greater depths, possibly from beneath the Top Brygge horizon.

Free gas-related anomalies are absent above the BPU and fluids appear to be trapped underneath, suggesting that the BPU acts as a seal to upward fluid migration. Sealing of the underlying Kai Formation is likely due to the lower permeability and higher density of the glacigenic Naust Formation sediments compared to the Kai Formation sediments (Caston, 1976), and the rapid covering of the Kai Formation sediments during the Pleistocene (Hjelstuen et al., 2004a).

However, the BPU seal is not intact over the entire study area. It appears to have been breached ~900 m northeast of the northern pipe where a vertical, chimney-like anomaly extends from the

BPU to the seafloor (Fig. 3.10). We interpret the acoustic blanking and stacked high-amplitude reflections in the 2D seismic and Parasound data as indications for the presence of gas. 3D seismic data support this interpretation through increased attenuation of higher frequencies at and immediately beneath the BPU (Fig. 3.10C).

We interpret the shallow depression in which the vertical anomaly terminates as a pockmark. Its dimensions are similar to pockmarks in the North Sea, e.g. in the South Fladen area where average widths and depths of 156 m and 1.4 m, respectively, were measured (Hovland and Judd, 1988). As pockmarks are formed by seepage, active fluid expulsion may have taken place at this location. Although we did not observe anomalies in the water column during surveying, this does not rule out the case for recent seepage as it is well known from other areas that seepage may be periodic on time scales as short as minutes (Leifer et al., 2004; Krabbenhoeft et al., 2010). Thus, the time of passing this feature could have been an intermittent period of quiescence.

Geochemical analyses of sediment samples from this site would help to clarify whether seepage occurs at this chimney. Unfortunately, such samples do not exist. Two gravity cores taken above the northern pipe (cores 660 and 661 in Fig. 3.3) show methane concentrations below 11 nmol l^{-1}, and no indication for strong fluid advection in the profiles of total alkalinity, sulphate, Cl$^-$ and Br$^-$. However, free gas may be present deeper in the Naust Formation, as we infer from slightly increased attenuation of higher seismic frequencies above the BPU at the centre of the northern pipe (Fig. 3.9). This may be a first indication for seal bypass at the northern pipe.

3.6.1.2   Structural deformation

The distribution of shallow faults with respect to Miocene polygonal faults indicates that shallow propagation of polygonal faults is taking place in the survey area. Shallow faults located above a polygonal fault identified in 3D seismic data indicate reactivation of a buried polygonal fault which then propagated into the Naust Formation. Fault reactivation has already been inferred from 3D data (Laurent et al., 2012), and the new high-resolution data support this hypothesis.

Reactivation of polygonal faults of the Kai Formation is probably a regional process, rather than a local phenomenon. Gay and Berndt (2007) observed shallow propagation of polygonal faults at the Storegga scarp, about 280 km south of the GGV, and proposed that faulting within the lower Naust Formation was induced by the overlying debris flow deposit, i.e., by an instantaneous process. We suggest that a similar process inducing fault reactivation could be represented by rapid loading by glacigenic debris flows of the Naust Formation. As the glacial deposits are unsorted and of low permeability, they probably act similarly to submarine debris flow deposits, even though the loading process was not as instantaneous as the emplacement of the debris flow at Storegga.

While regional reactivation of polygonal faulting is certainly responsible for many of the observed shallow faults, other factors may also be involved. Based on the relatively high density of shallow faults related to polygonal faults within 10 km of the GGV, we suggest that the vent influences and possibly promotes fault reactivation and shallow propagation. The GGV also appears to induce the formation of new faults, as inferred from the high number of faults not related to polygonal

faults and located within a 15 km radius from the northern pipe. A relation between vent activity and faulting, or deformation, is further indicated by faults identified in 2D seismic data just at the edges of the zone of strong BPU deformation and underlying chaotic reflections.

Recent structural deformation is implied by seafloor-piercing faults, whose distribution shows that structural deformation is not restricted to the vent vicinity but also occurs in two areas further to the northeast. While we attribute fault activity within 10 km from the pipes mainly to vent-induced deformation, it seems unlikely that faults located more than 10 km away are related to the vent system. They must therefore have been caused by other factors.

One possibility is that vent-independent faults represent centres of recent reactivation of polygonal faults. As there are no 3D seismic data available for these areas, we can neither confirm nor exclude this possibility. However, the distinct distance intervals of the two fault areas indicates that they are caused by local effects rather than regional reactivation of the polygonal fault system. There is no seismic evidence that tectonic stress in the basement is causing this near-surface deformation.

3.6.2 GGV relief – relict from the past?

3.6.2.1 Is the GGV a buried mud volcano?

Unconsolidated sediments can be mobilised in the subsurface if the boundary conditions are suitable (cf. Maltman and Bolton, 2003). Subsurface sediment mobilisation may form intrusive structures, e.g. diapirs, and extrusive structures, e.g. mud volcanoes (Huuse et al., 2010). Mud volcanoes typically have diameters of 1-4.5 km and heights of 10-200 m, e.g. in the Barents Sea (Hjelstuen et al., 1999b), the Black Sea (Ivanov et al., 1996), the Western Alborán Sea (Somoza et al., 2012), and on the Mediterranean Ridge (Ivanov et al., 1996). With a diameter of ∼5 km and heights of up to 38 m at the paleo-surface (BPU), the GGV is well within this range of mud volcano dimensions. To investigate whether the GGV is a buried mud volcano, we discuss the common characteristics of mud volcanoes, listed by Deville et al. (2003) as (1) dome-shaped outlets, (2) focused conduits, and (3) mud chambers or reservoirs, and evaluate whether these apply to the GGV.

Volcanic dome

From the new high-resolution data, it is evident that there is no dome-shaped outlet at the GGV. However, in a model of a mound structure associated with the GGV, Hansen et al. (2005) showed a mud volcano dome sitting upon a relatively undeformed BPU. If that were the case and the feature were now buried, we would have expected a dome-shaped anomaly on the paleo-seafloor, similar, for example, to buried sand volcanoes in the Norwegian-Danish Basin (Andresen et al., 2009). While such a dome could be inferred from the 3D data, which were the only data available to Hansen et al. (2005), our 2D seismic data clearly show that there is no dome on the BPU but that the BPU itself is up-doming and deformed (Fig. 3.8).

In addition to a dome on the BPU, the GGV also lacks stacked domes in the deeper subsurface. Separate domes stacked in a "Christmas tree" pattern reflect multiple eruption phases of mud

volcanoes (Stewart and Davies, 2006). These are often observed at mud volcanoes in areas with high sedimentation rates (e.g. Davies and Stewart, 2005; Deville et al., 2006, 2010). According to Hansen et al. (2005) and Huuse et al. (2010), the GGV represents a single-event mud volcano. While this would explain the absence of stacked domes, it seems unlikely that a mud volcano erupted only once about 2.6 Myr ago in an area characterised by high sedimentation rates during the Pleistocene.

Also absent are characteristic onlap patterns. Mud volcanoes that developed during times of high sedimentation rates are often characterised by conformable seismic reflections onlapping the flanks, representing phases during which sedimentation exceeded dome growth (e.g. Stewart and Davies, 2006). Stratigraphic onlaps would therefore be expected if there were a volcanic dome on the BPU, but they are not observed in our data.

Feeder channel

Feeder channels of mud volcanoes can be easily identified in seismic data as they are marked by opaque vertical zones that usually lack any reflections (Dimitrov, 2002). Although vertical amplitude anomalies are clearly identifiable at the GGV, they are not uniformly opaque but can be divided into a lower opaque unit beneath Top Brygge level and an upper unit marked by high-amplitude reflections. A mud diapir feeding a potential mud volcano must therefore have stopped at Top Brygge level (Hansen et al., 2005).

Above Top Brygge level, a different mode of migration must operate. Hansen et al. (2005) proposed that above Top Brygge level, the GGV is fed via a network of sub-vertical fractures rather than by a diapir. Vertical discontinuities are indicated by offset reflections in 3D seismic data just above the Top Brygge horizon (Fig. 3.6). We interpret these discontinuities as hydro-fractures, which can trigger mud diapirism and volcanism (Dimitrov, 2002; Deville et al., 2010) but are also associated with the initiation and upward propagation of gas chimneys (Hustoft et al., 2010; Netzeband et al., 2010). As the high amplitudes and chaotic character of the pipes above Top Brygge level indicate the presence of gas, and as gas is also present beneath the BPU, we suggest that above Top Brygge level, fluid migration in the GGV is driven by gas rather than mud.

Another feature common to both mud volcano systems and gas chimneys is down-bending of reflections, which occurs beneath the up-doming BPU (Fig. 3.6). Similar down-bending was observed at Håkon Mosby Mud Volcano in the Barents Sea (Hjelstuen et al., 1999b; Perez-Garcia et al., 2009) and Strakhov Mud Volcano in the Black Sea (Ivanov et al., 1996).

Reflection down-bending can be interpreted in several ways: as (1) a pull-down effect caused by decreasing seismic velocity in gas-rich fluids (Hovland and Judd, 1988; Løseth et al., 2009) or in gas-saturated mud (Dimitrov, 2002), (2) a collapse structure, e.g. collapse of a mud volcano dome (Ivanov et al., 1996; Perez-Garcia et al., 2009) or of a pipe structure (Moss and Cartwright, 2010), and (3) a volcanic bicone geometry consisting of an upward-pointing cone and a downward-pointing cone (Davies and Stewart, 2005; Stewart and Davies, 2006).

Since the high-resolution 2D seismic data do not show down-bending, we can rule out a structural feature such as a collapse structure, and there is also no conclusive evidence for a bicone geometry.

Instead, we favour the interpretation that the down-bending is caused by lower velocities within a gas chimney. The different effects observed in the seismic data – down-bending in 3D seismic data, chaotic reflections in 2D seismic data – are attributed to the different frequencies of the systems used.

Mud reservoir

If the vent is driven by mud mobilisation, there must be a mud reservoir of some kind. Hansen et al. (2005) suggest that mud is sourced from within the Brygge Formation. While mud from the Brygge Formation may have fed a mud diapir until Top Brygge times, a shallower source may have operated afterwards. Other studies proposed mud mobilisation within the Kai Formation, caused by lithological changes across the BPU and overpressure build-up beneath it (Caston, 1976; Hjelstuen et al., 1997; Hovland et al., 1998). Such mud mobilisation within the Kai Formation probably resulted in the formation of the Vema and Vigrid diapirs (Hjelstuen et al., 1997; Hovland et al., 1998). Due to the relative proximity of the GGV to these diapirs, it is possible that the process of mud mobilisation in the Kai Formation also occurred at the GGV. However, the GGV differs from the diapirs in that it shows several indications for free gas, suggesting gas migration rather than mud mobilisation.

If the vent is primarily gas-driven, it can still lead to mud mobilisation. Fluids migrating through overpressured sequences may entrain unconsolidated sediment (Davies et al., 2007; Huuse et al., 2010), for example at the edges of feeder pipes (Deville et al., 2010). Sediment entrainment in response to fluid migration is likely to occur in areas characterised by polygonal faulting (Løseth et al., 2003). We assume that if mud mobilisation by sediment entrainment occurs in the Kai Formation, it is restricted to the upper 80 ms TWT. Reflections within this zone are up-bending, which could indicate subsurface sediment mobilisation. In contrast, flat and undisturbed reflections in the lower Kai Formation do not seem to support subsurface sediment mobilisation.

3.6.2.2 Recent reactivation of the GGV

After initial vigorous methane venting and a later mud-diapir phase, which probably lasted until Top Brygge times, the GGV may have experienced a period of quiescence until deposition of the Naust Formation onto the Kai Formation occurred. Gay et al. (2012) suggested that fluid migration was reactivated at the Kai-Naust transition, based on the observation that deformed reflections exist only near the BPU and above but not within the deeper Kai Formation.

Another indication for reactivation during the Naust Formation is the absence of stratigraphic onlap at the deformed BPU. If deformation of the BPU had begun before deposition of the Naust Formation, reflections of the lower Naust Formation should be characterised by onlap onto the BPU. As onlap is absent in 2D and 3D seismic data, and the BPU is draped by conformable sediments, we interpret this to indicate that the deformation of the BPU occurred after the onset of the deposition of the Naust Formation.

Deformation and up-doming of the BPU and neighbouring reflections may be due to overpressure build-up beneath the BPU. Overpressure build-up can be internally driven by local processes in the sediments, or by an external fluid source (Løseth et al., 2003). Internal processes are often associated with pore space reduction during compaction (e.g. Osborne and Swarbrick, 1997), whereas external drivers of overpressure are derived from focused fluid migration towards a particular part of the subsurface (e.g. Crutchley et al., 2013).

At the GGV, internal overpressure beneath the BPU is likely caused by the strong lithological contrast between lower-permeability Naust Formation sediments and higher-permeability Kai Formation sediments, and by high sedimentation rates during deposition of the Naust Formation. Rapid burial by impermeable sediments favours disequilibrium compaction, leading to overpressure generation (Osborne and Swarbrick, 1997; Deville et al., 2010). Regional or internal overpressure is further indicated by polygonal faults in the upper Brygge, Kai and lower Naust formations (Chand et al., 2011).

However, fluid migration caused solely by regional overpressure disagrees with the localised deformation and focused pipes of the GGV. Recent fluid migration must therefore be at least partly related to a second, i.e., external, overpressure component. Externally driven overpressure is associated with fluid migration pipes, which always produce small amounts of overpressure (Osborne and Swarbrick, 1997). Gas ascending in an incompressible fluid also generates significant overpressure (Osborne and Swarbrick, 1997).

Recent to ongoing fluid migration must therefore also be related to the underlying pre-Top-Brygge mud diapir and former hydrothermal system of the GGV. We propose that slow fluid migration from the last main fluid-flow activity phase of the vent, which lasted from approximately Middle Oligocene to Lower Miocene (Top Brygge), is still ongoing, albeit at a much lower rate than during the main phase. Fluids are seeping into the Kai Formation and migrate upwards, forming two pipe structures terminating at the BPU.

At the pipes, local overpressure arising from buoyant, trapped fluids adds to the regional overpressure caused by the permeability contrast and loading. Consequently, overpressure beneath the BPU must be considerably greater at the GGV compared to the surrounding area. We suggest that greater overpressure at the GGV is a feasible explanation for up-doming and deformation of the BPU.

Overpressure build-up beneath the BPU is also inferred from the chimney location where the seal has been breached. Such seal failure typically occurs when a pressure threshold is reached beneath the seal and the fracture gradient, i.e., the rock's least principle stress, is exceeded (Huuse et al., 2010). Subsequently, hydro-fractures can form, which serve as migration pathways into the overlying sediments. Since fluid chimneys like the one observed at the BPU have been inferred to initiate by faulting (e.g. Netzeband et al., 2010), we propose that seal failure at the GGV also occurred by this process. The chimney feature must then have formed after deposition of the BPU, i.e., within the last 2.6 Myr.

3.6.2.3 Interpretation of the GGV

We conclude that the GGV is not a buried single-event mud volcano, as the absence of a dome-shaped outlet at the paleo-seafloor is inconsistent with the appearance of classic mud volcanoes. Moreover, the GGV is neither inactive, nor is it driven entirely by mud mobilisation. Instead, the upper part above Top Brygge level appears to be gas-driven. We therefore interpret the GGV as an active gas chimney above a former mud diapir. A change from a mud-dominated phase to gas-dominated activity at the same location is possible, as suggested for Håkon Mosby Mud Volcano (Perez-Garcia et al., 2009).

Gas-rich fluids at the GGV probably originate from different depth intervals: (1) from beneath the Top Brygge horizon, as a continuation of past activity phases, and (2) from within the Kai Formation due to dewatering in response to increased loading by Naust Formation sediments. Overpressure, caused by the combined effect of external and internal drivers associated with these two types of fluid migration, is probably sufficient to induce the observed deformation of the BPU and overlying strata. The interpretation that the BPU deformation arises from overpressured, trapped fluids pushing upwards beneath the seal is consistent with our observations.

It is difficult to constrain the onset of deformation of the BPU and the Naust Formation at the GGV from the seismic data. A rough estimate is 180,000 years after the BPU, although an even earlier onset cannot be ruled out. Up-doming and deformation have probably been continuous, as indicated by the progressive increase in flank steepness towards the seafloor (Fig. 3.7). The increasing surface relief probably influenced local bottom currents, promoting seabed erosion, which may explain the reduction in sediment thickness in the area of the highest degree of deformation. Alternatively, sediment could have been removed through fluid expulsion, as observed at pockmarks (Hovland and Judd, 1988).

The GGV still appears to be in an early phase of development since its possible reactivation at the Kai-Naust transition. This is suggested by the predominantly intact BPU seal and largely absent fluid migration features in the Naust Formation. According to Gay et al. (2012), up-doming of the BPU reflects an early stage of pipe formation. The GGV may eventually collapse to form pockmarks characterised by active seepage.

3.6.3 Evolution since the BPU

Prior to the Pleistocene, a period of transgression (Løseth and Henriksen, 2005) and possibly regression, causing erosion of the upper Kai Formation over much of the Norwegian shelf (Eidvin et al., 2000), produced a depositional hiatus on the Norwegian margin (Jansen and Sjøholm, 1991). Polygonal faults, which developed in the Miocene Kai Formation in response to volumetric contraction, possibly ceased to be active after the erosional event, at least in the Storegga area about 280 km south of the GGV (Gay and Berndt, 2007). With the beginning of the Pleistocene and deposition of the Naust Formation sediments, the depositional hiatus in the uppermost Kai Formation led to the development of an unconformity, the BPU. Based on our assumption that low-intensity

fluid migration continued after the last main activity phase of the GGV, we devised the following model for the vent's evolution since the BPU, i.e., for the last 2.6 Myr.
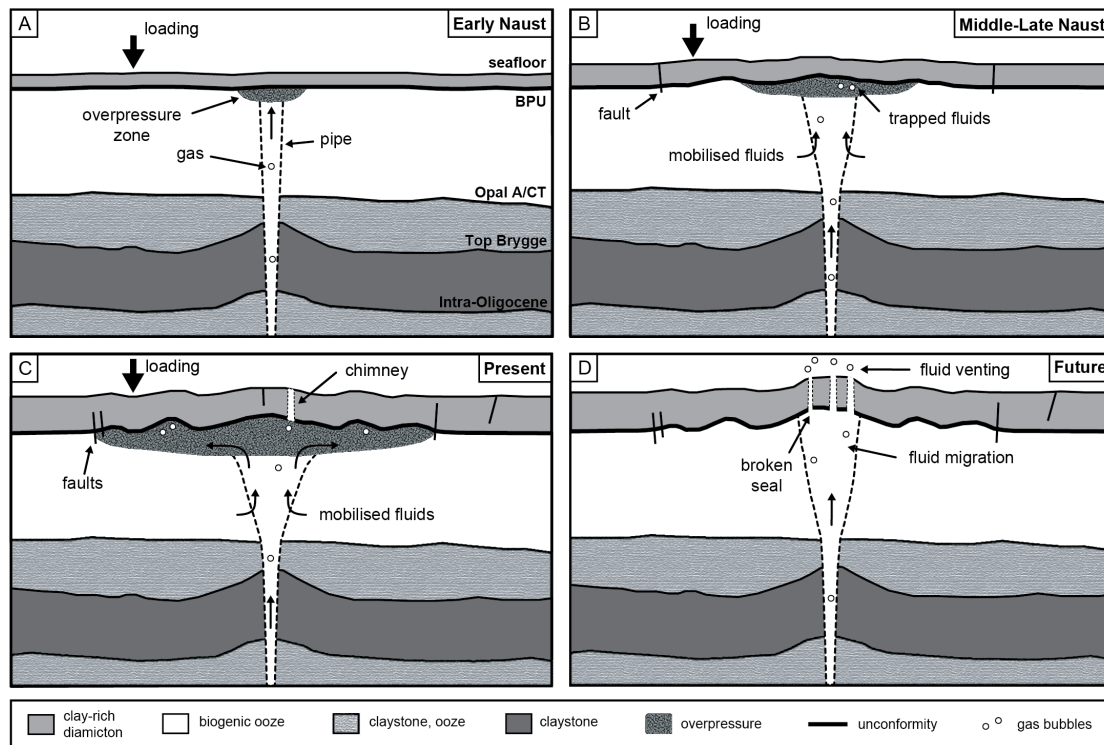

Figure 3.13: Model of vent evolution since deposition of the Naust Formation. **(A)** Early Naust period: Base Pleistocene Unconformity (BPU) and overlying Naust Formation sediments act as seal. **(B)** Middle to Late Naust period: fluids accumulating beneath the BPU induce overpressure and deformation. **(C)** Present: increased overpressure and deformation, seal bypass in at least one location. **(D)** Future: extensive seal bypass enables new phase of active fluid venting.

3.6.3.1   Early Naust period

During the Pleistocene, the weak Kai Formation was progressively loaded by dense glacigenic Naust Formation sediments that were deposited onto the BPU. Due to the lower porosity and higher density of the glacigenic sediments compared to the Kai Formation ooze (Caston, 1976), the BPU acted as a seal, trapping upward-migrating fluids (Fig. 3.13A).

Consequently, overpressure began to build up beneath the BPU, favoured by increased, rapid burial of the sealed Kai Formation, which led to disequilibrium compaction and dewatering (Osborne and Swarbrick, 1997; Chand et al., 2011). Fluids that mobilised as the result of dewatering reactions then migrated upwards towards the BPU.

Overpressure was greatest at the GGV where local overpressure derived from buoyant, trapped fluids added to the regional, loading-induced overpressure. This combined overpressure beneath the BPU was probably sufficient to cause progressive up-doming and deformation of the sealing sequence.

3.6.3.2 Middle to Late Naust period

Overpressure continued to build up beneath the BPU while deformation of the BPU and the Naust Formation progressively increased (Fig. 3.13B). Burial of the Kai Formation caused reactivation of Miocene polygonal faults, while new faults formed due to overpressure-induced deformation at the GGV.

3.6.3.3 Present

At present, increasing overpressure beneath the BPU seal has caused seal bypass in at least one location where a 100 m wide chimney feature extends into the Naust Formation and up to the seafloor (Fig. 3.13C). While this is the only seal bypass feature yet observed, other locations may exist but may not have been detected due to limited coverage of 2D seismic profiles and the low resolution of the 3D dataset (Fig. 3.10). It is possible that seafloor venting is already taking place, although indications for seepage were not observed during the survey.

3.6.3.4 Future

If overpressure continues to increase as fluids accumulate beneath the BPU, it is likely that seal bypass will occur at other locations (Fig 3.13D). Eventually, we expect the BPU seal to fail over a larger area, i.e., several square kilometres, enabling fluids and possibly mobilised mud to freely migrate into the Naust Formation and towards the seafloor. Once fluids reach the seafloor and are expelled into the water column, a new phase of fluid venting begins at the GGV.

Fluid venting may lead to pockmark formation and possibly later collapse of the upper pipe structure (Gay et al., 2012). If fluid supply to the system were to remain active long enough, typical seep facies such as chemoautotrophic fauna (Barry et al., 1996) and carbonate chemoherms (Aharon, 1994) could develop at the seabed and in the shallow subsurface, indicating long-lasting fluid seepage.

3.6.4 A window into the deep basin?

The new high-resolution data provide more insight into the GGV system than was previously possible. We therefore re-evaluated the suggestion that the GGV can act as a window into the geological processes active in the deep Vøring Basin.

While Gay et al. (2012) inferred from the 3D dataset that the GGV may be used as a window into the deep basin, we cannot support this hypothesis based on our new high-resolution data. The processes characterising the GGV today – fluid accumulation, overpressure build-up, up-doming, and faulting – are mainly shallow processes originating in the Naust Formation and upper Kai Formation. With the exception of possible low-intensity fluid migration remaining from the last main activity phase, these processes appear to be unrelated to the deeper vent system that was dominated by sill-associated explosive fluid escape at the Paleocene-Eocene transition and later

mud diapirism between the Intra-Oligocene and Top Brygge horizons. We therefore conclude that the GGV does not serve as a window into the deep Vøring Basin. Instead, the vent reflects a long-lived, polyphase history marked by focused fluid flow, reactivation with different modes of fluid migration and fluid composition, seal establishment, and seal failure.

To further clarify whether deep processes contribute to present-day activity at the GGV, geochemical data such as methane signatures would be required from seepage sites. Methane of biogenic origin would indicate that only shallow processes are active at the GGV, whereas a thermogenic signature implies deep processes and hence a possible window into the deeper basin. At present, the most promising location for taking methane samples to address this question is the chimney site. More detailed seafloor investigations should be carried out in order to corroborate if fluids from the deep parts of the Vøring Basin reach the seafloor at present.

3.7   Conclusions

New high-resolution 2D seismic and Parasound data complement existing 3D seismic data and provide new insights into the evolution of the GGV. Our seismic data show that the GGV is presently active in terms of fluid migration and structural deformation. Fluids originating from beneath the Top Brygge horizon and from dewatering within the Kai Formation accumulate beneath the BPU, which separates the Kai and Naust formations and acts as a seal to upward fluid migration. Overpressure associated with the trapping of fluids is highest above the two pipes and is probably sufficient to cause up-doming and deformation of the BPU, as well as faulting up to 10 km away from the vent.

Various seismic anomalies led us to suggest that fluid migration is gas-driven above the Top Brygge horizon. Together with the absence of a potential dome-shaped outlet on the BPU, these results indicate that the GGV is not a buried mud volcano as suggested by Hansen et al. (2005). Rather, the GGV reflects a polyphase history characterised by phases of mud-dominated and gas-dominated activity. The current gas-driven phase was probably initiated by the deposition of Naust Formation sediments onto the BPU, which caused sealing of the Kai Formation.

We suggest that this seal is beginning to fail, allowing fluids to migrate into the Naust Formation and towards the seafloor. Although this is currently observed at only one location, we propose that progressive seal failure will occur in the future and start a new phase of active fluid venting at the seabed. The GGV thus represents a promising location to study the evolution of a fluid migration system at an early stage of its development since reactivation. Understanding hydrothermal systems such as the GGV is important to gain insight into the effects these systems had, and still have, on the ocean and atmospheric composition.

Our study further highlights the importance of additional high-resolution seismic data for the interpretation of conventional 3D seismic data, which is often not able to resolve shallow (upper 100 m) features due to its lower resolution.

3.8 Acknowledgements

Chapter 4

Case study 3 - Svalbard margin seeps

Temporal constraints on hydrate-controlled methane seepage off Svalbard[1]

Christian Berndt, Tomas Feseker, Tina Treude, Sebastian Krastel, Volker Liebetrau, Helge Niemann, Victoria J. Bertics, Ines Dumke, Karolin Dünnbier, Bénédicte Ferré, Carolyn Graves, Felix Gross, Karen Hissmann, Veit Hühnerbach, Stefan Krause, Kathrin Lieser, Jürgen Schauer, Lea Steinle

4.1   Abstract

Methane hydrate is an icelike substance that is stable at high pressure and low temperature in continental margin sediments. Since the discovery of a large number of gas flares at the landward termination of the gas hydrate stability zone off Svalbard, there has been concern that warming bottom waters have started to dissociate large amounts of gas hydrate and that the resulting methane release may possibly accelerate global warming. Here, we corroborate that hydrates play a role in the observed seepage of gas, but we present evidence that seepage off Svalbard has been ongoing for at least 3000 years and that seasonal fluctuations of 1° to 2°C in the bottom-water temperature cause periodic gas hydrate formation and dissociation, which focus seepage at the observed sites.

4.2   Temporal constraints on methane seepage off Svalbard

Large quantities of methane, a powerful greenhouse gas, are present in the continental margin west off Svalbard, where they are stored as marine gas hydrate (Carcione et al., 2005; Westbrook et al., 2008a; Chabert et al., 2011). Because hydrate stability is temperature-dependent, Arctic warming is a potentially major threat to both the environment and the global economy. If even a fraction of the methane contained in Arctic hydrates were released to the atmosphere, the effect on climate could be dramatic (Post et al., 2009; Whiteman et al., 2013).

Water-column temperature measurements and mooring data suggest a 1°C bottom-water temperature warming for the past 30 years (Westbrook et al., 2009; Ferré et al., 2012). Numerical modelling of hydrate stability predicts that such warming would result in the dissociation of hydrates in the shallowest sediments (Reagan et al., 2009; Westbrook et al., 2009; Ferré et al., 2012; Thatcher et al., 2013). Therefore, the discovery of numerous gas flares, – that is, trains of gas bubbles in the water column precisely at the water depth where gas hydrate is expected to dissociate – was interpreted as the onset of submarine Arctic gas hydrate dissociation in response to global warming, which may potentially lead to large-scale escape of methane into the water column and ultimately into the atmosphere (Westbrook et al., 2009). In order to assess the consequences of methane venting on ocean and atmosphere composition, it is necessary to establish how the rates of methane emissions from hydrate systems change through time (Dickens, 2011).

The margin of Svalbard (Fig. 4.1) can be considered a model system to study a temperature-related gas hydrate destabilisation scenario, because water temperature in the Fram Strait oceanographic gateway will be more affected by changes in global atmospheric temperature than elsewhere in the Arctic; therefore, any corresponding changes to a hydrate system should be easier to observe here than elsewhere (Spielhagen et al., 2011). The continental margin of Svalbard is characterised by abundant contourite deposits (Eiken and Hinz, 1993) that consist of fine-grained sediments with high water content, which cover most of the margin between water depths of 800 and 3000 m. It is likely that these contourites are underlain by Miocene sediments with 3% (by weight) of total organic carbon as found at Ocean Drilling Project site 909 (Knies and Mann, 2002) and that the emanating gas was produced by these sediments. Proximally, that is, shallower than 700- to 800-m water depth, Pleistocene and Pliocene highly heterogeneous, terrigeneous glacial deposits overlie the contourites (Vorren et al., 1989; Solheim et al., 1996). In the glacial deposits, there is only limited evidence for free gas and no clear geophysical evidence for gas hydrate, such as a bottom-simulating reflector. Yet, seismic evidence for gas hydrate occurrence is conclusive for the contourite deposits farther west (Sarkar et al., 2012), where gas hydrate has also been sampled at a vent site in ∼900-m water depth (Fisher et al., 2011).

Several oceanographic expeditions were able to corroborate the location of the gas flares discovered in 2008. During the MSM21/4 survey in August 2012, we collected a series of Parasound 18-kHz parametric echosounder profiles with 40-m spacing around the site of the MASOX (Monitoring Arctic Seafloor-Ocean Exchange) observatory (Fig. 4.1). A ∼40-m footprint of the Parasound system at 390-m water depth allowed us to obtain a complete coverage of the flare locations within the area of this survey, which means these data were no longer biased by selection of ship tracks as
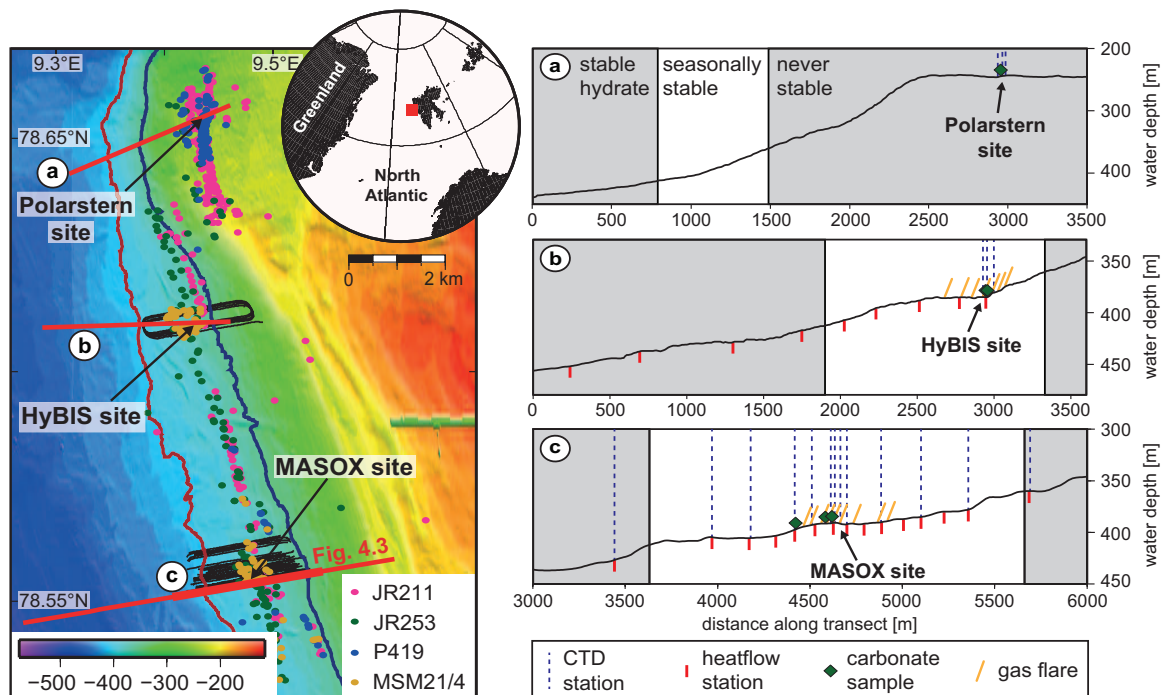
Figure 4.1: The Svalbard gas hydrate province is located on the western margin of the Svalbard archipelago (inset). At water depths shallower than 398 m, numerous gas flares have been observed in the water column (color-coded dots for different surveys) by using EK60 echosounders and high-resolution sidescan sonar. The gas flares are located between the contour lines at which gas hydrate is stable in the subsurface at 3°C (brown) and 2°C (blue) average bottom-water temperature. The black lines show the location of Parasound profiles with 40-m separation, that is, complete coverage, for flare mapping. The black arrows point to the location of submarine dives discussed in the text. The red line shows the location of the modelling transect (bold section shown in Fig. 4.3). The large cluster of seeps at the northern limit of the gas flare line at a water depth of 240 to 260 m can be explained by the presence of an elsewhere-absent glacial debris flow deposit that is deviating gas laterally within the prograding debris flow deposits and cannot have anything to do with gas hydrate dynamics (Rajan et al., 2012a; Sarkar et al., 2012). CTD – conductivity, temperature, and depth.

previous surveys. Our results show that the gas flares align between 380- and 400-m water depths, which corresponds to the upper limit of the gas hydrate stability zone (GHSZ) considering present-day bottom-water temperature of around 3°C (Sarkar et al., 2012). Geological structures that may focus gas from deeper parts of the plumbing system are absent (Sarkar et al., 2012). Thus, we interpret this match of gas flare origination depth and the calculated landward termination of the gas hydrate stability zone in the sediments as strong circumstantial evidence for a link between gas hydrate dynamics and gas seepage. At the gas flares, significant amounts of methane are liberated into the water column, leading to bottom-water CH_4 concentrations of up to 825 nM and a net flux of methane to the atmosphere (see supplementary material in Appendix A.2).

One objective of this study was to deduce a minimum age for the onset of marine methane release from the sea floor. For detailed sampling of the gas seeps, we carried out 10 dives with the manned submersible JAGO. Our observations substantiate the presence of more than 5-m-wide and typically more than 20- to 40-cm-thick outcropping carbonate crusts at the Polarstern (246 m) and the HyBIS (385 m) (Fig. 4.2) sites; small carbonate nodules at the MASOX site (395 m) were found in gravity cores. We analysed carbonates from the HyBIS and the MASOX site. The mineralogi-

cal composition of the carbonates was heterogeneous and admixed with high amounts of detrital silicates. They were characterised by low $\delta^{13}C$ isotope values between -27.1 and -41.4 per mil (‰) Vienna pee dee belemnite (V-PDB) (see supplementary material in Appendix A.2). Consequently, these carbonates can be regarded as an archive of microbially-induced, methane-related authigenic precipitation processes (Luff et al., 2004). The most reliable single-age data were obtained from aragonite-dominated surface samples. U-Th isotope measurements and resulting minimum seepage age for the MASOX site imply that significant methane-related precipitation was already occurring at 3000 years before the present (yr B.P.) (see supplementary material in Appendix A.2). For comparison, the derived ages for the HyBIS site are overlapping or older, for example, sample SV-2 (8200 ± 500 yr B.P.) or sample SV-3 (4600 ± 500 yr B.P.). The youngest isochron-based age of ∼500 yr B.P. was deduced from carbonates that were found in sediments at the MASOX site at 40- to 50-cm depth below the sea floor. Because of changes in the path of methane-bearing fluids, inclusion of impurities, and alteration of sample material, it was not possible to decipher potential on/off stages or chemical variation of the seeping fluids beyond the results presented in this paper. Hence, it is possible that seepage strength and transport of methane from the sediment to the water column and atmosphere varied over time.
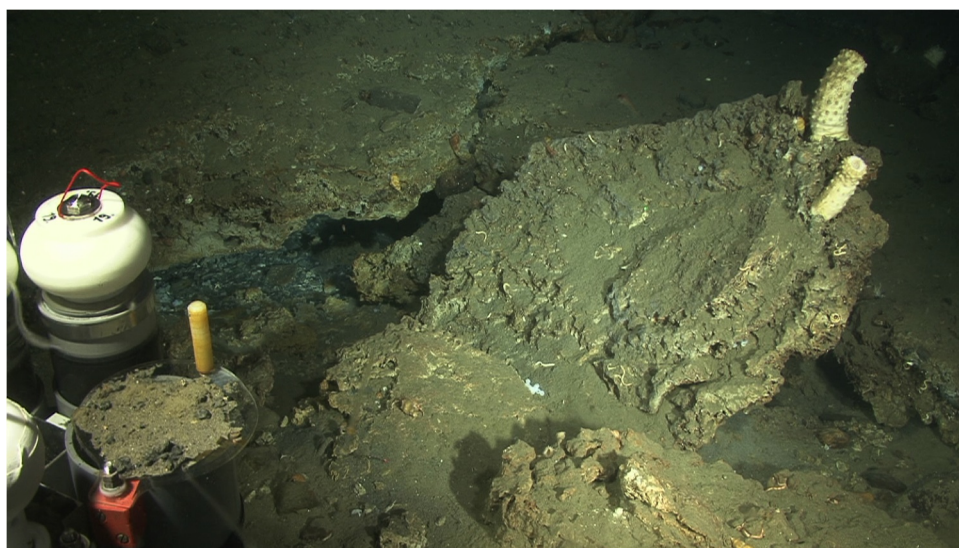

Figure 4.2: Photograph of the massive authigenic carbonate crusts observed at the HyBIS site in 385-m water depth. For scale, the total length of the larger white sessile ascidia (white stalklike animal on the crest of the uplifted carbonate plate) is approximately 15 cm. Carbonate crusts such as these take at least several hundred years to develop through anaerobic oxidation of methane.

We propose that carbonate formation in this area continues until today, because surface sediments (0- to 10-cm depth below sea floor) at gas vents at both the HyBIS and the MASOX sites were characterised by high rates of anaerobic oxidation of methane (AOM; maximum of 11.3 μmol CH_4 $cm^{-3}day^{-1}$), which is the driver for carbonate precipitation at methane seeps (Luff et al., 2004). AOM correlated with high concentrations of methane (maximum of 14,800 nM), sulfide (maximum of 11,000 nM) and total alkalinity (maximum of 29 meq l^{-1}) in the sediment. Chemosyn-

thetic communities (sulfur bacteria mats and frenulate tubeworms) were present at both sites (see supplementary material in Appendix A.2).

Observations of old carbonate crusts imply that seepage must have been ongoing at all three sites for more than 500 years. Detailed paleoceanographic reconstructions for the Svalbard area (Spielhagen et al., 2011) show a pronounced warming since the end of the 19th century. However, even this 100-year time span seems too short to explain the observed thicknesses. The ages of the recovered carbonate crusts, which are all significantly older than 100 years, support this conclusion. Thus, it is unlikely that an anthropogenic decadal-scale bottom-water temperature rise is the primary reason for the origin of the observed gas flares, although it may contribute to keeping gas pathways open longer and further.

During the cruise, we recovered the MASOX observatory, which had been deployed twice for a total of 22 months within a cluster of flares between 390- and 400-m water depth. The observatory contained a bottom-water temperature sensor sampling every 15 min during both deployments. The recorded time series reveals fluctuations of bottom-water temperature between 0.6° and 4.9°C with lowest temperatures between April and June and highest temperatures between November and March (Fig. 4.3). In both years, the temperature difference between spring and fall/winter was around 1.5°C, but during the second year the average bottom-water temperature was generally about 0.5° higher than that recorded during the first deployment. The time series implies that there is a strong seasonal change of sea floor temperature.

In order to obtain better constraints on the heat exchange between the sediment and the bottom water, we conducted in situ sediment temperature and thermal conductivity measurements using a 6-m-long heat flow probe along transects down the slope. Between 500- and 360-m water depths, our measurements revealed a landward increase in thermal conductivity from 1.5 to 2.6 W $m^{-1}K^{-1}$, with a maximum around the position of the MASOX observatory. High sediment thermal conductivity, large temporal variability in bottom-water temperature, and possibly formation and dissociation of gas hydrates resulted in very irregular sediment temperature profiles, which made it difficult to determine the heat flow along the transect line from our data. Based on our measurements at 500-m water depth, we estimate the regional heat flow to be around 0.05 W m^{-2}. Given the comprehensive evidence for seepage this value is likely modulated by convective heat transport.

On the basis of the recorded bottom-water temperature time series and the acquired thermal conductivity data, we developed a two-dimensional model of the evolution of the GHSZ along the transect line. As illustrated in Fig. 4.3, the seasonal changes in bottom-water temperature are accompanied by large lateral shifts of the GHSZ at least within the top 5 m of surface sediments. During the cycle of a year in which bottom-water temperature varies as observed in 2011 and 2012, the volume of the GHSZ varied between a maximum value in summer and a minimum value in winter. During the time period covered by our measurements, the GHSZ was at its maximum in June 2011, when it extended to 360-m water depth. Increasing bottom-water temperatures from June until December were accompanied by a retreat of the GHSZ at the seafloor to more than 410-m water depth. In the subsurface, the GHSZ retreated further until it reached its minimum in March 2012.
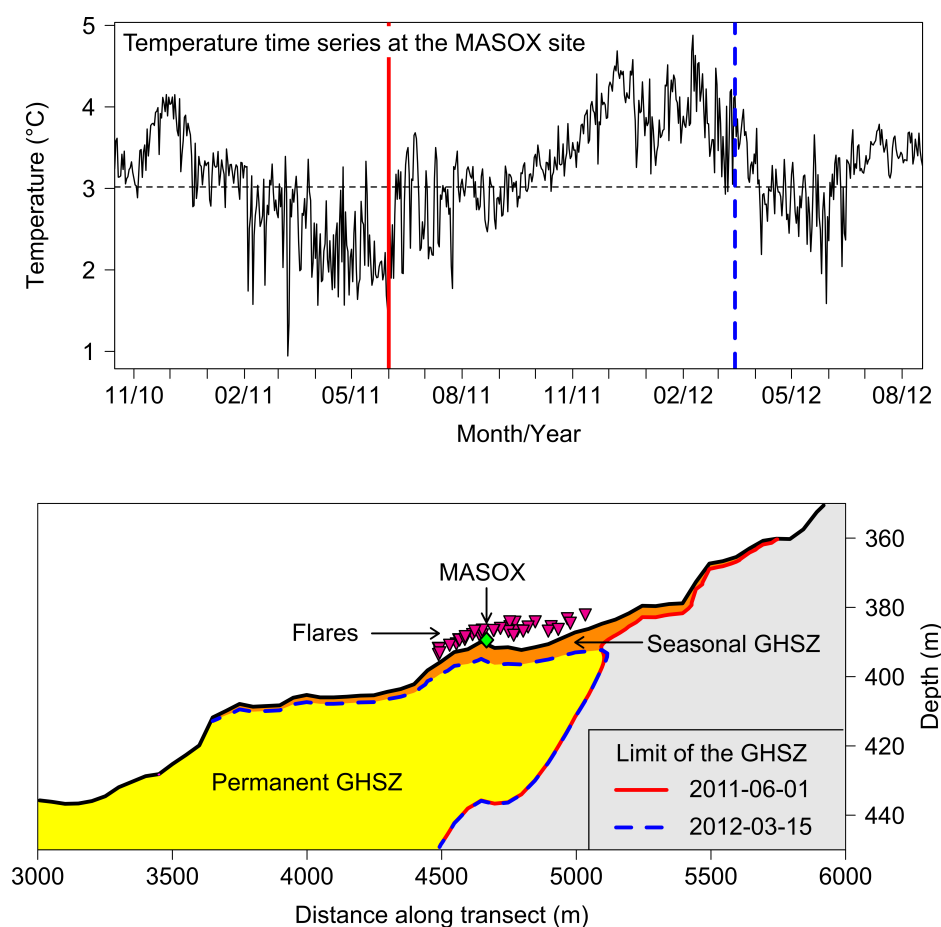
Figure 4.3: Temperature and the GHSZ. **Top**: Daily means of bottom-water temperature recorded by the MASOX observatory. The times when the extent of the GHSZ was at its maximum and minimum are marked by solid red and dashed blue lines, respectively. **Bottom**: The seasonal dynamics of the GHSZ. Driven by changes in bottom-water temperature, the GHSZ advances and retreats in the course of the year. The solid red lines and the dashed blue lines indicate the maximum and minimum extent of the GHSZ, respectively. The area in which gas hydrates are stable in the long-term is shaded in yellow. The difference between the maximum and minimum extent of the hydrate stability zone is shaded in orange and corresponds to the seasonal GHSZ, in which gas hydrate dissociation and formation alternate periodically. The triangles filled in magenta represent the projected locations of all flares detected within 1000 m of the transect line. The green diamond shows the position of the MASOX observatory. An animated illustration of the modelling results is provided in the online supplements at http://www.sciencemag.org/content/suppl/-2014/01/02/science.1246298.DC1.htm.

The modelling shows that persistent supply of dissolved methane from below the GHSZ in this section of the slope would lead to the formation of hydrate from winter until summer. The newly formed hydrate would dissociate again during the second half of the year and thus augment methane emissions from the seabed both by opening pathways to gas ascending from underneath and by releasing gas from the hydrate phase. The total volume of sediment that was affected by seasonal shifts of the GHSZ amounted to between 3000 and 5000 m^3 per meter of the margin. Assuming a gas hydrate concentration of 5% of the pore space and a porosity of 50%, the seasonal GHSZ has the potential to periodically store and release between 9 and 15 tons of CH_4 per meter of the margin. However, these amounts represent the upper limits of the seasonal buffering capacity,

as the latent heat of hydrate kinetics was not included in the simulation. Depending on the concentration and distribution of gas hydrates in the sediment, alternating formation and dissociation would dampen the oscillation of the GHSZ and thus reduce its volume.

Although the modelling shows that seasonal bottom-water temperature variations are capable of modulating the observed gas emissions, we found no direct evidence in the heat flow data that would suggest that the slope sediments experienced decadal-scale warming. The combined data demonstrate that hydrate is playing a fundamental role in modulating gas seeps between 380- and 400-m water depth at the upper limit of the GHSZ, whereas ascending gas would be trapped or deviated up along the base of the GHSZ further seaward. Long-term variations in seepage may exist, but presently available data are insufficient to document annual, decadal, or centennial changes in seepage. Our data suggest that shallow hydrate accumulations are sensitive to bottom-water temperature changes and therefore that significant anthropogenic warming will affect the shallow parts of the hydrate system. This sensitivity demonstrates the need for quantifying the total amount of gas hydrate in the shallowest part of the GHSZ if climate feedback mechanisms are to be assessed beyond simple global models (Archer and Buffett, 2005; Biastoch et al., 2011). Our observations show that methane seepage west off Svalbard has been ongoing for much longer than anthropogenic warming. Therefore, observations of large contemporary emissions reported in other studies cannot be considered proof of accelerating hydrate destabilisation, although neither do they prove that catastrophic destabilisation is not accelerating.

4.3   Acknowledgements

Chapter 5

Case study 4 - Hikurangi Margin

Sidescan backscatter variations of cold seeps on the Hikurangi Margin (New Zealand): indications for different stages in seep development[1]

Ines Dumke, Ingo Klaucke, Christian Berndt, Jörg Bialas

5.1 Abstract

Cold seeps on the Hikurangi Margin off New Zealand exhibit various seabed morphologies producing different intensity patterns in sidescan backscatter images. Acoustic backscatter characteristics of 25 investigated seep sites fall into four distinct types characterised by variations in backscatter intensity, distribution and inferred structural heights. The types reflect different carbonate morphologies including up to 20 m high structures (type 1), low-relief crusts (type 2), scattered blocks (type 3) and carbonate-free sites (type 4). Each seep corresponds to a single type; intermediates were not observed. This correlates well with published data on seep fauna at each site, with the four types representing three different faunal habitats of successive stages of seep development. Backscatter signatures in sidescan sonar images of cold seeps may therefore serve as a convenient proxy for variations in faunal habitats.

5.2 Introduction

Cold seep sites have been studied extensively over the past three decades and under various geo-logical, biological, chemical and physical aspects. Cold seeps are associated with seafloor venting of relatively cold fluids, as opposed to hot vents with fluid temperatures of more than 350°C (e.g. MacDonald et al., 1980; Spiess et al., 1980). The fluids expelled at cold seeps are typically methane-rich and consequently make an important but still poorly quantified contribution to the global carbon cycle (Judd, 2003). The expelled methane might even reach the atmosphere and thus have an impact on climate change, but this is still controversially discussed. Judd et al. (2002) esti-mated that 6.6–19.5 Tg yr^{-1} of oceanic methane enter the atmosphere, which agrees well with 11.0–18.0 Tg yr^{-1} calculated by Cicerone and Oremland (1988) and interpreted to correspond to about 2–3% of the total annual methane release to the atmosphere. In contrast, McGinnis et al. (2006) and Schmale et al. (2010) argue that most expelled methane is dissolved close to the seafloor and that only methane from water depths < 100 m may reach the atmosphere.

Cold seeps occur on both active and passive margins. Their presence indicates complex sedimen-tological and tectonic processes, including sediment dewatering, porosity reduction, mineral dehy-dration, production of hydrocarbons, reservoir development, and formation of faults and fractures (Moore and Vrolijk, 1992; Judd and Hovland, 2007). These processes eventually lead to upward migration of hydrocarbon-enriched fluids and establishment of seep sites at the surface.

At the seabed, cold seeps represent unique ecosystems as they are commonly inhabited by abun-dant benthic fauna living on carbon-based chemosymbiosis (e.g. Barry et al., 1996; Sahling et al., 2002; Bowden et al., 2013). Depending on the species, different substrates are colonised: bacte-rial mats, ampharetid polychaetes and vesicomyid clams settle on the sediment surface at locations characterised by seepage and anaerobic oxidation of methane; siboglinid tubeworms, mussels and sponges colonise authigenic carbonate precipitates at active seep sites; non-seep epifauna such as corals settle on carbonate substrate after seepage has ceased (Bowden et al., 2013).

Anaerobic oxidation of methane (AOM; Boetius et al., 2000) occurs at all cold seep sites and results in the precipitation of carbonate at the seafloor or in the near-surface sediments. Carbonate crusts generally grow downwards into the sediment (Kutterolf et al., 2008; Bayon et al., 2009) but, in high-flux areas, carbonate growth may be within the water column (Teichert et al., 2005). Clogging and subsequent cessation of seepage in the centre (Hovland, 2002; Gay et al., 2006) cause seeps to move to the edges of the crust, resulting in lateral growth of crusts (Dupré et al., 2010). Intense or prolonged carbonate precipitation leads to the build-up of chemoherm structures (Aharon, 1994) of various morphologies and dimensions, ranging from tubular chimneys (Ritger et al., 1987; Stakes et al., 1999; Díaz-del-Río et al., 2003; Mazzini et al., 2008) over tabular slabs (Stakes et al., 1999; Mazzini et al., 2008), massive blocks (Van Dover et al., 2003), flat pavements (Stakes et al., 1999) and mounds (Buerk et al., 2010; Klaucke et al., 2012) to steep pinnacles up to 90 m in height (Teichert et al., 2005).

Seabed cold seeps may be recognized by distinctive morphological and/or backscatter signatures on sidescan sonar images. In particular, a strong difference in impedance contrast, small-scale rough-ness and morphology between carbonate precipitates and the seafloor produces elevated backscatter

in sidescan sonar images from which seep carbonates can be identified easily (Johnson et al., 2003; Holland et al., 2006). This is especially true for marine environments with muddy, hemipelagic seafloor sediments that are of low backscatter. Surface expressions of cold seeps have been observed to differ within seep regions in terms of backscatter intensity patterns and seep morphology in, for example, the Black Sea (Naudts et al., 2008), offshore Nicaragua (Buerk et al., 2010), and on the Hikurangi Margin (Klaucke et al., 2010). So far, the factors responsible for the formation of different seep morphologies, as well as the processes controlling the evolution of seep surface structures, remain largely unclear. Buerk et al. (2010) attribute variations in backscatter patterns to a complex interplay between fluid flow, erosion and sedimentation processes, and Naudts et al. (2008) relate backscatter intensity to the degree of authigenic carbonate formation. Klaucke et al. (2010) suggest a similar relation along the Hikurangi Margin, with high backscatter indicating the presence and low backscatter indicating the absence of authigenic carbonates.

This study is based on a re-analysis of sidescan data from 2007 and additional sidescan data obtained in 2011 in three areas along the Hikurangi Margin (Fig. 5.1). The aim of this study is to present a refined differentiation of backscatter intensity patterns, and to compare seeps of different backscatter patterns in terms of seep fauna in order to determine to what extent sidescan sonar data can be used as a proxy for faunal habitats. Carbonate precipitation and changes in fluid flow are then discussed in order to provide an explanation for the presence of different seep types on the Hikurangi Margin.
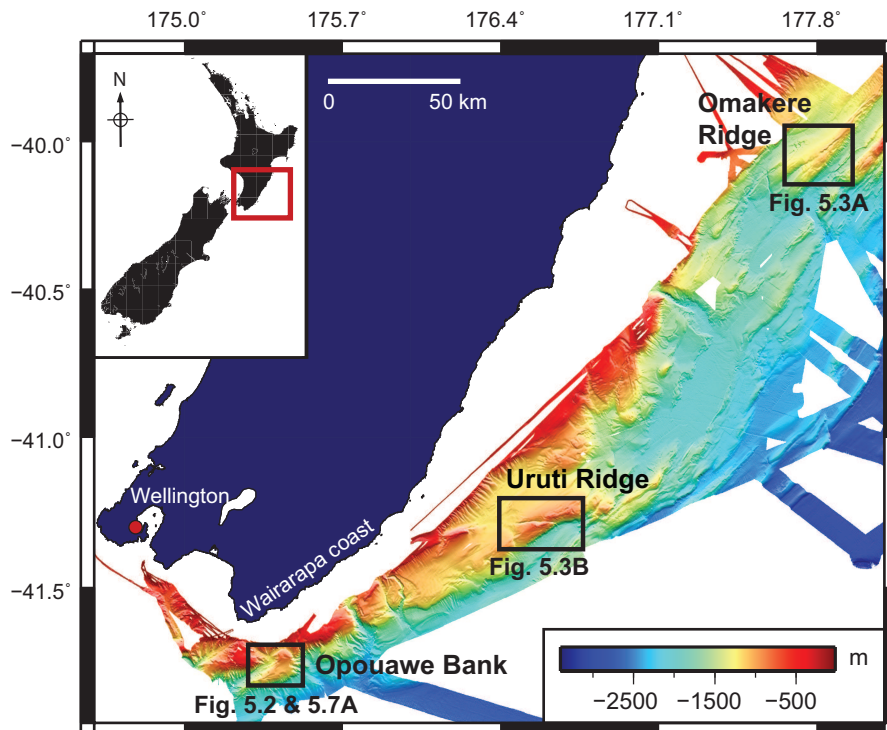

Figure 5.1: Overview map of the Hikurangi Margin and location of the study areas Omakere Ridge, Uruti Ridge and Opouawe Bank. Bathymetry was acquired during RV SONNE cruises SO191 and SO214. Inset: Location offshore New Zealand's North Island.

5.3   Geological setting and previous work

5.3.1   Geological setting

The Hikurangi Margin forms the southern part of the Tonga-Kermadec-Hikurangi subduction system in the southwest Pacific (Fig. 5.1). Located east of New Zealand's North Island, it marks the subduction of the igneous Hikurangi Plateau beneath the Australian Plate (Wood and Davy, 1994). Convergence direction and subduction rate vary strongly along the Hikurangi Margin, with subduction becoming increasingly oblique towards the south (Collot et al., 1996; Wallace et al., 2004). Whereas the northern part of the margin is dominated by tectonic erosion induced by subducting seamounts, the central and southern segments are characterised by the Hikurangi accretionary wedge (Lewis et al., 1998). The conveyor-belt-like input of thick, water-logged sediments and the fast rate of convergence result in rapid burial (Barnes et al., 2010). A sedimentation rate of 0.65 m kyr^{-1} was calculated by Barnes and Mercier de Lépinay (1997) for the trench-fill sediments during the last 0.4 Myr.

Fluid flow to the seabed plays an important role along the Hikurangi Margin and is evidenced by gas hydrates and numerous cold seeps (cf. Greinert et al., 2010a, and references therein; Table 5.1 and 5.2). Cold seep sites have been mapped in five main areas: Builder's Pencil, Omakere Ridge, Rock Garden, Uruti Ridge, and Opouawe Bank, all representing margin-parallel, anticlinal ridges on the mid-slope, landward of the accretionary prism (Barnes et al., 2010). This study focuses on the areas Opouawe Bank, Omakere Ridge, and Uruti Ridge (Fig. 5.1). Opouawe Bank and Omakere Ridge are draped by thick hemipelagic sediments; Uruti Ridge, which is dissected by the E–W striking Palliser-Kaiwhata Fault (Barnes et al., 1998), is less sediment-covered.

5.3.2   Previous work on the Hikurangi Margin

Work on the Hikurangi margin prior to 2010 is summarised by Greinert et al. (2010a, 2010b, and references therein). Seismic data show that most seep sites in the study area are associated with fluid chimneys in the subsurface (Crutchley et al., 2010a; Netzeband et al., 2010; Krabbenhoeft et al., 2013). The chimneys were characterised by vertical zones of suppressed amplitudes of 100–500 m in diameter, as well as shallow high-amplitude reflections and seismic pull-ups (Crutchley et al., 2010a, 2010b; Netzeband et al., 2010; Krabbenhoeft et al., 2013). They represent fluid pathways from beneath the base of the gas hydrate stability zone to the seafloor.

Echosounder, Parasound and sidescan sonar data revealed hydroacoustic flares at most seeps on Opouawe Bank and Uruti Ridge, and at LM-9 on Omakere Ridge (Lewis and Marshall, 1996; Greinert et al., 2010a; Jones et al., 2010). The flares indicate active fluid venting at the seafloor. In addition, elevated methane concentrations determined from water samples (Faure et al., 2010) and seabed methane sensors (Krabbenhoeft et al., 2010) indicate active seepage even at sites where flares were not observed (e.g. Kea, Kaka, Moa and Bear's Paw on Omakere Ridge). The highest methane concentrations in the study area (up to 920 nM) were measured at Tui seep on Opouawe Bank, while Bear's Paw (up to 380 nM) was the site with the highest methane concentrations on Omakere

Ridge (Faure et al., 2010). Venting activity strongly varies in terms of methane concentration and expulsion rates. Fluid expulsion is correlated with tides (Krabbenhoeft et al., 2010) but also varies over smaller timescales of minutes to hours (Faure et al., 2010; Klaucke et al., 2010).

Table 5.1: Location, dimensions of elevated backscatter (BS) areas, and U-Th ages from carbonates of the seeps associated with backscatter patterns of types 1 and 2. Coordinates and water depths are from Greinert et al. (2010a, 2010b), except for the seeps marked by an asterisk (*) that were discovered in 2011. OR – Omakere Ridge, UR – Uruti Ridge, OB – Opouawe Bank.

Seep	Area	Latitude S	Longitude E	Water depth [m]	BS area [km^2]	U-Th ages [ka BP]
Type 1						
Moa	OR	40°03.235′	177°48.802′	1118	0.214	4.39±0.13 1.16±0.05
Toroa*	OR	40°05.670′	177°45.730′	1230	0.016 (main patch) 250–3500 m^2 (patches)	–
Tomtit	UR	41°17.446′	176°33.187′	729	0.064	–
Hihi	UR	41°17.687′	176°33.548′	744	0.274	–
LM-10	UR	41°17.470′	176°33.017′	729	0.154	4.12±0.04 4.31±0.04 12.40±0.16
Type 2						
LM-9	OR	40°01.089′	177°51.616′	1150	0.060	–
Kea	OR	40°02.240′	177°47.714′	1168	0.049	–
Kaka	OR	40°02.140′	177°47.937′	1168	0.083	–
Kakapo	OR	40°02.141′	177°48.400′	1167	0.025	–
Bear's Paw	OR	40°03.187′	177°49.252′	1100	0.041	2.36±0.07 2.09±0.85
Matuku*	OR	40°05.870′	177°48.050′	1270	0.011	–
Tuatara	OB	41°43.239′	175°26.558′	827	0.054	–
Tui	OB	41°43.288′	175°27.091′	815	0.084	–
Tieke	OB	41°43.639′	175°26.983′	851	0.039	–
Tete	OB	41°44.531′	175°27.214′	972	0.045	–
Papango	OB	41°45.704′	175°27.267′	1065	0.004	–
North Tower	OB	41°46.911′	175°24.083′	1052	0.056	2.92±0.19 2.67±0.03 2.53±0.02 2.39±0.04 3.96±0.05 4.26±0.04 3.36±0.48 4.27±0.05 4.29±0.04 4.95±0.65
South Tower	OB	41°47.300′	175°24.521′	1056	0.048	–
Piwakawaka	OB	41°47.664′	175°22.348′	1095	0.033	–

Table 5.2: Location, dimensions of elevated backscatter (BS) areas, and U-Th ages from carbonates of the seeps associated with backscatter patterns of types 3 and 4. Coordinates and water depths are from Greinert et al. (2010a, 2010b), except for the seeps marked by an asterisk (*) that were discovered in 2011. OR – Omakere Ridge, UR – Uruti Ridge, OB – Opouawe Bank.

Seep	Area	Latitude S	Longitude E	Water depth [m]	BS area [km^2]	U-Th ages [ka BP]
Type 3						
Pukeko	OB	41°47.153′	175°23.465′	1060	0.060 (total) 80–940 m^2 (patches)	–
Riroriro	OB	41°47.360′	175°22.754′	1084	0.088 (total) 60–3280 m^2 (patches)	–
Hoiho*	OB	41°47.370′	175°22.360′	1050	0.003 (total) 400–1500 m^2 (patches)	–
Type 4						
Takahe	OB	41°46.368′	175°25.651′	1058	0.066	–
Takapu	OB	41°46.750′	175°26.245′	1086	0.051	–
Tawaki*	OB	41°48.420′	175°18.280′	1250	0.029	–

In sidescan sonar images of the seafloor, the seeps were characterised by patches (up to 1 km^2) of moderate to high backscatter (Jones et al., 2010; Klaucke et al., 2010), except for two seeps on Opouawe Bank, Takahe and Takapu. These sites were marked by backscatter intensities that were only slightly higher than the background backscatter associated with featureless, hemipelagic seafloor (Klaucke et al., 2010). Klaucke et al. (2010) interpreted the lower-backscatter sites as carbonate-free, with the slightly elevated backscatter arising from free gas or hydrate in the near subsurface. Up to 1 cm thick hydrate layers found at depths of 2.2 to 2.7 m in sediment cores at Takahe (Schwalenberg et al., 2010; Bialas, 2011) appear to support this interpretation. In contrast, the moderate- to high-backscatter sites were interpreted to indicate carbonate crusts with relief of a few metres (Jones et al., 2010; Klaucke et al., 2010).

The presence of seafloor carbonates at the moderate- to high-backscatter sites was confirmed by video observations (Greinert et al., 2010a; Jones et al., 2010; Bowden et al., 2013). Video transects were conducted at all seeps on Omakere Ridge, and at most seeps on Opouawe Bank and Uruti Ridge. Video data do not exist for Pukeko, Riroriro, Papango, Takapu, Tieke, Tete (all Opouawe Bank) and Tomtit (Uruti Ridge), as well as for seeps newly discovered during SO214.

Visual observations also showed abundant benthic fauna at all investigated seep sites. The main benthic communities found on the Hikurangi Margin are vesicomyid clams (*Calyptogena* sp.), siboglinid tubeworms (*Lamellibrachia* sp.), mussels (*Bathymodiolinae* sp.), sponges (*Pseudosuberites* sp. and *Stelletta* sp.), as well as white bacterial mats and ampharetid polychaete worms (Lewis and Marshall, 1996; Baco et al., 2010; Greinert et al., 2010a; Jones et al., 2010; Sommer et al., 2010; Bowden et al., 2013). Based on the benthic communities found at the visually inspected seep sites, Bowden et al. (2013) proposed three extreme states of faunal distribution: (1) the Takahe extreme, which is characterised by the absence of carbonates and mega-epifauna but presence of bacterial mats, ampharetid patches and *Calyptogena* sp. shells; (2) the Southwest Moa extreme, which has

carbonates and the highest density of seep-associated fauna; and (3) the Moa extreme, which is characterised by massive carbonates, cold-water corals and the absence of seep-related fauna.

Significant differences between the eastern and south-western part of the Moa site (Omakere Ridge) have also been noted by Jones et al. (2010) based on sidescan imagery and video observations. Eastern Moa has been interpreted as an inactive site transformed into a cold-water reef (Jones et al., 2010; Bowden et al., 2013), due to its massive carbonates, absence of seep fauna, and presence of scleractinian and antipatherian corals (Bowden et al., 2013) with ages of up to 4,400 years (Liebetrau et al., 2010). Jones et al. (2010) proposed that active seepage at this site occurred over a long time in the past but has now ceased, allowing heterotrophic fauna to settle on the carbonate surfaces. Scleractinian corals have also been found at the Uruti Ridge seeps (Baco et al., 2010; Bowden et al., 2013), which are characterised by massive carbonates at the summits of knoll-like mounds (Baco et al., 2010; Liebetrau et al., 2010).

In contrast, Southwest Moa is characterised by low-relief carbonates and abundant, live chemosynthetic fauna, including *Lamellibrachia* sp. tubeworms, *Bathymodiolin* sp. mussels, *Calyptogena* sp. clams and *Stelletta* sp. sponges (Jones et al., 2010; Bowden et al., 2013). Similar fauna and habitats are reported from North Tower, South Tower, Piwakawaka and Tui (all Opouawe Bank; Baco et al., 2010; Greinert et al., 2010a; Bowden et al., 2013). At the Omakere Ridge sites Kea, Kaka, Kakapo and Bear's Paw, the high abundance of living, seep-related fauna (tubeworms, clams, mussels, ampharetid patches) indicates past and ongoing active seepage even though hydroacoustic flares were not observed at these sites (Jones et al., 2010).

Bowden et al. (2013) suggested that the presence of specific biological communities at the seep sites is controlled by how long methane seepage has been ongoing. A long history of fluid flow and seepage was further indicated by U-Th ages of carbonate samples recovered by a video-guided grab at Moa and Bear's Paw (Omakere Ridge), North Tower (Opouawe Bank), and LM-10 (Uruti Ridge) (Liebetrau et al., 2010). The oldest samples were those from LM-10 with U-Th ages of up to 12,400 years. Samples from Bear's Paw were significantly younger (2,000–2,400 years), while the nine samples from North Tower revealed an age succession between 3,000 and 5,000 years (Table 5.1). At Moa, only reef substrate with a maximum U-Th age of about 4,400 years could be sampled (Liebetrau et al., 2010).

5.3.3 Previous work on sidescan sonar imaging of seeps

Backscatter intensity on sidescan sonar records is controlled primarily by (1) seafloor morphology and small-scale roughness, (2) the impedance contrast between seawater and seafloor, (3) acquisition geometry (grazing angle) and (4) sonar frequency (e.g. Johnson and Helferty, 1990; Mitchell, 1993; Augustin et al., 1996; Blondel, 2009), but also by artefacts such as along-track stripe noise (e.g. Wilken et al., 2012). The depth of the signal penetration depends on the sonar frequency (Johnson and Helferty, 1990). According to Mitchell (1993), who estimated maximum penetration depths at 30° incidence, the theoretical penetration depth of a 75-kHz system like the DTS-1 system used in this study should be about 1–2 m. However, experience with the DTS-1 has shown that penetration is usually less than 1 m (Klaucke et al., 2008).

Sidescan sonars are commonly used in the study of cold seeps and other fluid expulsion features such as mud volcanoes. The sidescan method is most suitable for the detection of seeps with massive carbonates as these produce high backscatter (e.g. Johnson et al., 2003; Holland et al., 2006). In contrast, carbonate-free sites are harder to image but may be detected if gas bubbles in near-surface sediments cause volume reverberation and elevated backscatter (Klaucke et al., 2010). Gas-rich fluids emitted from seeps cause scattering of the acoustic energy if the sonar passes over or close to them, resulting in flare-shaped anomalies in the water column of the raw sidescan data from which seeps may also be identified (e.g. Klaucke et al., 2006).

5.4   Materials and methods

Sidescan sonar and subbottom profiler data were acquired during two cruises aboard RV SONNE in 2007 (SO191; Bialas et al., 2007) and 2011 (SO214; Bialas, 2011; Figs. 5.2 and 5.3), using the DTS-1 system operated by GEOMAR. The system consists of a modified EdgeTech sidescan sonar with a frequency of 75 kHz and an integrated chirp (2–10 kHz) subbottom profiler. Sidescan data were acquired with a constant range of 750 m and an across-track resolution of 5.6 cm. Along-track resolution is lower and depends on survey speed. The average speed of 2.5–3.0 knots resulted in a resolution of about 1.3 m.
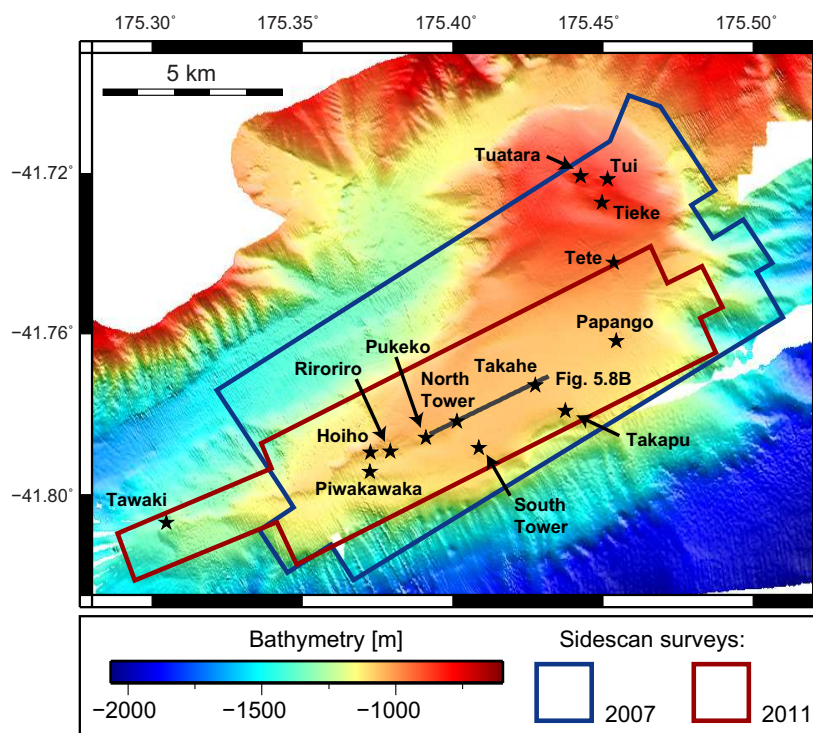

Figure 5.2: Bathymetry map of Opouawe Bank with locations of studied cold seeps (stars) and areas of sidescan surveys. Bathymetry was acquired during SO191. Map location is shown in Fig. 5.1.

Towfish altitude was kept between 70 and 130 m above the seafloor (average 100 m), except for a profile across the Kea, Kaka and Kakapo seeps (Omakere Ridge). Along this profile, the altitude

was only 10–30 m, so that the constant range of 750 m resulted in lower grazing angles and, hence, stronger backscatter emphasising small-scale relief (Augustin et al., 1996).

Navigation was provided by a USBL system with precision of approximately 15 m (1% of the cable length) in 2007. Due to technical problems with the system in 2011, towfish navigation for this survey was obtained from the ship's position via a layback method that accounts for cable length and survey speed. This method has an accuracy of up to 15 m for towfish distance behind the ship.
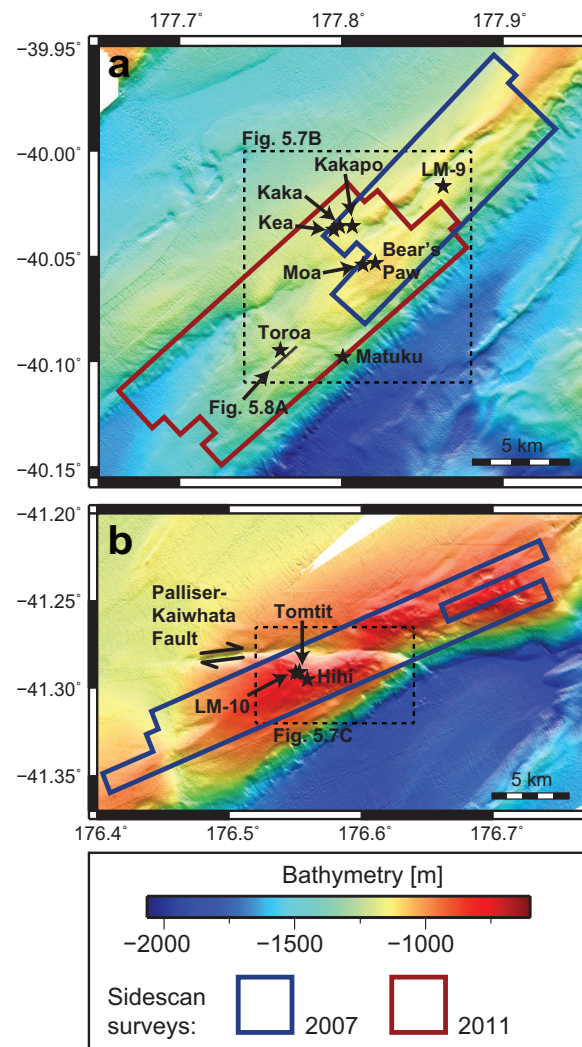

Figure 5.3: Bathymetry maps of **(A)** Omakere Ridge and **(B)** Uruti Ridge, with locations of studied cold seeps (stars) and areas of sidescan surveys. Bathymetry was acquired during SO191. Map locations are shown in Fig. 5.1.

The sidescan data were processed to a pixel size of 1.0 m using the Caraibes software package developed by IFREMER, and the PRISM software package (Le Bas et al., 1995). First inspection of the processed sidescan profiles showed some obvious along-track shifts between adjacent profiles that had been run in opposite directions. To correct for these shifts, the profiles were inspected for features crossing profile boundaries. Profiles were then re-aligned so that the feature parts on either side of the profile boundary matched. As boundary-crossing features were found along all profile boundaries, it is proposed that the layback method also has absolute navigation errors of

only 15–25 m in areas with multiple profiles. For single profiles, the error can be considerably larger. Also, the layback method does not account for lateral deviation due to currents, which can amount to a few hundred metres.

The resulting sidescan backscatter maps mostly show the distribution of seep carbonates that cause high backscatter due to a high impedance contrast, small-scale surface roughness or morphology. Acoustic shadows observed at some seep sites were used to estimate structural heights based on the following equation (Blondel, 2009):

$$h = \Delta R \times \frac{H}{R} \tag{5.1}$$

where h is the structural height, ΔR the length of the shadow zone, H the altitude of the sonar above the seabed, and R the maximum slant range to the far end of the shadow zone. H was recorded during the survey, whereas R and ΔR were picked manually in the raw sidescan data. Picking accuracy was ± 1.5 m. Depending on the combination of sonar altitude, distance to the shadow, and shadow length, the resulting error for calculated structural heights ranged between ± 0.2 and ± 1.4 m (Table 3).

The subbottom profiler was operated with a 20 ms chirp pulse of 2–10 kHz, resulting in maximum penetration in the order of 40 m below the seabed. Data processing was conducted using in-house scripts based on Seismic UNIX (Stockwell, 1997) and GMT (Wessel and Smith, 1998).

Bathymetry data were obtained using ship-borne multibeam echosounders resulting in grid spacings between 30 and 150 m (see also Greinert et al., 2010a). The relatively low resolution of the bathymetry maps did not allow reliable height estimations of the seep surface structures.

5.5   Results

A total of 25 seep sites were studied along the Hikurangi Margin (Table 5.1 and 5.2). Of these, 21 sites had already been confirmed as cold seeps by video observations and sampling (see above): three on Uruti Ridge, six on Omakere Ridge and 12 on Opouawe Bank. In addition, four sites (Toroa and Matuku on Omakere Ridge, and Hoiho and Tawaki on Opouawe Bank) were identified for the first time in sidescan images from 2011. Toroa, Matuku, and Tawaki were located in areas not mapped before 2011 by either sidescan sonar or multibeam; Hoiho, located between Piwakawaka and Riroriro, had been mapped in 2007 but had not been identified due to its small size and unfavourable sidescan profile geometry.

5.5.1   Seep seabed characteristics

The seeps are marked by increased backscatter intensity over areas of 0.003 to 0.274 km^2 (Table 5.1 and 5.2). Their surface expressions exhibit four distinct patterns (Fig. 5.4) characterised by their backscatter intensity, distribution and inferred structural heights. For most of the seep sites, video observations confirmed that elevated sidescan backscatter arises from authigenic carbonates. The observed backscatter patterns appear to reflect differences in amount, distribution and height

of carbonate precipitates. Based on the determined heights (Fig. 5.5, Table 5.3) and the surface expression for a sonar altitude of approximately 100 m, each seep was associated with a single type of pattern. Intermediates were not observed.
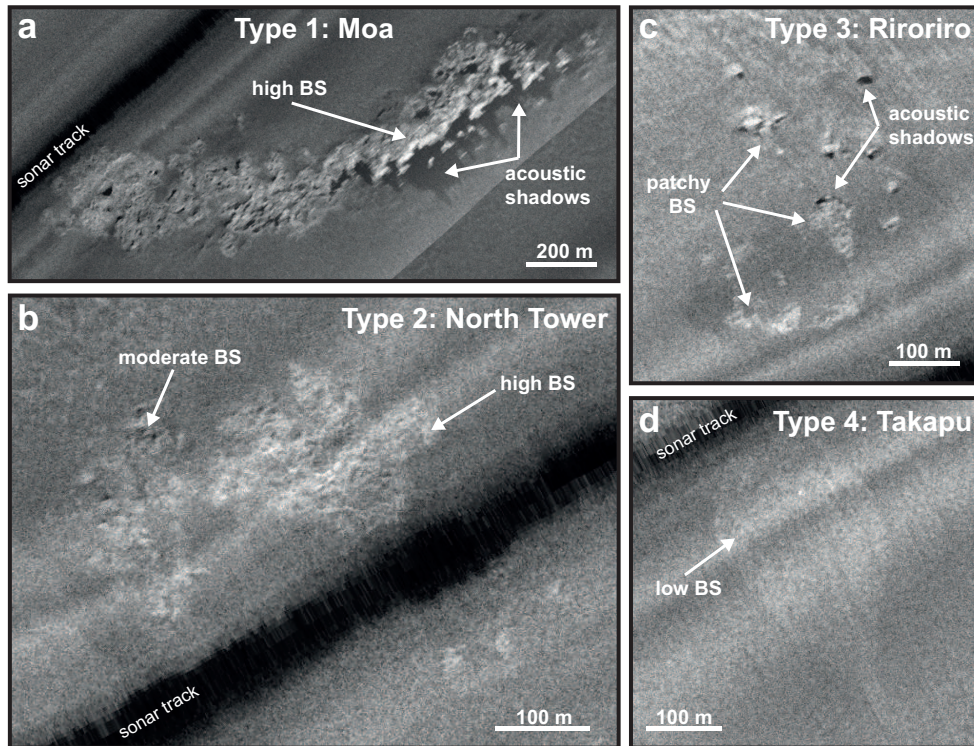

Figure 5.4: Sidescan sonar images of the four distinct types of backscatter patterns. **(A)** Type 1: high backscatter and structural relief of up to 20 m (example: Moa, Omakere Ridge). **(B)** Type 2: moderate to high backscatter and low relief (example: North Tower, Opouawe Bank). **(C)** Type 3: moderate, patchy backscatter and low relief (example: Riroriro, Opouawe Bank). **(D)** Type 4: low backscatter and no relief (example: Takapu, Opouawe Bank). Seep locations are shown in Figs. 5.2 and 5.3.

Type 1 sites

Type 1 sites (Fig. 5.4A) are marked by continuous areas of high backscatter that range between $0.016\,\mathrm{km}^2$ (Toroa) and $0.274\,\mathrm{km}^2$ (Moa) in size (Table 5.1). Prominent acoustic shadows face away from the sonar track. The combination of sonar altitude, shadow length and lateral distance to the shadow results in maximum structural heights of more than 10 m above the surrounding seafloor, reaching 20.5 ± 0.4 m at eastern Moa, 17.1 ± 1.3 m at LM-10, 14.8 ± 0.4 m at Tomtit, 12.2 ± 0.7 m at Toroa, and 12.2 ± 0.4 m at Hihi (Fig. 5.5, Table 5.3). At Toroa, four smaller (up to $0.003\,\mathrm{km}^2$) moderate- to high-backscatter patches lacking acoustic shadows occur about 400–600 m east and southeast of the 12 m high structure.

Type 2 sites

Type 2 sites (Fig. 5.4B) also generally appear as continuous $0.004\,\mathrm{km}^2$ (Papango) to $0.084\,\mathrm{km}^2$ (Tui) large areas of moderate to high backscatter (Table 5.1). Acoustic shadows were observed

only at lower towfish heights of 10 to 40 m at the sites Kea, Kaka and Kakapo (Fig. 5.6), due to the greater sensitivity to small-scale relief at these altitudes (Augustin et al., 1996). Calculated maximum heights were 3.5±0.4 m at Kea, 2.6±0.2 m at Kaka, and 2.0±0.8 m at Kakapo (Fig. 5.5, Table 5.3).

Table 5.3: Parameters for calculation of structural heights based on sonar altitude H, distance to shadow R and shadow length ΔR . R and ΔR are associated with a picking accuracy of 1.5 m. pt – pointers.

| Seep	Altitude H [m]	Slant range R [pt]	Shadow length ΔR [pt]	Height $h\pm$error [m]
Type 1				
Moa	103.68	537.75	55.50	10.7±0.6
	104.28	690.00	135.75	20.5±0.4
	105.57	663.75	100.50	16.0±0.5
	110.26	666.00	77.25	12.8±0.5
Toroa	110.15	472.50	52.50	12.2±0.7
	109.44	433.50	21.75	5.5±0.8
	112.87	405.75	23.25	6.5±0.8
	110.98	483.00	32.25	7.4±0.7
	110.93	477.75	48.00	11.1±0.7
Hihi	87.13	538.50	46.50	7.5±0.5
	89.51	519.00	36.75	6.3±0.5
	88.01	571.50	79.50	12.2±0.4
Tomtit	88.43	456.75	24.00	4.6±0.6
	91.86	531.00	80.25	13.9±0.5
	94.47	597.75	93.75	14.8±0.4
	107.38	621.75	51.75	8.9±0.5
LM-10	133.50	276.00	24.75	12.0±1.4
	137.73	291.75	33.00	15.6±1.4
	142.35	305.25	36.75	17.1±1.3
Type 2				
Kea	14.14	96.75	24.00	3.5±0.4
	13.52	95.25	24.00	3.4±0.4
	9.74	65.25	9.75	1.5±0.4
Kaka	17.19	213.00	32.25	2.6±0.2
	19.15	220.00	13.00	1.1±0.3
	17.51	235.50	12.75	0.9±0.2
Kakapo	37.13	141.75	7.50	2.0±0.8
Type 3				
Riroriro	100.43	303.75	5.25	1.7±1.0
Hoiho	96.00	415.50	12.00	2.8±0.7
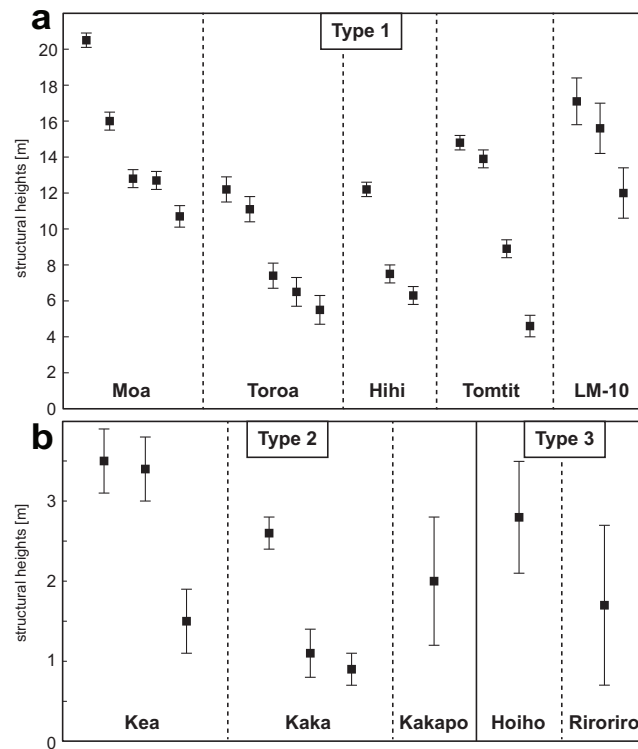
Figure 5.5: Structural heights and associated errors estimated from lengths of acoustic shadows in sidescan sonar images. **(A)** Type 1 sites, **(B)** the few type 2 and type 3 sites for which it was possible to determine structural heights. Note the different scale in (B).
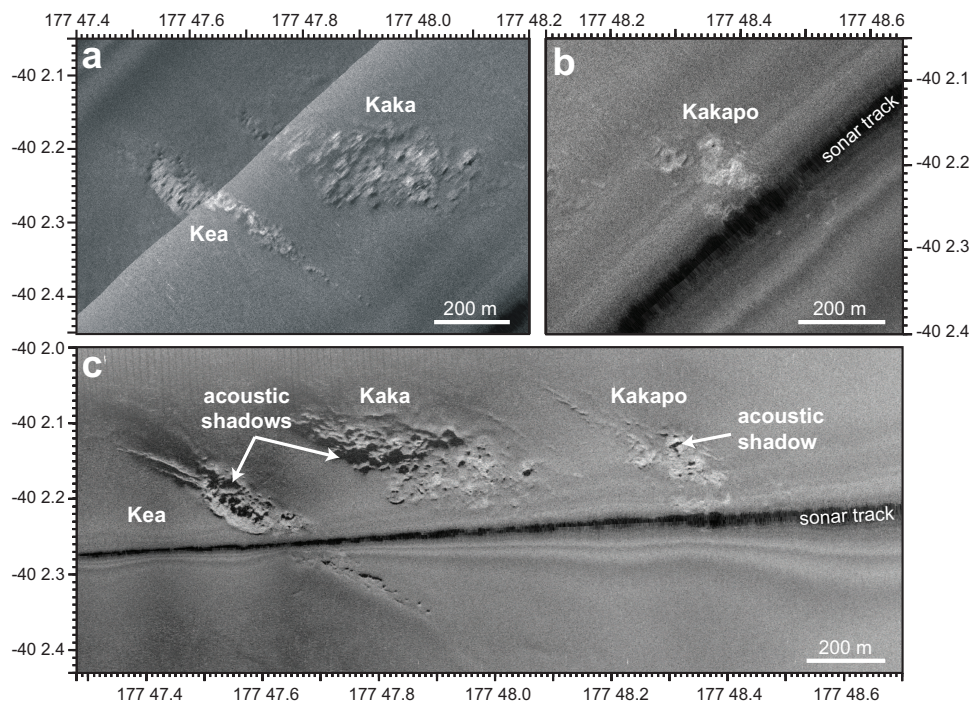

Figure 5.6: Sidescan sonar images of Kea, Kaka and Kakapo (Omakere Ridge) at different sonar altitudes. **(A)** Kea and Kaka imaged at ca. 100 m altitude. **(B)** Kakapo imaged at ca. 100 m altitude. **(C)** Kea, Kaka and Kakapo imaged at sonar altitudes increasing from 10 m near Kea to 40 m near Kakapo. Locations are shown in Fig. 5.4B.

Type 3 sites

Type 3 sites (Fig. 5.4C) consist of a cluster of moderate- to high-backscatter patches that appear randomly distributed over areas of 0.003 km^2 (Hoiho) to 0.088 km^2 (Riroriro) in size (Table 5.1). Diameters of individual patches range between 10 and 80 m. Some patches have small acoustic shadows. They either face away from the sonar, indicating positive relief, or they face the track, suggesting depressions. Structural heights were determined at Hoiho and Riroriro, amounting to 2.8±0.7 and 1.7±1.0 m respectively (Fig. 5.5, Table 5.2).

Type 4 sites

Type 4 sites (Fig. 5.4D) differ from types 1 to 3 in that their backscatter intensities are significantly lower, i.e., only slightly elevated compared to ordinary seabed backscatter. They cover continuous areas of 0.029 km^2 (Tawaki) to 0.066 km^2 (Takahe; Table 5.1). Relief-indicating acoustic shadows are absent.

5.5.2   Distribution of backscatter patterns

The four backscatter patterns are not evenly distributed throughout Omakere Ridge, Uruti Ridge, and Opouawe Bank (Fig. 5.7). In fact, none of the types is present in all three areas. Type 2 sites are the most numerous on both Omakere Ridge and Opouawe Bank (Fig. 5.7A,B), but they do not occur on Uruti Ridge where all three seep sites were associated with type 1 (Fig. 5.7C). Type 1 sites are also present on Omakere Ridge but not on Opouawe Bank, whereas seeps of types 3 and 4 are restricted to Opouawe Bank only. Clustering of seeps belonging to the same type is frequently observed – e.g. Kea, Kaka and Kakapo (type 2), and Takahe and Takapu (type 4).

5.5.3   Occurrence of water-column flares

Flares were observed in the water column of the raw sidescan sonar data for all four types of backscatter patterns, though not at every seep site. Toroa was the only type 1 site at which a flare was detected by sidescan sonar. It occurred at one of the smaller high-backscatter patches, about 400 m east of the 12 m high structure. At the type 2 sites Tui, North Tower and South Tower, flares were observed in raw sidescan data in 2007 (all three sites), and in 2011 (only North Tower and South Tower were mapped). Flares were also detected at Piwakawaka (type 2) in 2011. At Kakapo (type 2), a flare was seen in 2011 but it was not observed when the same location was passed again a few hours later. Two flares were observed in the 2007 sidescan data at type 3 site Pukeko, as well as at type 4 site Takahe in both 2007 and 2011.

5.5.4   Shallow subbottom characteristics

Acoustic turbidity in the shallow subsurface is present at nearly all seep sites where the towfish passed across or within about 100 m of the surface expressions (Fig. 5.8). Lengths of turbidity sections range between a few tens of metres to several hundred metres, often exceeding the dimensions

of elevated backscatter patches in the sidescan data. Penetration of the chirp signal was 30–40 m on Opouawe Bank and Omakere Ridge. Although acoustic turbidity was sometimes observed within 5 m of the seabed – e.g. at Toroa, Kakapo and Takahe – it generally occurred at greater depths beneath a distinct sedimentary reflector (Fig. 5.8). This reflector was observed across most of the subbottom profiles on both Opouawe Bank and Omakere Ridge, occurring in sediment depths of 14–20 and 4–10 m, respectively. Near Pukeko and Riroriro on Opouawe Bank, truncated reflectors were observed. On Uruti Ridge, subbottom penetration was only a few metres and anomalies were not apparent.
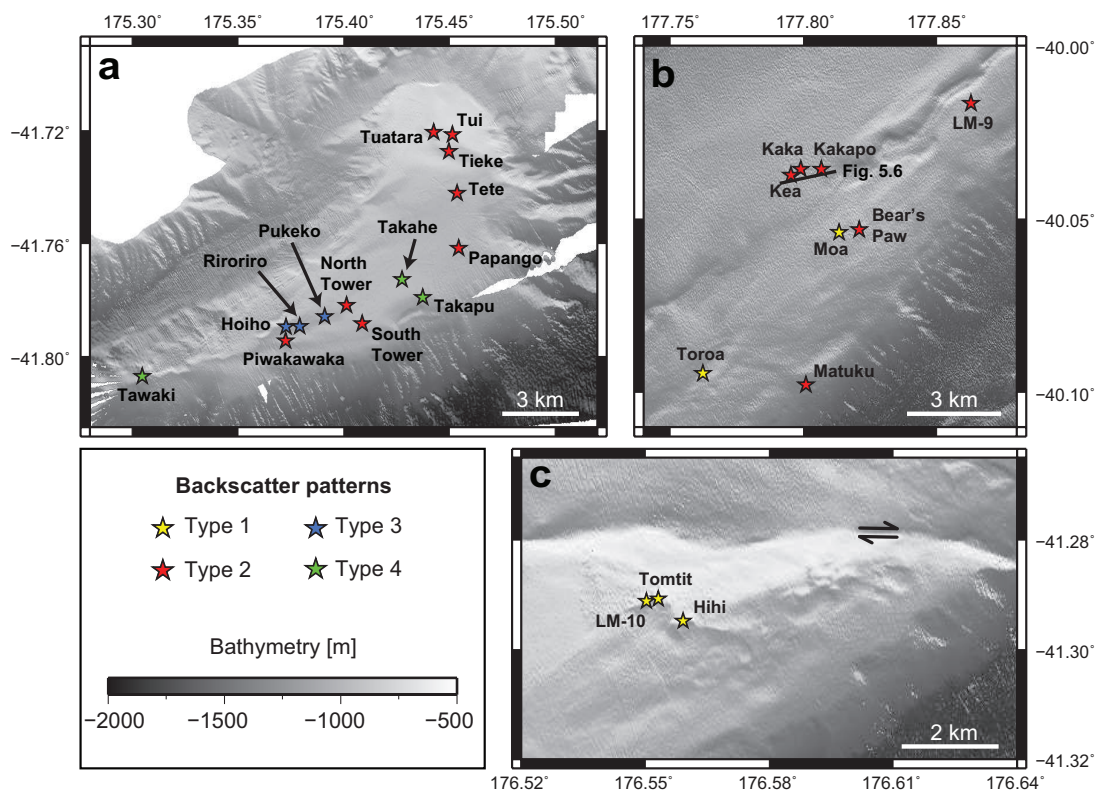

Figure 5.7: Distribution of the four types of sidescan backscatter patterns in the study areas. **(A)** Opouawe Bank, **(B)** Omakere Ridge, **(C)** Uruti Ridge. Bathymetry was acquired during SO191. Map locations are shown in Fig. 5.1 (Opouawe Bank) and Fig. 5.3 (Omakere Ridge, Uruti Ridge).

5.6   Discussion

5.6.1   Nature of the seeps

The studied sites exhibit four types of backscatter patterns that are interpreted to reflect different carbonate morphologies, including up to 20 m high structures (type 1), low-relief crusts (type 2), scattered blocks (type 3), and carbonate-free sites (type 4).

5.6.1.1   Type 1

Type 1 sites represent extensive areas of massive carbonates with structural heights exceeding 10 m. High-relief carbonates indicate a long duration of fluid flow (Luff et al., 2004), which is supported by the U-Th ages of about 12.4 and 4.3 kyr BP determined for two carbonate samples from up to 17 m high LM-10 on Uruti Ridge (Liebetrau et al., 2010). Carbonate structures are highest at eastern Moa on Omakere Ridge ($\sim$20.5 m). This site has been interpreted as inactive due to the absence of seep-related fauna and flares, and presence of sessile heterotrophic fauna (scleractinian and antipatharian corals; Jones et al., 2010; Bowden et al., 2013). Sampled reef substrate revealed a U-Th age of about 4.4 kyr BP (Liebetrau et al., 2010), suggesting that seepage ceased at least 4,400 years ago.
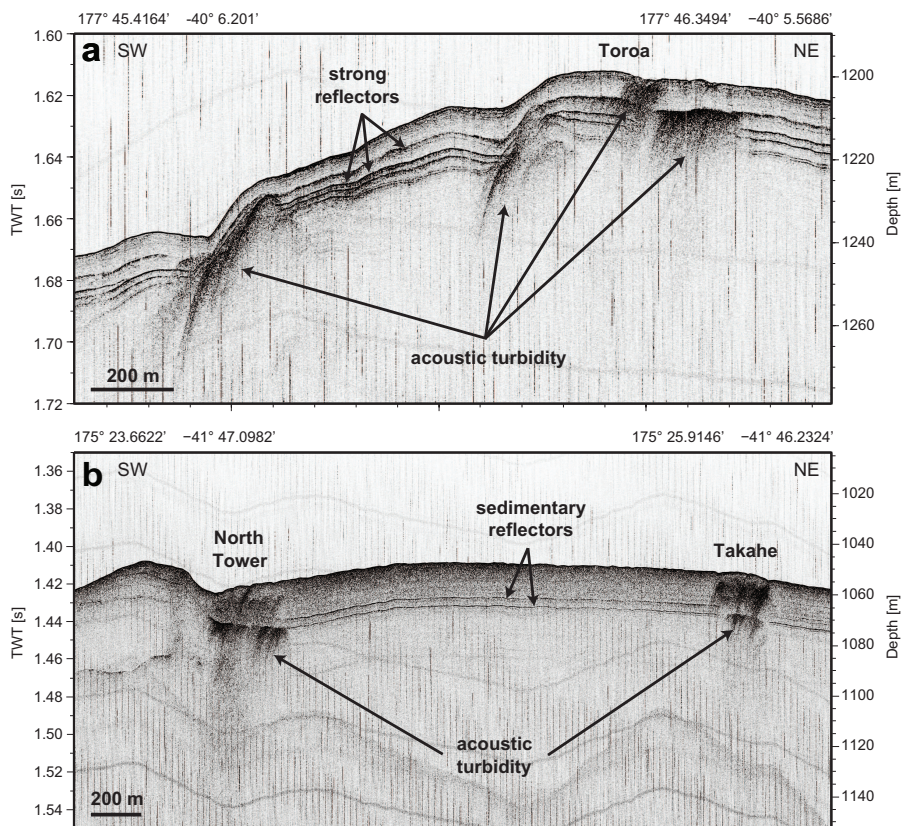

Figure 5.8: Subbottom profiler data showing acoustic turbidity. **(A)** Near Toroa seep (Omakere Ridge). **(B)** At North Tower and Takahe (Opouawe Bank). Profile locations are shown in Fig. 5.4.

Colonies and fragments of scleractinian and antipatharian corals were also found at LM-10 and Hihi on Uruti Ridge (Baco et al., 2010; Bowden et al., 2013), indicating that these sites have also become inactive. However, flares were observed at both sites (Lewis and Marshall, 1996; Baco et al., 2010; Greinert et al., 2010a), and live *Lamellibrachia* sp. tubeworms as well as scattered *Calyptogena* sp. shells were found close to the flare locations (Baco et al., 2010; Bowden et al., 2013). Consequently, methane seepage is still ongoing at LM-10 and Hihi, although parts of these sites must now be inactive in order to explain the presence of corals.

The activity status of the other two type 1 sites, Toroa (Omakere Ridge) and Tomtit (Uruti Ridge), remains unclear as there are no video observations. Due to the close proximity to LM-10 and Hihi, Tomtit may have a similar history as these sites, with at least part of the seep having become inactive. At Toroa, active seepage is indicated by the presence of acoustic turbidity in subbottom profiler data and a flare in sidescan data. However, both features were observed ~400 m east of the 12 m high carbonate mound, which therefore cannot exclude the possibility that the high-relief part of the site is now inactive and has been settled by corals. Video data are required to test this hypothesis.

Based on the above observations, the type 1 sites are interpreted as being at least partly inactive seeps with massive carbonate precipitates. In terms of their fauna, they correspond to the "Moa extreme" of Bowden et al. (2013), which is characterised by cold-water corals and absence of seep fauna.

5.6.1.2 Type 2

Type 2 sites are interpreted as low-relief carbonate crusts with structural heights of less than 4 m. The presence of authigenic carbonates suggests a long history of fluid flow, which is supported by carbonate samples from North Tower (Opouawe Bank) and Bear's Paw (Omakere Ridge) with maximum U-Th ages of ~4.95 and ~2.36 kyr BP, respectively (Liebetrau et al., 2010). Recent to ongoing activity of the seeps is suggested by (1) the presence of gas-indicating acoustic turbidity observed in subbottom profiler data (also Jones et al., 2010; Klaucke et al., 2010), (2) hydroacoustic flares (also Greinert et al., 2010a; Klaucke et al., 2010), and (3) elevated methane concentrations in the water column (Faure et al., 2010; Krabbenhoeft et al., 2010). Sometimes all three indications were observed at the same seep site – for example, at North Tower and South Tower.

In addition, ongoing seep activity is indicated by the abundant chemoautotrophic fauna observed at all type 2 sites of which video data exist. All sites featured *Lamellibrachia* sp. tubeworms and live *Calyptogena* sp. clams or clam shells (Baco et al., 2010; Greinert et al., 2010a; Jones et al., 2010; Bowden et al., 2013). Other benthic fauna found at type 2 sites included *Stelletta* sp. sponges, which were restricted to Omakere Ridge, and bathymodiolin mussels, lithodid crabs, pagurid crabs, gastropod molluscs, echinoids and ampharetid polychaete worms (Baco et al., 2010; Greinert et al., 2010a; Jones et al., 2010; Bowden et al., 2013). The high abundance of seep-associated fauna suggests that the type 2 sites correspond to the "Southwest Moa extreme" of Bowden et al. (2013), which is characterised by the highest density of seep-associated fauna, as well as carbonates.

5.6.1.3 Type 3

Patchy backscatter at the type 3 sites (Pukeko, Riroriro and Hoiho) suggests scattered carbonate blocks with heights of up to a few metres. Alternatively, the sites could represent partially buried carbonate structures of which only the highest tips protrude out of the sediment. Buried seep facies should produce strong reflections in subbottom profiler records, as observed offshore Nicaragua (Buerk et al., 2010) and Costa Rica (Klaucke et al., 2008). However, subbottom data from across

Pukeko and Riroriro do not show such reflections. Instead, free gas is indicated by acoustic turbidity (also Klaucke et al., 2010). In addition, truncated reflections near these sites indicate erosion – e.g. from bottom currents, which is also suggested by moats or depressions at some of the backscatter patches. Therefore, sediment burial is unlikely and the type 3 sites are interpreted as clusters of carbonate blocks.

Ongoing seep activity of the type 3 sites is indicated by hydroacoustic flares observed at Pukeko (Klaucke et al., 2010) and Riroriro (Greinert et al., 2010a). As video transects were not conducted at any of the three sites, it is not known what benthic fauna may be present at the type 3 sites. However, due to the presence of carbonates and active methane seepage of at least two of the three sites, it is suggested that the faunal characteristics of the type 3 sites resemble those of the type 2 sites.

5.6.1.4   Type 4

The type 4 sites Takahe, Takapu and Tawaki are characterised by only slightly elevated backscatter, which Klaucke et al. (2010) attributed to the absence of carbonates and presence of gas bubbles or even gas hydrate in the shallow subsurface. Gas hydrate veins were found in cores at Takahe in sediment depths of 2.2–2.7 m (Schwalenberg et al., 2010; Bialas, 2011). However, these depths are beyond the penetration of the DTS-1 system. In order to influence the sidescan backscatter signal, gas accumulations would need to be present within the upper 1 m of sediment.

Multiple hydroacoustic flares indicate active seepage at Takahe (Greinert et al., 2010a; Klaucke et al., 2010), and a flare was also observed in Parasound data from Takapu (S. Koch, pers. comm.). Activity is further indicated by live seep fauna at Takahe. The site is characterised by ampharetid patches of up to 2 m^2 in size, white bacterial mats as large as 1 m^2, and occasional patches of *Calyptogena* sp. shells, summarised by Bowden et al. (2013) as the "Takahe extreme" and further characterised by an absence of carbonate. Due to the lack of carbonate at the surface coupled with the presence of activity-indicating fauna, Greinert et al. (2010a) interpreted Takahe as a fairly young seep.

Video observations are not available for Takapu and Tawaki and it is therefore not known whether these sites host similar fauna. However, as their backscatter signatures are similar to that of carbonate-free Takahe and as active seepage occurs at Takapu, it is proposed that Takapu and Tawaki also represent active, carbonate-free seeps.

5.6.2   Sidescan sonar imagery as proxy for faunal habitats

The four types of backscatter patterns can be correlated with the three extreme states of faunal communities described by Bowden et al. (2013): the carbonate-free type 4 sites correspond to the "Takahe extreme", type 2 and possibly also type 3 sites represent the "Southwest Moa extreme" characterised by abundant seep fauna and low-relief carbonates, and at least parts of the type 1 sites are inactive and have become coral reefs of the "Moa extreme".

The four types can be further correlated with the five hypothetical successional stages of cold seeps on the Hikurangi Margin that Bowden et al. (2013) proposed based on their seabed observations. These are (1) colonisation by aerobic microbial communities, ca. 1–10 years after the onset of localised methane flux; (2) colonisation by ampharetid polychaetes (ca. 1–100 years); (3) colonisation by clams (> 50 years); (4) precipitation of carbonates, which enables colonisation by lamellibrachid tubeworms (several 100 years); and (5) colonisation by non-chemosynthetic fauna after sealing of the seep due to continued carbonate build-up (several 1,000 years).

The type 4 sites are interpreted as seeps at stage 2–3, due to the presence of ampharetid polychaete worms (stage 2) but also shells of *Calyptogena* sp. clams (stage 3) at Takahe. Based on the estimates of duration since the onset of fluid flow given by Bowden et al. (2013), it is inferred that, in a few hundred years, carbonate precipitation will commence at these sites. At the type 2 sites, authigenic carbonates and abundant seep fauna, including *Lamellibrachia* sp. tubeworms and bathymodiolin mussels, indicate succession stage 4. Stage 4 is also assumed for the type 3 sites due to the presence of low-relief carbonate blocks. The type 1 sites represent stage 5 where the colonisation by sessile heterotrophic fauna indicates ceased seepage, although some sites such as LM-10 and Hihi may still have parts characterised by active seepage.

The good correlation between types of backscatter patterns and differences in benthic fauna allows sidescan sonar to be used as a convenient proxy for seep habitats. Although the backscatter does not image biological communities as such, it distinguishes between different seep substrates (e.g. carbonate vs. no carbonate) commonly colonised by distinct faunal communities. Sidescan sonar data thus facilitate the targeting of sites for subsequent biological investigations.

5.6.3 Controls on carbonate precipitation

Carbonate precipitation is required over a long time span in order to build up carbonate structures of several metres height. Evidence is given by numerical modelling for Hydrate Ridge on the Cascadia Margin (Luff and Wallmann, 2003; Luff et al., 2004). Luff and Wallmann (2003) proposed a carbonate precipitation rate of 0.5 cm per 100 years, and Luff et al. (2004) calculated rates of 0.32–0.64 cm per 100 years.

On the Hikurangi Margin, carbonate precipitation has occurred since at least 12.4 kyr BP (Liebetrau et al., 2010). Combined with maximum structural heights of about 17 m at this site, this age suggests a carbonate precipitation rate of about 13.5 cm per 100 years, i.e., 27 times higher than at Hydrate Ridge. However, this rate should be treated with caution as carbonate sampling in the study area was strongly biased and, hence, the 12,400 years old sample does not necessarily represent the oldest seep carbonate on the Hikurangi Margin. Carbonates older than 12.4 kyr would lead to a lower calculated rate of carbonate precipitation.

Although rates of carbonate precipitation are affected by a number of factors, including methane and calcium concentrations of fluids, sedimentation, and bioturbation, the most important factor is the rate of upward fluid flow (Luff and Wallmann, 2003; Luff et al., 2004; Bayon et al., 2009; Karaca et al., 2010). According to numerical modelling, carbonate precipitation is restricted to

fluid flow velocities of 3–60 cm yr^{-1} (Luff et al., 2004; Karaca et al., 2010). Rates of upward fluid flow at the Hikurangi Margin can only be constrained by observations of different carbonate morphologies. The absence of carbonates at the type 4 sites could be explained by either too low or too high flow rates. However, fluid flow rates at the other three types would all have to lie in this relatively narrow range of about 3–60 cm yr^{-1} in order to ensure carbonate precipitation. This makes it unlikely that carbonate morphologies of types 2–4 are related to strong differences in fluid flow rates.

Fluid flow rates have therefore most likely been similar at all seeps. The differences in carbonate heights could then relate to different times of onset of carbonate precipitation, which does not occur immediately after the initiation of seepage but requires several hundreds of years of fluid flow to the seabed (e.g. Bowden et al., 2013). The high-relief type 1 sites could thus represent seeps with long-term carbonate precipitation, whereas seeps of the other types could be younger, with the carbonate-free type 4 sites the youngest of all.

Different ages of the Hikurangi Margin seeps have been indicated by the U-Th ages of carbonates (Liebetrau et al., 2010), and they appear to correlate with structural heights. However, carbonate sampling was strongly biased and the small data base of only 15 ages from four sites does not allow an extrapolation to the entire Hikurangi Margin. Many more carbonate samples, ideally from all seep sites, would be required to test if the four types could be related to variations in the onset of carbonate precipitation.

If the four types are related to variations in the onset of carbonate precipitation, then the absence of intermediates between the types indicates that precipitation on the Hikurangi Margin is episodic. Alternating phases of intensified carbonate precipitation and relative quiescence have already been suggested by Liebetrau et al. (2010) based on distinct U-Th ages representing times of increased precipitation. If carbonate precipitation was episodic rather than continuous, the seep surface expressions would not develop continuously but grow predominantly during the high-precipitation phases. As carbonate morphologies grow, they may eventually reach a transition stage – e.g. individual blocks of type 3 sites beginning to merge into connected type 2 sites. The absence of such intermediates is not a data acquisition bias, as all three ridges (Opouawe Bank, Omakere Ridge and Uruti Ridge) were mapped completely by sidescan sonar.

Episodic carbonate precipitation, however, does not imply episodic fluid seepage. Episodic carbonate precipitation is induced by changes in fluid flow, with carbonate precipitation being inhibited during times when fluid flow rates are either too high or too low to allow the formation of carbonate crusts. Consequently, seepage may have been continuous since the first establishment of the seeps at the surface, while carbonate precipitation was not.

5.6.4   Changes in fluid flow rate

5.6.4.1   External factors

External factors causing variations in fluid flow that affect carbonate precipitation rates include sea level (Teichert et al., 2003; Kiel, 2009), sedimentation (Plaza-Faverola et al., 2011), bottom-water

temperatures (Jung and Vogt, 2004; Westbrook et al., 2009; Mienert et al., 2010; Biastoch et al., 2011; Ferré et al., 2012) and tectonic activity (Sibson, 1994; Aharon et al., 1997; Brown et al., 2005; Mau et al., 2007).

A low sea level – e.g. during glacial stages – reduces the hydraulic head, i.e., the pressure of the overlying water column, promoting increased fluid flow towards the seabed, while sea-level highstands increase the hydraulic head and hence reduce the flow rate (Teichert et al., 2003). Rapid loading by, for instance, glacigenic sediments may lead to overpressure in the underlying sediments and promote focused fluid flow (Plaza-Faverola et al., 2011). U-Th ages from seep carbonates around the world correlate with periods of low sea level (Teichert et al., 2003; Kutterolf et al., 2008; Kiel, 2009), suggesting that low sea level enhances the rate of carbonate precipitation at cold seeps. On the Hikurangi Margin, U-Th ages from seep carbonates only span the past 12,400 years. Liebetrau et al. (2010) consider this time span too short to infer any relation between seep activity and sea level.

In another scenario, a rapid increase in water temperatures occurred in the Southern Ocean during the last deglaciation at 20–15 ka (Barrows et al., 2007). Increasing bottom-water temperatures affect gas hydrate stability and can cause hydrate dissociation (Jung and Vogt, 2004; Westbrook et al., 2009; Mienert et al., 2010; Biastoch et al., 2011; Ferré et al., 2012), leading to an increased supply of methane-rich fluids available for AOM and carbonate precipitation.

Moreover, the Hikurangi Margin is an active subduction margin characterised by thrust faulting, and several of the seep sites are associated with deep-reaching faults that are considered fluid migration pathways (Law et al., 2010; Netzeband et al., 2010; Krabbenhoeft et al., 2013; Plaza-Faverola et al., 2014). If fluid flow along these faults changes, the rate of carbonate precipitation may be affected as well. For example, fault activity may close off conduits or create new pathways for fluid migration (Aharon et al., 1997). In addition, seismic activity may lead to increased fluid release at seeps fed by active faults, which has been inferred from methane concentration measurements and long-term fluid flow-meter studies at seeps offshore Costa Rica (Brown et al., 2005; Mau et al., 2007).

5.6.4.2 Internal factors

Internal drivers of fluid flow dynamics include clogging of pathways due to carbonate precipitation (Aharon et al., 1997; Hovland, 2002), and the build-up of an internal reservoir (Leifer et al., 2004). Clogging of fluid pathways is caused by long-lasting or intense carbonate precipitation that over time cements migration pathways, thereby gradually reducing fluid escape until it is inhibited, leading to self-sealing of seeps (Hovland, 2002). Such self-sealing processes have been reported from an 800 m wide pockmark offshore Angola where Gay et al. (2006) suggest an activity shift from fossil carbonate domes in the centre to outward chemoherms. On the Hikurangi Margin, clogging and subsequent formation of new fluid pathways is likely taking place at, for example, Moa seep on Omakere Ridge. Here, Jones et al. (2010) proposed that self-sealing of the eastern, up to 20 m high carbonate structure possibly led to seep activity migrating westwards to lower-relief south-western Moa or, alternatively, to the neighbouring Bear's Paw site. Shifting activity was also

suggested by flares (active venting) that were located outside of major carbonate accumulations on Opouawe Bank (Klaucke et al., 2010).

On timescales of minutes to hours, fluid seepage appears transient at several seeps on the Hikurangi Margin (Faure et al., 2010; Klaucke et al., 2010; Krabbenhoeft et al., 2010). Leifer et al. (2004) relate transient seepage events on the Santa Barbara Channel, California, to fluid flow controlled by a capacitor, described as a reservoir that has to fill up first before conditions for fluid release are met. Klaucke et al. (2010) proposed that such a system could control fluid flow on Opouawe Bank, with gas hydrates acting as capacitors. Transient fluid flow on the Hikurangi Margin might also apply on larger timescales, with phases of quiescence during which fluid seepage as well as carbonate precipitation do not occur at any site. Such quiescent periods may be inferred from the time gaps between the U-Th ages of carbonate samples (Liebetrau et al., 2010), but these gaps could also be due to sampling bias.

5.7   Conclusions

Sidescan sonar data were used to study surface expressions of 25 cold seeps on the Hikurangi Margin. Each seep was associated with one of four types of backscatter patterns that represent variations in height and distribution of seep carbonates. Carbonate morphologies range from up to 20 m high structures (type 1), over low-relief crusts (type 2) and scattered blocks (type 3), to an absence of carbonates (type 4). The differences in carbonate morphologies correlate with variations in biological communities inhabiting the seep sites. It is therefore proposed that backscatter variations in sidescan sonar images can indirectly reflect differences in seep fauna, thus providing a basis for target studies of biological communities at cold seeps. Without further sampling (ideally from drill cores) and dating of seep carbonates on the Hikurangi Margin, it is not possible to determine whether carbonate precipitation episodicity is externally or internally controlled.

5.8   Acknowledgements

Chapter 6

Conclusions and outlook

6.1 Conclusions

This work has presented new insights into fluid flow systems in three different areas. All of the research questions posed in section 1.3 could be answered, although some results were unexpected, and new questions have arisen. In the following, answers to the original research questions will be summarised for each case study, and the implications on climate warming will be discussed.

6.1.1 Summary of the key results

Case study 1 - Knipovich Ridge

The Knipovich Ridge strongly influences heat flow on the western Svalbard margin. According to the results of the petroleum system modelling, heat flow has been high enough to allow at least one phase of petroleum production from source rocks north of the ridge. This phase occurred in the middle Miocene ($\sim$15-10 Ma) but appears to be unrelated to the thermal effects of the ridge. Rather, it is controlled by rapid sedimentation and associated deeper burial of organic-rich sediment sequences.

Another potential production phase may have occurred prior to this phase, during initial rifting in early Eocene. If Eocene source rocks, which are known to exist in the Arctic Basin, are also present on the Svalbard margin, they would have been exposed to the very high temperatures (possibly >300°C) at the Knipovich Ridge spreading centre. This would have enabled petroleum production from Eocene source rocks despite an absence of overburden. The Eocene phase is therefore directly influenced by the Knipovich Ridge, but its occurrence remains speculative, as the existence of Eocene rocks on the Svalbard margin is not confirmed.

The modelling results show that north of the Knipovich Ridge, the conditions necessary for thermogenic methane production have probably been met, which is supported by the findings of thermogenic gas on Vestnesa Ridge. Therefore, thermogenic methane is an important contributor to the extensive gas hydrate reservoir offshore Svalbard, in addition to microbial methane

that has been found on the upper continental slope. The presence of a third component – abiogenic methane derived from serpentinization – cannot be excluded but is more likely for the less-sediment-covered central and southern parts of the Knipovich Ridge.

Case study 2 - Giant Gjallar Vent

The new high-resolution seismic and Parasound data have shown that the up to 12 m high surface relief at the GGV is due to up-doming of the BPU and the overlying Naust Formation sediments. This up-doming is likely due to the build-up of overpressure as fluids are trapped beneath the BPU. At one location, the seal is penetrated and a narrow chimney structure extends up to the seafloor. However, there are presently no indications for active fluid release into the water column. Nevertheless, the GGV is active in terms of fluid migration. In addition, the up-doming of the uppermost sediments appears to be accompanied by faulting activity, as evidenced by several seafloor-piercing shallow faults that occur in the vicinity around the GGV.

The evolution of the GGV is characterised by reactivation, and the processes that lead to the present fluid migration and overpressure build-up are mostly shallow in origin. Fluids are likely sourced from dewatering of the Kai Formation in response to overpressure induced by the growing overburden. Although fluids could also be sourced from deeper levels, e.g. from the Brygge Formation, they likely constitute only a small proportion. Any deeper geological processes that could still be active at the GGV are thus overprinted by shallower processes. Consequently, the GGV is presently not suited as a study site to constrain the geological processes of the deeper Vøring Basin.

Case study 3 – Svalbard margin seeps

On the upper continental slope off Svalbard, bottom-water temperatures vary seasonally by about 1-2°C, which causes shifts in the depth of the BGHSZ. As a consequence, the intersection of the BGHSZ with the seafloor moves downslope or upslope, leading to periodic hydrate dissociation (downslope movement) and formation of gas hydrates (upslope movement). The observed gas seepage is thus caused by dissociating methane hydrates. However, this is no large-scale, irreversible hydrate dissociation in response to global warming effects over the past 30 years. Instead, hydrate dissociation appears to be part of a repeated and possibly self-regulating process. This is supported by the presence of seafloor carbonates with ages of at least ∼3 kyr BP (MASOX site) and ∼8 kyr BP (HyBIS site), which show that seepage offshore Svalbard must have been going on for a long time and thus cannot be exclusively related to decadal-scale ocean warming.

Case study 4 – Hikurangi Margin

The surface expressions of cold seeps on the Hikurangi Margin are characterised by four distinct types of backscatter patterns in sidescan sonar data. These patterns vary in the intensity, extent, and distribution of sonar backscatter. They are related to the amount and height of seabed carbonates, ranging from massive, 20-m-high structures (type 1) over up to 4-m-high crusts (type 2) and

scattered blocks (type 3) to carbonate-free sites (type 4). The types correlate with the distribution of typical seep fauna: communities living on sediment surfaces dominated at type 4 sites, seep fauna settling on hard substrate were found predominantly at type 2 and 3 sites, and non-seep epifauna were observed on type 1 carbonates of extinct seepage sites. The results show that sidescan sonar surveys can be used for relatively quick mapping of seabed areas to provide the basis for subsequent targeted sampling of benthic seep fauna.

6.1.2 Implications

The results show parallels between the seeps on the Hikurangi Margin and the upper slope of the Svalbard margin, which is surprising as fluid seepage in these areas is driven by very different processes – focused gas migration from beneath the GHSZ on the Hikurangi Margin and hydrate dissociation on the Svalbard margin. In both cases, seep sites are characterised by authigenic carbonates which vary in their morphology and distribution throughout the respective study area. U-Th ages of carbonates show that fluid venting has been going on for several 1000 years in both regions. Also, both systems lack indications for catastrophic methane release, rather, fluid release appears regulated and varies temporally over relatively short (minutes to months) time spans.

The area between Vestnesa Ridge and Knipovich Ridge is presently not very developed with respect to fluid venting, as indications for upward fluid migration and potential seepage sites are scarce. However, if conditions within the fluid system change, e.g. if fluid pressures beneath the BSR increase, more fluid pathways may form that transport methane from beneath the GHSZ towards the seabed. Due to the large extent of the gas reservoir, the resulting fluid venting may be long-lived and could eventually lead to the formation of surface expressions such as those on the Hikurangi Margin.

It is not possible to tell whether any of the methane released at the seabed enters the atmosphere. However, none of the hydroacoustic flares observed on the Hikurangi Margin and off Svalbard was sufficiently high to imply methane reaching the sea surface. On the Hikurangi Margin, the water depths of 800 m to >1000 m are probably too high to allow an escape of methane into the atmosphere before it is dissolved in the water column. Water depths on the Svalbard margin are significantly lower (<400 m), and hence methane release into the atmosphere cannot be excluded, but measurements of Fisher et al. (2011) show that atmospheric methane inputs are presently restricted to terrestrial rather than oceanic sources. Both fluid flow systems are therefore unlikely to contribute significantly to the present climate warming, as is the GGV, where seepage has not been observed so far and the water depth of >1300 m would probably prevent any seeping methane from reaching the atmosphere.

Nevertheless, because gas hydrates are highly sensitive to temperature changes, hydrate dissociation must have played a role in past climate warming events, e.g. during the PETM. This applies especially to substantial gas hydrate reservoirs such as found on the Svalbard margin. However, as the actual distribution of gas hydrates appears to be considerably less than that inferred from global hydrate models, this role may be smaller than previously assumed.

In addition to gas hydrate dissociation, hydrothermal vent systems such as the GGV certainly also contributed to climate warming events. The presently available data do not allow the estimation of the amount and duration of methane release from the GGV at its initial formation around the Paleocene-Eocene transition. However, the fact that there are more than 700 similar systems on the Norwegian margin alone implies that the release from this region must have been massive and thus likely influenced climate, also on a global scale.

At present, it is impossible to determine whether hydrate dissociation and hydrothermal vent systems represent the only contributors to warming events such as the PETM. Consequently, other potential contributors such as bolide impacts and thawing of permafrost areas need to be taken into account in the assessment of the causes of global climate warming.

6.2   Outlook

This work has contributed to an improved understanding of the studied fluid flow systems. However, there are still aspects that are not yet fully understood, and new questions have arisen during the course of this work. The following outlook presents recommendations for future surveys in each of the study areas. In addition, directions for future research on the PETM and other climate warming events are suggested.

Svalbard margin

For the Svalbard margin, drilling operations using the seafloor drill rig MeBo had originally been planned by MARUM (Bremen) for the summer of 2014, but had to be postponed due to technical problems with the vessel. The operations should hopefully take place within the next few years and will allow to asses (1) if gas hydrates exist – and dissociate – on the upper slope where they have been predicted to occur but a BSR has not been observed, (2) how much hydrate is present in the pore space and if this agrees with hydrate concentrations estimated from seismic velocity modelling (e.g. Vanneste et al., 2005a; Westbrook et al., 2008a), and (3) what are the hydrate compositions and gas origin(s).

Determination of the origin of the hydrate gas is of interest especially for the area between Vestnesa Ridge and Knipovich Ridge. Findings of thermogenic gas hydrates would strongly support the results of the petroleum system modelling and corroborate that hydrates in this area are of a similar composition as those on Vestnesa Ridge. In addition, hydrate samples from areas close to the rift axis would help to clarify whether serpentinization processes contribute to methane production besides thermogenic and microbial processes.

Another target for future studies on the Svalbard margin would be the classification of seabed characteristics at the intersection with the BGHSZ. The submersible dives conducted during cruise MSM21/4 showed that seabed characteristics, especially in terms of seabed carbonates, differed notably between the studied seep sites MASOX, HyBIS, and Polarstern. Such differences could be mapped on a larger scale using deep-towed sidescan sonar systems or AUV-mounted sonars in

order to investigate the relation between seabed carbonate distribution and the underlying seep systems. The results would contribute to the better understanding of the development of seepage along the Svalbard margin.

Giant Gjallar Vent

The GGV remains a mystery with respect to the degree of its present fluid venting activity. Future work should aim at acquiring more high-resolution seismic data – ideally P-Cable 3D seismic data – across the entire vent structure to image any further potential leakage pathways such as the discovered chimney structure. If there are several more leakage pathways across the vent structure, overpressure beneath the sealing sequence is likely bleeding off.

At the potential seepage sites, targeted water column imaging over several hours would reveal hydroacoustic flares indicating the release of gas-bearing fluids. Subsequently, sediment and gas bubble samples should be taken at these sites using, for example, a gravity corer or a ROV. Geochemical analyses of these samples would allow determination of the gas composition, which would indicate if the seeping fluids are of microbial origin, and thus produced by shallow processes. Alternatively, a thermogenic origin would indicate that deeper processes are involved. If authigenic carbonates are found on the seabed or within sediments, U-Th dating of recovered samples would reveal how long seepage has been going on. Prolonged venting – i.e., several 1000 years – accompanied by carbonate precipitation would lead to the build-up of chemoherm structures such as on the Hikurangi Margin.

Hikurangi Margin

For the cold seeps on the Hikurangi Margin, additional sampling of seep carbonates is recommended – ideally from every seep site, but at least from each of the three types characterised by carbonate occurrence. Subsequent U-Th age dating would show if the different types of surface expressions could be related to different ages of seep sites, which would reflect intermittent periods of increased carbonate precipitation on the Hikurangi Margin. Also, seafloor video observations of potential benthic communities at sites that have not been surveyed before would help to establish whether surface expressions in sidescan sonar data can indeed serve as a proxy for differences in seabed habitat.

The existing sidescan sonar data, along with the subbottom profiler data, should also be combined with other high-resolution subsurface data, e.g. sediment echosounder and P-Cable seismic data. The interpretation of seep sites using such a multidisciplinary dataset would improve the understanding of the link between surface and subsurface characteristics of fluid venting and migration processes.

Future PETM research

Future studies that aim at constraining the factors responsible for global climate warming events such as the PETM should focus on the following two questions:

1. How much methane had to be injected into the atmosphere to cause the δ^{13}C anomaly (-2 to -3‰) and the increase in bottom-water temperatures of at least 4°C during the PETM?

2. How can the potential factors have influenced each other with respect to methane release?

According to Dickens et al. (1995) and Dickens (1999), the injection of 1000-2000 Gt of methane into the atmosphere was sufficient to cause the δ^{13}C anomaly of the PETM, with the methane being released solely from dissociating hydrates. However, some of the global hydrate models arrive at much lower values for the amount of hydrates that can potentially dissociate (e.g. Burwicz et al., 2011; Wallmann et al., 2012; Piñero et al., 2013), and the actual amount of hydrates may be even lower, as suggested by the comparatively limited BSR occurrences. Climate models and global hydrate models that also take into account the BSR-inferred hydrate distributions should therefore be combined to constrain the minimum amount of methane required to cause the δ^{13}C anomaly, and to assess whether hydrate dissociation could in fact be the sole contributor to the PETM.

In addition, it should be estimated how potential contributors could have influenced each other in the causing of the PETM. For example, methane release from hydrothermal systems formed in response to magmatic intrusions could have led to initial climate warming and an increase in bottom-water temperatures, which could then have resulted in additional methane release from hydrate dissociation. The combined effect of these two processes could have caused a major climate warming event. Models should attempt to quantify how much methane would need to be released from hydrothermal systems in order to set off hydrate dissociation, and subsequently assess the implications on atmospheric δ^{13}C and the associated climate-warming potential.

Chapter 7

References

Aarnes, I., Svensen, H., Connolly, J.A.D., Podladchikov, Y.Y. (2010). How contact metamorphism can trigger global climate changes: Modeling gas generation around igneous sills in sedimentary basins. Geochimica et Cosmochimica Acta 74, 7179-7195.

Aharon, P. (1994). Geology and biology of modern and ancient submarine hydrocarbon seeps and vents: an introduction. Geo-Marine Letters 14, 69–73.

Aharon, P., Schwarcz, H.P., Roberts, H.H. (1997). Radiometric dating of submarine hydrocarbon seeps in the Gulf of Mexico. Geological Society of America Bulletin 109, 568–579.

Anderson, A.L., Bryant, W.R. (1990). Gassy sediment occurrence and properties: northern Gulf of Mexico. Geo-Marine Letters 10, 209-220.

Andresen, K.J., Clausen, O.R., Huuse, M. (2009). A giant (5.3×10^7 m^3) middle Miocene (c. 15 Ma) sediment mound (M1) above the Siri Canyon, Norwegian–Danish Basin: Origin and significance. Marine and Petroleum Geology 26, 1640-1655.

Andresen, K.J., Huuse, M., Schødt, N.H., Clausen, L.F., Seidler, L. (2011). Hydrocarbon plumbing systems of salt minibasins offshore Angola revealed by three-dimensional seismic analysis. AAPG Bulletin 95, 1039-1065.

Andresen, K.J. (2012). Fluid flow features in hydrocarbon plumbing systems: What do they tell us about the basin evolution? Marine Geology 332-334, 89-108.

Archer, D., Buffett, B. (2005). Time-dependent response of the global ocean clathrate reservoir to climatic and anthropogenic forcing. Geochemistry, Geophysics, Geosystems 6, Q03002.

Archer, D., Buffett, B., Brovkin, V. (2009). Ocean methane hydrates as a slow tipping point in the global carbon cycle. Proceedings of the National Academy of Sciences of the United States of America 106, 20,596-20,601.

Augustin, J.M., Suave, R., Lurton, X., Voisset, M., Dugelay, S., Satra, C. (1996). Contribution of the multibeam acoustic imagery to the exploration of the sea-bottom. Marine Geophysical Researches 18, 459–486.

Baco, A.R., Rowden, A.A., Levin, L.A., Smith, C.R., Bowden, D.A. (2010). Initial characterization of cold seep faunal communities on the New Zealand Hikurangi margin. Marine Geology 272, 251–259.

Barnes, P.M., Mercier de Lépinay, B. (1997). Rates and mechanics of rapid frontal accretion along the very obliquely convergent southern Hikurangi margin, New Zealand. Journal of Geophysical Research 102, 24,931–24,952.

Barnes, P.M., Mercier de Lépinay, B., Collot, J.-Y., Delteil, J., Audru, J.-C. (1998). Strain partitioning in the transition area between oblique subduction and continental collision, Hikurangi margin, New Zealand. Tectonics 17, 534–557.

Barnes, P.M., Lamarche, G., Bialas, J., Henrys, S., Pecher, I., Netzeband, G.L., Greinert, J., Mountjoy, J.J., Pedley, K., Crutchley, G. (2010). Tectonic and geological framework for gas hydrates and cold seeps on the Hikurangi subduction margin, New Zealand. Marine Geology 272, 26–48.

Barnes, R.O., Goldberg, E.D. (1976). Methane production and consumption in anoxic marine sediments. Geology 4, 297-300.

Barrows, T.T., Juggins, S., De Deckker, P., Calvo, E., Pelejero, C. (2007). Long-term sea surface temperature and climate change in the Australian-New Zealand region. Paleoceanography 22, PA2215.

Barry, J.P., Greene, H.G., Orange, D.L., Baxter, C.H., Robison, B.H., Kochevar, R.E., Nybakken, J.W., Reed, D.L., McHugh, C.M. (1996). Biologic and geologic characteristics of cold seeps in Monterey Bay, California. Deep Sea Research I 43, 1739–1762.

Bayon, G., Henderson, G.M., Bohn, M. (2009). U-Th stratigraphy of a cold seep carbonate crust. Chemical Geology 260, 47–56.

Berndt, C., Planke, S., Alvestad, E., Tsikalas, F., Rasmussen, T. (2001). Seismic volcanostratigraphy of the Norwegian Margin: constraints on tectonomagmatic break-up processes. Journal of the Geological Society 158, 413-426.

Berndt, C., Bünz, S., Mienert, J. (2003). Polygonal fault systems on the mid-Norwegian margin: a long-term source for fluid flow. Geological Society, London, Special Publications 216, 283-290.

Berndt, C., Bünz, S., Clayton, T., Mienert, J., Saunders, M. (2004). Seismic character of bottom simulating reflectors: examples from the mid-Norwegian margin. Marine and Petroleum Geology 21, 723-733.

Berndt, C. (2005). Focused fluid flow in passive continental margins. Philosophical Transactions of the Royal Society A 363, 2855-2871.

Berndt, C., Dumke, I., Feseker, T., Graves, C., Franek, P., Hissmann, K., Hühnerbach, V., Krastel, S., Lieser, K., Niemann, H., Steinle, L., Treude, T. (2014a). Fluid dynamics and slope stability offshore W-Spitsbergen: effect of bottom water warming on gas hydrates and slope stability. Cruise No. MSM21/4, August 12 – September 11, 2012, Reykjavik (Iceland) – Emden (Germany), MARIA S. MERIAN-Berichte, MSM21/4, DFG-Senatskommission für Ozeanographie, 96 pp.

Berndt, C., Feseker, T., Treude, T., Krastel, S., Liebetrau, V., Niemann, H., Bertics, V.J., Dumke, I., Dünn-bier, K., Ferré, B., Graves, C., Gross, F., Hissmann, K., Hühnerbach, V., Krause, S., Lieser, K., Schauer, J., Steinle, L. (2014b). Temporal constraints on hydrate-controlled methane seepage off Svalbard. Science 343, 284-287.

Bialas, J., Greinert, J., Linke, P., Pfannkuche, O. (Eds.) (2007). FS Sonne Fahrtbericht / Cruise Report SO 191 New Vents. IFM-GEOMAR, Leibniz-Institut für Meereswissenschaften, Kiel, Germany.

Bialas, J. (Ed.) (2011). FS SONNE Fahrtbericht / Cruise Report SO-214 NEMESYS. IFM-GEOMAR, Leibniz-Institut für Meereswissenschaften, Kiel, Germany.

Biastoch, A., Treude, T., Rüpke, L.H., Riebesell, U., Roth, C., Burwicz, E.B., Park, W., Latif, M., Böning, C.W., Madec, G., Wallmann, K. (2011). Rising Arctic Ocean temperatures cause gas hydrate destabilization and ocean acidification. Geophysical Research Letters 38, L08602.

Blondel, P. (2009). The handbook of sidescan sonar. Springer, Berlin.

Blystad, P., Brekke, H., Færseth, R.B., Larsen, B.T., Skogseid, J., Tørudbakken, B. (1995). Structural elements of the Norwegian continental shelf. Part II: The Norwegian Sea Region. Norwegian Petroleum Directorate Bulletin 8.

Boetius, A., Ravenschlag, K., Schubert, C.J., Rickert, D., Widdel, F., Gieseke, A., Amann, R., Jørgensen, B.B., Witte, U., Pfannkuche, O. (2000). A marine microbial consortium apparently mediating anaerobic oxidation of methane. Nature 407, 623–626.

Bokuniewicz, H.J. (1992). Analytical descriptions of subaqueous groundwater seepage. Estuaries 15, 458-464.

Bouriak, S., Vanneste, M., Saoutkine, A. (2000). Inferred gas hydrates and clay diapirs near the Storegga Slide on the southern edge of the Vøring Plateau, offshore Norway. Marine Geology 163, 125-148.

Bowden, D.A., Rowden, A.A., Thurber, A.R., Baco, A.R., Levin, L.A., Smith, C.R. (2013). Cold seep epifaunal communities on the Hikurangi Margin, New Zealand: composition, succession, and vulnerability to human activities. PLoS ONE 8, e76869.

Brinkhuis, H., Schouten, S., Collinson, M.E., Sluijs, A., Sinninghe Damsté, J.S., Dickens, G.R., Huber, M., Cronin, T.M., Onodera, J., Takahashi, K., Bujak, J.P., Stein, R., van der Burgh, J., Eldrett, J.S., Harding, I.C., Lotter, A.F., Sangiorgi, F., van Konijnenburg-van Cittert, H., de Leeuw, J.W., Matthiesen, J., Backman, J., Moran, K., the Expedition 302 Scientists (2006). Episodic fresh surface waters in the Eocene Arctic Ocean. Nature 441, 606-609.

Brooks, J.M., Cox, B.H., Brvant, W.R., Kennicutt, M.C. II, Mann, R.G., McDonald, T.J. (1986). Association of gas hydrates and oil seepage in the Gulf of Mexico. Organic Geochemistry 10, 221-234.

Brothers, D. Ruppel, C., Kluesner, J.W., ten Brink, U.S., Chaytor, J.D., Hill, J.C., Andrews, B.D., Flores, C. (2013). Seabed fluid expulsion along the upper slope and outer shelf of the U.S. Atlantic continental margin. Geophysical Research Letters 41, 96-101.

Brown, K., Westbrook, G.K. (1988). Mud diapirism and subcretion in the Barbados Ridge Accretionary Complex: The role of fluids in accretionary processes. Tectonics 7, 613-640.

Brown, K.M., Tryon, M.D., DeShon, H.R., Dorman, L.M., Schwartz, S.Y. (2005). Correlated transient fluid pulsing and seismic tremor in the Costa Rica subduction zone. Earth and Planetary Science Letters 238, 189–203.

Buerk, D., Klaucke, I., Sahling, H., Weinrebe, W. (2010). Morpho-acoustic variability of cold seeps on the continental slope offshore Nicaragua: result of fluid flow interaction with sedimentary processes. Marine Geology 275, 53–65.

Buffett C., Archer, D. (2004). Global inventory of methane clathrate: sensitivity to changes in the deep ocean. Earth and Planetary Science Letters 227, 185-199.

Bünz, S., Mienert, J., Berndt, C. (2003). Geological controls on the Storegga gas-hydrate system of the mid-Norwegian continental margin. Earth and Planetary Science Letters 209, 291-307.

Bünz, S., Mienert, J. (2004). Acoustic imaging of gas hydrate and free gas at the Storegga Slide. Journal of Geophysical Research: Solid Earth 109, B04102.

Bünz, S., Mienert, J., Vanneste, M., Andreassen, K. (2005). Gas hydrates at the Storegga Slide: Constraints from an analysis of multicomponent, wide-angle seismic data. Geophysics 70, B19-B34.

Bünz, S., Petersen, J., Hustoft, S., Mienert, J. (2008). Environmentally-sensitive gas hydrates on the W-Svalbard margin at the gateway to the Arctic Ocean. Proceedings of the 6th International Conference on Gas Hydrates, Vancouver, British Columbia, Canada.

Bünz, S., Polyanov, S., Vadakkepuliyambatta, S., Consolaro, C., Mienert, J. (2012). Active gas venting through hydrate-bearing sediments on the Vestnesa Ridge, offshore W-Svalbard. Marine Geology 332–334, 189-197.

Burwicz, E.B., Rüpke, L.H., Wallmann, K. (2011). Estimation of the global amount of submarine gas hydrates formed via microbial methane formation based on numerical reaction-transport modelling and a novel parameterization of Holocene sedimentation. Geochimica et Cosmochimica Acta 75, 4562-4576.

Carcione, J.M., Gei, D., Rossi, G., Madrussani, G. (2005). Estimation of gas-hydrate concentration and free-gas saturation at the Norwegian-Svalbard continental margin. Geophysical Prospecting 53, 803-810.

Cartwright, J. (1994a). Episodic basin-wide fluid expulsion from geopressured shale sequences in the North Sea basin. Geology 22, 447-450.

Cartwright, J. (1994b). Episodic basin-wide hydrofracturing of overpressured Early Cenozoic mudrock sequences in the North Sea Basin. Marine and Petroleum Geology 11, 587-607.

Cartwright, J., Huuse, M., Aplin, A. (2007). Seal bypass systems. AAPG Bulletin 91, 1141-1166.

Caston, V.N.D. (1976). Tertiary sediments of the Vøring Plateau, Norwegian Sea, recovered by Leg 38 of the Deep Sea Drilling Project. In: Talwani, M., Udintsev, G., White, S. M. (Eds.), Initial Reports DSDP 38, pp. 761-782.

Chabert, A., Minshull, T.A., Westbrook, G.K., Berndt, C., Thatcher, K.E., Sarkar, S. (2011). Characterization of a stratigraphically constrained gas hydrate system along the western continental margin of Svalbard from ocean bottom seismometer data. Journal of Geophysical Research 116, B12102.

Chand, S., Mienert, J., Andreassen, K., Knies, J., Plassen, L., Fotland, B. (2008). Gas hydrate stability zone modelling in areas of salt tectonics and pockmarks of the Barents Sea suggest an active hydrocarbon vent system. Marine and Petroleum Geology 25, 625-636.

Chand, S., Rise, L., Knies, J., Haflidason, H., Hjelstuen, B.O., Bøe, R. (2011). Stratigraphic development of the south Vøring margin (Mid-Norway) since early Cenozoic time and its influence on subsurface fluid flow. Marine and Petroleum Geology 28, 1350-1363.

Cheng, H., Edwards, R.L., Hoff, J., Gallup, C.D., Richards, D.A., Asmerom, Y. (2000). The half-lives of uranium-234 and thorium-230. Chemical Geology 169, 17–33.

Cicerone, R.J., Oremland, R.S. (1988). Biogeochemical aspects of atmospheric methane. Global Biogeochemical Cycles 2, 299–327.

Clayton, C. (1992). Source volumetrics of biogenic gas generation. In: Vially, R. (Ed.), Bacterial gas. Editions Technip, Paris, pp. 191-204.

Clayton, C.J., Hay, S.J. (1994). Gas migration mechanisms from accumulation to surface. Bulletin of the Geological Society of Denmark 41, 12-23.

Cline, J.D. (1969). Spectrophometric determination of hydrogen sulfide in natural waters. Limnology and Oceanography 14, 454-458.

Collot, J.-Y., Delteil, J., Lewis, K.B., Davy, B., Lamarche, G., Audru, J.-C., Barnes, P., Chanier, F., Chaumillon, E., Lallemand, S., Mercier de Lépinay, B., Orpin, A., Pelletier, B., Sosson, M., Toussaint, B., Uruski, C. (1996). From oblique subduction to intra-continental transpression: structures of the southern Kermadec-Hikurangi Margin from multibeam bathymetry, side-scan sonar and seismic reflection. Marine Geophysical Researches 18, 357–381.

Corfield, S.M., Wheeler, W., Karpuz, R., Wilson, M., Helland, R. (2004). Exploration 3D seismic over the Gjallar Ridge, mid-Norway: Visualization of structures on the Norwegian Volcanic Margin from Moho to seafloor. Geological Society, London, Memoirs 29, 177-186.

Cramer, B.S., Kent, D.V. (2005). Bolide summer: The Paleocene/Eocene thermal maximum as a response to an extraterrestrial trigger. Palaeogeography, Palaeoclimatology, Palaeoecology 224, 144-166.

Crane, K., Eldholm, O., Myhre, A.M., Sundvor, E. (1982). Thermal implications for the evolution of the Spitsbergen transform fault. Tectonophysics 89, 1-32.

Crane, K., Sundvor, E., Foucher, J.-P., Hobart, M., Myhre, A.M., LeDouaran, S. (1988). Thermal evolution of the western Svalbard margin. Marine Geophysical Researches 9, 165-194.

Crane, K., Sundvor, E., Buck, R., Martinez, F. (1991). Rifting in the northern Norwegian-Greenland Sea: Thermal tests of asymmetric spreading. Journal of Geophysical Research: Solid Earth 96, 14,529-14,550.

Crane, K., Doss, H., Vogt, P., Sundvor, E., Cherkashov, G., Poroshina, I., Joseph, D. (2001). The role of the Spitsbergen shear zone in determining morphology, segmentation and evolution of the Knipovich Ridge. Marine Geophysical Researches 22, 153-205.

Crutchley, G.J., Pecher, I.A., Gorman, A.R., Henrys, S.A., Greinert, J. (2010a). Seismic imaging of gas conduits beneath seafloor seep sites in a shallow marine gas hydrate province, Hikurangi Margin, New Zealand. Marine Geology 272, 114–126.

Crutchley, G.J., Geiger, S., Pecher, I.A., Gorman, A.R., Zhu, H., Henrys, S.A. (2010b). The potential influence of shallow gas and gas hydrates on sea floor erosion of Rock Garden, an uplifted ridge offshore of New Zealand. Geo-Marine Letters 30, 283–303.

Crutchley, G.J., Berndt, C., Geiger, S., Klaeschen, D., Papenberg, C., Klaucke, I., Hornbach, M.J., Bangs, N.L.B., Maier, C. (2013). Drivers of focused fluid flow and methane seepage at south Hydrate Ridge, offshore Oregon, USA. Geology 41, 551-554.

Dalland, A., Worsley, D., Ofstad, K. (1988). A lithostratigraphic scheme for the Mesozoic and Cenozoic succession offshore mid- and northern Norway. Norwegian Petroleum Directorate Bulletin 4.

Davies, R.J., Cartwright, J. (2002). A fossilized Opal A to Opal C/T transformation on the northeast Atlantic margin: support for a significantly elevated Palaeogeothermal gradient during the Neogene? Basin Research 14, 467-486.

Davies, R.J., Stewart, S.A. (2005). Emplacement of giant mud volcanoes in the South Caspian Basin: 3D seismic reflection imaging of their root zones. Journal of the Geological Society 162, 1-4.

Davies, R.J., Swarbrick, R.E., Evans, R.J., Huuse, M. (2007). Birth of a mud volcano: East Java, 29 May 2006. GSA Today 17, 4-9.

Deville, E., Battani, A., Griboulard, R., Guerlais, S., Herbin, J.P., Houzay, J.P., Muller, C., Prinzhofer, A. (2003). The origin and processes of mud volcanism: new insights from Trinidad. Geological Society, London, Special Publications 216, 475-490.

Deville, E., Guerlais, S.-H., Callec, Y., Griboulard, R., Huyghe, P., Lallemant, S., Mascle, A., Noble, M., Schmitz, J. (2006). Liquefied vs stratified sediment mobilization processes: Insight from the South of the Barbados accretionary prism. Tectonophysics 428, 33-47.

Deville, E., Guerlais, S.-H., Lallemant, S., Schneider, F. (2010). Fluid dynamics and subsurface sediment mobilization processes: an overview from Southeast Caribbean. Basin Research 22, 361-379.

Díaz-del-Río, V., Somoza, L., Martínez-Frias, J., Mata, M.P., Delgado, A., Hernandez-Molina, F.J., Lunar, R., Martín-Rubí, J.A., Maestro, A., Fernández-Puga, M.C., León, R., Llave, E., Medialdea, T., Vázquez, J.T. (2003). Vast fields of hydrocarbon-derived carbonate chimneys related to the accretionary wedge/olistostrome of the Gulf of Cádiz. Marine Geology 195, 177–200.

Dick, H.J.B., Lin, J., Schouten, H. (2003). An ultraslow-spreading class of ocean ridge. Nature 426, 405-412.

Dickens, G.R., Quinby-Hunt, M.S. (1994). Methane hydrate stability in seawater. Geophysical Research Letters, 21, 2115-2118.

Dickens, G.R., O'Neil, J.R., Rea, D.K., Owen, R.M. (1995). Dissociation of oceanic methane hydrate as a cause of the carbon isotope excursion at the end of the Paleocene. Paleoceanography 10, 965-971.

Dickens, G.R. (1999). The blast in the past. Nature 401, 752-755. Nature 426, 405-412.

Dickens, G.R. (2011). Down the Rabbit Hole: toward appropriate discussion of methane release from gas hydrate systems during the Paleocene-Eocene thermal maximum and other past hyperthermal events. Climate of the Past 7, 831-846.

Dillon, W.P., Max, M.D. (2000). Oceanic gas hydrate. In: Max, M.D. (Ed.), Natural gas hydrate in oceanic and permafrost environments, Kluwer Academic Publishers, Netherlands, pp. 61-76.

Dimitrov, L.I. (2002). Mud volcanoes—the most important pathway for degassing deeply buried sediments. Earth-Science Reviews 59, 49-76.

Doré, A.G., Lundin, E.R., Jensen, L.N., Birkeland, Ø., Eliassen, P.E., Fichler, C. (1999). Principal tectonic events in the evolution of the northwest European Atlantic margin. Proceedings of the 5th Conference, Geological Society, London, pp. 41-61.

Dowdeswell, J. A., Ottesen, D., Rise, L. (2010). Rates of sediment delivery from the Fennoscandian Ice Sheet through an ice age. Geology 38, 3-6.

Dupré, S., Woodside, J., Klaucke, I., Mascle, J., Foucher, J.-P. (2010). Widespread active seepage activity on the Nile Deep Sea Fan (offshore Egypt) revealed by high-definition geophysical imagery. Marine Geology 275, 1–19.

Ebinger, C.J. (1989). Tectonic development of the western branch of the East African rift system. Geological Society of America Bulletin, 101, 885-903.

Ehlers, B.-M., Jokat, W. (2013). Paleo-bathymetry of the northern North Atlantic and consequences for the opening of the Fram Strait. Marine Geophysical Researches 34, 25-43.

Eidvin, T., Brekke, H., Riis, F., Renshaw, D.R. (1998). Cenozoic stratigraphy of the Norwegian Sea continental shelf, 64°N-68°N. Norsk Geologisk Tidsskrift 78, 125-151.

Eidvin, T., Jansen, E., Rundberg, Y., Brekke, H., Grogan, P. (2000). The upper Cainozoic of the Norwegian continental shelf correlated with the deep sea record of the Norwegian Sea and the North Atlantic. Marine and Petroleum Geology 17, 579-600.

Eidvin, T., Bugge, T., Smelror, M. (2007). The Molo Formation, deposited by coastal progradation on the inner Mid-Norwegian continental shelf, coeval with the Kai Formation to the west and the Utsira Formation in the North Sea. Norwegian Journal of Geology 87, 75-142.

Eiken, O., Hinz, K. (1993). Contourites in the Fram Strait. Sedimentary Geology 82, 15-32.

Eldholm, O., Sundvor, E., Myhre, A.M., Faleide, J.I. (1984). Cenozoic evolution of the continental margin off Norway and western Svalbard. In: Spencer, A.M. (Ed.), Petroleum Geology of the North European Margin. Springer, Netherlands, pp. 3-18.

Eldholm, O., Thiede, J., Taylor, E. (1989). Evolution of the Vøring Volcanic Margin. In: Eldholm, O., Thiede, J., Taylor, E. (Eds.), Proceedings of the Ocean Drilling Program, Scientific Results 104, pp. 1033-1065.

Engen, Ø., Faleide, J.I., Dyreng, T.K. (2008). Opening of the Fram Strait gateway: A review of plate tectonic constraints. Tectonophysics 450, 51-69.

Expedition 302 Scientists (2006). Sites M0001-M0004. In: Backman, J., Moran, K., McInroy, D.B., Mayer, L.A., the Expedition 302 Scientists (Eds.), Proceedings of the Integrated Ocean Drilling Program 302, Edinburgh (Integrated Ocean Drilling Program Management International, Inc.).

Faleide, J.I., Solheim, A., Fiedler, A., Hjelstuen, B.O., Andersen, E.S., Vanneste, K. (1996). Late Cenozoic evolution of the western Barents Sea-Svalbard continental margin. Global and Planetary Change 12, 53-74.

Faleide, J.I., Tsikalas, F., Breivik, A.J., Mjelde, R., Ritzmann, O., Engen, Ø., Wilson, J., Eldholm, O. (2008). Structure and evolution of the continental margin off Norway and the Barents Sea. Episodes 31, 82-91.

Faure, K., Greinert, J., Schneider von Deimling, J., McGinnis, D.F., Kipfer, R., Linke, P. (2010). Methane seepage along the Hikurangi Margin of New Zealand: geochemical and physical data from the water column, sea surface and atmosphere. Marine Geology 272, 170–188.

Ferré, B., Mienert, J., Feseker, T. (2012). Ocean temperature variability for the past 60 years on the Norwegian-Svalbard margin influences gas hydrate stability on human time scales. Journal of Geophysical Research 117, C10017.

Fiebig, J., Woodland, A.B., D'Alessandro, W., Püttmann, W. (2009). Excess methane in continental hydrothermal emissions is abiogenic. Geology 37, 495-498.

Fietzke, J., Liebetrau, V., Eisenhauer, A., Dullo, W.-Ch. (2005). Determination of Uranium isotope ratios by multi-static MIC-ICP-MS: method and implementation for precise U- and Th-series isotope measurements. Journal of Analytical Atomic Spectrometry 20, 395–401.

Fisher, R.E., Sriskantharajah, S., Lowry, D., Lanoisellé, M., Fowler, C.M.R., James, R.H., Hermansen, O., Lund Myhre, C., Stohl, A., Greinert, J., Nisbet-Jones, P.B.R., Mienert, J., Nisbet, E.G. (2011). Arctic methane sources: Isotopic evidence for atmospheric inputs. Geophysical Research Letters 38, L21803.

Flemings, P.B., Liu, X., Winter, W.J. (2003). Critical pressure and multiphase flow in Blake Ridge gas hydrates. Geology 31, 1057-1060.

Forsberg, C.F., Locat, J. (2005). Mineralogical and microstructural development of the sediments on the Mid-Norwegian margin. Marine and Petroleum Geology 22, 109-122.

Foustoukos, D.I., Seyfried, W.E. Jr. (2004). Hydrocarbons in hydrothermal vent fluids: The role of chromium-bearing catalysts. Science 304, 1002-1005.

Ganguly, N., Spence, G.D., Chapman, N.R., Hyndman, R.D. (2000). Heat flow variations from bottom simulating reflectors on the Cascadia margin. Marine Geology 164, 53-68.

Gay, A., Lopez, M., Ondreas, H., Charlou, J.L., Sermondadaz, G., Cochonat, P. (2006). Seafloor facies related to upward methane flux within a Giant Pockmark of the Lower Congo Basin. Marine Geology 226, 81–95.

Gay, A., Berndt, C. (2007). Cessation/reactivation of polygonal faulting and effects on fluid flow in the Vøring Basin, Norwegian Margin. Journal of the Geological Society 164, 129-141.

Gay, A., Lopez, M., Berndt, C., Séranne, M. (2007). Geological controls on focused fluid flow associated with seafloor seeps in the Lower Congo Basin. Marine Geology 244, 68-92.

Gay, A., Mourgues, R., Berndt, C., Bureau, D., Planke, S., Laurent, D., Gautier, S., Lauer, C., Loggia, D. (2012). Anatomy of a fluid pipe in the Norway Basin: Initiation, propagation and 3D shape. Marine Geology 332–334, 75-88.

Geissler, W.H., Jokat, W., Brekke, H. (2011). The Yermak Plateau in the Arctic Ocean in the light of reflection seismic data-implication for its tectonic and sedimentary evolution. Geophysical Journal International 187, 1334-1362.

Geissler, W.H., Gebhardt, A.C., Schmidt-Aursch, M.C. (2014a). The Hinlopen/Yermak Megaslide (HYM) - Understanding an exceptional submarine landslide, its consequences and relation to the deep structure of the Sophia Basin (Sophia-HYM). Cruise No. MSM31, August 17 - September 18, 2013, Tromsø (Norway) - Bremen (Germany), MARIA S. MERIAN-Berichte, MSM31, DFG-Senatskommission für Ozeanographie, 70 pp.

Geissler, W.H., Pulm, P.V., Jokat, W., Gebhardt, A.C. (2014b). Indications for the occurrence of gas hydrates in the Fram Strait from heat flow and multichannel seismic reflection data. Journal of Geological Research 12, doi:10.1155/2014/582424.

Ginsburg, G., Guseynov, R.A., Dadashev, A.A., Ivanova, G.A., Kazantsev, S.A., Soloviev, V.A., Telepnev, E.V., Askeri-Nasirov, P.Y., Yesikov, A.A., Mal'tseva, V.I., Mashirov, Y.G., Shabayeva, I.Y. (1992). Gas hydrates of the southern Caspian. International Geology Review 34, 765-782.

Gorman, A.R., Holbrook, W.S., Hornbach, M.J., Hackwith, K.L., Lizarralde, D., Pecher, I. (2002). Migration of methane gas through the hydrate stability zone in a low-flux hydrate province. Geology 30, 327-330.

Gradstein, F.M., Ogg, J.G., Hilgen, F.J. (2012). On the Geologic Time Scale. Newsletters on Stratigraphy 45, 171-188.

Greinert, J., Artemov, Y., Egorov, V., De Batist, M., McGinnis, D. (2006). 1300-m-high rising bubbles from mud volcanoes at 2080 m in the Black Sea: Hydroacoustic characteristics and temporal variability. Earth and Planetary Science Letters 244, 1-15.

Greinert, J., Lewis, K.B., Bialas, J., Pecher, I.A., Rowden, A., Bowden, D.A., De Batist, M., Linke, P. (2010a). Methane seepage along the Hikurangi Margin, New Zealand: overview of studies in 2006 and 2007 and new evidence from visual, bathymetric and hydroacoustic investigations. Marine Geology 272, 6–25.

Greinert, J., Bialas, J., Lewis, K., Suess, E. (2010b). Methane seeps at the Hikurangi Margin, New Zealand. Marine Geology 272, 1–3.

Grevemeyer, I., Villinger, H. (2001). Gas hydrate stability and the assessment of heat flow through continental margins. Geophysical Journal International 145, 647-660.

Haacke, R.R., Westbrook, G.K., Hyndman, R.D. (2007). Gas hydrate, fluid flow and free gas: Formation of the bottom-simulating reflector. Earth and Planetary Science Letters 261, 407-420.

Han, M.W., Suess, E. (1989). Subduction-induced pore fluid venting and the formation of authigenic carbonates along the Cascadia continental margin: implications for the global Ca-cycle. Palaeogeography, Palaeoclimatology, Palaeoecology 71, 97-118.

Hansen, J.P.V., Cartwright, J.A., Huuse, M., Clausen, O.R. (2005). 3D seismic expression of fluid migration and mud remobilization on the Gjallar Ridge, offshore mid-Norway. Basin Research 17, 123-139.

Harvey, L.D.D., Huang, Z. (1995). Evaluation of the potential impact of methane clathrate destabilization on future global warming. Journal of Geophysical Research 100, 2905-2926.

Hempel, P., Mayer, L., Taylor, E., Bohrmann, G., Pittenger, A. (1989). The influence of biogenic silica on seismic lithostratigraphy at ODP sites 642 and 643, eastern Norwegian Sea. In: Eldholm, O., Thiede, J., Taylor, E. (Eds.), Proceedings of the Ocean Drilling Program, Scientific Results 104, pp. 941-951.

Henrich, R. (1989). Glacial/interglacial cycles in the Norwegian Sea: Sedimentology, paleoceanography, and evolution of Late Pliocene to Quarternary Northern Hemisphere climate. In: Eldholm, O., Thiede, J., Taylor, E. (Eds.), Proceedings of the Ocean Drilling Program, Scientific Results 104, pp. 189-232.

Henriksen, S., Vorren, T.O. (1996). Late Cenozoic sedimentation and uplift history on the mid-Norwegian continental shelf. Global and Planetary Change 12, 171-199.

Henry, P., Thomas, M., Clennell, M.B. (1999). Formation of natural gas hydrates in marine sediments 2. Thermodynamic calcuations of stability conditions in porous sediments. Journal of Geophysical Research 104, 23005-23022.

Hesselbo, S.P., Gröcke, D.R., Jenkyns, H.C., Bjerrum, C.J., Farrimond, P., Morgans Bell, H.S., Green, O.R. (2000). Massive dissociation of gas hydrate during a Jurassic oceanic anoxic event. Nature 406, 392-395.

Higgins, J.A., Schrag, D.P. (2006). Beyond methane: Towards a theory for the Paleocene-Eocene Thermal Maximum. Earth and Planetary Science Letters 245, 523-537.

Hill, T.M., Kennett, J.P., Spero, H.J. (2004). High-resolution records of methane hydrate dissociation: ODP Site 893, Santa Barbara Basin. Earth and Planetary Science Letters 223, 127-140.

Hjelstuen, B.O., Eldholm, O., Skogseid, J. (1997). Vøring Plateau diapir fields and their structural and depositional settings. Marine Geology 144, 33-57.

Hjelstuen, B.O., Eldholm, O., Skogseid, J. (1999a). Cenozoic evolution of the northern Vøring margin. Geological Society of America Bulletin 111, 1792-1807.

Hjelstuen, B.O., Eldholm, O., Faleide, J.I., Vogt, P.R. (1999b). Regional setting of Håkon Mosby Mud Volcano, SW Barents Sea margin. Geo-Marine Letters 19, 22-28.

Hjelstuen, B.O., Sejrup, H.P., Haflidason, H., Nygård, A., Berstad, I.M., Knorr, G. (2004a). Late Quaternary seismic stratigraphy and geological development of the south Vøring margin, Norwegian Sea. Quaternary Science Reviews 23, 1847-1865.

Hjelstuen, B.O., Sejrup, H.P., Haflidason, H., Berg, K., Bryn, P. (2004b). Neogene and Quaternary depositional environments on the Norwegian continental margin, 62°N–68°N. Marine Geology 213, 257-276.

Holbrook, W.S., Hoskins, H., Wood, W.T., Stephen, R.A., Lizarralde, D. (1996). Methane hydrate and free gas on the Blake Ridge from vertical seismic profiling. Science 273, 1840-1843.

Holbrook, W.S., Lizarralde, D., Pecher, I.A., Gorman, A.R., Hackwith, K.L., Hornbach, M., Saffer, D. (2002). Escape of methane gas through sediment waves in a large methane hydrate province. Geology 30, 467-470.

Holland, C.W., Weber, T.C., Etiope, G. (2006). Acoustic scattering from mud volcanoes and carbonate mounds. Journal of the Acoustical Society of America 120, 3553–3565.

Hornbach, M.J., Bangs, N.L., Berndt, C. (2012). Detecting hydrate and fluid flow from bottom simulating reflector depth anomalies. Geology 40, 227-230.

Hovland, M., Judd, A.G. (1988). Seabed pockmarks and seepages: Impact on geology, biology and the marine environment. Graham and Trotman, London.

Hovland, M., Nygaard, E., Thorbjørnsen, S. (1998). Piercement shale diapirism in the deep-water Vema Dome area, Vøring basin, offshore Norway. Marine and Petroleum Geology 15, 191-201.

Hovland, M. (2002). On the self-sealing nature of marine seeps. Continental Shelf Research 22, 2387–2394.

Hustoft, S., Mienert, J., Bünz, S., Nouzé, H. (2007). High-resolution 3D-seismic data indicate focussed fluid migration pathways above polygonal fault systems of the mid-Norwegian margin. Marine Geology 245, 89-106.

Hustoft, S., Bünz, S., Mienert, J., Chand, S. (2009). Gas hydrate reservoir and active methane-venting province in sediments on <20 Ma young oceanic crust in the Fram Strait, offshore NW-Svalbard. Earth and Planetary Science Letters 284, 12-24.

Hustoft, S., Bünz, S., Mienert, J. (2010). Three-dimensional seismic analysis of the morphology and spatial distribution of chimneys beneath the Nyegga pockmark field, offshore mid-Norway. Basin Research 22, 465-480.

Huuse, M., Jackson, C.A.L., Van Rensbergen, P., Davies, R.J., Flemings, P.B., Dixon, R.J. (2010). Subsurface sediment remobilization and fluid flow in sedimentary basins: an overview. Basin Research 22, 342-360.

Hyndman, R.D., Davis, E.E. (1992). A mechanism for the formation of methane hydrate and seafloor bottom-simulating reflectors by vertical fluid expulsion. Journal of Geophysical Research: Solid Earth 97, 7025-7041.

Hyndman, R.D., Foucher, J.-P., Yamano, M., Fisher, A. (1992). Deep sea bottom-simulating-reflectors: calibration of the base of the hydrate stability field as used for heat flow estimates. Earth and Planetary Science Letters 109, 289-301.

Ivanenkov, V.N., Lyakhin, V.N. (1978). Determination of total alkalinity in seawater. In: Bordovsky, O.K., Ivanenkov, V.N. (Eds.), Methods of hydrochemical investigations in the ocean (in Russian). Nauka Publishing House, Moscow, pp. 110-114.

Ivanov, M.K., Limonov, A.F., van Weering, T.C.E. (1996). Comparative characteristics of the Black Sea and Mediterranean Ridge mud volcanoes. Marine Geology 132, 253-271.

Ivanov, M., Blinova, V., Kozlova, E., Westbrook, G.K., Mazzini, A., Minshull, T., Nouzé, H. (2007). First sampling of gas hydrate from the Vøring Plateau. Eos Transactions AGU 88, 209-212.

Izawa, E., Cunningham, C.G. (1989). Hydrothermal breccia pipes and gold mineralization in the Iwashita Orebody, Iwato Deposit, Kyushu, Japan. Economic Geology 84, 715-724.

Jakobsson, M., Backman, J., Rudels, B., Nycander, J., Frank, M., Mayer, L., Jokat, W., Sangiorgi, F., O'Regan, M., Brinkhuis, H., King, J., Moran, K. (2007). The early Miocene onset of a ventilated circulation regime in the Arctic Ocean. Nature 447, 986-990.

Jamtveit, B., Svensen, H., Podladchikov, Y.Y., Planke, S. (2004). Hydrothermal vent complexes associated with sill intrusions in sedimentary basins. Geological Society, London, Special Publications 234, 233-241.

Jansen, E., Sjøholm, J. (1991). Reconstruction of glaciation over the past 6 Myr from ice-borne deposits in the Norwegian Sea. Nature 349, 600-603.

Johnson, H.P., Helferty, M. (1990). The geological interpretation of side-scan sonar. Reviews of Geophysics 28, 357–380.

Johnson, J.E., Goldfinger, C., Suess, E. (2003). Geophysical constraints on the surface distribution of authigenic carbonates across the Hydrate Ridge region, Cascadia margin. Marine Geology 202, 79–120.

Jolly, R.J.H., Lonergan, L. (2002). Mechanisms and controls on the formation of sand intrusions. Journal of the Geological Society 159, 605-617.

Jones, A.T., Greinert, J., Bowden, D.A., Klaucke, I., Petersen, C.J., Netzeband, G.L., Weinrebe, W. (2010). Acoustic and visual characterisation of methane-rich seabed seeps at Omakere Ridge on the Hikurangi Margin, New Zealand. Marine Geology 272, 154–169.

Jørgensen, B.B. (1978). A comparison of methods for the quantification of bacterial sulphate reduction in coastal marine sediments: I. Measurements with radiotracer techniques. Geomicrobiology Journal 1, 11-27.

Judd, A.G., Hovland, M. (1992). The evidence of shallow gas in marine sediments. Continental Shelf Research 12, 1081-1095.

Judd, A.G., Hovland, M., Dimitrov, L.I., García, G.S., Jukes, V. (2002). The geological methane budget at continental margins and its influence on climate change. Geofluids 2, 109–126.

Judd, A.G. (2003). The global importance and context of methane escape from the seabed. Geo-Marine Letters 23, 147–154.

Judd, A., Hovland, M. (2007). Seabed fluid flow: The impact on geology, biology and the marine environment. Cambridge University Press, Cambridge.

Jung, W.-Y., Vogt, P.R. (2004). Effects of bottom water warming and sea level rise on Holocene hydrate dissociation and mass wasting along the Norwegian-Barents Continental Margin. Journal of Geophysical Research 109, B06104.

Karaca, D., Hensen, C., Wallmann, K. (2010). Controls on authigenic carbonate precipitation at cold seeps along the convergent margin off Costa Rica. Geochemistry, Geophysics, Geosystems 11, Q08S27.

Kiel, S. (2009). Global hydrocarbon seep-carbonate precipitation correlates with deep-water temperatures and eustatic sea-level fluctuations since the Late Jurassic. Terra Nova 21, 279–284.

Kinoshita, M., Moore, G.F., Kido, Y.N. (2011). Heat flow estimated from BSR and IODP borehole data: Implication of recent uplift and erosion of the imbricate thrust zone in the Nankai Trough off Kumano. Geochemistry, Geophysics, Geosystems 12, Q0AD18.

Klaucke, I., Sahling, H., Weinrebe, W., Blinova, V., Bürk, D., Lursmanashvili, N., Bohrmann, G. (2006). Acoustic investigation of cold seeps offshore Georgia, eastern Black Sea. Marine Geology 231, 51–67.

Klaucke, I., Masson, D.G., Petersen, C.J., Weinrebe, W., Ranero, C.R. (2008). Multifrequency geoacoustic imaging of fluid escape structures offshore Costa Rica: implications for the quantification of seep processes. Geochemistry, Geophysics, Geosystems 9, Q04010.

Klaucke, I., Weinrebe, W., Petersen, C.J., Bowden, D. (2010). Temporal variability of gas seeps offshore New Zealand: Multi-frequency geoacoustic imaging of the Wairarapa area, Hikurangi margin. Marine Geology 272, 49–58.

Klaucke, I., Weinrebe, W., Linke, P., Klaeschen, D., Bialas, J. (2012). Sidescan sonar imagery of widespread fossil and active cold seeps along the central Chilean continental margin. Geo-Marine Letters 32, 489–499.

Knies, J., Mann, U. (2002). Depositional environment and source rock potential of Miocene strata from the central Fram Strait: introduction of a new computing tool for simulating organic facies variations. Marine and Petroleum Geology 19, 811-828.

Knies, J., Damm, E., Gutt, J., Mann, U., Pinturier, L. (2004). Near-surface hydrocarbon anomalies in shelf sediments off Spitsbergen: Evidences for past seepages. Geochemistry, Geophysics, Geosystems 5, Q06003.

Krabbenhoeft, A., Netzeband, G.L., Bialas. J., Papenberg, C. (2010). Episodic methane concentrations at seep sites on the upper slope Opouawe Bank, southern Hikurangi Margin, New Zealand. Marine Geology 272, 71–78.

Krabbenhoeft, A., Bialas, J., Klaucke, I., Crutchley, G., Papenberg, C., Netzeband, G.L. (2013). Patterns of subsurface fluid-flow at cold seeps: the Hikurangi Margin, offshore New Zealand. Marine and Petroleum Geology 39, 59–73.

Kretschmer, K., Biastoch, A., Ruepke, L., Burwicz, E. (submitted). Modeling the fate of methane hydrates under global warming. Global Biochemical Cycles.

Kutterolf, S., Liebetrau, V., Moerz, T., Freundt, A., Hammerich, T., Garbe-Schönberg, D. (2008). Lifetime and cyclicity of fluid venting at forearc mound structures determined by tephrostratigraphy and radiometric dating of authigenic carbonates. Geology 36, 707–710.

Kvarven, T., Hjelstuen, B.O., Mjelde, R. (2014). Tectonic and sedimentary processes along the ultraslow Knipovich spreading ridge. Marine Geophysical Research 35, 89-103.

Kvenvolden, K.A. (1988). Methane hydrate - a major reservoir of carbon in the shallow geosphere? Chemical Geology 71, 41-51.

Kvenvolden, K.A., Golan-Bac, M., McDonald, T.J., Pflaum, R.C., Brooks, J.M. (1989). Hydrocarbon gases in sediment of the Vøring Plateau, Norwegian Sea. In: Eldholm, O., Thiede, J., Taylor, E., et al. (Eds.), Proceedings of the Ocean Drilling Program, Scientific Results 104, 319-326.

Kvenvolden, K.A. (1993). Gas hydrates – geological perspective and global change. Reviews of Geophysics 31, 173-187.

Kvenvolden, K.A. (1995). A review of the geochemistry of methane in natural gas hydrate. Organic Geochemistry 23, 997-1008.

Kvenvolden, K.A. (2000). Natural gas hydrate: background and history of discovery. In: Max, M.D. (Ed.), Natural gas hydrate in oceanic and permafrost environments. Kluwer Academic Publishers, Netherlands, pp. 9-16.

Kvenvolden, K.A., Lorenson, T.D., Reeburgh, W.S. (2001). Attention turns to naturally occurring methane seepage. Eos Transactions American Geophysical Union 82, 457-458.

Laurent, D., Gay, A., Baudon, C., Berndt, C., Soliva, R., Planke, S., Mourgues, R., Lacaze, S., Pauget, F., Mangue, M., Lopez, M. (2012). High-resolution architecture of a polygonal fault interval inferred from geomodel applied to 3D seismic data from the Gjallar Ridge, Vøring Basin, Offshore Norway. Marine Geology 332–334, 134-151.

Law, C.S., Nodder, S.D., Mountjoy, J.J., Marriner, A., Orpin, A., Pilditch, C.A., Franz, P., Thompson, K. (2010). Geological, hydrodynamic and biogeochemical variability of a New Zealand deep-water methane cold seep during an integrated three-year time-series study. Marine Geology 272, 189–208.

Le Bas, T.P., Mason, D.C., Millard, N.C. (1995). TOBI image processing-the state of the art. IEEE Journal of Ocean Engineering 20, 85–93.

Leduc, A.M., Davies, R.J., Swarbrick, R.E., Imber, J. (2013). Fluid flow pipes triggered by lateral pressure transfer in the deepwater western Niger Delta. Marine and Petroleum Geology 43, 423-433.

Leifer, I., Patros, R.K. (2002). The bubble mechanism for methane transport from the shallow sea bed to the surface: A review and sensitivity study. Continental Shelf Research 22, 2409-2428.

Leifer, I., Boles, J.R., Luyendyk, B.P., Clark, J.F. (2004). Transient discharges from marine hydrocarbon seeps: spatial and temporal variability. Environmental Geology 46, 1038–1052.

Leifer, I., Luyendyk, B.P., Boles, J., Clark, J.F. (2006). Natural marine seepage blowout: Contribution to atmospheric methane. Global Biochemical Cycles 20, doi: 10.1029/2005GB002668.

Lewis, K.B., Marshall, B.A. (1996). Seep faunas and other indicators of methane-rich dewatering on New Zealand convergent margins. New Zealand Journal of Geology and Geophysics 39, 181–200.

Lewis, K.B., Collot, J.-Y., Lallemand, S.E. (1998). The dammed Hikurangi Trough: a channel-fed trench blocked by subducting seamounts and their wake avalanches (New Zealand–France GeodyNZ Project). Basin Research 10, 441–468.

Li, L., Lei, X., Zhang, X., Zhang, G. (2012). Heat flow derived from BSR and its implications for gas hydrate stability zone in Shenhu Area of northern South China Sea. Marine Geophysical Research 33, 77-87.

Liebetrau, V., Eisenhauer, A., Linke, P. (2010). Cold seep carbonates and associated cold-water corals at the Hikurangi Margin, New Zealand: new insights into fluid pathways, growth structures and geochronology. Marine Geology 272, 307–318.

Liu, X., Flemings, P.B. (2007). Dynamic multiphase flow model of hydrate formation in marine sediments. Journal of Geophysical Research 112, B03101.

Løseth, H., Wensaas, L., Arntsen, B., Hanken, N., Basire, C., Graue, K. (2001). 1000 m long gas blow out pipes. 63rd EAGE Conference and Exhibition, Extended abstract, pp. 524-527.

Løseth, H., Wensaas, L., Arntsen, B., Hovland, M. (2003). Gas and fluid injection triggering shallow mud mobilization in the Hordaland Group, North Sea. Geological Society, London, Special Publications 216, 139-157.

Løseth, H., Henriksen, S. (2005). A Middle to Late Miocene compression phase along the Norwegian passive margin. Proceedings of the 6th Petroleum Geology Conference, Geological Society, London, pp. 845-859.

Løseth, H., Gading, M., Wensaas, L. (2009). Hydrocarbon leakage interpreted on seismic data. Marine and Petroleum Geology 26, 1304-1319.

Løseth, H., Wensaas, L., Arntsen, B., Hanken, N.-M., Basire, C., Graue, K. (2011). 1000 m long gas blow-out pipes. Marine and Petroleum Geology 28, 1047-1060.

Ludwig, K.R. (2008). Isoplot 3.7: A geochronological toolkit for Microsoft Excel. Berkeley Geochronology Center Special Publication 4.

Luff, R., Wallmann, K. (2003). Fluid flow, methane fluxes, carbonate precipitation and biogeochemical turnover in gas hydrate-bearing sediments at Hydrate Ridge, Cascadia Margin: numerical modeling and mass balances. Geochimica et Cosmochimica Acta 67, 3403–3421.

Luff, R., Wallmann, K., Aloisi, G. (2004). Numerical modeling of carbonate crust formation at cold vent sites: significance for fluid and methane budgets and chemosynthetic biological communities. Earth and Planetary Science Letters 221, 337–353.

MacDonald, K.C., Becker, K., Spiess, F.N., Ballard, R.D. (1980). Hydrothermal heat flux of the "Black Smoker" vents on the East Pacific Rise. Earth and Planetary Science Letters 48, 1–7.

MacDonald, I.R., Leifer, I., Sassen, R., Stine, P., Mitchell, R., Guinasso, N. Jr. (2002). Transfer of hydrocarbons from natural seeps to the water column and atmosphere. Geofluids 2, 95-107.

Maclennan, J., Jones, S.M. (2006). Regional uplift, gas hydrate dissociation and the origins of the Paleocene-Eocene Thermal Maximum. Earth and Planetary Science Letters 245, 65-80.

Maltman, A.J., Bolton, A. (2003). How sediments become mobilized. Geological Society, London, Special Publications 216, 9-20.

Mann, U., Knies, J., Chand, S., Jokat, W., Stein, R., Zweigel, J. (2009). Evaluation and modelling of Tertiary source rocks in the central Arctic Ocean. Marine and Petroleum Geology 26, 1624-1639.

Martin, V., Henry, P., Nouzé, H., Noble, M., Ashi, J., Pascal, G. (2004). Erosion and sedimentation as processes controlling the BSR-derived heat flow on the Eastern Nankai margin. Earth and Planetary Science Letters 222, 131-144.

Maslin, M., Owen, M., Betts, R., Day, S., Dunkley Jones, T., Ridgwell, A. (2010). Gas hydrates: past and future geohazard? Philosophical Transactions of the Royal Society A 368, 2369-2392.

Mau, S., Rehder, G., Arroyo, I.G., Gossler, J., Suess, E. (2007). Indications of a link between seismotectonics and CH_4 release from seeps off Costa Rica. Geochemistry, Geophysics, Geosystems 8, Q04003.

Mazzini, A., Ivanov, M.K., Nermoen, A., Bahr, A., Bohrmann, G., Svensen, H., Planke, S. (2008). Complex plumbing systems in the near subsurface: geometries of authigenic carbonates from Dolgovskoy Mound (Black Sea) constrained by analogue experiments. Marine and Petroleum Geology 25, 457–472.

McGinnis, D.F., Greinert, J., Artemov, Y., Beaubien, S.E., Wüest, A. (2006). Fate of rising methane bubbles in stratified waters: how much methane reaches the atmosphere? Journal of Geophysical Research 111, C09007.

Mienert, J., Posewang, J., Baumann, M. (1998). Gas hydrates along the northeastern Atlantic margin: possible hydrate-bound margin instabilities and possible release of methane. Geological Society, London, Special Publications 137, 275-291.

Mienert, J., Posewang, J. (1999). Evidence of shallow- and deep-water gas hydrate destabilizations in North Atlantic polar continental margin sediments. Geo-Marine Letters 19, 143-149.

Mienert, J., Vanneste, M., Haflidason, H., Bünz, S. (2010). Norwegian margin outer shelf cracking: a consequence of climate-induced gas hydrate dissociation? International Journal of Earth Sciences 99, 207–225.

Milkov, A.V. (2004). Global estimates of hydrate-bound gas in marine sediments: how much is really out there? Earth-Science Reviews 66, 183-197.

Minshull, T.A., Muller, M.R., Robinson, C.J., White, R.S., Bickle, M.J. (1998). Is the oceanic Moho a serpentinization front? Geological Society, London, Special Publications 148, 71-80.

Mitchell, N.C. (1993). A model for attenuation of backscatter due to sediment accumulations and its application to determine sediment thicknesses with GLORIA sidescan sonar. Journal of Geophysical Research 98, 22,477–22,493.

Moore, J.C., Vrolijk, P. (1992). Fluids in accretionary prisms. Reviews of Geophysics 30, 113–135.

Moss, J.L., Cartwright, J. (2010). The spatial and temporal distribution of pipe formation, offshore Namibia. Marine and Petroleum Geology 27, 1216-1234.

Myhre, A.M., Eldholm, O. (1988). The western Svalbard margin (74°–80°N). Marine and Petroleum Geology 5, 134-156.

Myhre, A.M., Thiede, J., Firth, J.V., et al. (1995). Proceedings on ODP, Initial Reports, 151: College Station, TX (Ocean Drilling Program).

Naudts, L., Greinert, J., Artemov, Y., Beaubien, S.E., Borowski, C., Batist, M.D. (2008). Anomalous seafloor backscatter patterns in methane venting areas, Dnepr paleo-delta, NW Black Sea. Marine Geology 251, 253–267.

Netzeband, G.L., Krabbenhoeft, A., Zillmer, M., Petersen, C.J., Papenberg, C., Bialas, J. (2010). The structures beneath submarine methane seeps: seismic evidence from Opouawe Bank, Hikurangi Margin, New Zealand. Marine Geology 272, 59–70.

Niemann, H., Lösekann, T., De Beer, D., Elvert, M., Nadalig, T., Knittel, K., Aman, A., Sauter, E.J., Schlüter, M., Klages, M., Foucher, J.-P., Boetius, A. (2006). Novel microbial communities of the Haakon Mosby mud volcano and their role as a methane sink. Nature 443, 854-858.

Norris, R.D., Röhl, U. (1999). Carbon cycling and chronology of climate warming during the Palaeocene-Eocene transition. Nature 401, 775-778.

Osborne, M.J., Swarbrick, R.E. (1997). Mechanisms for generating overpressure in sedimentary basins: a reevaluation. AAPG Bulletin 81, 1023-1041.

Ottesen, D., Rise, L., Andersen, E.S., Bugge, T., Eidvin, T. (2009). Geological evolution of the Norwegian continental shelf between 61°N and 68°N during the last 3 million years. Norwegian Journal of Geology 89, 251-265.

Pecher, I.A., Henrys, S.A., Zhu, H. (2004). Seismic images of gas conduits beneath vents and gas hydrates on Ritchie Ridge, Hikurangi margin, New Zealand. New Zealand Journal of Geology and Geophysics 47, 275-279.

Pellenberg, R.E., Max, M.D. (2000). Introduction, physical properties, and natural occurrence of hydrate. In: Max, M.D. (Ed.), Natural gas hydrate in oceanic and permafrost environments, Kluwer Academic Publishers, Netherlands, pp. 1-8.

Pepper, A.S., Corvi, P.J. (1995). Simple kinetic models of petroleum formation. Part I: oil and gas generation from kerogen. Marine and Petroleum Geology 12, 291-319.

Perez-Garcia, C., Feseker, T., Mienert, J., Berndt, C. (2009). The Håkon Mosby mud volcano: 330 000 years of focused fluid flow activity at the SW Barents Sea slope. Marine Geology 262, 105-115.

Phrampus, B.J., Hornbach, M. (2012). Recent changes to the Gulf Stream causing widespread gas hydrate destabilization. Nature 490, 527-530.

Phrampus, B.J., Hornbach, M.J., Ruppel, C.D., Hart, P.E. (2014). Widespread gas hydrate instability on the upper U.S. Beaufort margin. Journal of Geophysical Research 119, 8594-8609.

Piñero, E., Marquardt, M., Hensen, C., Haeckel, M., Wallmann, K. (2013). Estimation of the global inventory of methane hydrates in marine sediments using transfer functions. Biogeosciences 10, 959-975.

Planke, S., Rasmussen, T., Rey, S.S., Myklebust, R. (2005). Seismic characteristics and distribution of volcanic intrusions and hydrothermal vent complexes in the Vøring and Møre basins. Geological Society, London, Petroleum Geology Conference Series 6, 833-844.

Plaza-Faverola, A., Westbrook, G.K., Ker, S., Exley, R.J.K., Gailler, A., Minshull, T.A., Broto, K. (2010). Evidence from three-dimensional seismic tomography for a substantial accumulation of gas hydrate in a fluid-escape chimney in the Nyegga pockmark field, offshore Norway. Journal of Geophysical Research 115, B08104.

Plaza-Faverola, A., Bünz, S., Mienert, J. (2011). Repeated fluid expulsion through sub-seabed chimneys offshore Norway in response to glacial cycles. Earth and Planetary Science Letters 305, 297–308.

Plaza-Faverola, A., Pecher, I., Crutchley, G., Barnes, P.M., Bünz, S., Golding, T., Klaeschen, D., Papenberg, C., Bialas, J. (2014). Submarine gas seepage in a mixed contractional and shear deformation regime: cases from the Hikurangi oblique-subduction margin. Geochemistry, Geophysics, Geosystems 15, 416-433.

Plaza-Faverola, A., Bünz, S., Johnson, J.E., Chand, S., Knies, J., Mienert, J., Franek, P. (2015). Role of tectonic stress in seepage evolution along the gas hydrate-charged Vestnesa Ridge, Fram Strait. Geophysical Research Letters 42, doi:10.1002/2014GL062474.

Poliakov, A.N.B., Podladchikov, Y.Y., Dawson, E.C., Talbot, C.J. (1996). Salt diapirism with simultaneous brittle faulting and viscous flow. Geological Society, London, Special Publications 100, 291-302.

Posewang, J., Mienert, J. (1999). High-resolution seismic studies of gas hydrates west of Svalbard. Geo-Marine Letters 19, 150-156.

Post, E., Forchhammer, M.C., Bret-Harte, M.S., Callaghan, T.V., Christensen, T.R., Elberling, B., Fox, A.D., Gilg, O., Hik, D.S., Høye, T.T., Ims, R.A., Jeppesen, E., Klein, D.R., Madsen, J., McGuire, A.D., Rysgaard, S., Schindler, D.E., Stirling, I., Tamstorf, M.P., Tyler, N.J.C., van der Wal, R., Welker, J., Wookey, P.A., Schmidt, N.M., Aastrup, P. (2009). Ecological dynamics across the Arctic associated with recent climate change. Science 325, 1355-1358.

Rajan, A., Mienert, J., Bünz, S. (2012a). Acoustic evidence for a gas migration and release system in Arctic glaciated continental margins offshore NW-Svalbard. Marine and Petroleum Geology 32, 36-49.

Rajan, A., Mienert, J., Bünz, S., Chand, S. (2012b). Potential serpentinization, degassing, and gas hydrate formation at a young (<20 Ma) sedimented ocean crust of the Arctic Ocean ridge system. Journal of Geophysical Research: Solid Earth 117, B03102.

Reagan, M.T., Moridis, G.J. (2007). Oceanic gas hydrate instability and dissociation under climate change scenarios. Geophysical Research Letters 34, L22709.

Reagan, M.T. , Moridis, G.J. (2008). Dynamic response of oceanic hydrate deposits to ocean temperature change. Journal of Geophysical Research 113, C12023.

Reagan, M.T., Moridis, G.J. (2009). Large-scale simulation of methane hydrate dissociation along the West Spitsbergen Margin. Geophysical Research Letters 36, L23612.

Reagan, M.T., Moridis, G.J., Elliott, S.M., Maltrud, M. (2011). Contribution of oceanic gas hydrate dissociation to the formation of Arctic Ocean methane plumes. Journal of Geophysical Research 116, C09014.

Reeburgh, W.S., Ward, B.B., Whalen, S.C., Sandbeck, K.A., Kilpatrick, K.A., Kerkhof, L.J. (1991). Black-Sea methane geochemistry. Deep-Sea Research Part A - Oceanographic Research Papers 38, 1189-1210.

Reemst, P., Skogseid, J., Larsen, B.T. (1996). Base Pliocene velocity inversion on the eastern Vøring margin— causes and implications. Global and Planetary Change 12, 201-211.

Ren, S., Faleide, J.I., Eldholm, O., Skogseid, J., Gradstein, F. (2003). Late Cretaceous–Paleocene tectonic development of the NW Vøring Basin. Marine and Petroleum Geology 20, 177-206.

Retallack, G.J., Jahren, A.H. (2008). Methane release from igneous intrusion of coal during Late Permian extinction events. The Journal of Geology 116, 1-20.

Rice, D.D., Claypool, G.E. (1981). Generation, accumulation, and resource potential of biogenic gas. AAPG Bulletin 65, 5-25.

Rise, L., Ottesen, D., Longva, O., Solheim, A., Andersen, E. S., Ayers, S. (2006). The Sklinnadjupet slide and its relation to the Elsterian glaciation on the mid-Norwegian margin. Marine and Petroleum Geology 23, 569-583.

Ritger, S., Carson, B., Suess, E. (1987). Methane-derived authigenic carbonates formed by subduction-induced pore-water expulsion along the Oregon/Washington margin. Geological Society of America Bulletin 98, 147–156.

Ritzmann, O., Jokat, W., Czuba, W., Guterch, A., Mjelde, R., Nishimura, Y. (2004). A deep seismic transect from Hovgård Ridge to northwestern Svalbard across the continental-ocean transition: A sheared margin study. Geophysical Journal International 157, 683-702.

Roberts, S.J., Nunn, J.A. (1995). Episodic fluid expulsion from geopressured sediments. Marine and Petroleum Geology 12, 195-204.

Röhl, U., Westerhold, T., Bralower, T.J., Zachos, J.C. (2007). On the duration of the Paleocene-Eocene thermal maximum (PETM). Geochemistry Geophysics Geosystems 8, Q12002.

Sahling, H.R., Rickert, D., Lee, R.W., Linke, P., Suess, E. (2002). Macrofaunal community structure and sulfide flux at gas hydrate deposits from the Cascadia convergent margin, NE Pacific. Marine Ecological Progress Series 231, 121–138.

Sahling, H., Römer, M., Pape, T., Bergès, B., dos Santos Fereirra, C., Boelmann, J., Geprägs, P., Tomczyk, M., Nowald, N., Dimmler, W., Schroedter, L., Glockzin, M., Bohrmann, G. (2014). Gas emissions at the continental margin west of Svalbard: mapping, sampling, and quantification. Biogeosciences 11, 6029-6046.

Sarkar, S. (2012). Glacial stratigraphy, gas-escape features and ocean fine-structures from multichannel high resolution seismic data offshore west Svalbard. Ph.D. thesis, School of Ocean and Earth Sciences, University of Southampton, Southampton, United Kingdom.

Sarkar, S., Berndt, C., Minshull, T.A., Westbrook, G.K., Klaeschen, D., Masson, D.G., Chabert, A., Thatcher, K.E. (2012). Seismic evidence for shallow gas-escape features associated with a retreating gas hydrate zone offshore west Svalbard. Journal of Geophysical Research: Solid Earth 117, B09102.

Saunders, P.M. (1981). Practical conversion of pressure to depth. Journal of Physical Oceanography 11, 573-574.

Schauer, U., Beszczynska-Möller, A., Walczowski, W., Fahrbach, E., Piechura, J., Hansen, E. (2008). Variation of measured heat flow through the Fram Strait between 1997 and 2006. In: Dickson, R.R., Meincke, J., Rhines, P. (Eds.), Arctic-subarctic ocean fluxes. Springer, Netherlands, pp. 65-85.

Schmale, O., Greinert, J., Rehder, G. (2005). Methane emission from high-intensity marine gas seeps in the Black Sea into the atmosphere. Geophysical Research Letters 32, L07609.

Schmale, O., Beaubien, S.E., Rehder, G., Greinert, J., Lombardi, S. (2010). Gas seepage in the Dnepr paleo-delta area (NW Black Sea) and its regional impact on the water column methane cycle. Journal of Marine Systems 80, 90–100.

Schoell, M. (1988). Multiple origins of methane in the Earth. Chemical Geology 71, 1-10.

Schroot, B.M., Klaver, G.T., Schüttenhelm, R.T.E. (2005). Surface and subsurface expressions of gas seepage to the seabed – examples from the Southern North Sea. Marine and Petroleum Geology 22, 499-515.

Schuur, E.A.G., Vogel, J.G., Crummer, K.G., Lee, H., Sickman, J.O., Osterkamp, T.E. (2009). The effect of permafrost thaw on old carbon release and net carbon exchange from tundra. Nature 459, 556-559.

Schwalenberg, K., Haeckel, M., Poort, J., Jegen, M. (2010). Evaluation of gas hydrate deposits in an active seep area using marine controlled source electromagnetics: results from Opouawe Bank, Hikurangi Margin, New Zealand. Marine Geology 272, 79–88.

Sheriff, R.E., Geldart, L.P. (1995). Exploration seismology, 2nd ed. Cambridge University Press, New York.

Shipboard Scientific Party (1995a). Site 908. In: Myhre, A.M., Thiede, J., Firth, J.V., et al. (Eds.), Proceedings on ODP, Initial Reports 151, pp. 113-158, College Station, TX (Ocean Drilling Program).

Shipboard Scientific Party (1995b). Site 909. In: Myhre, A.M., Thiede, J., Firth, J.V., et al. (Eds.), Proceedings on ODP, Initial Reports 151, pp. 159-220, College Station, TX (Ocean Drilling Program).

Shipley, T.H., Houston, M.H., Buffler, R.T., Shaub, F.J., McMillen, K.J., Ladd, J.W., Worzel, J.L. (1979). Seismic evidence for widespread possible gas hydrate horizons on continental slopes and rises. AAPG Bulletin 63, 2204-2213.

Sibson, R.H., Robert, F., Poulsen, K.H. (1988). High-angle reverse faults, fluid-pressure cycling, and mesothermal gold-quartz deposits. Geology 16, 551-555.

Sibson, R.H. (1994). Crustal stress, faulting and fluid flow. Geological Society, London, Special Publications 78, 69–84.

Skogseid, J., Eldholm, O. (1987). Early Cenozoic crust at the Norwegian continental margin and the conjugate Jan Mayen Ridge. Journal of Geophysical Research 92, 11,471-11,491.

Sloan, E.D. (1998). Clathrate hydrates of natural gases. Marcel Dekker, New York.

Smith, A.J., Mienert, J., Bünz, S., Greinert, J. (2014). Thermogenic methane injection via bubble transport into the upper Arctic Ocean from the hydrate-charged Vestnesa Ridge, Svalbard. Geochemistry, Geophysics, Geosystems 15, 1945-1959.

Solheim, A., Andersen, E.S., Elverhøi, A., Fiedler, A. (1996). Late Cenozoic depositional history of the western Svalbard continental shelf, controlled by subsidence and climate. Global and Planetary Change 12, 135-148.

Sommer, S., Linke, P., Pfannkuche, O., Niemann, H., Treude, T. (2010). Benthic respiration in a seep habitat dominated by dense beds of ampharetid polychaetes at the Hikurangi Margin (New Zealand). Marine Geology 272, 223–232.

Somoza, L., Medialdea, T., León, R., Ercilla, G., Vázquez, J.T., Farran, M.l., Hernández-Molina, J., González, J., Juan, C., Fernández-Puga, M.C. (2012). Structure of mud volcano systems and pockmarks in the region of the Ceuta Contourite Depositional System (Western Alborán Sea). Marine Geology 332–334, 4-26.

Spielhagen, R., Werner, K., Sørensen, S.A., Zamelczyk, K., Kandiano, E., Budeus, G., Husum, K., Marchitto, T.M., Hald, M. (2011). Enhanced modern heat transfer to the Arctic by warm Atlantic water. Science 331, 450-453.

Spiess, F.N., MacDonald, K.C., Atwater, T., Ballard, R., Carranza, A., Cordoba, D., Cox, C., Diaz Garcia, V.M., Francheteau, J., Guerrero, J., Hawkins, J., Haymon, R., Hessler, R., Juteau, T., Kastner, M., Larson, R., Luyendyk, B., Macdougall, J.D., Miller, S., Normark, W., Orcutt, J., Rangin, C. (1980). East Pacific Rise: hot springs and geophysical experiment. Science 207, 1421–1433.

Stakes, D.S., Orange, D., Paduan, J.B., Salamy, K.A., Maher, N. (1999). Cold-seeps and authigenic carbonate formation in Monterey Bay, California. Marine Geology 159, 93–109.

Stein, R., Boucsein, B., Meyer, H. (2006). Anoxia and high primary production in the Paleogene central Arctic Ocean: First detailed records from Lomonosov Ridge. Geophysical Research Letters 33, L18606.

Stein, R. (2007). Upper Cretaceous/lower Tertiary black shales near the North Pole: Organic-carbon origin and source-rock potential. Marine and Petroleum Geology 24, 67-73.

Stewart, S.A., Davies, R.J. (2006). Structure and emplacement of mud volcano systems in the South Caspian Basin. AAPG Bulletin 90, 771-786.

Stockwell, J. (1997). Free software in education: a case study of CWP/SU: Seismic Unix. The Leading Edge 16, 1045–1050.

Suess, E., Torres, M.E., Bohrmann, G., Collier, R.W., Greinert, J., Linke, P., Rehder, G., Tréhu, A., Wallmann, K., Winckler, G., Zuleger, E. (1999). Gas hydrate destabilization: enhanced dewatering, benthic material turnover and large methane plumes at the Cascadia convergent margin. Earth and Planetary Science Letters 170, 1-15.

Sundvor, E., Eldholm, O., Gladczenko, T.P., Planke, S. (2000). Norwegian-Greenland Sea thermal field. Geological Society, London, Special Publications 167, 397-410.

Svensen, H., Planke, S., Jamtveit, B., Pedersen, T. (2003). Seep carbonate formation controlled by hydrothermal vent complexes: a case study from the Vøring Basin, Norwegian Sea. Geo-Marine Letters 23, 351-358.

Svensen, H., Planke, S., Malthe-Sorenssen, A., Jamtveit, B., Myklebust, R., Rasmussen Eidem, T., Rey, S.S. (2004). Release of methane from a volcanic basin as a mechanism for initial Eocene global warming. Nature 429, 542-545.

Svensen, H., Planke, S., Chevallier, L., Malthe-Sørenssen, A., Corfu, F., Jamtveit, B. (2007). Hydrothermal venting of greenhouse gases triggering Early Jurassic global warming. Earth and Planetary Science Letters 256, 554-566.

Svensen, H., Corfu, F., Polteau, S., Hammer, Ø., Planke, S. (2012). Rapid magma emplacement in the Karoo Large Igneous Province. Earth and Planetary Science Letters 325–326, 1-9.

Talukder, A.R. (2012). Review of submarine cold seep plumbing systems: leakage to seepage and venting. Terra Nova 24, 255-272.

Talwani, M., and Eldholm, O. (1977). Evolution of the Norwegian-Greenland Sea. Geological Society of America Bulletin 88, 969-999.

Teichert, B.M.A., Eisenhauer, A., Bohrmann, G., Haase-Schramm, A., Bock, B., Linke, P. (2003). U/Th systematics and ages of authigenic carbonates from Hydrate Ridge, Cascadia Margin: recorders of fluid flow variations. Geochimica et Cosmochimica Acta 67, 3845–3857.

Teichert, B.M.A., Bohrmann, G., Suess, E. (2005). Chemoherms on Hydrate Ridge—unique microbially-mediated carbonate build-ups growing into the water column. Palaeogeography, Palaeoclimatology, Palaeoecology 227, 67–85.

Thatcher, K.E., Westbrook, G.K., Sarkar, S., Minshull, T.A. (2013). Methane release from warming-induced hydrate dissociation in the West Svalbard continental margin: Timing, rates, and geological controls. Journal of Geophysical Research: Solid Earth 118, 22-38.

Thiede, J., Pfirman, S., Schenke, H.-W., Reil, W. (1990). Bathymetry of Molloy Deep: Fram Strait between Svalbard and Greenland. Marine Geophysical Researches 12, 197-214.

Tishchenko, P., Hensen, C., Wallmann, K., Wong, C.S. (2005). Calculation of the stability and solubility of methane hydrate in seawater. Chemical Geology 219, 37-52.

Tissot, B.P., Welte, D.H. (1994). Petroleum formation and occurrence, 2nd ed. Springer Verlag, New York.

Townend, J. (1997). Estimates of conductive heat flow through bottom-simulating reflectors on the Hikurangi and southwest Fiordland continental margins, New Zealand. Marine Geology 141, 209-220.

Tréhu, A.M., Flemings, P.B., Bangs, N.L., Chevallier, J., Gràcia, E., Johnson, J.E., Liu, C.-S., Liu, X., Riedel., M., Torres, M.E. (2004). Feeding methane vents and gas hydrate deposits at south Hydrate Ridge. Geophysical Research Letters 31, L23310.

Treude, T., Boetius, A., Knittel, K., Wallmann, K., Jørgensen, B.B. (2003). Anaerobic oxidation of methane above gas hydrates at Hydrate Ridge, NE Pacific Ocean. Marine Ecology Progress Series 264, 1-14.

Treude, T., Krüger, M., Boetius, A., Jørgensen, B.B. (2005). Environmental control on anaerobic oxidation of methane in the gassy sediments of Eckernförde Bay (German Baltic). Limnology and Oceanography 50, 1771-1786.

Vail, P.R., Hardenbol, J. (1979). Sea-level changes during the Tertiary. Oceanus 22, 71-79.

Valentine, D.L., Blanton, D.C., Reeburgh, W.S., Kastner, M. (2001). Water column methane oxidation adjacent to an area of active hydrate dissociation, Eel River Basin. Geochimica et Cosmochimica Acta 65, 2633-2640.

Van Dover, C.L., Aharon, P., Bernhard, J.M., Caylor, E., Doerries, M., Flickinger, W., Gilhooly, W., Goffredi, S.K., Knick, K.E., Macko, S.A., Rapoport, S., Raulfs, E.C., Ruppel, C., Salerno, J.L., Seitz, R.D., Sen Gupta, B.K., Shank, T., Turnipseed, M., Vrijenhoek, R. (2003). Blake Ridge methane seeps: characterization of a soft-sediment, chemosynthetically based ecosystem. Deep Sea Research I 50, 281–300.

van Rensbergen, P., Poort, J., Kipfer, R., De Batist, M., Vanneste, M., Klerkx, J., Granin, N., Khlystov, O., Krinitsky, P. (2003). Near-surface sediment mobilization and methane venting in relation to hydrate destabilization in Southern Lake Baikal, Siberia. In: Van Rensbergen, P., Hillis, R.R., Maltman, A.J., Morley, C.K., Subsurface sediment mobilization. Geological Society, London, Special Publications 216, 207-221.

Vanneste, M., Guidard, S., Mienert, J. (2005a). Arctic gas hydrate provinces along the western Svalbard continental margin. Norwegian Petroleum Society Special Publications 12, 271-284.

Vanneste, M., Guidard, S., Mienert, J. (2005b). Bottom-simulating reflections and geothermal gradients across the western Svalbard margin. Terra Nova 17, 510-516.

Villinger, H., Davis, E.E (1987). A new reduction algorithm for marine heat flow measurements. Journal of Geophysical Research: Solid Earth 92, 12,846-12,856.

Vorren, T.O., Lebesbye, E., Andreassen, K., Larsen, K.B. (1989). Glacigenic sediments on a passive continental margin as exemplified by the Barents Sea. Marine Geology 85, 251-272.

Vogt, P.R., Sundvor, E. (1996). Heat flow highs on the Norwegian-Barents-Svalbard continental slope: Deep crustal fractures, dewatering, or "memory in the mud"? Geophysical Research Letters 23, 3571-3574.

Vogt, P.R., Crane, K., Sundvor, E., Hjelstuen, B.O., Gardner, J., Bowles, F., Cherkashev, G. (1999). Ground-truthing 11- to 12-kHz side-scan sonar imagery in the Norwegian–Greenland Sea: Part II: Probable diapirs on the Bear Island fan slide valley margins and the Vøring Plateau. Geo-Marine Letters 19, 111-130.

Vogt, P.R., Jung, W.-Y. (2002). Holocene mass wasting on upper non-Polar continental slopes – due to post-Glacial ocean warming and hydrate dissociation? Geophysical Research Letters 29, 1341.

Wallace, L.M., Beavan, J., McCaffrey, R., Darby, D. (2004). Subduction zone coupling and tectonic block rotations in the North Island, New Zealand. Journal of Geophysical Research 109, B12406.

Wallmann, K., Piñero, E., Burwicz, E., Haeckel, M., Hensen, C., Dale, A., Ruepke, L. (2012). The global inventory of methane hydrate in marine sediments: A theoretical approach. Energies 5, 2449-2498.

Walsh, P., Morawiecka-Zacharz, I. (2001). A dissolution pipe palaeokarst of mid-Pleistocene age preserved in Miocene limestones near Staszów, Poland. Palaeogeography, Palaeoclimatology, Palaeoecology 174, 327-350.

Wanninkhof, R., Asher, W.E., Ho, D.T., Sweeney, C., McGillis, W.R. (2009). Advances in quantifying air-sea gas exchange and environmental forcing. Annual Review of Marine Science 1, 213-244.

Wedepohl, K.H. (1995). The composition of the continental crust. Geochimica et Cosmochimica Acta 59, 1217–1232.

Welhan, J.A. (1988). Origins of methane in hydrothermal systems. Chemical Geology 71, 183-198.

Wessel, P., Smith, W.H.F. (1991). Free software helps map and display data. Eos Transactions AGU 72, 441-446.

Wessel, P., Smith, W.H.F. (1998). New, improved version of generic mapping tools released. Eos Transactions AGU 79, 579.

Westbrook, G.K., Chand, S., Rossi, G., Long, C., Bünz, S., Camerlenghi, A., Carcione, J. M., Dean, S., Foucher, J.-P., Flueh, E., Gei, D., Haacke, R.R., Madrussani, G., Mienert, J., Minshull, T.A., Nouzé, H., Peacock, S., Reston, T.J., Vanneste, M., Zillmer, M. (2008a). Estimation of gas hydrate concentration from multi-component seismic data at sites on the continental margins of NW Svalbard and the Storegga region of Norway. Marine and Petroleum Geology 25, 744-758.

Westbrook, G.K., Exley, R., Minshull, T., Nouzé, H., Gailler, A., Jose, T., Ker, S., Plaza, A. (2008b). High-resolution 3D seismic investigations of hydrate-bearing fluid-escape chimneys in the Nyegga region of the Vøring Plateau, Norway. Proceedings of the 6th International Conference on Gas Hydrates (ICGH 2008), Vancouver, British Columbia, Canada.

Westbrook, G.K., Thatcher, K.E., Rohling, E.J., Piotrowski, A.M., Pälike, H., Osborne, A.H., Nisbet, E.G., Minshull, T.A., Lanoisellé, M., James, R.H., Hühnerbach, V., Green, D., Fisher, R.E., Crocker, A.J., Chabert, A., Bolton, C., Beszczynska-Möller, A., Berndt, C., Aquilina, A. (2009) Escape of methane gas from the seabed along the West Spitsbergen continental margin. Geophysical Research Letters 36, L15608.

Whiteman, G., Hope, C., Wadhams, P. (2013). Climate science: Vast costs of Arctic change. Nature 499, 401-403.

Whiticar, M.J., Faber, E., Schoell, M. (1986). Biogenic methane formation in marine and freshwater environments: CO_2 reduction vs. acetate fermentation – isotope evidence. Geochimica et Cosmochimica Acta 50, 693-709.

Whiticar, M.J. (1999). Carbon and hydrogen isotope systematics of bacterial formation and oxidation of methane. Chemical Geology 161, 291-314.

Whiticar, M.J. (2002). Diagenetic relationships of methanogenesis, nutrients, acoustic turbidity, pockmarks and freshwater seepages in Eckernförde Bay. Marine Geology 182, 29-53.

Wiese, K., Kvenvolden, K.A. (1993). Introduction to microbial and thermal methane. U.S. Geological Survey Professional Paper 1570, 13-20.

Wiesenburg, D.A., Guinasso, N.L. (1979). Equilibrium solubilities of methane, carbon monoxide, and hydrogen in water and sea water. Journal of Chemical and Engineering Data 24, 356-360.

Wignall, P.B. (2001). Large igneous provinces and mass extinctions. Earth-Science Reviews 53, 1-33.

Wilken, D., Feldens. P., Wunderlich. T., Heinrich. C. (2012) Application of 2D Fourier filtering for elimination of stripe noise in side-scan sonar mosaics. Geo-Marine Letters 32, 337–347.

Wood, R., Davy, B. (1994) The Hikurangi Plateau. Marine Geology 118, 153–173.

Woodside, W., Messmer, J.H. (1961). Thermal conductivity of porous media. I. Unconsolidated sands. Journal of Applied Physics 32, 1688-1699.

Yamano, M., Uyeda, S., Aoki, Y., Shipley, T.H. (1982). Estimates of heat flow derived from gas hydrates. Geology 10, 339-343.

Yuan, F., Bennell, J.D., Davis, A.M. (1992). Acoustic and physical characteristics of gassy sediments in the western Irish Sea. Continental Shelf Research 12, 1121-1134.

List of Figures

List of Tables

Appendix A

Appendix

A.1   Supporting information: Case study 1 - Knipovich Ridge
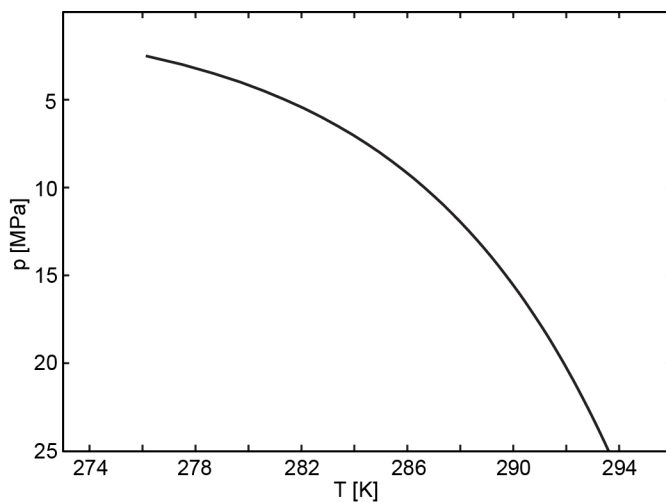
Methane hydrate stability curve

Figure A.1: Methane hydrate stability curve (Equation 2.1) determined using the CSMHYD program of Sloan (1998). The curve was calculated using as components seawater (pure water + 3.5 wt% NaCl) and the hydrate composition of Smith et al. (2014).

Uncertainty of BSR-derived heat flow

Due to the many factors involved in the assessment of the geothermal gradient and heat flow, the uncertainty of the final values depends on the errors associated with each of the contributing factors. We differentiate between errors defined prior to the calculation and errors resulting from those previously defined errors. Errors defined prior to the calculation include the error of (1) the BSR and seafloor travel times, (2) the seismic velocities of the water layer and the seafloor-BSR layer, (3) the seafloor temperature, and (4) the thermal conductivity.

The error of the BSR and seafloor takes into account the picking accuracy, the sampling interval, the seismic wavelet, static errors, and imaging problems such as interferences. We assumed an error of 5 ms for the seafloor horizon and 10 ms for the BSR. The difference is due to the picking mode: the seafloor was easy to follow and picked mostly with an automatic picking algorithm, whereas the BSR had to be picked manually.

The water velocity was relatively well constrained by CTD measurements, thus an error of only 5 m s^{-1} was assumed. In contrast, we estimated an error of 50 m s^{-1} for the velocity between seafloor and BSR as there was not enough velocity information available to constrain it well, and the velocity in this depth varies because of differences in hydrate saturation and lithological variations.

Based on these errors, we calculated the errors for the depth conversion of the BSR ($e(z_{BSRmbsf})$, $e(z_{BSRmbsl})$) and seafloor ($e(z_{SFL})$), and the pressure ($e(p_{BSR})$) and temperature ($e(T_{BSR})$) at the BSR, which were below 5% except for the BSR depth conversion ($<20\%$) (Table A.1). The $<2\%$ calculated for the error of the temperature at the BSR agree with the 0.7-2% of Hyndman et al. (1992).

Table A.1: Resulting errors for the BSR-derived heat flow calculation.

Resulting error	Value	Percentage [%]
$e(z_{SFL})$	10-19 m	<2
$e(z_{BSRmbsf})$	15-22 m	7-18
$e(z_{BSRmbsl})$	28-38 m	1-3
$e(p_{BSR})$	280-380 kPa	1-3
$e(T_{BSR})$	$<0.1°C$	<2
$e(Tgrad)$	8-60 °C km^{-1}	11-24
$e(H)$	18-110 mW m^{-2}	19-34

Estimation of the error of the geothermal gradient ($e(Tgrad)$) required the error of the seafloor temperature. Although the seafloor temperature is well constrained from the available CTD data, the data may not be representative for the entire study area and for the long-term average that controls the subbottom temperatures. Therefore, we assumed an error of 0.5°C for the seafloor temperature.

The thermal conductivity can often be approximated by a mean value (Grevemeyer and Villinger, 2001). The thermal conductivity is well constrained at the ODP sites and the value of 1.3 W m^{-1} K^{-1} also agrees with our heat flow probe measurements. We therefore assumed only a small error of 0.1 W m^{-1} K^{-1} for the thermal conductivity.

The final absolute uncertainty was 11-24% for the geothermal gradient and 19-34% for the heat flow uncertainty ($e(H)$). Our estimates agree with those of Grevemeyer and Villinger (2001), who estimated uncertainties of 5-35% for the geothermal gradient and 10->50% for the heat flow, and Ganguly et al. (2000), who calculated a total error of 20% for the BSR-derived heat flow. Obviously, within our study area, relative errors from one site to another are much lower, as the individual parameters do not vary randomly.

We note that the method involved another assumption, i.e., that the curve of methane hydrate stability used in the calculation is correct. If this is not the case because the gas composition differs from that of Smith et al. (2014), a different curve may introduce an error of more than 20% of the estimated heat flow (Hyndman et al., 1992). Again, this would only change the absolute values but not the spatial pattern.

Model parameters of Run 4

Table A.2: Geological model for model run 4. Layer thicknesses are given for different percentages of thicknesses determined at ODP Site 909, starting with 100%. The same thicknesses are used for site A and site B. The remaining model parameters are as given in Table 2.1.

Layer	Unit	Layer thickness [m]					
		100%	150%	200%	250%	300%	350%
8	I[a]	249[a]	374	498	623	747	872
7	II[a]	269[a]	404	538	673	807	942
6	IIIA[a]	405[a]	608	810	1013	1215	1418
5	IIIB − 1[b]	52[a,b]	78	104	130	156	182
4	IIIB − 2[b]	48[a,b]	72	96	120	144	168
3	IIIB − 3[b]	39[a,b]	59	78	98	117	137

[a]Shipboard Scientific Party (1995b), [b]Knies and Mann (2002)

A.2 Supporting information: Case study 3 - Svalbard margin seeps

Materials and Methods 1: Numerical model of the GHSZ

The MASOX observatory was deployed at 396 m water depth from 2010-10-15 until 2011-08-05 and at 389 m water depth from 2011-08-08 until 2012-08-18. The observatory contained a CTD, which acquired bottom-water temperature measurements every 15 minutes during both deployments. The two time series were merged into one, the resolution was reduced to daily means, and the three-day gap between the deployments of the observatory was interpolated. We selected the time interval from 2010-10-16 until 2011-10-16 as a generic annual time series because of the very small temperature difference between start and end (Fig. 4.3), noticing however, that the absolute temperature may be offset from the long-term average. The resulting time series was repeated for the duration of the modeling time and applied as a changing temperature boundary condition at the seafloor in a two-dimensional finite element model of time-dependent heat conduction in COMSOL Multiphysics.
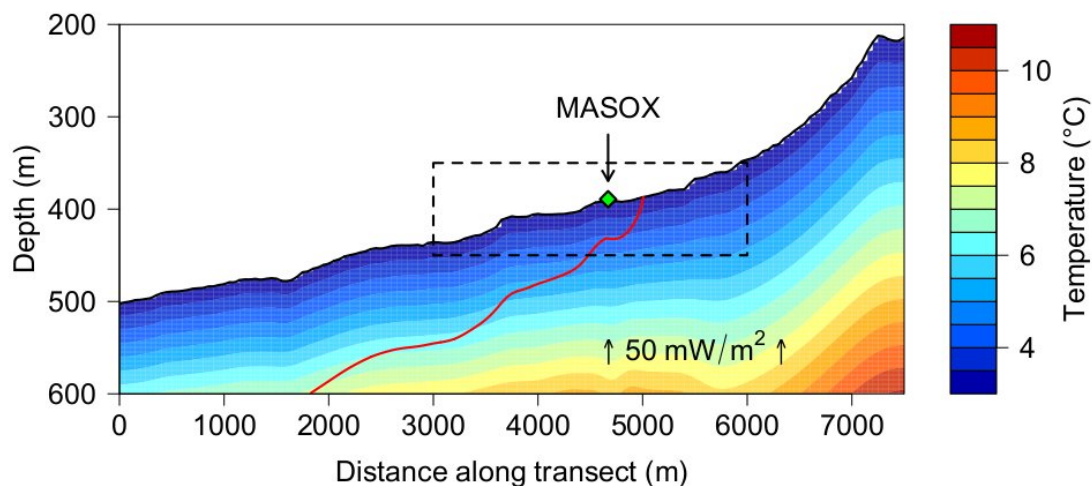

Figure A.2: Setup and initial temperature distribution of the numerical model. The lower boundary condition was a constant heat flow of 0.05 W m^{-2} into the model domain. Both sides of the model domain were thermally insulated. During each time step, the temperature along the entire seabed boundary was constant. At the start of the simulation, the temperature distribution in the sediment was in equilibrium with the median value of the bottom water temperature in a generic year. The solid red line shows the corresponding limit of the GHSZ. The dashed lines mark the section of the model domain that is shown in Fig. 4.3 and in the animation available in the supporting online material (http://www.sciencemag.org/content/suppl/2014/01/02/science.1246298.DC1.htm).

The model domain comprised a 7.5-km-long transect orthogonal to the slope from 502 to 214 m water depth and reached down to 600 m depth below sea floor (Fig. A.2). Using a 6-m-long heat flow probe, we conducted in situ thermal conductivity measurements at 26 stations along the transect line. The measurements were evaluated according to Villinger and Davis (1987). The thermal conductivity along this section of the slope varied between 1.5 and 2.6 W m^{-1} K^{-1} (Fig. A.3). Using the mixing model of Woodside and Messmer (1961) and assuming values of thermal

conductivity of 0.6 W m^{-1} K^{-1} for the pore water and 5 W m^{-1} K^{-1} for the quartz-rich solid phase, the range of thermal conductivity of the bulk sediment may be explained by values of porosity of between 34% and 57%.
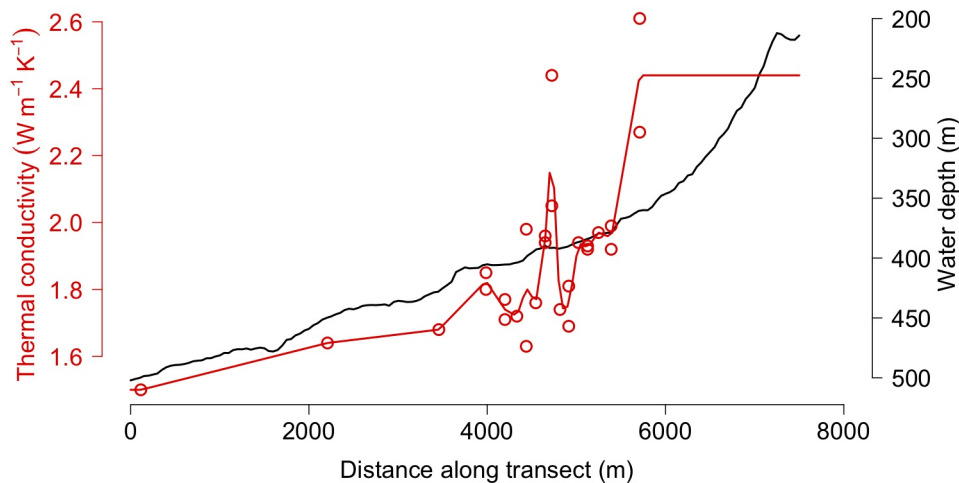

Figure A.3: Thermal conductivity of the sediment and water depth along the transect line. The red circles indicate the results of in situ measurements using the 6-m-long heat flow probe. The red line represents the values used in the numerical model.

The remaining properties of the sediment in the numerical model were defined according to this porosity model (Table A.3). All properties are constant in the vertical direction, but vary in the horizontal direction.

Based on our in situ sediment temperature measurements at 500 m water depth, the heat flow across the lower boundary into the model domain was set constant to 0.05 W m^{-2}. Both sides of the model domain were thermally insulated. The length of the time steps was limited to a maximum of half a day and at the seabed boundary, the cell size of the finite element mesh was limited to one square meter.

In order to eliminate artificial long-term changes during the simulation, the initial temperature distribution in the model was chosen to be in equilibrium with the median value of the generic annual bottom-water temperature time series (3.01757°C). The same time series was applied repeatedly for thirty years of modeled time, such that changes between successive years were negligible. During the 31st and 32nd year of the simulation, the bottom water temperature time series obtained from the two deployments of the MASOX observatory was applied as bottom water temperature boundary condition. The limit of the GHSZ was determined for the beginning and the middle of each month, assuming pure methane hydrates, a salinity of 35 PSU, and sulfate-free pore water (Tishchenko et al., 2005), which is consistent with the coring results. Pressure was converted to depth following Saunders (1981) and taking into account a standard atmospheric pressure of 101,325 Pa. The consumption and release of heat during hydrate dissociation and formation, respectively, were not included in the simulation.

Table A.3: Parameters of the numerical model.

	Parameter	Value
p_{Atm}	atmospheric pressure	101,325 Pa
q	background heat flow	0.05 W m^{-2}
T_0	initial bottom-water temperature	3.01757°C
k	thermal conductivity of the bulk sediment	1.50 to 2.44 W m^{-1} K^{-1}
k_W	thermal conductivity of water	0.6 W m^{-1} K^{-1}
k_S	thermal conductivity of sediment grains	5 W m^{-1} K^{-1}
$\Phi = log(\frac{k}{k_S})/log(\frac{k_W}{k_S})$	porosity	0.34 to 0.57
c_w	specific heat capacity of water	4184 J kg^{-1} K^{-1}
c_S	specific heat capacity of sediment grains	300 J kg^{-1} K^{-1}
$c = c_w\Phi + c_S(1-\Phi)$	specific heat capacity of bulk sediment	1614 to 2505 J kg^{-1} K^{-1}
ρ_w	density of water	1025 kg m^{-3}
ρ_S	density of sediment grains	2650 kg m^{-3}
$\rho = \rho_w\Phi + \rho_S(1-\Phi)$	density of bulk sediment	1727 to 2100 kg m^{-3}

Materials and Methods 2: U-Th geochronology & light stable isotopes of authigenic carbonates

Sample material and sub-sampling

During R/V Maria S. Merian cruise MSM21/4 massive carbonates and carbonate-enriched sediments were sampled by the submersible JAGO and by gravity coring (GC). Here, we present the analysis of surface and gravity corer samples from the MASOX site. They presumably represent the least mature authigenic precipitates from the deepest active methane emanation site sampled during MSM21/4. As reference two samples from the HyBIS site are also presented. Samples were dried at 20°C for 12 hrs and gently cleaned from loosely bound sediment remains. Homogeneous subsamples were collected by drilling material from solidified samples by a handheld mm-sized mini-drill and from less consolidated surrounding sediments. From the solidified samples the surface of each sub-sampling spot was scoured away in an area of ∼5×5 mm. Subsequently, the original sample powder was extracted by drilling small cavities. Prior to aliquot procedures all samples were finely ground in an agate mortar providing homogeneous aliquots of suitable grain size for the combined approach of mineral identification by X-ray diffractometry (XRD), δ^{18}O and δ^{13}C analyses by stable isotope ratio mass spectrometry (SIRMS) as well as for U-Th geochronology by multi-collector inductively-coupled plasma mass spectrometry (MC-ICP-MS).

X-ray diffraction analyses

We analyzed representative aliquots and semi-quantitatively identified minerals using X-ray diffraction (XRD) with a Philips X-ray diffractometer PW 1710 in monochromatic CuKα mode between 2 and 70 2θ (incident angle). Note, especially on small sample aliquots of few 10 mg as required in this study relative quantifications are generally accompanied by large uncertainties. Furthermore,

the sensitivity for mineral identification is typically restricted to fractions greater than 5% and significant amounts remained not identified. Resulting spectra were analysed with the software XPowder (XPowder, Spain).

Light stable isotope analysis (δ^{18}O and δ^{13}C)

From each homogenized carbonate powder sample (see above), an aliquot of 10 mg was separated for carbon δ^{13}C and oxygen δ^{18}O stable isotope analysis. A small part (approximately 1 mg) of this powder was dissolved by water-free phosphoric acid at 73°C in a "Carbo-Kiel" (Thermo Fisher Scientific) online carbonate preparation line and measured for carbon and oxygen stable isotope ratios with a MAT 253 mass spectrometer (Thermo Fisher Scientific). The δ^{13}C and δ^{18}O values were calculated as deviations from laboratory standard referred to the PDB scale and reported in ‰ relative to V-PDB. The reproducibility was confirmed by replicate analyses of laboratory standards as being usually better than ± 0.02‰ for δ^{13}C and δ^{18}O (1SD). In case of larger uncertainties of individual sample measurements, typical for impure materials, the higher value is presented.

U–Th geochronology

This study is based on U–Th age data determined for rather small samples (5.5 to 55.5 mg aliquots of the XRD and light stable isotope samples) in order to combine high structural resolution with the analytical precision of MC-ICP-MS. The U–Th isotope measurements were performed on a VG Elemental AXIOM MC-ICP-MS at GEOMAR applying the multi-static MIC (multi-ion-counting)-ICP-MS approach after Fietzke et al. (2005). For isotope dilution measurements a combined $^{233/236}$U/^{229}Th spike was used, with stock solutions calibrated for concentration using NIST-SRM3164 (U) and NIST-SRM3159 (Th) as combi-spike calibrated against CRM-145 uranium standard solution (also known as NBL-112A) for U-isotope composition, and against a secular equilibrium standard (HU-1, uranium ore solution) for determination of ^{230}Th/^{234}U activity ratio. Whole procedure blank values of this sample set were measured around 0.1 fg for ^{230}Th, around 7 pg for ^{232}Th and between 3 and 10 pg for U, which are in the typical range of this method and laboratory. Element separation procedure was based on Eichrom-UTEVA resin. Calculation of geochronological data and activity ratios is based on the decay constants given by Cheng et al. (2000).

From all original MASOX subsamples powder aliquots were attacked by 4 N acetic acid in order to provide weak leachates mainly dissolving the carbonate phase. Accepting that fractionation of U and Th may lead to a potential loss of ^{230}Th due to their difference in particle reactivity, these weak leachates result in minimum values in the direct ^{230}Th/^{234}U age determination. Where available, an additional powder aliquot of the original sample (marked by sample code suffix -2) was attacked by 2.25 N HNO$_3$ to provide a stronger leachate and potentially significant isochron spread. The 2.25 N HNO$_3$ attack was the only one applied to two aragonite-dominated HyBIS samples (see Table S2 provided in the supporting online material at http://www.sciencemag.org/content/suppl/-2014/01/02/science.1246298.DC1.htm).

Runs of aliquots of the HU-1 equilibrium standard solution to verify procedure reproducibility accompanied each set of element separation. A methodology dependent uncertainty of less than 0.5% on ^{230}Th/^{234}U activity ratios was reached. The geochronological uncertainties presented here are dominated by the analytical error of individual sample measurements and the uncertainty of correction factors. The applied data reduction includes a correction for isotopic composition of incorporated Th of detrital origin, according to average continental crust values (Wedepohl, 1995) as approximation for involved shelf sediments (see notes below Table S2 (supporting online material) for details). For the majority of the sub-samples the uncertainty of this correction is negligible, but some are dominated and even overcompensated to negative ^{230}Th/^{234}U activity ratios, due to low ^{230}Th/^{232}Th activity ratios and extreme high Th concentrations. An additional, more exact determination of potentially deviating isotope signatures of dissolved Th in the precipitation feeding cold seep fluid is hampered by the lack of adequate fluid sample material. An alternative, site-specific approach for isochron-based Th corrections, applicable for cold seep carbonates with elevated Th content is presented in a detailed small-scale case study by Bayon et al. (2009). The different scope and related sample selection strategy of our study is focused on direct age determination of single phases of predominately aragonitic composition as discussed in Liebetrau et al. (2010). However, Rosholt and Osmond isochron approaches presented here are based on the isoplot 3.75 software of the Berkeley Geochronology Center (CA, USA; Ludwig, 2008) and provide age estimates for two-point reference lines. The corresponding accuracy and reliability is limited by the fact that the measurements of the individual inherited detrital phase and adjacent pure sediment could not be finished during this initial measurement session. The ^{234}U/^{238}U ratios are presented in δ^{234}U notation (see notes below Table S2 (supporting online material) for details).

Geochronological implications

Characterized by generally low ^{230}Th/^{232}Th activity ratios, high Th concentration and low Ca-carbonate content, only few weak leachates provide the potential for single minimum age determination.

At ^{230}Th/^{232}Th activity ratios from 4.7 to 2.2 and δ^{13}C values from -41 to -32 ‰ (V-PDB) deduced single ages for MASOX samples are 6600 ± 400 yr (SV21), 11,900 ± 2600 yr (SV23-1), 3400 ± 300 yr (SV28) and 5000 ± 1100 yr (SV29) B.P. These data are supported by individual 2-point isochron reference lines of different leachates and parallel samples, covering at least similar age ranges (Table S2, supporting online material). The two latter samples are dominated by aragonite and represent the surface exposed today. Especially SV29, the most reliable aragonitic sample, reflects an age of authigenic carbonate precipitation similar to the findings on solidified material within the upper GC section (SV21).

With the caveat that the heterogeneous carbonates result in considerable uncertainty, the deduced ages for the GC samples increase systematically with depth suggesting a precipitation front following the prograding sediment deposition. The indicated age difference of approximately 5000 years between SV21 and SV23 and their depth difference of approximately 50 cm indicate a sedimentation rate around 0.1 mm/y, which is in accordance with outer shelf environments. The shallowest and

almost unconsolidated GC sample with highest δ^{13}C values of -27 ‰ (V-PDB) at lowest leachate yields of only 6 to 13% (SV20) and ^{230}Th/^{232}Th activity ratios around 1 seems to represent the least mature sample of this data set. This sample does not provide a reliable single age determination. However, a distinct isochron reference line suggests a precipitation phase around 550 ± 40 yr B.P., the youngest found so far. The 3-dimensional (3D-Rosholt1) and 2-dimensional (Osmond) isochron reference lines (see Table S2 (supporting online material) for all required isotope ratios) provide important additional age indications, but due to the restriction on 2-point correlations the results are hampered by system-immanent underestimation of the uncertainties as their spread is dominated by the relatively precise individual isotope measurements of two subsamples and not by the potentially much larger distortion of the correlation coefficient from further subsamples.

However, independent support of the early onset of methane emanation stems from two aragonite dominated surface samples from the HyBIS site reflecting low δ^{13}C values around -37 ‰ (V-PDB) and U-Th ages of 8200 ± 500 yr B.P. (SV-2) and 4600 ± 500 yr B.P. (SV-3) at rather high ^{230}Th/^{232}Th activity ratios of 5.12 ± 0.07 and 3.44 ± 0.04, respectively, when compared to the MASOX values (Table S2, supporting online material). The U measurements for these two samples were performed on a quadrupole inductively-coupled plasma mass spectrometer (Q-ICP-MS).

Materials and Methods 3: Fate of emitted methane in the water column

At the gas flares, significant amounts of methane were liberated into the water column, leading to bottom-water CH_4 concentrations of up to 825 nM and a net flux of methane to the atmosphere. A fraction of CH_4 was consumed at rates of up to 3.06 nM d^{-1} (Fig. A.4) in the lower part of the water column, but CH_4 concentrations in the well-mixed surface waters ($\sim$9 nM) were still generally exceeding the atmospheric equilibrium of $\sim$3 nM. This excess indicates that the seeps off the coast of Svalbard are a net - though small - CH_4 source to the atmosphere. Water column samples were collected from discrete depths at the MASOX and the HyBIS sites (Fig. 4.1) with a CTD/Rosette sampler equipped with 24 10-litre Teflon-lined Niskin bottles and a CTD device (Seabird SBE 9). Immediately upon recovery, we subsampled the Niskin bottles for onboard measurement of CH_4 concentrations and aerobic methane oxidation (MOx) rates. Methane concentrations were determined with a headspace method from $\sim$ 600 ml aliquots, which were subsampled bubble-free into triple-layer Evarex Barrier Bags (Oxford Nutrition, U.K.). A high-purity nitrogen headspace (20 ml) was added, and samples were vigorously shaken and allowed to equilibrate for several hours before subsampling 2 ml headspace for CH_4 quantification with a gas chromatograph (GC, Agilent 7890A) equipped with a packed stainless steel column (6 ft., 2 mm i.d.; 80/100 mesh HayeSep Q) and a flame ionisation detector. The GC was operated isocratically (60°C) with N_2 as carrier gas (33 ml min^{-1}). The analytical error of CH_4 concentrations is ±5% (standard deviation) as determined from triplicate subsamples. Seawater methane concentrations and the degree of saturation with respect to the atmospheric equilibrium were calculated with consideration of sample/headspace volume, temperature, salinity, atmospheric pressure and atmospheric CH_4 mixing ratio (Wiesenburg and Guinasso, 1979; Fisher et al., 2011). MOx rates were measured with a radio-tracer (^{3}H-CH_4) based assay (Reeburgh et al., 1991; Valentine et al.,

2001). Subsamples were collected in quadruplicate in 20 ml crimp top serum glass vials and sealed bubble-free with bromo-butyl stoppers (Helvoet Pharma, Belgium). Each subsample was amended with ^{3}H-labelled CH_4 (10 μl CH_4/N_2 mixture: $\sim$25 kBq, $<$50 pmol CH_4, American Radiolabeled Chemicals, USA) within a few h after subsampling and incubated for 72 h at in situ T ($\sim$4°C) in the dark. Total activity (^{3}H-CH_4 + ^{3}H-H_2O) was subsequently determined from a 2 ml sample aliquot by wet scintillation. The remaining sample was purged for 30 min with a constant stream of air ($\sim$50 ml min^{-1}) to remove unreacted CH_4 before measuring the activity of ^{3}H-H_2O from a 2 ml aliquot. We calculated MOx rates from the fractional turnover of labeled CH_4 and water column CH_4 concentrations assuming first order kinetics. MOx rates were corrected for (insubstantial) tracer turnover in killed controls (amended with 100 μl saturated HgCl).
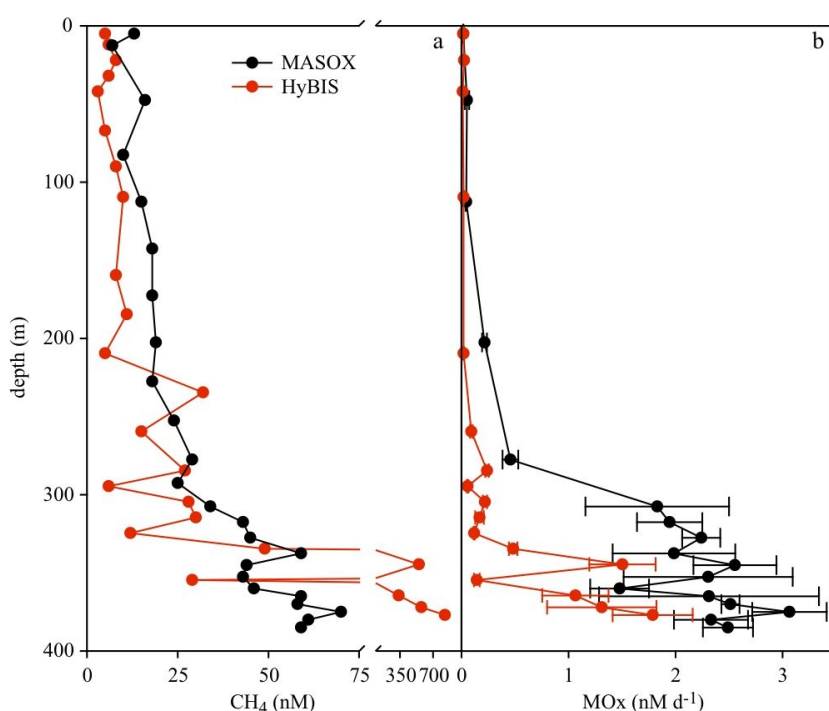

Figure A.4: Vertical profiles of **(A)** methane concentrations and **(B)** rates of aerobic methane oxidation in the water column at two active seepage sites off the coast of Svalbard. Errors are represented as standard deviation. Methane concentrations and rates of aerobic methane oxidation were variable but generally highest in bottom waters.

Methane concentrations were highest in bottom waters (Fig. A.4A) and decreased towards the sea surface. MOx rates showed similar trends (Fig. A.4B). However, MOx rates were substantially lower at the HyBIS site despite a $\sim$10-fold higher bottom water CH_4 concentrations. The decrease in CH_4 concentrations from seafloor to surface samples thus appears to be controlled by MOx as well as other factors, probably dilution and horizontal mixing by bottom currents. Nevertheless, CH_4 concentrations in the well-mixed surface waters (sampled at 4-5 m water depth, $\sim$9 nM) were supersaturated with respect to the atmospheric equilibrium (3 nM; calculated using Bunsen solubility coefficients from Wiesenburg and Guinasso (1979) and local atmospheric methane concentrations from Fisher et al. (2011) indicating a net CH_4 efflux from the water column above the Svalbard seeps to the atmosphere at least during the time of observation (Wanninkhof et al.,

2009). However, efflux from ∼300% methane saturation of surface waters was not found to produce pronounced local atmospheric methane anomalies in a study from the Black Sea (Schmale et al., 2005). Thus, the influence on the local atmospheric methane budget of the Svalbard seeps is probably minor.
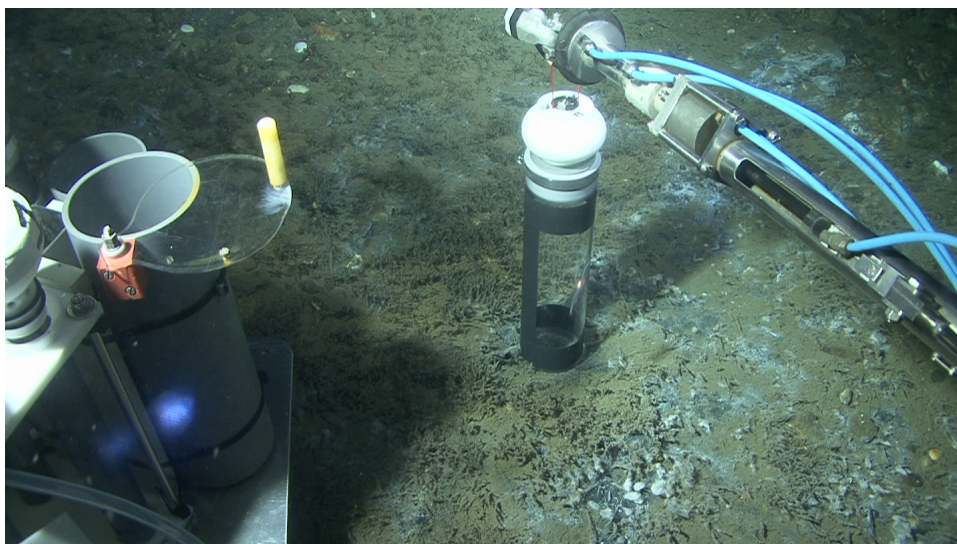

Figure A.5: Deployment of a sediment pushcore by the submersible Jago in a methane seep field at the HyBIS site. The sediment is covered by sulfur bacteria mats (white) and frenulate tubeworms (grass-like structures), which are typically found at methane seep locations featuring high activity of anaerobic oxidation of methane in the surface sediment (Treude et al., 2003; Niemann et al., 2006).

Geochemical analyses of surface sediments

Sediments were collected at the HyBIS and MASOX sites either with push cores (i.d. 60 and 26 mm) operated by the submersible JAGO or with a gravity corer (i.d. 120 mm). Push cores were taken in areas of visible gas releases and the presence of chemosynthetic communities (sulfur bacteria mats, frenulate tubeworms, Fig. A.5). The gravity core at the MASOX site was taken at a location at which gas flares were observed in the water column on EK60 profiles just prior to coring, and where the presence of extensive sulfur bacteria mats was confirmed by JAGO dives. From the 60 and 120 mm cores, a sediment sample of 2 cm^3 was taken with a cut-off plastic syringe to determine the methane concentration. The sample was then transferred into a 10 ml glass vial filled with 5 ml sodium hydroxide (2.5% w/w). The vial was closed immediately with a butyl rubber stopper, sealed with an aluminum crimp, and shaken thoroughly to equilibrate the pore water methane between the aqueous and the gaseous phases. After equilibration, the methane concentration of the sample was analysed with a gas chromatograph equipped with a flame ionization detector. Sediment pore water was squeezed from sediment sections of the 60 and 120 mm cores using a pressure filtration system at pressures up to 5 bar and filtered through 0.45 μm cellulose acetate membrane filters. Pore water samples were then immediately analysed onboard to

determine total alkalinity (Ivanenkov and Lyakhin, 1978) and sulfide concentrations (Cline, 1969). Rates of anaerobic oxidation of methane (AOM) were determined in the 26 mm cores using the whole-core injection method (Jørgensen, 1978). Radioactive methane tracer (aliquots of 5 kBq $^{14}CH_4$ dissolved in 15 μl water) were injected into the cores in 1-cm intervals. The cores were incubated at in situ temperature for 24 h in the dark. After incubation, reactions were terminated by fixing 1-cm sections in 2.5% sodium hydroxide. In control samples, activity was terminated before tracer addition. Methane oxidation rates were determined by gas chromatography, $^{14}CH_4$ combustion and $^{14}CO_2$ acidification as described in detail by Treude et al. (2005).

A.3   Acknowledgements

First of all, I want to thank Christian Berndt for the supervision and guidance over the past three years. I am very grateful that I could come by your office whenever I was in need of advice or feedback, and that you took the time to explain processes and discuss my research. I have learned a lot from these discussions. You also showed me that there was still a promising outcome from the cruise to the Giant Gjallar Vent, even though almost everything that could possibly go wrong did go wrong on this cruise and we could not acquire the P-Cable cube that would otherwise have constituted the bulk part of my PhD work. I also thank you for encouraging me to step out of my seismic/sidescan comfort zone and experiment with other methods like heat flow analyses and numerical modelling, which provided interesting additional insights.

I would like to thank Sebastian Krastel for being my second assessor.

I thank Volker Liebetrau for agreeing to be my second supervisor without even having met me before. As we never got those seafloor samples from the Giant Gjallar Vent, our collaboration was not as close as we had planned originally, but the thesis committee meetings were nevertheless enriched by your different point of view as a geochemist. I certainly know a lot more about carbonates now than I did when I started out on this project. Also, through our discussions I have learned that geochemical processes can be a lot more complex than a geophysicist would assume!

I thank the Future Ocean Cluster of Excellence for funding of my PhD position, and the Integrated School of Ocean Sciences (ISOS) for the PhD support framework provided. Although the compulsory reports and thesis committee meeting protocols sometimes required a certain effort to write, they helped me to focus and reflect on the progress of my work. I also benefitted from the PhD courses offered by ISOS, especially those on scientific writing.

I am grateful to all the colleagues who contributed to this work through discussions, advice, data processing, and help with software and Linux problems: Jörg Bialas, Ewa Burwicz, Gareth Crutchley, Jens Karstens, Dirk Kläschen, Ingo Klaucke, Stephanie Koch, Anne Krabbenhöft, Cord Papenberg, Sudipta Sarkar, Willi Weinrebe, and Timo Zander. Anne Krabbenhöft and Timo Zander are also thanked for proofreading parts of the thesis.

I wish to thank Christian Berndt, Jörg Bialas, Ingo Klaucke, Heidrun Kopp, and Sebastian Krastel, who let me participate in six different cruises that took up more than four months of my PhD time and greatly broadened my horizon – not just geographically, but especially in a scientific sense. Compared to the times I went on cruises as a lowly student assistant, I was entrusted with more and more responsibilities during those cruises, which gave me the feeling that I am now taken seriously as a scientist. The highlight of these cruises – and in fact, the highlight of my entire PhD time – was the Jago dive to the seafloor offshore Svalbard, which allowed me to observe seafloor methane seepage up close – a truly unforgettable experience! I deeply thank Jürgen Schauer, Karen Hissmann, Martin Fenske, and the crew of RV Maria S. Merian for the safe and smooth operations during this dive.

I thank Stephanie Koch and Jens Karstens for the company in two offices throughout the past three years, the many discussions and conversations on both work- and non-work-related issues, and the mutual support in various aspects. It helped a lot to know that I was not alone in this phase but that we were all going through the same process at the same time. It was also great to have someone right there in the room to whom I could turn to when I was stuck with a problem, or needed a second opinion on interpretations or figure design.

I would also like to thank everyone in the Geodynamics group for the nice times there, and especially Stephanie Koch, Anne Krabbenhöft, Anke Dannowski, Cord Papenberg, Timo Zander, Henning Schröder, Jens Karstens, Elodie Lebas, and Judith Elger for the company during lunch breaks and Wednesday morning coffee/tea breaks.

A huge thank you goes to my family for the support in many ways. Thank you for believing that I could do this, for being interested in what I do, for understanding my need (or desire) to go on cruises for weeks on end, and for providing a refuge where I could take a break from PhD life.

In addition to my family, I also want to thank my friends as well as the orchestra of the CAU Kiel for providing a counterbalance to my PhD life.

Finally, I want to thank Timo for being with me during the entire PhD time. Thank you for your support, advice, and encouragements, and for patiently listening to all my thesis-related problems and worries, especially during those last stressful weeks.

A.4 Curriculum Vitae

Ines Dumke

Date of birth	28 August 1986
Place of birth	Hannover
Citizenship	German
Permanent address	Sternstr. 10-12
	24116 Kiel

Education

since 01/2012	PhD student at GEOMAR Helmholtz Centre for Ocean Research Kiel
12/2012	MSc in Geophysics
02/2010 - 11/2010	studies in Geosciences, Marine Sciences and Surveying at University of Otago, Dunedin, New Zealand
10/2009 - 12/2011	studies in Geophysics at Christian-Albrechts-University Kiel
09/2009	BSc in Applied Geophysics
10/2006 - 09/2009	studies in Applied Geophysics at Christian-Albrechts-University Kiel
06/2006	Abitur
08/2003 - 01/2004	St. Aloysius Secondary School, Cork, Ireland
08/1999 - 06/2006	Gymnasium Käthe-Kollwitz-Schule, Hannover